# Defined microphysiologic 3D tumour models with aspects from the tumour microenvironment for the evaluation of cellular immunotherapies

# Definierte mikrophysiologische 3D-Tumormodelle mit Aspekten aus der Tumormikroumgebung zur Evaluierung von zellulären Immuntherapien

Doctoral thesis for a doctoral degree

at the Graduate School of Life Sciences (GSLS),

Julius-Maximilians-Universität Würzburg,

Section Biomedicine

submitted by

**Johanna Kühnemundt**

born in Würzburg

conducted at

*Chair Tissue Engineering & Regenerative Medicine*

of the

*University Hospital Würzburg*

Würzburg 2021

"For an idea that does not first seem insane, there is no hope."

„Wenn eine Idee am Anfang nicht absurd klingt, dann gibt es keine Hoffnung für sie.“

~Albert Einstein~

Submitted on: …………………………………………………………..……..

*Members of the Thesis Committee:*

Chairperson: Prof. Dr. Markus Sauer

Primary Supervisor: Prof. Dr. Heike Walles

Supervisor (Second): Prof. Dr. Michael Hudecek

Supervisor (Third): Dr. Julia Schüler

Supervisor (Fourth): Dr. Gudrun Dandekar

Date of Public Defence: …………………………………………….…………

Date of Receipt of Certificates: ……………………………………………….

# Table of contents

## Abstract

Adoptive cellular immunotherapy with chimeric antigen receptor (CAR) T cells is highly effective in haematological malignancies. This success, however, has not been achieved in solid tumours so far. In contrast to hematologic malignancies, solid tumours include a hostile tumour microenvironment (TME), that poses additional challenges for curative effects and consistent therapeutic outcome. These challenges manifest in physical and immunological barriers that dampen efficacy of the CAR T cells.

Preclinical testing of novel cellular immunotherapies is performed mainly in 2D cell culture and animal experiments. While 2D cell culture is an easy technique for efficacy analysis, animal studies reveal information about toxicity *in vivo*. However, 2D cell culture cannot fully reflect the complexity observed *in vivo,* because cells are cultured without anchorage to a matrix and only short-term periods are feasible. Animal studies provide a more complex tissue environment, but xenografts often lack human stroma and tumour inoculation occurs mostly ectopically.

This emphasises the need for standardisable and scalable tumour models with incorporated TME-aspects, which enable preclinical testing with enhanced predictive value for the clinical outcome of immunotherapies. Therefore, microphysiologic 3D tumour models based on the biological SISmuc (Small Intestinal mucosa and Submucosa) matrix with preserved basement membrane were engaged and improved in this work to serve as a modular and versatile tumour model for efficacy testing of CAR T cells. In order to reflect a variety of cancer entities, TME-aspects, long-term stability and to enhance the read-out options they were further adapted to achieve scalable and standardisable defined microphysiologic 3D tumour models.

In this work, novel culture modalities (semi-static, sandwich-culture) were characterised and established that led to an increased and organised tissue generation and long-term stability. Application of the SISmuc matrix was extended to sarcoma and melanoma models and serial bioluminescence intensity (BLI)-based *in vivo* imaging analysis was established in the microphysiologic 3D tumour models, which represents a time-efficient read-out method for quality evaluation of the models and treatment efficacy analysis, that is independent of the cell phenotype.

Isolation of cancer-associated-fibroblasts (CAFs) from lung (tumour) tissue was demonstrated and CAF-implementation further led to stromal-enriched microphysiologic 3D tumour models with *in vivo*-comparable tissue-like architecture. Presence of CAFs was confirmed by CAF-associated markers (FAP, α-SMA, MMP-2/-9) and cytokines correlated with CAF phenotype, angiogenesis, invasion and immunomodulation. Additionally, an endothelial cell barrier was implemented for static and dynamic culture in a novel bioreactor set-up, which is of particular interest for the analysis of immune cell diapedesis. Studies in microphysiologic 3D Ewing's sarcoma models indicated that sarcoma cells could be sensitised for $G_{D2}$-targeting CAR T cells.

After enhancing the scale of assessment of the microphysiologic 3D tumour models and improving them for CAR T cell testing, the tumour models were used to analyse their sensitivity towards differently designed receptor tyrosine kinase-like orphan receptor 1 (ROR1) CAR T cells and to study the effects of the incorporated TME-aspects on the CAR T cell treatment respectively. ROR1 has been described as a suitable target for several malignancies including triple negative breast cancer (TNBC), as well as lung cancer. Therefore, microphysiologic 3D TNBC and lung cancer models were established. Analysis of ROR1 CAR T cells that differed in costimulation, spacer length and targeting domain, revealed, that the microphysiologic 3D tumour models are highly sensitive and can distinguish optimal from sub-optimal CAR design. Here, higher affinity of the targeting domain induced stronger anti-tumour efficacy and anti-tumour function depended on spacer length, respectively. Long-term treatment for 14 days with ROR1 CAR T cells was demonstrated in dynamic microphysiologic 3D lung tumour models, which did not result in complete tumour cell removal, whereas direct injection of CAR T cells into TNBC and lung tumour models represented an alternative route of application in addition to administration via the medium flow, as it induced strong anti-tumour response.

Influence of the incorporated TME-aspects on ROR1 CAR T cell therapy represented by CAF-incorporation and/or TGF-β supplementation was analysed. Presence of TGF-β revealed that the specific TGF-β receptor inhibitor SD-208 improves ROR1 CAR T cell function, because it effectively abrogated immunosuppressive effects of TGF-β in TNBC models. Implementation of CAFs should provide a physical and immunological barrier towards ROR1 CAR T cells, which, however, was not confirmed, as ROR1 CAR T cell function was retained in the presence of CAFs in stromal-enriched microphysiologic 3D lung tumour models. The absence of an effect of CAF enrichment on CAR T cell efficacy suggests a missing component for the development of an immunosuppressive TME, even though immunomodulatory cytokines were detected in co-culture models. Finally, improved gene-edited ROR1 CAR T cells lacking exhaustion-associated genes (PD-1, TGF-β-receptor or both) were challenged by the combination of CAF-enrichment and TGF-β in microphysiologic 3D TNBC models. Results indicated that the absence of PD-1 and TGF-β receptor leads to improved CAR T cells, that induce strong tumour cell lysis, and are protected against the hostile TME.

Collectively, the microphysiologic 3D tumour models presented in this work reflect aspects of the hostile TME of solid tumours, engage BLI-based analysis and provide long-term tissue homeostasis. Therefore, they present a defined, scalable, reproducible, standardisable and exportable model for translational research with enhanced predictive value for efficacy testing and candidate selection of cellular immunotherapy, as exemplified by ROR1 CAR T cells.

# Zusammenfassung

Die adoptive Immuntherapie mit chimären Antigenrezeptor (CAR) exprimierenden T-Zellen zeigt bei hämatologischen Krebsformen eine hohe Wirksamkeit. Bisher konnte dieser Erfolg für solide Tumore nicht erreicht werden. Im Gegensatz zu hämatologischen Krebsformen zeigen solide Tumore eine feindliche Tumormikroumgebung (TME), die zusätzliche Herausforderungen für die Erlangung kurativer Effekte und konsistenter Therapieergebnisse darstellen. Diese Herausforderungen äußern sich in physikalischen und immunologischen Barrieren, welche die Wirksamkeit der CAR-T-Zellen abschwächt.

Zur präklinischen Testung neuartiger zellulärer Immuntherapien werden hauptsächlich 2D-Zellkulturen und Tierstudien durchgeführt. 2D-Zellkulturexperimente eignen sich vor allem für Wirksamkeitsanalysen, während Tierstudien Aufschluss über die Toxizität *in-vivo* geben können. Allerdings kann die 2D-Zellkultur die Komplexität der *in-vivo* Situation nicht vollständig widerspiegeln, da die Zellen ohne Verankerung an einer Matrix kultiviert werden und nur kurzfristige Zeiträume abgebildet werden können. Tierstudien bieten einen komplexeren Gewebekontext, wobei Xenografts aber oft das humane Stroma fehlt und die Tumorinokulation meist ektopisch erfolgt.

Dies unterstreicht den Bedarf an standardisierbaren und skalierbaren Tumormodellen mit inkorporierten TME-Aspekten, die präklinische Testungen mit erhöhtem Vorhersagewert für den klinischen Erfolg von Immuntherapien ermöglichen. Daher wurden in dieser Arbeit mikrophysiologische 3D-Tumormodelle auf Basis der biologischen SISmuc (Small Intestinal mukosa und Submukosa)-Matrix mit erhaltener Basalmembran eingesetzt und verbessert, um als modulares und vielseitiges Tumormodell für die Wirksamkeitsprüfung von CAR T-Zellen zu dienen. Um eine Vielzahl von Krebsentitäten, TME-Aspekte und Langzeitstabilität abzubilden und um die Ausleseparamter zu verbessern, wurden die Tumormodelle weiter angepasst um skalierbare und standardisierbare definierte mikrophysiologische 3D Tumormodelle zu erhalten.

In der vorliegenden Arbeit wurden neue Kulturmodalitäten (semistatische Kultur, Sandwich-Kultur) charakterisiert und etabliert, die zu einer vermehrten und erhöhten Gewebebildung sowie Langzeitstabilität der Modelle führen. Die Anwendung der SISmuc-Matrix wurde auf Sarkom- und Melanom-Modelle erweitert und in den mikrophysiologischen 3D-Tumormodellen wurde ein serielles Biolumineszenz-Intensitäts (BLI)-basiertes *In-vivo*-Analyse-Verfahren etabliert, welches eine zeiteffiziente Methode für die Qualitätsbewertung der Modelle sowie die Analyse der Therapiewirksamkeit darstellt, welche unabhängig vom Zell-Phänotyp ist.

Die Isolation von Krebs-assoziierten Fibroblasten (CAFs) aus Lungen-(Tumor) Gewebe wurde demonstriert und die CAF-Implementierung führte des Weiteren zu stromal-angereicherten mikrophysiologischen 3D-Tumormodellen mit *in-vivo* vergleichbarer gewebeähnlicher Architektur. CAFs wurden mit Hilfe von CAF-assoziierten Markern (FAP, α-SMA, MMP-2/-9) und einer Zytokinanalyse in den Modellen identifiziert. Diese bestätigte ebenfalls Zytokine, welche mit Angiogenese, Invasion und Immunmodulation assoziiert sind. Zusätzlich wurde eine Endothelzellbarriere sowohl in statischer als auch in der dynamischen Kultur implementiert, wofür ein neuer Bioreaktoraufbau verwendet wurde, welcher insbesondere für die Analyse der Immunzelldiapedesis interessant ist. Studien in mikrophysiologischen 3D-Ewing-Sarkom-Modellen zeigten, dass diese für $G_{D2}$-spezifische CAR-T-Zellen sensibilisiert werden können.

Nach der Erweiterung des Untersuchungsumfangs der mikrophysiologischen 3D-Tumormodelle und deren Verbesserung für die CAR-T-Zell-Testung wurden die Tumormodelle verwendet, um ihre Sensitivität gegenüber unterschiedlich designten Rezeptor-Tyrosinkinase-like Orphan-Rezeptor 1 (ROR1) -spezifischen CAR-T-Zellen zu analysieren. Des Weiteren wurden die Auswirkungen der eingebauten TME-Aspekte auf die CAR-T-Therapie untersucht. ROR1 wurde als geeignetes Ziel für verschiedene maligne Erkrankungen beschrieben, darunter auch triple-negtive-breast-cancer (TNBC) und Lungenkrebs. Daher wurden mikrophysiologische 3D-TNBC- und Lungenkrebs-Modelle für die Testungen aufgebaut. Die Analyse von ROR1-CAR-T-Zellen, die sich in Kostimulation, Spacerlänge und der Ziel-Domäne unterschieden, zeigte, dass die mikrophysiologischen 3D-Tumormodelle eine hohe Sensitivität zur Unterscheidung von suboptimal und optimal designten CARs aufweisen. Dabei induzierte eine Ziel-Domäne mit höherer Affinität eine stärkere Anti-Tumor-Wirkung. Zusätzlich war die Anti-Tumor-Funktion abhängig von der Spacerlänge. In dynamischen mikrophysiologischen 3D-Lungentumormodellen wurde eine Langzeitbehandlung über 14 Tage mit ROR1-CAR-T-Zellen realisiert, die jedoch nicht zu einer vollständigen Entfernung der Tumorzellen führte. Die direkte Injektion von CAR-T-Zellen in TNBC- und Lungentumormodellen induzierte eine starke Anti-Tumorantwort und stellt somit neben der Zugabe über den Medienstrom einen alternativen Applikationsweg dar.

Des Weiteren wurde der Einfluss der inkorporierten TME-Aspekte auf die ROR1 CAR T-Zelltherapie untersucht, welche sich durch CAF-Inkorporation und/oder TGF-β-Supplementierung darstellten. Die Zugabe von TGF-β zeigte, dass der spezifische TGF-β-Rezeptor-Inhibitor SD-208 die Funktion der ROR1 CAR T-Zellen verbesserte, da er die immunsuppressiven Effekte von TGF-β in TNBC-Modellen effektiv aufhob. Die Implementierung von CAFs sollte eine physikalische und immunologische Barriere gegenüber ROR1 CAR T-Zellen darstellen, was sich jedoch nicht bestätigte, da die Funktion der ROR1 CAR T-Zellen in Anwesenheit von CAFs in stromal-angereicherten mikrophysiologischen 3D-Lungentumormodellen erhalten blieb. Das Fehlen eines Effekts der CAF-Anreicherung auf die

CAR T-Zell-Effektivität deutet auf eine fehlende Komponente für die Entwicklung eines immunsuppressiven TME hin, obwohl immunmodulatorische Zytokine in Co-Kultur-Modellen nachgewiesen wurden. Schließlich wurden verbesserte gen-editierte ROR1-CAR-T-Zellen, denen erschöpfungsassoziierte Gene (PD-1, TGF-β-Rezeptor oder beide) fehlten, durch die Kombination von CAF-Anreicherung und TGF-β in mikrophysiologischen 3D-TNBC-Modellen herausgefordert. Die Ergebnisse zeigten, dass ROR1 CAR T Zellen ohne PD-1 und TGF-β-Rezeptor überlegen sind, eine starke Tumorzell-Lyse induzieren und vor der feindlichen TME geschützt sind.

Zusammenfassend spiegeln die in dieser Arbeit vorgestellten mikrophysiologischen 3D-Tumormodelle Aspekte der feindlichen TME solider Tumore wider, ermöglichen BLI-basierte Analysen und bieten eine langfristige Gewebehomöostase. Daher stellen sie ein definiertes, skalierbares, reproduzierbares, standardisierbares und exportierbares Modell für die translationale Forschung mit erhöhtem Vorhersagewert dar. Sie können für die Wirksamkeitsprüfung sowie Kandidatenauswahl von zellulären Immuntherapie verwendet werden, was vor allem am Beispiel der ROR1 CAR T-Zellen gezeigt wurde.

# List of figures

# List of tables

## List of abbreviations and units

*Table 1. List of abbreviations and units*

| Abbreviation | Meaning |
|---|---|
| % | percent |
| © | copyright |
| ® | registered |
| 2D | two-dimensional |
| 3D | three-dimensional |
| ab | antibody |
| ALL | acute lymphoblasticleukemia |
| alpha-SMA/α-SMA | alpha-smooth muscle actin |
| AMPK | adenosine monophosphate (AMP)-activated protein kinase |
| B-CLL | B cell chronic lymphocytic leukaemia |
| BioVaSC® | biological vascularised scaffold (registered) |
| BLI | bioluminescence intensity |
| BM | basement membrane |
| BMP | bone morphogenetic protein |
| CAF | cancer-associated fibroblasts |
| CALD1 | high molecular weight caldesmon 1 |
| CAR | chimeric antigen receptor |
| CAS | CRISPR-associated system |
| CAV1 | Calveolin 1 |
| CC | co-culture |
| ccK18 | caspase-cleaved cytokeratin 18 |
| CCL | chemokine ligand |
| CD | cluster of differentiation |
| CFD | Complement Factor D |
| CK18 | cytokeratin-18 |
| cm | centimetre |
| CM | costimulatory molecules |
| $cm^2$ | square centimetre |
| $CO_2$ | carbon dioxide |
| COL | Collagen |
| CRISPR | Clustered Regularly Interspaced Short Palindromic Repeats |
| CRS | cytokine release syndrome |
| CSCs | cancer stem cells |
| CTLA-4 | cytotoxic T-lymphocytes-associated protein 4 |
| Ctrl | control |
| CXCL | chemokine (C-X-C motif) ligand |
| DAB | 3,3’-Diaminobenzidine |
| DAPI | 4’,6-diamidino-2-phenylindole |
| $ddH_20$ | double distilled water |
| Dkk-1 | Dickkopf-1 |
| DKO | PD-1 gene and TGF-β receptor knock-out |
| DMEM | Dulbecco’s modified Eagle medium |
| DMSO | dimethyl sulfoxide |
| DNA | deoxyribonucleic acid |
| DNase | deoxyribonuclease |

*Table 1. List of abbreviations and units (continued)*

| Abbreviation | Meaning |
|---|---|
| e.g. | exempli gratia |
| EC | endothelial cells |
| E-cad | E-cadherin |
| ECM | extracellular matrix |
| EDTA | ethylenediaminetetraacetic acid |
| EGF | epidermal growth factor |
| EGFR | epidermal growth factor receptor |
| EGFRt | truncated epidermal growth factor receptor |
| EGFRvIII | epidermal growth factor receptor version III |
| ELISA | enzyme-linked immunosorbent assay |
| EMT | epithelial-mesenchymal transition |
| EpCAM | epithelial cell adhesion molecule |
| ER | estrogen receptor |
| et al | et alii |
| EwS | Ewing's sarcoma |
| EWSR1 | Ewing sarcoma breakpoint region 1 protein |
| EZH2 | Enhancer of Zeste Homolog 2 |
| FAP | Fibroblast Activation Protein |
| Fc region | fragment crystallisable region |
| FCS | fetal calf serum |
| FDA | Food and Drug Administration (of the United States) |
| FGFR2 | fibroblast growth receptor 2 |
| Fig. | figure |
| FITC | fluorescein isothiocyanate |
| FLI1 | friend leukaemia integration 1 transcription factor |
| g | gram |
| G-CSF | granulocyte colony-stimulating factor |
| GDF | growth and differentiation factor |
| GFP | Green Fluorescent Protein |
| GM-CSF | granulocyte-macrophage colony-stimulating factor |
| GPR77 | G protein-coupled receptor 77 |
| h | hours |
| H&E staining | haematoxylin and eosin staining |
| $H_2O_2$ | hydrogen peroxide |
| HCl | hydrochloric acid |
| hdF | human dermal fibroblasts |
| hDF | human dermal fibroblasts |
| heK | human epidermal keratinocytes |
| hEK | human epidermal keratinocytes |
| HER 2 | human epithelial growth receptor 2 |
| HGF | hepatocyte growth factor |
| hLF | human lung fibroblasts |
| hmvECS | human microvascular endothelial cells |
| HRP | horseradish peroxidase |
| ICAM-1 | intracellular adhesion molecule 1 |
| IF staining | immunofluorescence staining |

*Table 1. List of abbreviations and units (continued)*

| Abbreviation | Meaning |
|---|---|
| IFN | interferon |
| IGFBP-2/-3 | Insulin-like growth factor-binding protein-2/-3 |
| IHC staining | staining immunohistochemical staining |
| IL | Interleukin |
| iPSCs | induced pluripotent stem cells |
| ITAM | immunoreceptor tyrosine-based activation motifs |
| IVIS | In Vivo Imaging System |
| JAK | janus kinase |
| kDa | kilo Dalton |
| kg | kilogram |
| KO | knock-out |
| l | litre |
| LGL | lethal giant larvae |
| M | molar (mol) |
| MC | monoculture |
| MCL | mantle cell lymphoma |
| MCP-1/CCL2 | monocyte chemoattractant protein-1 |
| MDSCs | myeloid-derived suppressor cells |
| MET | mesenchymal to epithelial transition |
| metCAF | cancer-associated fibroblasts derived from metastatic tumour site |
| MFAP5 | Microfibrill-associated Protein 5 |
| mg | milligram |
| MHC | major histocompatibility complex |
| MIF | Macrophage migration inhibitory factor |
| min | minutes |
| MIP-3α | macrophage inflammatory protein-3 |
| MIS | Muellerian inhibiting substance |
| ml | millilitre |
| mM | millimolar |
| mm | millimetre |
| $mm^2$ | square millimetre |
| MMP | matrix-metalloprotease |
| Mock | non-transduced control T cells |
| mTOR | mechanistic target of rapamycin |
| MTT | 3-(4,5-dimethylthiazol-2-yl)-2,5-diphenyltetrazolium bromide |
| $N_2$ | nitrogen |
| NaCl | sodium chloride |
| NG2 | neural/glial antigen 2 |
| NK cells | natural killer cells |
| nm | nanometre |
| NSCLC | non-small cell lung cancer |

*Table 1. List of abbreviations and units (continued)*

| **Abbreviation** | **Meaning** |
|---|---|
| NT | non-transduced/control T cells |
| OPN | Osteopontin |
| P/sec/mm/sq | mean/photon value per square millimetre |
| PARP | poly ADP ribose polymerase |
| PATJ | PALS1-associated tight junction protein |
| PBS | phosphate buffered saline |
| $PBS^-$ | phosphate buffered saline without calcium/magnesium |
| $PBS^+$ | phosphate buffered saline with calcium/magnesium |
| PBS-T | phosphate buffered saline with Tween-20 |
| PCK | Pan-cytokeratin |
| PD-1 | Programmed cell death protein 1 |
| PDGF-AA | platelet-derived growth factor-AA |
| PDGFR | platelet-derived growth factor receptor |
| PDGF | platelet-derived growth factor |
| PD-L1 | programmed cell death ligand-1 |
| PDPN | Podoplanin |
| PECAM | platelet and endothelial cell adhesion molecule 1 |
| PEEK | polyetheretherketone |
| Pen/Strep | penicillin/streptomycin |
| PET | Polyethylenterephthalat |
| pg | picogram |
| PKO | PD-1 gene knock-out |
| PLA | polylactic acid |
| POSTN | Periostin |
| PR | progesterone receptor |
| primCAF | cancer-associated fibroblasts derived from primary tumour site |
| PTPRC | protein tyrosine phosphatase |
| RNA | ribonucleic acid |
| ROR1 | receptor tyrosine kinase-like orphan receptor 1 |
| rpm | revolutions per minute |
| RPMI-1640 | Roswell Park Memorial Institute medium 1640 |
| RT | room temperature |
| RTK | receptor tyrosine kinase |
| scFv | single-chain variable fragments |
| SCLC | small cell lung cancer |

*Table 1. List of abbreviations and units (continued)*

| **Abbreviation** | **Meaning** |
|---|---|
| SD | standard deviation |
| SDF-1 | Stromal Cell-Derived Factor-1 |
| SEM | standard error of the mean |
| SIS | small intestinal submucosa |
| SISmuc | small intestinal submucosa with mucosa |
| SMAD | small mothers against decapentaplegic homolog |
| SMTN | Smoothelin |
| SOP | standard operation protocol |
| STAT | signal transducers and activators of transcription |
| Tab. | table |
| TAM | tumour-associated macrophages |
| TFF3 | trefoil factor 3 |
| TGF-b/TGF-β | transforming growth factor alpha/beta |
| TKI | tyrosine kinase inhibitor |
| TKO | TGF-β receptor knock-out |
| TMB | 3,3’,5,5’-tetramethylbenzidine |
| TME | Tumour Microenvironment |
| TNBC | triple negative breast cancer |
| TN-C | Tenascin-C |
| TNF | tumour necrosis factor |
| TRUCKs | T cell redirected for universal cytokine-mediated killing |
| TβR | TGF-β-receptors I and II |
| ™ | trademark |
| uPAR | urokinase plasminogen activator surface receptor |
| v/v | volume per volume |
| v/w | volume per weight |
| VBM | vascular basement membrane |
| VEGF | vascular endothelial growth factor |
| VIM | vimentin |
| WHO | World Health Organisation |
| Wnt | wingless |
| WT | wildtype |

# 1. Introduction

Per definition, cancer is a group of diseases, which can occur in nearly all body sites when cells start to grow abnormally. During disease progression, cancer cells can then spread to other parts of the body. The extravasation from the initial tumour site to distinct organs manifests in metastasis and often leads to a worse patient outcome.

With 9.6 million deaths in 2018, cancer is the second leading cause of death worldwide, which affects about one in six people. The most common types of cancer in women are breast followed by colorectal, lung, cervical and thyroid cancer. In men, lung cancer is most frequent, followed by prostate, colorectal, stomach and liver cancer. Taken together, this accounts for lung and breast cancer as the most prevalent diagnosed forms of cancer in the year 2018. In addition, lung cancer also has the worst prognosis with 1.76 million deaths in 2018. This overview raises the question why cancer occurs often and still has such a poor prognosis (*Cancer*, 2020).

There are different classes of risk factors that favour cancer formation e.g. physical carcinogens (e.g. ionising radiation, UV light), chemical carcinogens (e.g. tobacco smoke, arsenic and asbestos) and biological carcinogens (e.g. specific infectious diseases). Furthermore, the World Health Organisation states that 30 to 50% of cancer can be prevented by changing to a healthier lifestyle as, for instance, the use of tobacco is responsible for about 22% of all cancer deaths worldwide. In addition to this, the genetic predisposition contributes tremendously to specific types of tumours (*Cancer*, 2020).

The survival rate and treatment options vary between different types of cancer and depend on the time of diagnosis. Even though prevention can be a powerful tool, high death rates require efficient treatment strategies. Therefore, the present work explores novel immunotherapeutic approaches by engaging chimeric antigen receptor (CAR) T cells.

This work focuses primarily on the study of breast and lung cancer as most prevalent types. The following chapter describes those cancer types in more detail.

## 1.1 Classification of breast and lung cancer

The classification of breast cancer is complex. Different characteristics help to generate an overview within this heterogenic disease. At first, a distinction regarding the stage of invasive growth of cancer cells into carcinoma *in situ* and invasive carcinoma is important. A carcinoma *in situ* is a premalignant cell mass, that is formed by neoplastic epithelial cells that have not yet crossed the basement membrane, while an invasive breast cancer is stated to be malignant as it overcomes this barrier (Cowell *et al.*, 2013). From this, further sub-classifications are possible as the WHO lists over 20 different breast tumour types according to their 5th edition of their “Blue Book” (*WHO classification of tumours. Breast Tumours*, 2019). The largest group of the invasive breast cancer type is the breast cancer of no specific type (NST). To assess prognostic implications, other aspects like tumour size, lymph node status (Cserni *et al.*, 2018) and histological type (Elston & Ellis, 1991) are taken into account. Furthermore, molecular biomarkers like human epithelial growth receptor 2 (HER2), estrogen receptor (ER) and progesterone receptor (PR) as well as proliferation index via the marker Ki67 of tumour cells are important indicators for distinct therapy approaches. Classification based on these markers leads to the distinction into 5 different subtypes, which is shown in Table 2 (Leitlinienprogramm Onkologie, 2018). It has been demonstrated that targeting specific hormone receptors is an indicator for therapy success (Shea *et al.*, 2020). For instance, targeting Her2 with the antibody-based therapy trastuzumab lead to promising results (Piccart-Gebhart *et al.*, 2005). Furthermore, gene expression profiling has prognostic value regarding therapy response in addition to the intrinsic classification (Parker *et al.*, 2009).

*Table 2. Classification of breast cancer based on gene expression analysis and hormone receptor status (Leitlinienprogramm Onkologie, 2018).*

| **Subclass name** | **ER status** | **PR status** | **HER2 status** | **Ki67** |
|---|---|---|---|---|
| Luminal A | + | +or- | - | low |
| Luminal B: | | | | |
| →Luminal B: HER2-negative | + or - | + or - | - | high |
| →Luminal B: HER2-positive | + or - | + or - | + | high or low |
| HER2 positive | - | - | + | / |
| triple-negative | - | - | - | / |

From these markers the term triple negative breast cancer (TNBC) derived, which describes an invasive type of breast cancer that is negative for HER2, ER and PR. It often occurs in young women and accounts for up to 17% of all breast cancers. It is holding a poor prognosis with a strong tendency to metastasise (Foulkes *et al.*, 2010). The loss of those receptors paired with its aggressive growth makes hormone receptor targeting therapy unavailable. Treatment options combine surgery, radiation therapy and chemotherapy in early stages, but targeted therapies also showed promising results. Here, poly ADP ribose polymerase (PARP)-inhibitors influencing DNA- repair mechanisms improved therapy outcome. Furthermore, drugs targeting epidermal growth factor receptor (EGFR), fibroblast growth receptor 2 (FGFR2), vascular endothelial growth factor (VEGF), and mechanistic target of rapamycin (mTOR) are developed (Wahba & El-Hadaad, 2015).

In addition, immunotherapies targeting checkpoint inhibitors are promising, if the tumour is classified as immunogenic (Bergin & Loi, 2019). Taken together, although new therapies for TNBC are in development, there is still a substantial need to identify new effective treatment options. Therefore, microphysiologic 3D tumour models of TNBC were employed in this work to assess receptor tyrosine kinase-like orphan receptor 1 (ROR1)-targeting CAR T cells as a novel therapy for TNBC and overcome the dependency on hormone receptors for effective treatment.

Lung cancer is divided by tissue and cell morphology into the groups of small cell lung cancer (SCLC, 15% of all lung cancers) and non-small cell lung cancer (NSCLC, 85% of all lung cancers). NSCLCs can be further classified as adenocarcinoma, squamous cell carcinoma and large cell carcinoma (Inamura, 2017). Smoking is a general risk factor for the development of lung cancer. In most cases it causes squamous cell carcinoma, while adenocarcinomas are associated with non-smoking patients (Herbst *et al.*, 2008). Diagnosis of lung cancer often occurs late, as there is no general check-up as for breast cancer. After diagnosis, it depends on the distinct type of lung cancer in which way therapy is carried out. Normally, the treatment includes the removal of the tumour by surgery in combination or followed by radiation as well as different types and combinations of chemotherapy (Duma *et al.*, 2019; Wang *et al.*, 2019). As the commonly used chemotherapies are not completely tumour-cell specific and do not lead to promising results, especially in NSCLC patients, new therapies emerged in the recent years. Those so called targeted therapies aim for the unique molecular profile of lung cancer cells (Mayekar & Bivona, 2017). In addition, new immunotherapeutic approaches influencing the immune response are extensively studied during the last years (Rolfo *et al.*, 2017; Osmani *et al.*, 2018; Proto *et al.*, 2019). The present work is engaging an immunotherapeutic approach with ROR1 CAR T cells, which are tested in microphysiologic 3D lung and breast tumour models in order to assess efficacy of cellular immunotherapeutic approaches for solid tumours.

## 1.2 New approaches to treat cancer

Hanahan and Weinberg published the Hallmarks of Cancer in 2000, where they described distinct features that cancer cells obtain to form and maintain malignant tissues (Hanahan & Weinberg, 2000). Among the hallmarks are different properties of cells like the maintenance of proliferative signalling, the insensitivity of growth suppressors, the activation of invasion and metastasis formation, replicative immortality, induction of angiogenesis and resistance to cell death (Hanahan & Weinberg, 2000). In 2011, those Hallmarks were updated and reprogramming of the cellular metabolism as well as the immune evasion of cancer cells were included. (Hanahan & Weinberg, 2011).

From the increasing knowledge about the importance of the immune system in cancer, the field of cancer immunotherapy emerged.

### 1.2.1 Cancer immunotherapy

Immunomodulatory effects of cancer cells can be mediated via different mechanisms. Cancer cells can secrete immunosuppressive cytokines like transforming growth factor beta (TGF-β) (Trapani, 2005), downregulate major histocompatibility complex (MHC) molecules (Romano *et al.*, 2020), upregulate proteins activating immune checkpoint inhibition in order to supress T cell function (Krummel & Allison, 1995; Okazaki & Honjo, 2007) and many others. With an increased understanding of the immune system and its role in cancer, the field of cancer immunotherapy emerged. In immunotherapy, the aim is to influence the immune response in order to use the cell-destructive forces of the immune system to fight a disease.

There are different ways to influence the immune system either directly or indirectly. Moreover, the aim can be the activation or suppression of distinct immunomodulatory mechanisms. In cancer therapy, three main approaches show promising results in preclinical experiments or clinical studies: 1) tumour vaccines, 2) checkpoint inhibitors and 3) adoptive T cell transfer (da Silva *et al.*, 2019; Waldman *et al.*, 2020). Tumour vaccines aim to induce an immune response in the body against the specific malignancy by injection of immune sensitising antigens, allowing the tumour cell to be detected and attacked by the immune system (Tran *et al.*, 2019). So far, the clinical application is limited because it is difficult to sensitise the host immune system sufficiently to overcome immunosuppressive mechanisms of the tumour stroma. Checkpoint inhibitors are another approach to combine different types of immunotherapy in order to increase the clinical outcome (Gibney *et al.*, 2015). As James P Allison and Tasuku Honjo were awarded the Nobel Prize in Physiology or Medicine in 2018, the approach on checkpoint inhibitors also gained attention. They discovered the proteins programmed cell death protein 1 (PD-1) and cytotoxic T-lymphocytes-associated protein 4 (CTLA-4) which function as a brake for the T cell response. Both proteins are receptors on the T cell surface and after being blocked showed impressive results in mice with metastatic tumours leading to high remission rates (*The Nobel Prize in Physiology or Medicine 2018*, 2020). Today, widely used immunotherapies with ipilimumab, nivolumab and pembrolizumab are available for different types of cancer ranging from melanoma, lymphoma over to lung and breast cancer. Here, different combinations have shown favourable results (Ardolino & Joshua, 2019). Another approach in the field of immunotherapy is the use of CAR T cells engaging the functions of T cells to lyse the target cell. This approach is described in more detail in chapter 1.2.2. Engaging the immune system in order to treat cancer is the main aim of the present work as ROR1-targeting CAR T cells were evaluated in defined microphysiologic 3D tumour models of different solid tumours to analyse the sensitivity of the microphysiologic 3D tumour models as well as the efficacy of this immunotherapeutic approach in more detail.

### 1.2.2 CAR T cell therapy for cancer

Dr Zelig Eshhar in Israel described the first CAR T cell in the 1980s (Gross *et al.*, 1989). Over 20 years later, the first CAR T cell was approved in 2017 by the Food and Drug administration (FDA) to treat acute lymphoblasticleukemia (ALL) by targeting the surface marker CD19 present on tumour cells (ESMO, 2018; *FDA*, 2019).

CAR T cells are genetically modified T cells harbouring a CAR specifically binding a distinct neo-antigen on the tumour cells and by this facilitating T cell mediated toxicity. The neo-antigen of interest needs to be expressed on distinct tumour cells exclusively, but ideally not on healthy cells of the body. To generate CAR T cells, blood is taken from a donor or patient and specific populations of leukocytes are isolated via their surface markers. In most cases, $CD4^+$ T helper cells and $CD8^+$ cytotoxic T cells are obtained. These cells are then genetically modified in order to express the antigen of choice. For this, different approaches can be used. Lentiviral or retroviral vectors are common, but also genetic editing via the Clustered Regularly Interspaced Short Palindromic Repeats (CRISPR)- CRISPR-associated system (CAS) and utilisation of sleeping beauty transposase is increasing (Morgan & Schambach, 2018). After the genetic modification, CAR T cells are activated using specific beads to present them with the B cell-surface-markers CD3 and CD28. These activated cells are then expanded in the next steps. After this procedure they are reinfused into the patient or used for experiments (Wang & Rivière, 2016). At the tumour site, these genetically engineered T cells recognise the antigen, become activated and mediate antitumor toxicity (Waldman *et al.*, 2020).

A huge advantage over naturally occurring tumour-specific lymphocytes is the MHC independency of CAR T cells. As their CAR consists of an antibody, which is fused to an internal activation domain, the signal is mediated upon binding of the specific antigen. So far, 5 generations of CAR T cells have been developed over time and are shown in Figure 1.

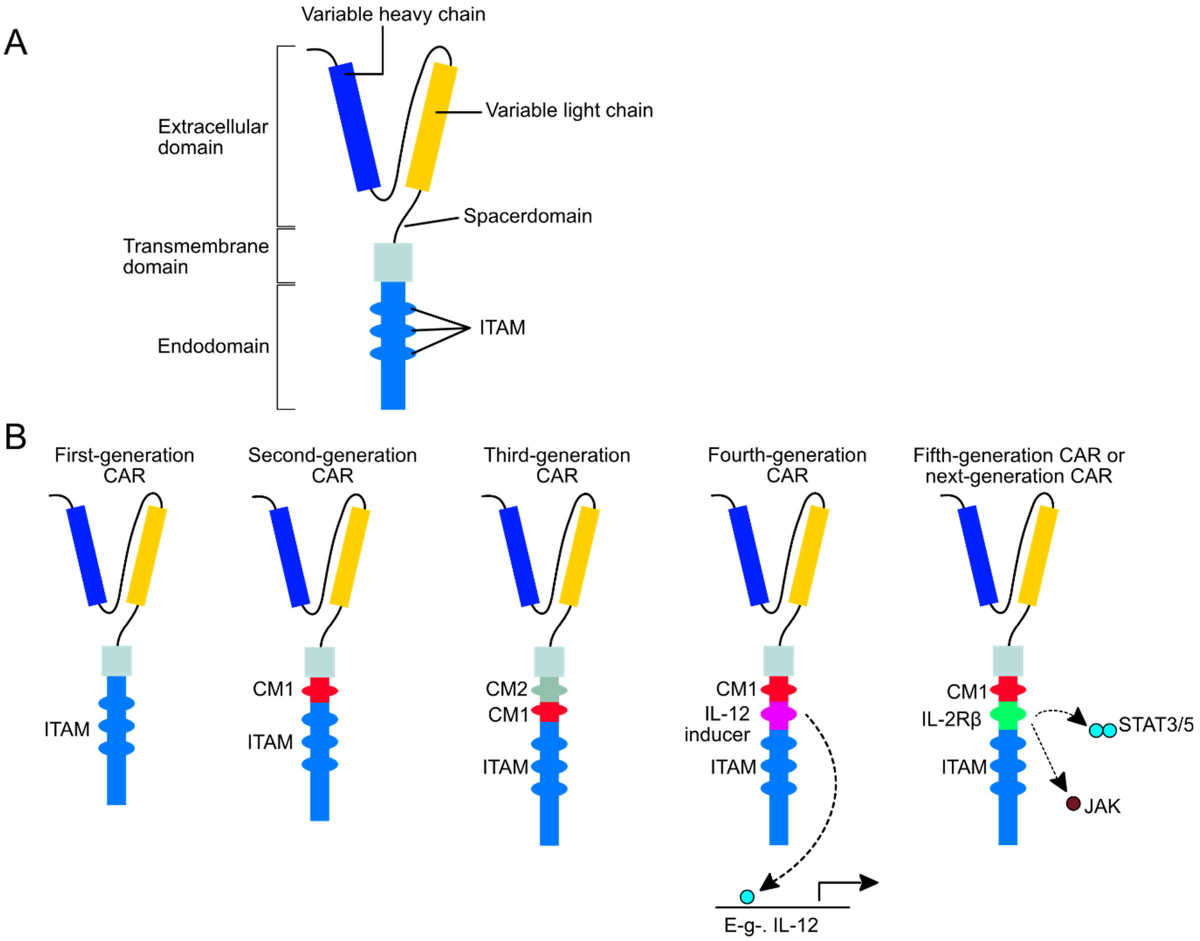

**Figure 1. Design of different generations of chimeric antigen receptors (CARs).**

(A): The general structure of a CAR includes the extracellular domain that is targeting the antigen, which consists of the variable heavy and light chain of the respective antibody as well as a variable spacer domain. This is attached to the transmembrane domain anchoring the CAR in the cell membrane, followed by an endodomain inside the cell. The endodomain harbours the intracellular domain of the T cell co-receptor CD3ζ that contains three immunoreceptor tyrosine-based activation motifs (ITAM), which mediate signal transduction. (B): Over the years, several generations of CARs have been developed and differ mainly in the costimulatory molecules (CM). The first-generation CAR only harbours the ITAM motif, derived from the CD3ζ domain. Second-generation CARs contain one CM, while third-generation CARs included a second CM. Those are often derived from CD28 or 4-1BB. The fourth-generation CAR contains all elements of the second-generation but further has an inducible or constitutively expressed chemokine (e.g. IL-12). T cells from the fourth generation are also termed T cells redirected for universal cytokine-mediated killing (TRUCKs). CARs of the fifth generation are similar to the fourth but contain intracellular domains of cytokine receptors (e.g. IL-2 receptor-β chain fragment that is interacting with the transcription factor STAT3/5 further modulating signalling and activation of the T cell). Image modified after (Tokarew *et al.*, 2019).

A CAR consists of an extracellular domain, which targets the antigen and is harbouring the variable light and heavy chain of the antibody fragment, a linker between the heavy, and the light chain. A spacer domain is bridging the transmembrane domain to the intracellular domain (the endodomain). The intracellular domain is also the most variable part between the different CAR generations. The first generation started with one tyrosine-based activation motif (ITAM) from CD3ζ. In the second generation of CAR T cells a costimulatory molecule (CM) was introduced, which was either derived from CD28 or CD137 (also referred to as 4-1BB). This CM enhanced proliferation of the CAR T cells as well as the T cell cytotoxicity (Subklewe *et al.*, 2019; Tokarew *et al.*, 2019). CAR T cells of the second generation are mostly applied in clinical trials or approved therapies (Brentjens & Curran, 2012; Brentjens *et al.*, 2013). CAR T cells of the 3rd generation harbour more than two costimulatory domains. From the 4th generation onwards, additional segments were introduced into the CAR T cells leading to increased cytokine secretion upon T cell activation (e.g. IL-2). Especially in the 5th generation of CAR T cells, cytokine related signalling is induced in the T cells upon activation in addition to general activation. Those CAR T cells are also called T cells redirected for universal cytokine-mediated killing (TRUCKs) (Li & Li *et al.*, 2019; Tokarew *et al.*, 2019). Recently, approaches combining the idea of bispecific antibodies and CAR T cells have shown good results for glioblastoma in mouse experiments. Here, a CAR T cell was generated which was secreting bispecific antibodies upon activation via epidermal growth factor receptor version III (EGFRvIII). It could selectively augment antitumor function without targeting somatic cells (Choi *et al.*, 2019).

CAR T cells have been approved for the use in the clinic concerning different hematologic malignancies, mostly targeting CD19, which is strongly expressed on malignant B cells. These studies show convincing results (Turtle *et al.*, 2016; Gardner *et al.*, 2017). Nevertheless, these therapies are not easily transferable to solid tumours. Many efforts have been made to take the idea of CAR T cells into the clinic for the treatment of solid tumours, but the success rates of these trials remained low (Schmidts & Maus, 2018). Several reasons are known to influence the efficacy and the engraftment of CAR T cells in patients with solid tumours. One problem is to find suitable neo-antigens with a high and homogenous expression on tumour cells and absent expression on healthy tissue (Schmidts & Maus, 2018; Majzner & Mackall, 2019). Here, it could be shown that a patient infused with a high number of Her2 specific CAR T cells died due to the side effects mediated either through on-target off-tumour toxicity of Her2 expression in the heart tissue (Morgan *et al.*, 2010) or through the often observed cytokine release syndrome (CRS) (Majzner & Mackall, 2019). Furthermore, solid tumours pose additional challenges to the CAR T cells compared to hematologic malignancies. In solid tumours the CAR T cells have to traffic to the distinct tumour site, overcome physical barriers of a highly dense tumour as well as the hostile immunosuppressive tumour microenvironment (TME) (D'Aloia *et al.*, 2018; Li & Li *et al.*, 2019). As CAR design and the tumour microenvironment can strongly influence the performance of a CAR T cell, these aspects were studied in the present work by engaging microphysiologic 3D tumour models with implemented patient-derived cells to represent aspects of the tumour microenvironment. Additionally, different CAR designs were investigated in order to find the optimal CAR construct regarding the target ROR1 and to challenge the sensitivity of the microphysiologic 3D tumour models.

### 1.2.3 $G_{D2}$ as a target in Ewing's sarcoma

James Ewing first described Ewing's sarcoma (EwS) in 1921. It is a malignancy of the bone or soft tissue arising mostly during adolescence. Genetically, EwS originates due to chromosomal translocations which occur in most cases in chromosomes 22 and 11 (t(11,22)(q24;12)). The translocation leads to an alteration of the friend leukaemia integration 1 transcription factor (FLI1) leading to the aberrant chimeric transcription factor Ewing sarcoma breakpoint region 1 protein (EWSR1)-FLI1, which is a dominant oncoprotein. This genetic alteration manifests in different ways leading to tumour progression in terms of cell-cycle regulation, signal transduction, cell migration, telomerase activity, chromatin architecture (Grünewald *et al.*, 2018). So far, it is not completely clear from which type of cell this tumour arises. Most likely, it develops from cells of the neural crest as gene signatures and surface markers are very similar. Also mesenchymal stem cells are possible as indicated by the surface marker CD99 shown by differentiation trials and fusion protein expression in mice (Tu *et al.*, 2017). Treatment options are still limited and include surgery, radiation therapy and chemotherapy. Since EwS has a strong tendency to form metastasis, the clinical outcomes are poor and patients often suffer from relapses (Yu *et al.*, 2017; Grünewald *et al.*, 2018).

To increase patient outcome in the future, immunotherapies including CAR T cells are extensively studied. Here, the surface marker disialoganglioside $G_{D2}$ showed promising results for neuroblastoma patients treated with $G_{D2}$ targeted CAR T cells (Heczey *et al.*, 2017). It has been shown that $G_{D2}$ also is a target for EwS by successfully using $G_{D2}$ CAR T cells (Kailayangiri *et al.*, 2017). However, its expression remains heterogeneous within the tumour with different high or low expressing cell subpopulations (Kailayangiri *et al.*, 2012). The importance of epigenetic regulation in EwS is a key to overcome this obstacle caused by the heterogonous expression of $G_{D2}$ (Suzuki *et al.*, 2011). The oncoprotein (EWSR1)-FLI1 leads to a high Enhancer of Zeste Homolg 2 (EZH2) expression that further favours epigenetic plasticity with the result of phenotypic heterogeneity among EwS cell populations (Krook *et al.*, 2016). This axis could be an option to manipulate gene expression and sensitise EwS cells for novel therapies targeting $G_{D2}$. Here, especially inhibition of EZH2 could increase $G_{D2}$ expression. In the present work, GSK126 an EZH2 inhibitor was used to increase $G_{D2}$ expression in EwS cells to perform testing of $G_{D2}$ CAR T cells in microphysiologic 3D tumour models of Ewing's sarcoma.

### 1.2.4 ROR1 is a promising target in different solid malignancies

To fight cancer in solid tumours with the approach of CAR T cell therapy, tumour cell specific neo-antigens are essential. The Receptor tyrosine kinase-like Orphan Receptor 1 (ROR1) belongs to the ROR family together with ROR2. ROR1 and ROR2 are both important during embryonic development and adult somatic cells show low expression. They are genetically conserved between species. This supports their influence on developmental processes (Borcherding *et al.*, 2014). In addition to embryonic cells, it has been found that several different types of cancer cells express ROR1, amongst them several hematologic malignancies like B cell chronic lymphocytic leukaemia (B-CLL), mantle cell lymphoma (MCL), acute lymphatic leukaemia (ALL), but also several solid tumours like breast, lung, ovarian, skin, prostate and colorectal cancer. Mechanistically, it is known that Wingless (Wnt) ligands bind to ROR1, which activates pathways, which modulate cancer cell migration, proliferation, chemotaxis and survival. Furthermore, ROR1 expression is associated with cancer stem cell traits (Balakrishnan *et al.*, 2017; Karvonen *et al.*, 2019).

To utilise this high expression of ROR1 on different malignancies, mice experiments for B-CLL and mantel cell lymphoma using ROR1 CAR T cells were performed and showed promising results (Hudecek *et al.*, 2010). To address the expression of ROR1 on immature B cell precursors, as well as, tissues like adipocytes, pancreas and lung, safety testing in non-human primates was conducted. Here, no increased toxicity was detected and CAR T cells accumulated in the tumour tissue. With the high genetic conservation of ROR1 between species and limited adverse toxicity, this supports further use and study of ROR1-specific CAR T cells (Berger *et al.*, 2015). Today, there are several clinical trials targeting ROR1 either via the antibody Cirmtuzumab (Choi *et al.*, 2018) or ROR1 CAR T cells (NCT02706362/ NCT02706392) (Specht *et al.*, 2018). In the Cirmtuzumab trial an inhibition of ROR1-signalling was observed and no side effects correlating with ROR1 expression on healthy tissue were detected. Based on these results, targeting ROR1 in different malignancies can be a promising tool for future CAR T cell-based therapies. Therefore, the present work focussed on the assessment of ROR1 CAR T cells in the context of lung and breast cancer studied in defined microphysiologic 3D tumour models in order to utilise them for candidate selection and efficacy testing for cellular immunotherapeutic approaches.

## 1.3 Epithelial to mesenchymal transition leads to plasticity of tumour cells

Diagnosis of many cancers often occurs at a late stage of disease leading to a poor patient outcome. A reason for this is that during tumour progression, metastasis begin to form and the cancer cells can spread from the primary tumour site into the whole body. Within the process of metastasis formation, tumour cells gain motility. To acquire this trait the process of epithelial to mesenchymal transition (EMT) is crucial.

EMT describes the process of epithelial cells undergoing a conversion to become more mesenchymal. It was first described in the processes during gastrulation, where it is important to form germ layers and to allow cell migration (Nakaya & Sheng, 2008; Acloque *et al.*, 2009).

Today, it is known that EMT plays an important role in tissue morphogenesis and wound healing, as well as in cancer. In the development of carcinomas that arise from epithelial cells, EMT plays an important role in regulating metastasis, invasion and cancer stem cell formation. An overview of the EMT process and its reversion process called mesenchymal to epithelial transition (MET) is shown in Figure 2.

A normal epithelium is characterised by specific markers like E-cadherin and certain cytokeratins. Epithelial cells have tight junctions, adherence junctions and desmosomes and hemidesmosomes, which keep the polar structure in shape on top of the basement membrane. When the EMT programme is activated, the cells become more motile and gain invasive traits. This is accompanied by the downregulation of epithelial markers and the expression of mesenchymal marker proteins like vimentin (VIM), fibronectin, N-cadherin and integrins (especially β1 and β3). In addition, the polarity and cell-cell-connections via tight junctions are lost. As a normal epithelium is anchored to the basement membrane, those connections also disappear during the EMT process to gain motility. To further increase invasion and motility, matrix-metalloproteases (MMPs) are often secreted, which remodel the basement membrane and surrounding tissue. It ought to be mentioned that cancer cells do not necessarily convert fully, but there are intermediate stages as well as the reversion MET (Dongre & Weinberg, 2019).

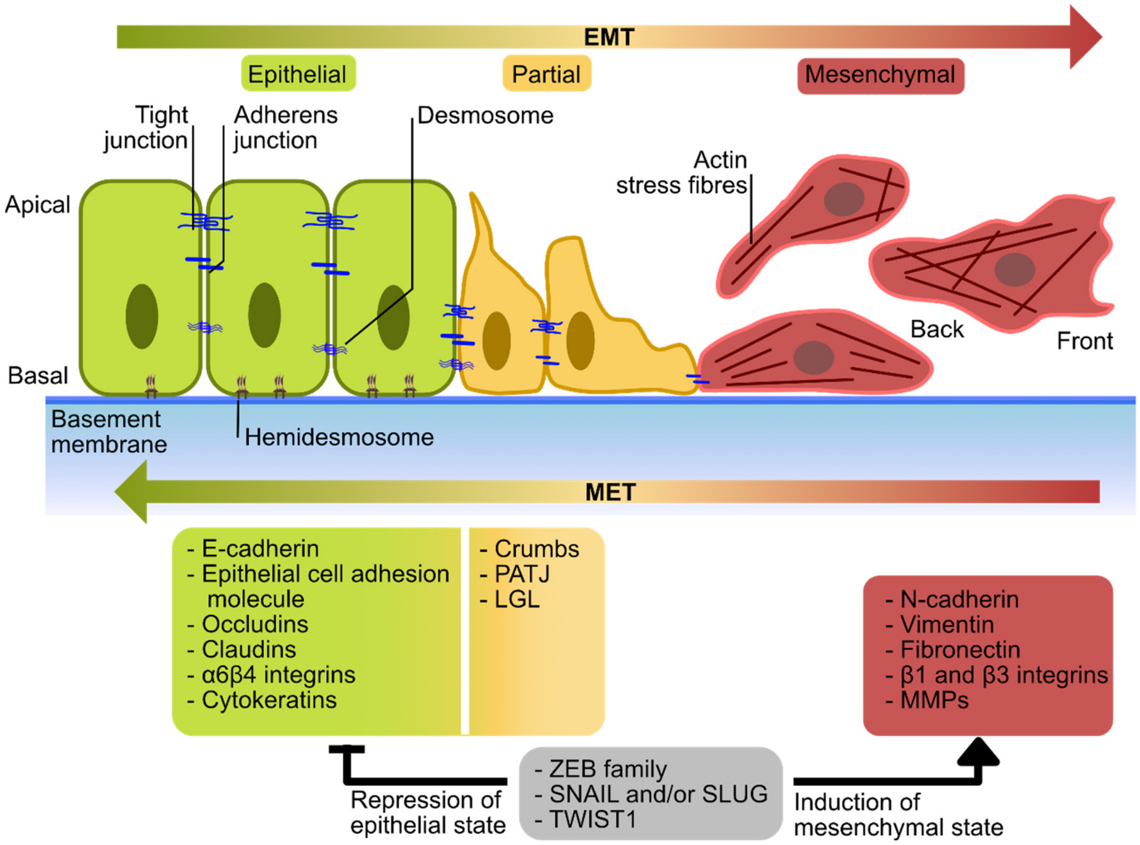

**Figure 2. Mechanisms of EMT and MET change the fate of epithelial cells and mediate tumour initiation, progression and metastasis formation.**

Epithelial cells show a characteristic architecture with an apical-basal polarity. They are anchored to a basement membrane via hemidesmosomes and connected to each other by tight and adherens junctions as well as desmosomes. While in an epithelial and intermediate state, cells express molecules listed in the green and yellow box. Upon induction of epithelial-to-mesenchymal-transition (EMT) cells enter an intermediate state becoming partially epithelial and mesenchymal. In this state EMT-inducing transcription factors like ZEB, SNAIL and TWIST, listed in the grey box, are expressed. They inhibit gene expression of epithelial-specific genes (green box) and induce expression of mesenchymal-specific genes (red box). Mesenchymal cells are characterised by a front-to-back polarity and a reorganised cytoskeleton. During the process of EMT cell-cell junctions are disassembled and cell polarity is lost. This is mediated by repression of crumbs, PALS1-associated tight junction protein (PATJ) and lethal giant larvae (LGL). As cells become mesenchymal they gain motility and acquire invasive traits. The process of EMT is reversible and called mesenchymal-to-epithelial-transition (MET). Of note, complete conversions to the mesenchymal state are rare in cancer cells and mostly intermediate states are observed. E-cadherin, epithelial cadherin; MMP, matrix metalloproteinase; N-cadherin, neural cadherin. Image modified after (Dongre & Weinberg, 2019).

The EMT process is induced by secreted ligands from the tumour microenvironment inducing several different signalling pathways. Especially TGF-β receptors, WNT and NOTCH pathways play a role during EMT, but also receptor tyrosine kinases activating PI3K/-AKT or Janus Kinase (JAK) / Signal Transducers and Activators of Transcription (STAT) signalling can be involved. Their mode of action is that they all activate the transcription factors ZEB, SNAIL and

TWIST to start the transformation from epithelial to mesenchymal. Factors activating these listed signalling pathways include TGF-β, IL-6, tumour necrosis factor (TNF) and hepatocyte growth factor (HGF). The latter factors are produced mainly by cancer-associated fibroblasts (CAFs), tumour-associated macrophages (TAMs), but also $CD4^+$ and $CD8^+$ T cells, myeloid-derived suppressor cells, as well as NK cells. Cancer cells undergoing EMT also manipulate the immune system. They secrete higher amounts of TGF-β than epithelial cancer cells, which dampens the immune response and drives T cells into dysfunction and exhaustion. In addition, the MHC is downregulated, as well as PD-L1 is upregulated on the tumour cells also promoting immune evasion (Dongre & Weinberg, 2019). The understanding of this immune modulation also offers new perspectives for novel treatment strategies and intervention during immunotherapeutic studies. As a central step in tumour progression, metastasis and the EMT process needs to be studied in preclinical models. The main technique used while testing new therapies *in vitro* is still conventional 2D cell culture. This does not resemble the complexity of *in vivo* tissues (Edmondson *et al.*, 2014), which allow metastasis formation, and only recapitulates short-term observations up to 72 h. To overcome common drawbacks, new techniques are essential that enable the cancer cells to invade and represent this plasticity. Microphysiologic 3D tumour models were used during this work to resemble a tissue-like surrounding for tumour cell growth including a basement membrane. The use of a biological matrix allows the study of EMT and MET processes to some extent.

## 1.4 The tumour microenvironment encompasses cellular, soluble and matrix components

Beside cancer cells, the tumour microenvironment (TME) is an important component of solid tumours. It is composed of non-tumorous cells, the extracellular matrix (ECM) and soluble factors. The cellular components include immune cells such as tumour-associated macrophages (TAMs), lymphocytes, endothelial cells, as well as stromal cells like fibroblasts (Baghban *et al.*, 2020). The TME comprises also the subcalssification of the tumour stroma, which can vary in definition. According to Valkenburg *et al.*, the stroma includes the stromal cells (specifically fibroblasts, mesenchymal stromal cells and osteocytes) and the extracellular matrix within the TME. D'Arcangelo *et al.* also include endothelial cells, pericytes, adipocytes and immune cells into the stroma characterisation (Valkenburg *et al.*, 2018; D'Arcangelo *et al.*, 2020). Additionally, more detailed classficiation approaches can define the TME in more distinct niches dividing it into aspects of metabolism, hypoxia, acidity, innervation, mechanical properties and immune microenvironment (Jin & Jin, 2020). In the present work addition of TGF-β and implementation of primary fibroblasts are termed TME-aspects, whereas fibroblasts especially recapitulate a stromal enrichment. In addition, the biological matrix SISmuc provides matrix component.

A detailed visualisation of the TME is shown in Figure 3, which focusses on cellular and the extracellular matrixFigure 3. The tumour microenvironment (TME) depicts a complex interplay of different cell types and the extracellular matrix (ECM)..

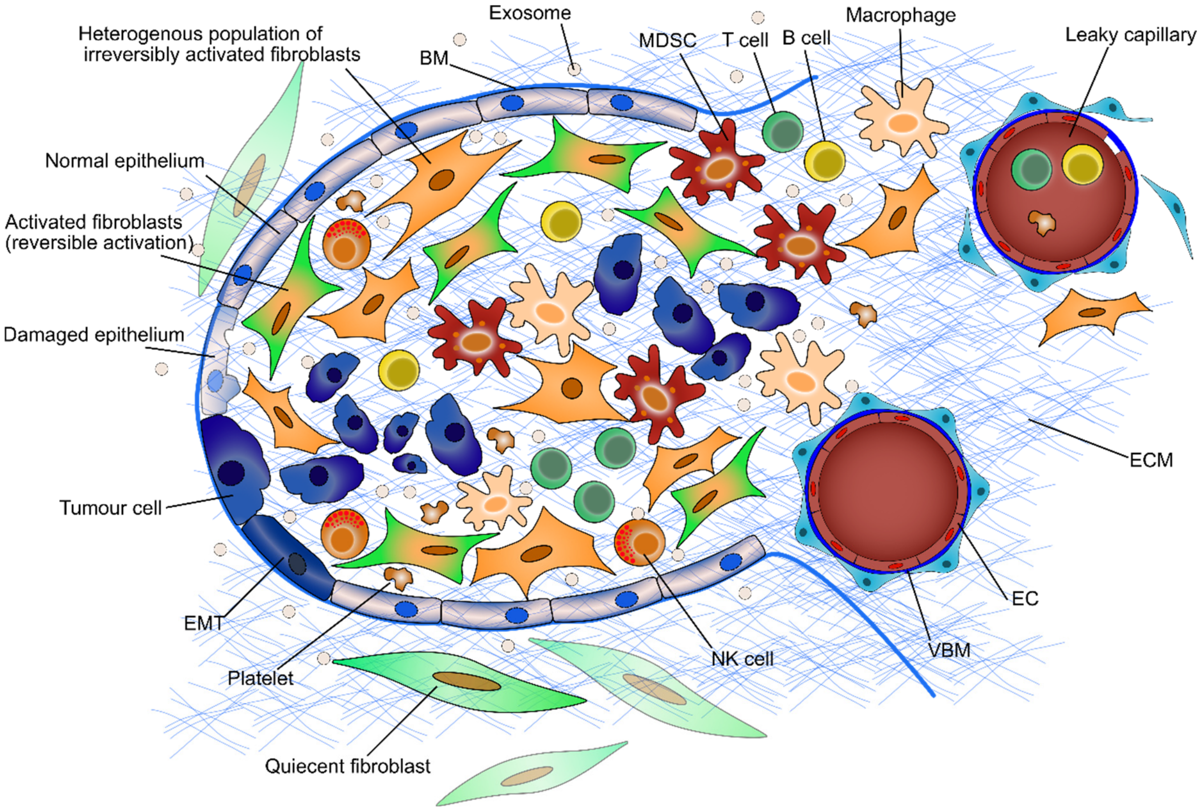

**Figure 3. The tumour microenvironment (TME) depicts a complex interplay of different cell types and the extracellular matrix (ECM).**

Different types of fibroblasts are part of the TME. Here, normal fibroblasts, quiescent fibroblasts and cancer-associated fibroblasts (CAFs) can be found. Additionally, normal epithelial, as well as injured and neoplastic epithelial cells are present, that are anchored to a basement membrane (BM). Furthermore, blood vessels including endothelial cells (EC), pericytes and a vascular basement membrane (VBM) are present. Another important cellular component are immune cells e.g. T and B cells, as well as macrophages and natural killer (NK) cells and myeloid-derived suppressor cells (MDSCs). The colour scheme from lighter blue (epithelial cell) over dark blue and purple (intermediate cell and motile mesenchymal-like cell) also depicts the mechanism of epithelial to mesenchymal transition (EMT). In addition to the BM also structures of the extracellular matrix (ECM) are indicated, representing an important non-cellular component of the TME. Image modified after (Kalluri, 2016).

During the last years, it became evident that the tumour microenvironment has a strong influence on tumour progression, metastasis formation and therapy outcome. The secretion of different soluble factors and cytokines, as well as ECM modulation mediates these events. The ECM as non-cellular compartment of a tumour poses an important role in providing the cellular components with biochemical and physical support. Furthermore, it impacts nutrient and gas supply and the distribution of signalling molecules from the TME (Poltavets *et al.*, 2018). The ECM divides into the basement membrane (BM) and the interstitial or stromal ECM. The BM forms a layer that normally divides the epithelial tissue from the mesenchyme and is composed mainly of collagen IV and specific laminins in most tissues. As already mentioned, the ECM plays an important role during the EMT process. The stromal ECM is produced by the mesenchymal cells, primarily CAFs and contains collagen I, III and fibronectin (Malik *et al.*, 2015).

The main factors by which the TME influences tumour cells include proteases to modulate the ECM and cytokines secreted by cells from the TME and cancer cells, maintaining a complicated cross talk. Crucial proteases in the TME are matrix metalloproteases (MMPs), which directly degrade the ECM.

Cytokines are also part of the TME and mediate their function via binding to specific receptors, activating different signalling pathways. Relevant cytokines are interleukins (IL), interferons (IFN) and growth factors. (Breznik *et al.*, 2017). As the TME is described to impair CAR T cell therapy in solid tumour, special attention was given in the present work to represent these aspects in the microphysiologic 3D tumour models by implementing patient-derived stromal cells like CAFs and immunosuppressive factors like TGF-β to analyse their effects on ROR1 CAR T cell therapy. Additionally, the microphysiologic 3D tumour models are based on a biological matrix representing an ECM as part of the TME.

Important factors such as TGF-β and CAFs as TME-components are described in more detail in the following chapters 1.4.1 and 1.4.2.

### 1.4.1 Cancer-associated fibroblasts comprise physical and immunological barriers

To understand what a cancer-associated fibroblast is, it is important to understand the role of fibroblasts in healthy tissue. Fibroblasts are a heterogeneous cell population that arises mainly from the mesoderm during gastrulation and belongs to the population of mesenchymal cells. Identification of a fibroblast is always a combination of positive markers (Platelet-Derived-Growth-Factor Receptor (PDGFR) α/β, VIM, Fibroblast-Specific-Protein-1 (FSP-1), Periostin (POSTN), collagen 1(COL1)) and negative markers (Epithelial Cell Adhesion Molecule (EPCAM), high molecular weight caldesmon 1 (CALD1), Smoothelin (SMTN), protein tyrosine phosphatase (PTPRC), platelet and endothelial cell adhesion molecule 1 (PECAM1)) (Nurmik *et al.*, 2020) as well as the evaluation of cell shape and location in the tissue. The role of fibroblasts is very diverse as it covers production of the ECM, tissue repair upon damage (e.g. wound healing), promotion of angiogenesis, as well as influencing the immune system by secretion of cytokines. During their activation, for instance during wound healing, fibroblasts enter a state of activation where they can change their marker expression (e.g. α-SMA) and are then referred to as myofibroblasts (Kalluri, 2016; Sahai *et al.*, 2020).

In addition, CAFs often show traits of activated fibroblasts and can be identified with CAF-associated markers (Fibroblast-Activation-Protein (FAP), α-Smooth-Muscle-Actin (α-SMA), Microfibril-Associated Protein 5 (MFAP5), collagen 11A (COL11A), Tenascin-C (TN-C), Podoplanin (PDPN), integrin α11β1, neural/glial antigen 2 (NG2)). As CAFs can make up to 90% of the tumour mass in distinct malignancies (Nazemi & Rainero, 2020), the theory of different subpopulations was tested and confirmed based on breast cancer biopsies. Costa *et al.* described a distinct pattern of surface markers ($CD29^{Med}$ $FAP^{Hi}$ $FSP1^{Low\text{-}Hi}$ $\alpha SMA^{Hi}$ $PDGFR\beta^{Med\text{-}Hi}$ Calveolin 1 $(CAV1)^{Low}$), which are associated with immunosuppression (Costa *et al.*, 2018). Furthermore, Su *et al.* defined a subpopulation of CAFs positive for the surface markers CD10 and G protein-coupled receptor 77 (GPR77) present in breast and lung cancer. There it influences cancer cell stemness, cancer progression and leads to a poor patient prognosis (Su *et al.*, 2018). The origin of CAFs is as diverse as their functions. Tumour cells and stimuli from the TME can recruit or influence normal fibroblasts to become CAFs. This is mediated by the secretion of distinct factors (e.g. TGF-β, epidermal growth factor (EGF)), platelet-derived growth factor (PDGF), and fibroblast growth factor 2 (FGF2) or the influence of hypoxia and oxidative stress (Liu *et al.*, 2019). In addition, other cells of mesenchymal origin such as mesenchymal stem cells, pericytes and adipocytes have been described to become CAFs. Endothelial or epithelial cells can undergo EndMT (Endothelial to mesenchymal transition) or EMT to develop into CAFs (LeBleu & Kalluri, 2018; Yoshida, 2020), but further studies are necessary to fully understand the origin of CAFs.

The role and functions of CAFs range from tumour preventing to tumour promoting properties. In brief, CAFs have been described to promote tumorigenesis by influencing angiogenesis, metastasis formation, immunosuppression, drug resistance, cancer cell stemness, ECM remodelling and metabolic reprogramming. The tumour preventing properties of CAFs are promoted via their effects on the immune system, as it is possible that CAFs recruit macrophages, natural killer cells and T lymphocytes through cytokine secretion. Nevertheless, these aspects of CAF-functions still remain elusive and the focus of research remains upon pro-tumorigenic functions (Kalluri, 2016; LeBleu & Kalluri, 2018).

The main mediators of tumour promotion are secreted factors by CAFs, which either directly promote cancer cell survival or indirectly remodel the TME to their favour. CAFs secrete factors like CXCL12, CCL7, TGF-βs, FGFs, HGF, periostin (POSTN) and TN-C, which are all direct inducers of cancer cell survival, stemness and proliferation, as well as metastasis formation. The indirect tumour promoting actions are conveyed by factors like VEGFs, FGFs and IL-6 favouring a tumour promoting vasculature and MMPs, as well as ECM proteins to remodel the surrounding matrix and their stiffness. With this, they also promote tumour cell invasion and metastasis and can form a physical barrier of dense ECM. In addition, IL-1, IL-6, Tumour Necrosis Factor α (TNFα), TGFβs, Stromal Cell-Derived Factor-1 (SDF-1) and monocyte chemoattractant protein-1 (MCP-1/ CCL2) have effects on immune cells, which favour pro-tumorigenic inflammation (LeBleu & Kalluri, 2018; Barbazán & Matic Vignjevic, 2019).

The present work includes the use of CAR T cells, therefore, the effect of CAFs on immune cells is an important topic and CAFs are described to promote an immunosuppressive TME, which poses immunological barriers towards immune cells. Consequently, they can have a strong influence on the therapy outcome of CAR T cells. To date, it is known that CAFs can inhibit the response of cytotoxic T cells via PD-1 and PD-2 signalling (Lakins *et al.*, 2018). Both proteins are expressed on either CAFs themselves or cancer cells. In addition, effects can be mediated by CXCL5 and TGF-β that is secreted by CAFs and can have immunosuppressive effects. The impact of TGF-β on CAR T cell therapy will be discussed in the next chapter (1.4.2) (Barrett & Puré, 2020). Furthermore, antigen presentation by CAFs resulting in CD4$^+$ T cell activation and CD8$^+$ T cell suppression has been described (Kalluri, 2016). To conclude, CAFs can influence therapy outcome of immunotherapies in multiple ways. Further research is needed to fully understand these aspects. As CAFs have a strong effect on tumour biology, CAF targeting treatment strategies are currently developed. For this purpose, CAR T cells targeting CAF markers or antibodies against secreted factors are used (Liu *et al.*, 2019). The present work aims to implement CAFs in microphysiologic 3D tumour models as stromal enrichment an aspect of the TME. This work includes characterisation of the secretory phenotype, as well as analysis of distinct CAF-related markers of the implemented fibroblasts. Additionally, the physiological and immunological barrier mediated by CAFs was investigated in the context of ROR1 CAR T cell therapy in microphysiologic 3D lung and breast cancer models.

### 1.4.2 The soluble factor TGF-β mediates immunosuppressive effects within the tumour microenvironment

As already mentioned in the previous chapter, TGF-β plays an important role within the TME. It is secreted by tumour cells and other cells from the TME. Amongst other functions, TGF-β has a strong influence on immune cells and CAFs. Furthermore, it is a mediator of the desmoplastic reaction. During desmoplasia, the ECM stiffens and connective tissue expands around the tumour, leading to tumour progression and a poor patient outcome (Papageorgis & Stylianopoulos, 2015).

The TGF-β-family is a group of proteins including two distinct subfamilies namely the TGF-β/Activin/Nodal subfamily and the bone morphogenetic protein (BMP) growth and differentiation factor (GDF) Muellerian inhibiting substance (MIS) BMP/GDF/MIS-subfamily.

Both groups engage different specific signalling pathways (Shi & Massagué, 2003). The members of the TGF-β-family are important during embryonic development, but especially TGF-β 1, 2, and 3 are also involved in different diseases like fibrosis, autoimmune disease and cancer (Blobe *et al.*, 2000; Shi *et al.*, 2011).

An important feature of TGF-β is that it is present in two different forms, a latent and an activated form. The latent form is present in larger amounts and activated TGF-β is released upon cleavage of the pro-peptide. Several proteins and external factors within the microenvironment have been reported to activate TGF-β. Among those are plasmin, MMP-2, MMP-9, thrombospondin, several integrins. Furthermore, reactive oxygen species and changes to a mild acidic pH can activate TGF-β (Sato *et al.*, 1990; Annes *et al.*, 2003; Shi *et al.*, 2011).

The active form of TGF-β acts as a ligand to the TGF-β-receptors (TβR) I and II. TGF-β binds to TβRII that then recruits TβRI. Phosphorylation and activation leads to phosphorylation of the transcription factors and signal mediators small mothers against decapentaplegic homolog (SMAD) SMAD2 and SMAD3, which then form a complex with SMAD4. This complex can then enter the nucleus and modify gene expression.

In addition to SMAD-dependent signalling also non-canonical signalling pathways are influenced by TGF-β such as PI3-kinase, p38 kinase and small GTPase pathways (RhoA, PKN, and Rock) (Massagué *et al.*, 2005; Yang *et al.*, 2010). The effect of TGF-β signalling alters cells growth, differentiation and apoptosis. Furthermore, as it influences cell adhesion and migration it also plays and important role during the process of EMT (Santibañez *et al.*, 2011; Hao *et al.*, 2019).

In the context of cancer, the role of TGF-β is described as double-edged sword as it can have pro- and anti-tumorigenic effects. The tumour preventing effects occur mostly in premalignant lesions, which is comparable to the effect of TGF-β on normal epithelial cells, where it induces an anti-proliferative response, increased apoptosis and cell differentiation.

In contrast to that, the tumour promoting effects arise at more advanced stages of tumorigenesis and are accompanied by resistance to the tumour-suppressive effect of TGF-β due to mutations or epigenetic silencing (Akhurst & Derynck, 2001; Seoane & Gomis, 2017).

Another important effect of TGF-β is its influence on the immune system, especially T cells. As the present work includes testing of CAR T cells, the impact of TGF-β on this cellular immunotherapy is of particular importance. It has been shown that TGF-β has a strong inhibitory influence on resting T cells (Rich *et al.*, 1995; Cottrez & Groux, 2001). Inhibition of T cells impairs therapy outcome as it reduces tumour cell eradication and promotes T cell exhaustion (Thomas & Massagué, 2005). This is the reason why different interventions are tested to overcome the inhibition caused by TGF-β (Kloss *et al.*, 2018). During the present work, different intervention strategies were assessed to overcome immunosuppressive actions of TGF-β in order to improve efficacy of ROR1 CAR T cell therapy in TNBC models. Here, pharmacological intervention by engaging a TGF-β receptor inhibitor was evaluated and the desensitisation of CAR T cells towards TGF-β by distinct gene editing in the CAR T cells was determined.

## 1.5 3D culture and tissue engineering for the representation of the cellular tissue environment

3D cell culture techniques are often applied in order to generate tissue-engineered products. Even tough tissue engineering rather defines the establishment of healthy tissue-like constructs for organ or tissue replacement, its techniques can be useful for translational approaches in cancer research. Therefore, an overview is given about the approach to tissue engineering as well as different 3D culture techniques in cancer research are described in the following chapters.

### 1.5.1 Tissue engineering and regenerative medicine

In the 1960s, the field of tissue engineering emerged when researchers tried to find alternative ways of tissue or organ replacement. Vacanti *et al.* defined the term tissue engineering as an “interdisciplinary field combining principles of engineering and life science to develop biological substitutes, which aim to maintain, restore or improve tissue function”. Later in the 1980s, the discovery of stem cells became a strong driver and influenced the field as it revealed even more possibilities (Vacanti, 2006; Chaignaud *et al.*, 2013; Lanza, 2020). Furthermore, tissue engineering belongs to the field of regenerative medicine. This also includes technologies like gene therapy, administration of soluble factors, stem cell transplantation, as well as cell reprogramming. All approaches aim to restore a normal function of the human body and aim to improve patient outcome (Mason & Dunnill, 2008).

The main idea of tissue engineering is to use a sample from a patient, isolate the cells of interest and from that establish the tissue-engineered product which is later implanted back into the patient. As primary cells are often not easy to isolate and maintain, approaches with stem cells and reprogrammed cells might help overcome these obstacles in the future, especially when it comes to diseased donor tissue (Shafiee & Atala, 2017). As the field of tissue engineering grows, the applications also broaden for different research questions. Therefore, approaches for basic research that study cell behaviour in a more advanced 3D environment than 2D culture are developed. In addition, the modelling of diseases in 3D models shows promising results (Holmes *et al.*, 2009; Khademhosseini & Langer, 2016; *Tissue-engineered disease models*, 2018).

The basis of nearly any tissue engineering approach is the use of a specific scaffold also called matrix, which forms the support structure for the cells and tissue. From that, two different strategies emerged: 1.) Where either cell free scaffolds or matrixes are used to support tissue regeneration directly in the body or 2.) Where the scaffold is seeded with patient-specific cells prior implantation. With this, the cells grow within the support structure already before implantation, which can favour tissue maturation. Regarding the scaffold or matrix there is the approach to generate synthetic structures (e.g. synthetic polymers, silicone, Polyethylenterephthalat (PET) membranes) or use biological materials (e.g. hydrogels from alginate or collagen, decellularised tissue matrices) (Olson *et al.*, 2011).

Synthetic and biological scaffolds have different advantages and disadvantages, but they unite the need of cells to grow in a three dimensional (3D) way and allow the cells to grow more physiologically than standard two dimensional (2D) cell culture (Lanza, 2020). Taken together, the fundamental idea of tissue engineering also paves the way for a variety of different models in cancer research. The focus of the present work was to use a biological scaffold derived from porcine jejunum to build defined microphysiologic 3D tumour models with implemented stromal cells as TME-aspects for novel treatment strategies that reflects some advantages of tissue engineering for cancer research.

### 1.5.2 3D culture techniques for cancer research

In cancer research, 2D cell cultures and mouse trials are common ways to study and test new therapy strategies as 600.000 animals are still used in the European Union for cancer studies alone (*EUR-Lex - 52020DC0016 - EN - EUR-Lex*, 2021). Even though, this is the “gold standard” some studies showed that the predictivity of such model systems can be quite low, which is also reflected by high attrition rates of about 95% in the developmental process of new drugs especially regarding cancer (Langhans, 2018; Kunnumakkara *et al.*, 2019; van Norman, 2019). There are several reasons for this, for instance the simplicity of a 2D surface which does not resemble the aforementioned complex tissue structure and homeostasis *in vivo* (Bissell & Radisky, 2001; Langhans, 2018), as well as the often missing human stroma in murine xenografts especially (Hylander *et al.*, 2013). Furthermore, it was shown that murine transcription factors do not activate human receptors, which further disables testing in mouse models and undermines the importance of alternative models, which can support these studies (Baur *et al.*, 2019). Hence, many different approaches have been invented during the last years. The overall goal is to overcome the simplicity of 2D cell culture and to contribute the concept of “3R” *(Reduce, Refine, Replace)* to reduce the need of animal experiments (Russell & Burch, 1992; Hughes & Health, JH Bloomberg School of Public, 2020).

An easy and common way to bring tumour cells into a 3D environment are spheroids, where cell aggregates are cultured in a multi-well format with or without added extracellular matrix molecules. In most cases, cell lines are used, but also primary cells like endothelial cells (Lazzari *et al.*, 2018) or immune cells (Courau *et al.*, 2019) can be implemented. Therefore, spheroids combine high throughput with easy experimental set up (Sant & Johnston, 2017). In contrast, spheroids are often less complex and lack long-term culture homeostasis. Another major drawback is the fact that not all cell lines form spheroids. Additional steps are often required to force the cells into aggregate formation. Furthermore, the culture time of spheroids is limited (Kapałczyńska *et al.*, 2018).

Another approach on 3D culture is the generation of organoids from patient or mouse biopsies. Here, the tissue sample is digested and sheared, resulting in distinct cell aggregates which can be cultured for several months without the occurence of genomic instability (Sachs *et al.*, 2019). Unfortunately, organoids often loose stromal cells and immune cells during culture time, reducing tissue complexity (Kim *et al.*, 2019). Moreover, the use of Matrigel® is often required, which leads to reduced standardisation as it includes undefined factors (Drost & Clevers, 2018). Besides, organoid culture is very expensive due to the need of specific factors and inhibitors that have to be added thoroughly. Also the access to biopsies is limited and it is not always possible to obtain organoids from every biopsy (Drost & Clevers, 2018; Dijkstra *et al.*, 2020).

To study tissue complexity in a patient-specific way, another approach is the use of tumour slice cultures. Here, the fresh specimen obtained from mouse experiments or clinical patients is cut with a Vibratome® and subsequently cultured in medium for up to seven days (Sivakumar *et al.*, 2019). During culture, a treatment can be administered and afterwards histological analysis can be performed. Therefore, the tumour slice culture enables the study of the complex tissues as well as stromal influences. The main drawbacks are limitation of primary material, slice to slice variability and short *ex vivo* survival of the tissue (Naipal *et al.*, 2016; Misra *et al.*, 2019).

Further approaches to enable the incorporation of different cells or cells from different organs are organ-on-a-chip models. Here, several compartments are mounted on a chip connecting different cells via channels to study their interplay. Therefore, these organ-on-a-chip models are complex and allow the incorporation of aforementioned methods like spheroids. In addition, the possibility to add a medium flow mimics the vascularisation from the *in vivo* situation resulting in even more complexity (St-Georges-Robillard *et al.*, 2019; Nashimoto *et al.*, 2020). As those chips are designed to fit a standard glass slide, the compartments are limited and only a small number of cells and low amount of medium can be administered. This reduces the tissue-size, which is available for further analysis dramatically. In addition, the small amount of medium limits sampling and administration of substances. (Sontheimer-Phelps *et al.*, 2019; Trujillo-de Santiago *et al.*, 2019).

To overcome some of those before mentioned obstacles, the present work focuses on a human standardisable, modular microphysiologic 3D tumour model for different solid tumours that enables evaluation of different cellular immunotherapeutic strategies within a tissue-like surrounding. The microphysiologic 3D tumour models are prepared using a porcine matrix derived from the jejunum, which is chemically decellularised and sterilised, placed into trans-well format and seeded with the cells of interest. This technology is based on the BioVaSC-TERM® (Biological vascularized scaffold – Tissue Engineering and Regenerative Medicine) (Linke *et al.*, 2007; Schanz *et al.*, 2010). The matrix is termed Onco-VaSC-TERM® (Ref, DE 30 2014 008, Int.: 1 255 634, US: 7916870) as soon as it is seeded with tumour cells and it harbours the option for vascularisation. The biological matrix without the vascular tree utilised in this work, is called SISmuc (Small Intestinal mucosa with preserved submucosa) and provides a collagen-rich matrix with a preserved basement membrane structure (Stratmann *et al.*, 2014). This scaffold allows the cells to grow naturally in three dimensions and on top of a natural barrier. For the set-up of a microphysiologic 3D tumour model, the cells of interest are incorporated and grown for several weeks under static or dynamic conditions. This represents long-term stability of several weeks. After maturation of the model, the treatment is administered when the cells reach a homeostasis-like state. For standardisation, commercially available tumour cell lines are currently used. To implement stromal components, skin fibroblasts have been implemented previously. In addition to a multi-well format, models under dynamic conditions mimicking the blood flow for the application of further stimuli like shear stress are also feasible. This offers the possibility of drug administration via a flow system, as well as improved waste removal, and a steady nutrient exchange. Furthermore, a larger tumour cell mass is growing naturally under dynamic conditions as well as invasive traits can manifest (Nietzer *et al.*, 2016). The aim of this work was to improve the microphysiologic 3D tumour models and to apply them particularly for cellular immunotherapeutic approaches like CAR T cell therapy. Patient-derived stromal cells were implemented to representing aspects of the TME. Additionally, patient biopsies were used to enable organoid isolation and culture.

## 1.6 Aim of this work

CAR T cell therapy demonstrates notable anti-tumour efficacy in hematologic malignancies, but approaches for solid tumours only show limited success. In comparison to haematological malignancies, a hostile TME in solid tumours poses additional immunological and physical barriers towards the CAR T cells, which reduce therapeutic efficacy (Martinez & Moon, 2019; Mhaidly & Mechta-Grigoriou, 2020; Nazemi & Rainero, 2020). When novel cellular immunotherapeutic approaches are evaluated, the standard tools are mainly 2D cell culture and animal models (Wegner, 2017; Mhaidly & Mechta-Grigoriou, 2020; Srivastava *et al.*, 2021). Two dimensional cell culture especially represents a simple cell environment, as distinct anchorage on the matrix and tissue is missing, while only short-term stability is facilitated

(Edmondson *et al.*, 2014; Langhans, 2018). Animal models, mainly xenografts, attain representation of the tumour tissue architecture but lack human stroma and tumour inoculation occurs frequently on foreign sites compared to the respective tumour entity (Hylander *et al.*, 2013; Wegner, 2017; Srivastava *et al.*, 2021).

Given these drawbacks, a tremendous need arises to generate tumour models, that represent solid tumours in a tissue-like context, that incorporate aspects of the TME and facilitate long-term stability for several weeks.

Therefore, the aim of this work comprises the *improvement of previously described microphysiologic 3D tumour models for the evaluation of cellular immunotherapies, with focus on implementation of inhibitory factors from the hostile TME of solid tumours in order to increase their predictive value. This should lead to defined, scalable, reproducible and exportable microphysiologic 3D tumour models particularly applicable for the evaluation of cellular immunotherapies*.

This work encompasses three specific aims:

1) Improvement of the microphysiologic 3D tumour models in order to extend the represented tumour entities and culture time, to incorporate cellular und soluble aspects of the immunosuppressive TME and to establish a time efficient novel analysis method.

So far, microphysiologic 3D tumour models have been established for epithelial cancers such as breast, lung and colon, which are based on the biological porcine derived SISmuc matrix (Stratmann *et al.*, 2014; Göttlich *et al.*, 2016; Göttlich *et al.*, 2018; Baur *et al.*, 2019). Incorporation of primary dermal fibroblasts demonstrated interactions between tumour and stromal cells in models of colon cancer (Nietzer *et al.*, 2016). Therefore, primary cells depict a promising complementary cell source to cell lines, which can improve representation of the *in vivo* situation in the microphysiologic 3D tumour models. Regarding the tumour microenvironment, CAFs have been demonstrated to strongly influence tumour progression and the efficacy of cellular immunotherapies by posing physical and immunological barriers towards them (Martinez & Moon, 2019; Mhaidly & Mechta-Grigoriou, 2020; Nazemi & Rainero, 2020; Baker *et al.*, 2021). Considering this, it would be beneficial to isolate and implement tumour tissue-derived CAFs into the microphysiologic 3D tumour models, in order to study if a CAF phenotype is preserved in the tumour models.

***This led to the hypothesis, that the SISmuc matrix is also suitable to promote cell growth of additional cancer types and that additional stromal cells such as CAFs can be incorporated, reflecting important aspects of the hostile TME when derived from tumour tissue. Furthermore, the tissue-like context of the microphysiologic 3D tumour models makes them suitable for the application of luminescence-based in vivo imaging, which***

***can offer a novel time efficient read-out method with a high predictive value***. Together, this should increase the predictive value of the microphysiologic 3D tumour models by reflecting important aspects from the hostile TME of solid tumours and expanding their scale of assessment.

In this work, microphysiologic 3D tumour models were established from lung, breast and colorectal cancer cell lines, as well as from sarcoma and melanoma cell lines. Static, semi-static and dynamic culture conditions were compared to prove, if prolonged tissue-homeostasis over a time of several weeks could be achieved in semi-static culture conditions, while providing the advantage of being less elaborate than dynamic culture in complex bioreactors.

Lung (tumour) biopsies were used for isolation of primary tumour cells, fibroblasts and organoids. Isolated fibroblasts were incorporated into the microphysiologic 3D tumour models in order to form stromal-enriched microphysiologic 3D tumour models and to analyse, if they can reflect TME-specific aspects better than fibroblasts from healthy tissues. The lung tissue-isolated fibroblasts were phenotypically analysed to reveal presence of a CAF phenotype. In order to establish an endothelial cell barrier endothelial cells, which can be easily obtained from skin biopsies, were incorporated into different microphysiologic 3D tumour models. This included the application of a novel two-circuit bioreactor approach for several tumour entities. A protocol for BLI-based *in vivo* imaging was then established. Microphysiologic 3D tumour models of Ewing's sarcoma were further engaged to test $G_{D2}$-targeting CAR T cells.

<u>2) Testing of differently designed ROR1 CAR T cells to analyse the sensitivity of the microphysiologic 3D tumour models.</u>

The microphysiologic 3D tumour models have already been extensively studied for the evaluation of chemotherapeutic as well as targeted therapy in lung and colorectal cancer (Göttlich *et al.*, 2016; Nietzer *et al.*, 2016; Göttlich *et al.*, 2018; Baur *et al.*, 2019). Furthermore, it was demonstrated that anti-tumour efficacy of CAR T cells strongly depends on CAR design, as it has been shown by Hudecek *et al.* that a high affinity targeting domain induced favourable effects compared to a low affinity targeting domain. Additionally, the targeting domain needs to be combined with a suitable spacer in order to work effectively (Hudecek *et al.*, 2013; Berger *et al.*, 2015; Hudecek *et al.*, 2015; Boroughs *et al.*, 2019; Weinkove *et al.*, 2019). From this, ***the next hypothesis was derived, that microphysiologic 3D tumour models reflect a strong sensitivity to reveal differences in anti-tumour efficacy of CAR T cells, which depends on CAR design respectively.***

This was assessed by treating static microphysiologic 3D breast and lung tumour models with differently designed ROR1 CAR T cells, where the CAR construct differed in costimulation, intracellular spacer and targeting domain. Anti tumour efficacy was evaluated by secretion of cytokines, expression of surface antigens, histological stainings of the tumour models and BLI based imaging.

3) Evaluation of ROR1 CAR T cell efficacy in the improved microphysiologic 3D tumour models with incorporated aspects from the TME

During the recent years, it became evident that the TME in solid tumours influences therapy outcome strongly, which affects immunotherapy especially. This is also reflected in the lacking results of CAR T cell therapy in solid tumours in the clinic (Martinez & Moon, 2019; Baker *et al.*, 2021). Thus, TME aspects need to be addressed in preclinical tumour models. From this, the hypothesis derived:

***If incoporated TME aspects reflect the physical and immunological barriers of solid tumours within the stromal-enriched microphysiologic 3D tumour models, they challenge different CAR T cell products with immunosuppressive in vivo-like conditions, which will increase the predictive value of the microphysiologic 3D tumour model.***

Microphysiologic 3D breast and lung cancer models were cultured under static, semi-static or dynamical conditions. TME aspects were reflected by CAF-enrichment and/or the immunosuppressive factor TGF-β and treated with different ROR1 CAR T cells to evaluate their anti-tumour efficacy accordingly. Furthermore, long-term treatment (14 days) of dynamic lung tumour models with ROR1 CAR T cells was analysed. An alternative route of application compared to T cell administration via the medium flow was established, which enables direct injection into sandwich-culture tumour models. Additionally, pharmacological intervention with a specific TGF-β receptor inhibitor was studied to analyse, if this would improve CAR T cell function by overcoming immunosuppressive effects. Finally, improved gene-edited ROR1 CAR T cells were administered in microphysiologic 3D tumour models of TNBC, which combined stromal-enrichment with CAFs and immunosuppressive effects mediated by TGF-β to investigate, if they are sufficiently shielded from the barriers of the TME in order to mediate effective anti-tumour function.

***Consequently, this work will provide insights into the defined microphysiologic 3D tumour models, that are scalable, reproducible, and standardisable with specific improvements for the evaluation of cellular immunotherapies.***

# 2. Materials

## 2.1 Laboratory Equipment

*Table 3. List of laboratory equipment and devices*

| Equipment/Device | Producer/Supplier |
|---|---|
| Analytical balances:<br>Kern ABJ 220-4M,<br>Kern EG 2200-2NM | Kern & Sohn GmbH, Balingen-Frommern (D) |
| Aspiration device (VacuBoy) | Integra Biosciences, Fernwald (D) |
| Autoclaves:<br>Systec DX-45<br>Systec VX-150 | Systec GmbH, Wettenberg (D) |
| Bioreactor board | Chair of Tissue Engineering & Regenerative Medicine, Würzburg (D) |
| Cell freezing container styrofoam (Mr. Frosty™)<br>Cell freezing container with isopropanol (Mr. Frosty™) | VWR, Darmstadt (D)<br>Thermo Fisher Scientific, Dreieich (D) |
| Cell incubator (37°C, 5% $CO_2$) | Heraeus, Hanau (D) |
| Centrifuges:<br>Centrifuge 5417R<br>Multifuge X1R<br>Rotilabo | Eppendorf, Hamburg (D)<br>Thermo Fisher Scientific, Dreieich (D)<br>Carl Roth GmbH, Karlsruhe (D) |
| Cold storage room (4°C) | Genheimer, Höchberg (D) |
| Cooling plate MEDITE TES Valida | Medite GmbH, Burgdorf (D) |
| Digital Camera | Canon, Krefeld (D) |
| Embedding cassette printer VCP-5001 | Vogel Medizintechnik, Gießen (D) |
| Embedding machine (Microm STP120) | Thermo Fisher Scientific, Dreieich (D) |
| Fine Scale Sartorius MSE3.6P-000-DM | Sartorius, Göttingen (D) |
| Freezers:<br>-80°C HFU586 Basic<br>-20°C Comfort | Heraeus, Hanau (D)<br>Liebherr, Biberach a.d. Riss (D) |
| Fume hood | Prutscher Laboratory Systems, Neudörfl (A) |
| Hand tally counter | neoLab, Heidelberg (D) |
| Hazardous material cabinet | MSG Produkte, Schöllkrippen (D) |
| Hot air sterilizer | Memmert, Schwabach (D) |
| Ice machine AF-80 | Scotsman, Milano (I) |
| Imaging station FluorChem Q | Biozym Scientific GmbH, Hessisch Oldendorf (D) |
| Immersion thermostat for water bath | Lauda, Lauda-Königshofen (D) |
| In Vivo Imaging System Xtreme II | Bruker, Massachusetts (USA) |

*Table 3. List of laboratory equipment and devices (continued)*

| Equipment/Device | Producer/Supplier |
|---|---|
| Laboratory dish washer | Miele, Gütersloh (D) |
| Laminar flow cabinet Safe 2020 | Thermo Fisher Scientific, Dreieich (D) |
| Liquid nitrogen storage tank MVE 815 P190 | German-cryo, Jüchen (D) |
| Magnetic stirrer with integrated heater 720-HPS | VWR, Darmstadt (D) |
| Magnetic stirrer small IKA topolino | IKA-Werke GmbH& CO. KG, Staufen (D) |
| Microscopes: | |
| Bright field (Axio Lab.A1) | Carl Zeiss Microscopy GmbH, Göttingen (D) |
| Bright field EVOS Core XL | Thermo Fisher Scientific, Dreieich (D) |
| Confocal (SP8) | Leica, Wetzlar (D) |
| Fluorescence (BZ-9000) | Keyence, Neu-Isenburg (D) |
| Multichannel pipettes:<br>Research® plus<br>8 channel (10 – 100 µl and 30 – 300 µl)<br>12 channel (10 – 100 µl and 30 – 300 µl) | Eppendorf, Hamburg (D) |
| Neubauer cell counting chamber (hemocytometer) | Marienfeld GmbH & Co. KG, Lauda-Königshofen (D) |
| Object slide printer VSP-5001 | Vogel Medizintechnik, Gießen (D) |
| Orbital shaker:<br>KM-2 Akku<br>KM CO2-FL | Edmund Bühler GmbH, Hechingen (D) |
| Paraffin embedding module MEDITE TES Valida | Medite GmbH, Burgdorf (D) |
| Peristaltic pump | Ismatec, Wertheim-Mondfeld (D) |
| pH-Meter | Mettler Toledo, Gießen (D) |
| Pipettes:<br>Research® Plus<br>0.5 – 10 µl, 10 – 100 µl, 100 – 1000 µl | Eppendorf, Hamburg (D) |
| Pipetting aid (accu-jet® pro) | Brand, Wertheim (D) |
| Pressure sensor: reusable transducer SP844 | HJK Sensoren + Systeme GmbH & Co. KG, Merching (D) |
| Pump tubing cassette | Ismatec, Wertheim-Mondfeld (D) |
| Refrigerator (MediLine) | Liebherr, Biberach a.d. Riss (D) |
| Rocking platform shaker | VWR, Darmstadt (D) |
| Rotating mixer | neoLab, Heidelberg (D) |
| Sliding microtome (Leica SM2010 R) | Leica, Wetzlar (D) |
| Steamer (MultiGourmet) | Braun, Kronberg/Taunus (D) |
| Thermomixer (comfort) | Eppendorf, Hamburg (D) |
| Tissue Drying Oven TD066 | Medite GmbH, Burgdorf (D) |
| Tissue float bath GFL1052 | GFL Gesellschaft für Labortechnik GmbH, Burgwedel (D) |
| Vortexer (Genie) | Carl Roth GmbH, Karlsruhe (D) |
| Water purification system (MilliQ®) | Merck-Millipore, Darmstadt (D) |

## 2.2 Consumables

*Table 4. List of consumables*

| **Product** | **Producer/Supplier** |
|---|---|
| Air filter, sterile (16596-HYK) | Sartorius, Göttingen (D) |
| Cell culture flasks (25 cm$^2$, 75 cm$^2$, 150 cm$^2$) | TPP Techno Plastik Products AG Trasadingen (CH) |
| Cell scraper | Sarstedt, Nümbrecht (D) |
| Cell strainer<br>(40 µm, 70 µm, 100 µm)<br>(400 µm) pluriStrainer® | <br>BD Biosciences, Heidelberg (D)<br>pluriSelect Life Science, Leipzig (D) |
| Centrifuge tubes (15 ml, 50 ml) | Greiner Bio-One, Frickenhausen (D) |
| Cover slips for object slides (24x60 mm) | Menzel-Gläser, Braunschweig (D) |
| Cover slips (round,12 mm) | Marienfeld GmbH & Co. KG, Lauda-Königshofen (D) |
| Cryo tubes (Cryo.s™) | Greiner Bio-One, Frickenhausen (D) |
| serological pipettes(5 ml, 10 ml, 25 ml, 50 ml) | Greiner Bio-One, Frickenhausen (D) |
| Embedding cassettes | Klinipath, Duiven (NL) |
| Embedding filter paper | Labonord, Mönchengladbach (D) |
| Gloves: Peha-soft nitrile | Paul Hartmann AG, Heidenheim (D) |
| Liquid Blocker Pens:<br>PAP pen<br>Grease pen | <br>Science Services GmbH, Munich (D)<br>Dako, Hamburg (D) |
| Microtome disposable blades | pfm Medical, Köln (D) |
| Object slides:<br>Superfrost<br>Polylysine™ | <br>Menzel, Braunschweig (D)<br>Langenbrinck, Emmendingen (D) |
| O-rings (sealing rings) for bioreactors | Dichtelemente arcus GmbH, Seevetal (D) |
| Parafilm®M | Carl Roth GmbH, Karlsruhe (D) |
| Pasteur pipettes | Brand, Wertheim (D) |
| Petri dishes (145x20mm, 6x20mm) | Greiner Bio-One, Frickenhausen (D) |
| Pipette tips: 0.5 – 10 µl, 10 – 100 µl, 100 – 1200 µl | Eppendorf, Hamburg (D) |
| Pressure dome: sterile and disposable dome 844-28 | Memscap AS, Skoppum (N) |
| Pump tubing (SC0746) | Ismatec, Wertheim-Mondfeld (D) |
| Scalpel blades (rounded) | Bayha, Tuttlingen (D) |
| Silicone tube (9531.1) | Carl Roth GmbH, Karlsruhe (D) |
| Sterile filter (attachment for disposable syringes): Diameter 50 mm, Pore size: 0.2 µm | Sartorius , Göttingen (D) |
| Syringes with Luer Lock (2 ml, 3 ml, 5 ml) | B. Braun GmbH, Melsungen (D) |
| Vasofix® Safety:<br>18G (4269136S-01)<br>20G (4269110S-01) | B.Braun Melsungen GmbH, Melsungen (D) |

## 2.3 Laboratory Materials

*Table 5. List of laboratory materials*

| Product | Producer/Supplier |
|---|---|
| Beaker (250 ml, 500 ml, 1l, 2l, 5l)<br>glass<br>plastic | <br>Schott, Mainz (D)<br>Bürkle GmbH, Bad Bellingen (D) |
| Cell crowns for three-dimensional culture | GT-Labortechnik, Arnstein (D) |
| Glass cuvettes with lid (100x90x80 mm) | Mercateo, München (D) |
| Humidity chamber | Chair of Tissue Engineering & Regenerative Medicine, Würzburg (D) |
| Laboratory glass bottles (50 ml, 100 ml, 250 ml, 500 ml, 1000 ml, 2000 ml) | Brand, Wertheim (D) & Schott, Mainz (D) |
| Magnetic stirring bars | Hartenstein, Würzburg (D) |
| Measuring cylinders (50 ml, 100 ml, 250 ml, 500 ml, 1000 ml)<br>glass<br>plastic | <br>Brand, Wertheim (D)<br>Vitlab GmbH, Großostheim (D) |
| Object slide racks (glass, stainless steel) | Mercateo, München (D) |
| Scalpel blade handles | Bayha, Tuttlingen (D) |
| Small components for bioreactor (Luer lock adapters, etc.) | Nordson Medical, Loveland (USA) |
| Stainless steel casting moulds for embedding tissue(24x37x9 mm) | Labonord, Mönchengladbach (D) |
| Sterile filter (bottle top) | Hartenstein, Würzburg (D) |

## 2.4 Chemicals and Solutions

*Table 6. List of general chemicals and solutions*

| Product | Producer/Supplier | Catalog No. |
|---|---|---|
| 2-Propanol | Carl Roth GmbH, Karlsruhe (D) | 6752.2 |
| 3-(4,5-Dimethylthiazol-2-yl)-2,5-diphenyltetrazoliumbromide (MTT) | Serva, Heidelberg (D) | 20395.01 |
| 4',6-Diamidino-2-phenylindoldihydrochloride (DAPI) | Sigma-Aldrich, München (D) | D9542 |
| A83-01 | Tocris/BioTechne GmbH, Wiesbaden (D) | 2939 |
| Advanced Dulbecco's Modified Eagle Medium (DMEM) F12 | Gibco® Life Technologies™, Darmstadt (D) | 12634010 |

*Table 6. List of general chemicals and solutions (continued)*

| Product | Producer/Supplier | Catalog No. |
|---|---|---|
| Antibody dilution buffer | DCS Innovative Diagnostik-Systeme, Hamburg (D) | AL120R500 |
| Anti-Anti 100x | Gibco® Life Technologies™, Darmstadt (D) | 15240-062 |
| Aqix® Liquid Life | Aqix Life Science Group, Bedford (UK) | AQIX-RSI-L |
| B27 supplement without Vitamin A | Gibco® Life Technologies™, Darmstadt (D) | 12587-010 |
| Cell Recovery Solution | Thermo Fisher Scientific, Dreieich (D) | 11543560 |
| Citric acid monohydrate | VWR, Darmstadt (D) | 1.00244.1000 |
| DAPI Fluoromount-G™ eBioScience™ | Thermo Fisher Scientific, Dreieich (D) | 00-4959-53 |
| Descosept® AF | Dr. Schumacher GmbH, Melsungen (D) | 00-311-050 |
| Deoxycholic acid sodium salt (≥ 98%) | Carl Roth GmbH, Karlsruhe (D) | 3484.2 |
| Dimethyl sulfoxide (DMSO) | Sigma-Aldrich, München (D) | D2438-50ML |
| Donkey serum | BIOZOL Diagnostica Vertrieb GmbH, Eching (D) | ECLECS0217D |
| Dulbecco's Modified Eagle Medium (DMEM) (4.5 *g/l* D-Glucose) + GlutaMax™-I | Gibco® Life Technologies™, Darmstadt (D) | 32430-027 |
| Dulbecco's Modified Eagle Medium/ F-12 (DMEM/F12) + GlutaMax™-I | Gibco® Life Technologies™, Darmstadt (D) | 31331-28 |
| Eosin 1%, aqueous | Morphisto GmbH, Frankfurt am Main (D) | 10177 |
| Ethanol: | | |
| Absolute | Carl Roth GmbH, Karlsruhe (D) | 9056.4 |
| 96%, denatured | Carl Roth GmbH, Karlsruhe (D) | T171.4 |
| Ethylenediamintetraacetic acid (EDTA) | Sigma-Aldrich, München (D) | E5134-1KG |
| Fetal calf serum | PAN Biotech, Aidenbach (D) | P30-3306<br>Lot. P150508 |
| FGF 7 | Peprotech, Hamburg (D) | 100-19-100 |
| FGF 10 | Peprotech, Hamburg (D) | 100-26-100 |
| Formaldehyde/Formalin,phosphate buffered (4%, pH7) | Carl Roth GmbH, Karlsruhe (D) | P087.3 |

*Table 6. List of general chemicals and solutions (continued)*

| Product | Producer/Supplier | Catalog No. |
|---|---|---|
| Gentamycin | Genaxxon bioscience GmbH, Ulm (D) | CAS-Nr: 1405-41-0 |
| GlutaMAX 100x | Gibco® Life Technologies™, Darmstadt (D) | 35050038 |
| Haematoxylin acid according to MAYER | Morphisto GmbH, Frankfurt am Main (D) | 10231 |
| HEPES 1M | Sigma-Aldrich, München (D) | H3662 |
| Hydrochloric acid (HCl) | | |
| 37 % (fuming) | Carl Roth GmbH, Karlsruhe (D) | 4625.2 |
| 1 M columetric standard solution | Carl Roth GmbH, Karlsruhe (D) | K025.1 |
| 6 M columetric standard solution | Carl Roth GmbH, Karlsruhe (D) | 0281.1 |
| Hydrogen peroxide (30 %) | Sigma-Aldrich, München (D) | 216763-500ML |
| Incidin® plus | Ecolab Healthcare, Monheim/Rhein (D) | 3011520 |
| Luciferin | Promega, Wisconsin (USA) | P1041 |
| Matrigel® Matrix | Omnilab, Bremen (D) | FALC356231 |
| Mounting Media: Entellan® | Merck Chemicals GmbH, Darmstadt (D) | 107960 |
| N-Acetylcysteine | Sigma-Aldrich, München (D) | A9165-5G |
| Nicotinamid | Sigma-Aldrich, München (D) | N0636-100G |
| Noggin | Peprotech, Hamburg (D) | 250-38-1MG |
| Paraffin | Carl Roth GmbH, Karlsruhe (D) | 6642.6 |
| Penicillin/Streptomycin (PenStrep, 100x conc.) | Sigma-Aldrich, München (D) | P4333 |
| Phosphate buffered saline (PBS): | | |
| powder (w/o $Ca^{2+}$ and $Mg^{2+}$) | Biochrom GmbH, Berlin (D) | L182-50 |
| solution (w/ $Ca^{2+}$ and $Mg^{2+}$) | Sigma-Aldrich, München (D) | D8662 |
| solution (w/o $Ca^{2+}$ and $Mg^{2+}$) | Sigma-Aldrich, München (D) | D8537 |
| SB202190 | Absource Diagnostics GmbH, Munich (D) | S1077-0100 |
| Roswell Park Memorial Institute Medium 1640 (RPMI 1640) + GlutaMax™-I | Gibco® Life Technologies™, Darmstadt (D) | 61870-101 |
| Sodium azide ($NaN_3$) | Carl Roth GmbH, Karlsruhe (D) | 4221.1 |
| Sodium chloride ($NaCl$) | Carl Roth GmbH, Karlsruhe (D) | HN00.3 |

*Table 6. List of general chemicals and solutions (continued)*

| Product | Producer/Supplier | Catalog No. |
|---|---|---|
| Sodium hydroxide (NaOH)<br>Pellets<br>1M volumetric standard<br>5M volumetric standard | <br>Carl Roth GmbH, Karlsruhe (D)<br>Carl Roth GmbH, Karlsruhe (D)<br>Carl Roth GmbH, Karlsruhe (D) | <br>6771.3<br>K021.1<br>KK71.1 |
| Sodium pyruvate (100mM) | Invitrogen, Darmstadt (D) | 11360-039 |
| R-Spondin 1 | Peprotech, Hamburg (D) | 120-38-500UG |
| TGF-β (Isoform 1) | R&D Systems, Minneapolis (USA) | 240-B010 |
| Total bile acids assay control | Diazyme Europe GmbH, Dresden (D) | DZ042A-Con |
| Triton™ X-100 | Sigma-Aldrich, München (D) | X100-1L |
| Trypan blue 0.4 % | Sigma-Aldrich, München (D) | T8154-100ML |
| Tween®-20 | Sigma-Aldrich, München (D) | P7949-500ML |
| VascuLife VEGF-Mv (Microvascular Endothelial Cell Culture Medium) | CellSystems GmbH, Troisdorf (D) | LL-0005 |
| Xylene | Carl Roth GmbH, Karlsruhe (D) | 9713.3 |
| Y-27632 | Tocris/BioTechne GmbH, Wiesbaden (D) | 1254/10 |

## 2.5 Solutions and Media for Cell Culture

*Table 7. List of prepared solutions and media for cell culture work*

| Media/Solution | Composition |
|---|---|
| 0.05 % Trypsin/EDTA working solution | 10 *ml* Trypsin/EDTA 0.5% (10x)<br>90 *ml* PBS- solution stored at 4°C |
| A549 culture medium | 10% (v/v) FCS in Roswell Park Memorial Institute Medium 1640 (RPMI 1640), stored at 4°C |
| Collagenase solution (10-20 mg/ml) | 10-20 mg Collagenase NB4<br>10 ml Advanced DMEM F12<br>Freshly prepared prior use |
| DNase I solution | 100 *mg* DNase I (grade II)<br>300 *ml* PBS+ with 1% Pen/Strep<br>freshly prepared prior to use |
| Fibroblast culture medium | 10% (v/v) FCS<br>1x Penicillin/Streptomycin<br>1 mM Sodium Pyruvate<br>In Dulbecco’s Modified Eagle Medium (DMEM),stored at 4°C |

*Table 7. List of prepared solutions and media for cell culture work (continued)*

| **Medium/Solution** | **Composition** |
|---|---|
| HCC-827 | 20 % (v/v) FCS in Roswell Park Memorial Institute Medium 1640 (RPMI 1640),<br>stored at 4°C |
| HROC24 and HROC87 culture medium | 10 % (v/v) FCS in Dulbecco's Modified Eagle Medium/F-12 (DMEM/F-12)<br>stored at 4°C |
| Luciferin stock solution 10 mg/ml | 50 mg luciferin powder<br>5 ml ultrapure water (MilliQ®)<br>Sterile filtered and stored at -20°C |
| MDA-MB-231 culture medium | 10 % (v/v) FCS in Roswell Park Memorial Institute Medium 1640 (RPMI 1640),<br>1x Penicillin/Streptomycin<br>stored at 4°C |
| MTT reagent | 3 mg/ml MTT solved in ultrapure water |
| MTT working solution (1 mg/ml) | 1 volume MTT reagent (3 mg/ml)<br>2 volumes cell specific media prepared immediately before use |
| PBS- | 9.55 g PBS powder (w/o $Ca^{2+}$ and $Mg^{2+}$)<br>in 1 L Ultrapure water<br>(MilliQ®) |
| PBS-/EDTA | 500 ml PBS solution without $Ca^{2+}$, $Mg^{2+}$<br>500 µl 0.5 M $Na_2$-EDTA $2H_2O$ |
| RD-ES and SK-ES1 culture medium | 10% (v/v) FCS in Roswell Park Memorial Institute Medium 1640 (RPMI 1640),<br>2 mM L-glutamine<br>1x Penicillin/Streptomycin, stored at 4°C |
| SW480 culture medium | 10% (v/v) FCS in Roswell Park Memorial Institute Medium 1640 (RPMI 1640),<br>stored at 4°C |
| TGF-β stock solution | 100 µg/mL<br>in sterile 4 mM HCl containing at least 0.1 % human serum of BSA |
| TGF-β working solution | 10 ng/ml in cell specific media |

*Table 8. Composition of organoid media for isolated lung organoids; modified after (Sachs et al., 2019)*

**Organoid Media composition**

| Media Component | Final Concentration |
|---|---|
| R-Spondin 1 | 500 ng·ml$^{-1}$ |
| FGF 7 | 25 ng·ml$^{-1}$ |
| FGF 10 | 100 ng·ml$^{-1}$ |
| Noggin | 100 ng·ml$^{-1}$ |
| A83-01 | 500 nM |
| Y-27632 | 5 µM |
| SB202190 | 500 µM |
| B27 supplement | 1x |
| N-Acetylcysteine | 1.25 mM |
| Nicotinamide | 5 mM |
| GlutaMax 100x | 1x |
| Hepes | 10 mM |
| Penicillin / Streptomycin | 100 U·ml$^{-1}$ / 100 µg·ml$^{-1}$ |
| Advanced DMEM/F12 | 1x |

## 2.6 Solutions for Histology

*Table 9. List of prepared solutions and buffers for histology work*

| Buffer/Solution | Composition |
|---|---|
| Blocking Solution | 5% (v/v) Donkey serum<br>in Antibody dilution buffer freshly prepared prior use |
| Citrate buffer stock solution (10x concentrated) | 42 g/l Citric acid monohydrate<br>17.6 g/l *NaOH* pellets<br>in dd$H_2O$, pH6 stored at 4°C |
| Citrate buffer working solution | 10% (v/v) Citrate buffer stock solution<br>in dd$H_2O$ |
| Hydrogen peroxide 3% | 10% (v/v) $H_2O_2$ 30% ($H_2O_2$) in dd$H_2O$ prepared immediately before use |
| Washing buffer stock solution (PBS, 10x concentrated) | 1370 mM NaCl<br>26.8 mM KCl14.5mM $KH_2PO_4$<br>64.6 mM $Na_2PO_4$ $2H_2O$<br>in dd$H_2O$<br>pH 7.2, autoclaved<br>before use<br>stored at RT |
| Washing buffer (PBS-T) | 10 % (v/v) Washing buffer stock solution<br>0.5 % (v/v) Tween®-20<br>in dd$H_2O$<br>stored at RT |

## 2.7 Antibodies

In the following table all antibodies used during this work for immunofluorescence and DAB staining are listed. If not stated otherwise all primary antibodies were diluted 1:100 and all secondary antibodies were diluted 1:400.

*Table 10. List of antibodies with respective clone and host animal*

| Antibody | Clone | Host | Producer |
|---|---|---|---|
| AlexaFluor® 555 anti-Mouse IgG (H+L) | - | Donkey | Thermo Fisher Scientific, Dreieich (D), Cat. No. A-31570 |
| Alexa Fluor® 555 anti-Rabbit IgG (H+L) | - | Donkey | Thermo Fisher Scientific, Dreieich (D), Cat. No. A-31571 |
| Alexa Fluor® 647 anti-Mouse IgG (H+L) | - | Donkey | Thermo Fisher Scientific, Dreieich (D), Cat. No. A-31571 |
| Alexa Fluor® 647 anti-Rabbit IgG (H+L) | - | Donkey | Thermo Fisher Scientific, Dreieich (D), Cat. No. A-31573 |
| Alexa Fluor® 488 anti-Rabbit IgG (H+L) | - | Donkey | Thermo Fisher Scientific, Dreieich (D), Cat. No. A-11055 |
| α-SMA | 1A4 | mouse (IgG2a) | Abcam pcl, Cambridge (GB), Cat. No. 7817 |
| CD31 | JC70A | mouse (IgG1k) | Agilent Technologies Inc. (USA), Cat. No. M0823 |
| CD44 | EPR1013Y | Rabbit (IgG) | Abcam pcl, Cambridge (GB), Cat. No. 51037 |
| CD45 | 2B11 + PD7/26 | mouse (IgG1 kappa) | Agilent Technologies Inc. (USA), Cat. No. M0701 |

*Table 10. List of antibodies with respective clone and host animal (continued)*

| Antibody | Clone | Host | Producer |
|---|---|---|---|
| cytokeratin, Pan (PCK) | C-11+PCK-26+CY-90+KS-1A3+M20+A53-B/A2 | Mouse (IgG1/IgG2a) | Sigma-Aldrich, München (D), Cat. No. C2562 |
| E-cadherin | 36/ECadherin | Mouse (IgG2 a kappa) | BD Transduction Laboratories, Heidelberg (D), Cat. No. 610181 |
| FAP | EPR20021 | rabbit (IgG) | Abcam pcl, Cambridge (GB), Cat. No. 207178 |
| GFP | - | goat (IgG) | Rockland Immunochemicals Inc., Limerick (IRL) Cat. No. 600-101-215 |
| Ki67 | SP6 | rabbit (IgG) | Abcam pcl, Cambridge (GB), Cat. No. 166667 |
| MMP-2 | 6E3F8 | mouse (IgG) | Abcam pcl, Cambridge (GB), Cat. No. 86607 |
| MMP-9 | 56-2A4 | mouse (IgG1) | Abcam pcl, Cambridge (GB), Cat. No. 58803 |
| vimentin | EPR3776 | rabbit (IgG) | Abcam pcl, Cambridge (GB), Cat. No. 92547 |

## 2.8 Cell lines and primary cells

*Table 11. List of used cell lines*

| Cell line | Description | Source |
|---|---|---|
| A549 | A cell line derived from a lung carcinoma of a 58-year-old Caucasian man. Epithelial and adherent growing cells. | DSMZ (ACC 107) |
| HCC827 | A cell line derived from a 39-year-old woman with Non-small cell lung cancer (adenocarcinoma type). Large epithelial and adherent growing cells (typically monolayer). | DSMZ (ACC 566) |

*Table 11. List of used cell lines (continued)*

| Cell line | Description | Source |
|---|---|---|
| HROC87 | A xenopatient-derived early-passage cell line established from a grade 3 primary adenocarcinoma of the colon ascendens of a 76-year-old Caucasian woman. TNM stage: T3N0M0. Epithelial and adherent growing cells. | University of Rostock, Division of Molecular Oncology and Immunotherapy, Rostock (D) |
| MCF-7 | A cell line derived from a pleural effusion of a 69-year-old Caucasian woman with metastatic mammary carcinoma (after radio- and hormone therapy) in 1970. Epithelial and adherent growing cells (typically monolayers). | DSMZ (ACC 115) |
| MDA-MB-231 | A cell line derived from a pleural effusion of a 51-year-old Caucasian woman with breast carcinoma (after chemotherapy). Epithelial and adherent growing cells (typical monolayers). | ATCC® (CRM-HTB-26™) |
| RD-ES | A cell line derived from the primary tumour of a 19-year old Caucasian man with Ewing’s Sarcoma (from Humerus) in 1984. Adherent growing cells (monolayers, adherent clusters). | DSMZ (ACC 260) |
| SK-ES1 | A cell line derived from the Ewing’s sarcoma of an 18-year-old man in 1971. Adherent fibroblastoid cells (monolayer, adherent clusters, no confluency). | DSMZ (ACC 518) |
| SK-MEL-28 | A cell line derived from skin tumour tissue of a 51-year-old man with malignant melanoma. Adherent growing epithelial-like cells (monolayer). | gifted from Freia Schmid<br>(AG Groeber-Becker) |
| SW480 | A colon adenocarcinoma cell line established from a grade 4 tumour (Duke class B) of a 50-year-old Caucasian man. Epithelial and adherent growing cells. | SW480<br>(ATCC® CCL-228™) |

*Table 12. List of used primary cells*

| Cell type | Description | Source |
|---|---|---|
| CAFs (Cancer-associated Fibroblasts: e.g. prim CAFs from biopsy #127, metCAFs from biopsy #130) | Primary fibroblasts isolated from malignant lung tissue of lung tumour patients. Mesenchymal adherently growing cells. | University of Würzburg |
| hDF<br>(human dermal Fibroblasts) | Primary fibroblasts isolated from foreskin biopsies. Mesenchymal adherently growing cells. | University of Würzburg |
| hLF (human lung Fibroblasts) | Primary fibroblasts isolated from healthy lung tissue of lung tumour patients. Mesenchymal adherently growing cells. | University of Würzburg |
| hmvECS<br>(human microvascular Endothelial cells) | Primary human microvascular endothelial cells isolated from foreskin biopsies. | University of Würzburg |

## 2.9 Enzymes

*Table 13. List of used enzymes during tissue preparation*

| Media/Solution | Description | Producer/Supplier |
|---|---|---|
| Collagenase lyophilisate | Collagenase NB4 or Clostridiopeptidase A from *Clostridium histolyticum* Protease specific for collagen, degenerates extracellular matrix. | Serva,<br>Heidelberg (D),<br>Cat. No. 17454.01 |
| Deoxyribonuclease I (DNase I) | DNase I (grade II) is a double-strand-specific endonuclease from bovine pancreas. Used for DNA degradation during the preparation of the SISmuc. | Roche,<br>Penzberg (D),<br>Cat. No. 10104159001 |
| Trypsin/EDTA stock solution, 0.5 % (10x concentrated) | Trypsin is a serine protease used to digest cell adherence molecules for detachment of cells from their culture vessels. | Invitrogen,<br>Darmstadt (D),<br>Cat. No 15400-054 |

## 2.10 Kits

*Table 14. List of kits used during this work*

| Kit | Description | Producer/Supplier |
|---|---|---|
| IHC-Kit DCS<br>SuperVision 2 HRP | Two-step polymer system for immunohistochemical staining with horse radish peroxidase (HRP) and 3,3'-diaminobenzidine (DAB) using. Secondary anti-mouse and anti-rabbit antibodies. | DCS Innovative Diagnostik-Systeme GmbH & Co.KG, Hamburg (D),<br>Cat. No. PD000KIT |
| IL-2 and IFN-γ ELISA | Immunoassay for the quantitative determination of human IL-2 and IFN-γ concentrations in cell culture supernatant, serum, plasma and other biological fluids. | BioLegend,<br>San Diego (USA),<br>Cat. No. 431815 (IL-2)<br>Cat. No. 430115 (IFNγ) |
| M30 CytoDeath™ ELISA | One step *in vitro* immunoassay for the quantitative determination of apoptosis in cultured human, monkey or bovine epithelial cells expressing the intermediate filament protein keratin 18 (K18). | Peviva, Bromma (S),<br>Cat. No. 10900 |
| Proteome Profiler™ Human XL Cytokine Array (ARY022B) | A membrane-based antibody array for the parallel determination of the relative levels of selected human cytokines and chemokines. | R&D Systems, Inc.,<br>Minneapolis (USA),<br>Cat. No.ARY022B |
| Total Bile Acids<br>Assay Kit | Assay for the quantitative determination of total bile acids. Used for controlling the bile acid residues of the SISmuc after decellularisation with deoxycholic acid. | Diazyme Europe GmbH, Dresden (D),<br>Cat. No. DZ042A-K |

## 2.11 Software

*Table 15. List of used software*

| Software | Description | Developer/Manufacturer |
|---|---|---|
| Affinity Designer 1.9.0.932 | Vector-based graphic software | Serif (Europe) Ltd, Nottingham (UK) |
| AlphaView FluorChem Q 3.2.2 | Imaging and analysis tool for protein and nucleotide gels | ProteinSimple, San Jose (USA) |
| Bruker MI Se 7.5.2 | Imaging analysis tool for luminescence measurements. | Bruker, Massachusetts (USA) |
| BZ Analyzer | Software for microscopy | Keyence Corporation, Neu-Isenburg (D) |
| FlowJo 7.2/10.6.1 | Software for analysis of flow cytometry data | Becton Dickinson Bioscience, Franklin Lakes (USA) |
| GraphPad Prism 7.03 | Software for statistical analysis. | GraphPad Software, San Diego (USA) |
| ImageJ | Open source image processing program | Wayne Rasband, National Institute for Health (USA) |
| InteractiVenn | Web-based tool for the analysis of sets through Venn diagrams | Heberle, H.; Meirelles, G. V.; da Silva, F. R.(Heberle *et al.*, 2015) |
| Microsoft Office Package 2016 | Presentation software, Spreadsheet processing, text documents | Microsoft Corporation, Redmond (USA) |
| Origin 2019 | Data analysis and graphing software | OriginLab Corporation, Northampton (USA) |
| Pressure Control | Software for controlling pumping speed at the bioreactor panel. | Chair of Tissue Engineering & Regenerative Medicine, Würzburg (D) |

# 3. Methods

## 3.1 Cell culture

For cell culture work, a safety level laminal flow hood was used to ensure sterility. The incubator was set to standard conditions with 37 °C 5 % $CO_2$ and 95 % humidity to allow for optimal growing conditions. To provide sterility all used products and liquids were purchased sterile, autoclaved or sterile-filtered, if possible. All used instruments were cleaned with disinfectant, sealed single-use products were used or the respective good was also autoclaved.

### 3.1.1 Culture of cell lines

During this work, different cell lines were used (see Table 11). Most experiments were conducted using A549 cells derived from a lung adenocarcinoma and MDA-MB-231 cells derived from TNBC. To enable visualisation via luminescence they were transduced using a lentiviral vector containing the *firefly-luciferase*. Dr Lars Wallstabe, who kindly provided the transfected cells, performed the transduction.

The cells were cultured using Rosewell Parks Memorial Institute (RPMI) 1640 medium with 10 % fetal calf serum (FCS) and 1 % Penicillin/ Streptomycin (P/S). All cells were cultured and treated according to supplier's instructions (see Table 7). Medium exchange was performed every 2 to 3 days until the cells reached a confluency of 80 to 90%.

### 3.1.2 Passaging of cells

At a confluency of about 80 %, the medium was aspirated and the cells were washed with 10 to 15 ml phosphate buffered saline (PBS) / Ethylenediaminetetraacetic acid (EDTA) solution. The washing buffer was incubated for up to 5 minutes. Trypsin solution was used for cell detachment (1.5 ml: T25, 3 ml: T75, 6 ml: T 150). After 3 to 5 minutes the reaction was stopped by adding the respective medium containing FCS (3 ml: T25, 6 ml: T75, 12 ml: T 150). The cell solution was transferred to a 50 ml test tube and centrifuged for 5 min at 300 *xg*. Afterwards, the supernatant was aspirated and the cell pellet was resuspended in fresh cell specific medium. The cells were counted using a Neubauer Chamber and Trypan Blue to distinguish from dead cells. For splitting ratios of used cell lines, see Table 16.

*Table 16. List of used cell lines, with disease description and splitting ratios*

| **cell line** | **disease** | **splitting ratio** | **flask size ($cm^2$)** |
|---|---|---|---|
| A549 | Lung carcinoma | 1:8 for 3 days<br>1:10 for 4 days | T75 |
| HCC-827 | Non-small cell lung carcinoma | 1,2x$10^6$ for 3 days<br>1x$10^6$ for 4 days | T150 |
| HROC-87 | colorectal carcinoma | 3–5·$10^5$cells/75 $cm^2$ | T75 |
| MCF-7 | Breast adenocarcinoma | 1:3 for 4 days<br>1:5 for 5 days | T75 |
| MDA-MB-231 | Breast adenocarcinoma | 1:5 for 3 days<br>1:6 for 4 days | T75 |
| RD-ES | Ewing’s Sarcoma | 1:10 for 4 days | T25 collagen coated |
| SK-ES-1 | Ewing’s Sarcoma | 1:10 for 4 days | T25 collagen coated |

### 3.1.3 Freezing and thawing of cells

To freeze cells, the cell number was calculated as described in 3.1.2 and cells were frozen at a concentration of 1x$10^6$ per ml in specific freezing medium (respective cell medium + 20 % FCS and 10 % Dimethylsulfoxide (DMSO)). Cryotubes were transferred to a so-called Mr. Frosty™, which is a container for controlled cryopreservation of cells. It allows for regulated change in temperature with 1 °C per minute down to -80 °C over-night. On the next day, the cells were transferred to liquid nitrogen for long time storage.

To thaw cells, the cell specific medium was pipetted into the cell culture flasks (T25: 5 ml, T75: 10 ml, T150: 20 ml) and allowed to adjust to the pH in the incubator for about 30 minutes. Then tubes were collected from liquid nitrogen and placed in warm water bath at 37 °C to defrost. The cell solution was transferred using a micropipette into the respective cell culture flask and was resuspended with a serological pipette. Medium was changed the next day to remove remaining DMSO residues.

### 3.1.4 Primary cell isolation and culture

Although conventional cell lines provide a reproducible source of cells to generate standardisable results, they are often genetically altered due to the long culture periods and immortalisation. Therefore, primary cells are an additional option to represent the *in vivo* situation. They were isolated and used during this work to incorporate parts of the tumour stroma as aspects of the TME in the microphysiologic 3D tumour models. In the following paragraphs, the different isolation procedures and culture methods are described.

In Table 17, all used primary cells and their origin are listed.

*Table 17. List of used primary cells with tissue origin and splitting ratios*

| cell type | tissue of origin | origin of tissue | flask size (cm$^2$) |
|---|---|---|---|
| hDF | Human foreskin | University of Würzburg | T150 |
| hmvECS | Human foreskin | University of Würzburg | T75 |
| hEK | Human foreskin | University of Würzburg | T150/T175 |
| hLF<br>#131 | Human healthy lung tissue | Magdeburg University Clinic | T150 |
| primCAF<br>Primary tumour site<br>#127 | Human lung tumour tissue (primary tumour) | Magdeburg University Clinic | T150 |
| metCAF<br>Metastatic site<br>#130 | Human lung tumour tissue (metastatic site) | Magdeburg University Clinic | T150 |
| healthy lung Organoids | Human healthy lung tissue | Magdeburg University Clinic | / |
| Lung cancer organoid | Human lung tumour tissue | Magdeburg University Clinic | / |

### 3.1.5 Isolation of human dermal fibroblasts and human microvascular endothelial cells from skin biopsies

As human skin can be easily obtained from circumcisions. It is a reliable source for the isolation of different primary cells. In addition, donors are mostly young of age, leading to superior cell survival and culture compared to older patients. Another advantage is that the tissue is healthy and not needed for any further analysis in the clinic. The biopsies were obtained under informed consent according to ethical approval granted by the Institutional Ethics Committee of the University Hospital Würzburg (ethics approval: 182-10 and 280-18).

From human skin, three cell types can be isolated with the following protocol: human epidermal keratinocytes (hEK), human microvascular endothelial cells (hmvEC) and human dermal fibroblasts (hDF). The isolation of those cells was previously described (Groeber *et al.*, 2016). In brief, the tissue was received in transportation medium in a sterile container, transferred to a sterile petri dish and washed with PBS$^+$ three times. Tissue was examined and fat as well as inflamed regions were excised. The biopsy was cut into pieces of 2 - 3 mm and digested in dispase at 4 °C for about 16 hours. On the next day, dermis and epidermis were separated using sterile tweezers. The epidermis can be used for the isolation of keratinocytes, while fibroblasts and endothelial cells can be obtained from the dermis. The dermis was washed with 10 ml versene-solution and incubated with 10 ml trypsin/EDTA for 40 min at 37 °C with vigorous shaking every 5 to 10 minutes. Enzyme reaction was stopped by adding 1 % FCS and tissue pieces were transferred to a petri dish containing 10 ml VascuLife™ medium. By using the back of a scalpel, the cells were carefully scraped out from the tissue. The obtained cell suspension was collected in 50 ml reaction tube, sieved over a 100 µm cell sieve and centrifuged for 5 min at 300 *xg*. The respective cell pellet was resuspended using VascuLife™ medium and plated into T25 tissue culture flasks at a density of $5x10^4$ cells per $cm^2$.

For the isolation of primary human fibroblasts, the obtained tissue pieces from the isolation of endothelial cells was used. The dermis pieces were digested using 5 ml collagenase X for 45 min at 37 °C with vigorous shaking every 10 min. Suspension was then centrifuged for 5 min at 300 *xg*. The received pellet was resuspended using Dulbecco's Modified Eagle's Medium (DMEM). Tissue pieces were plated into T75 flasks with 4 ml of medium. After 3 to 5 days, fibroblasts started to grow out and were treated as all other cells described 3.1.2. For primary cells, the passage number of 5 was not exceeded for experiments.

### 3.1.6 Isolation of primary fibroblast from lung biopsies

The biopsies were obtained under informed consent according to ethical approval granted by the Institutional Ethics Committee of the University Hospital Würzburg (ethics approval: 182-10 and 280-18). In most cases tumour tissue as well as healthy control tissue was obtained. The biopsies were received by overnight express in a Styrofoam box containing cooling packs. The specimen itself was placed in a 50 ml tube containing 10 ml AQIX® solution. The biopsies were transferred to a petri dish containing $PBS^+$, measured, weighed and evaluated for necrotic areas and inflammation. For isolation of fibroblasts, a piece of approximately 1 g was excised and used for further procedures. From the remaining sample, pieces for fixation and paraffin embedding were taken as described in 3.1.7. For isolation of primary cells, tissue was cut into 2x2 mm large pieces using a sterile scalpel. The minced tissue pieces were transferred to a tube containing collagenase solution (10 mg/ml), which was incubated for 1 h at 37 °C under continuous shaking at 100 rpm. After incubation, reaction was stopped using 2 % FCS. The solution containing the tissue pieces was strained over cell strainers with descending diameter from 400 µm to 100 µm to collect the small tissue pieces. The flow-through is an additional source for different cell types but in the present study, most protocols did not lead to sufficient cell numbers. For fibroblast isolation, the digested tissue pieces were pipetted into T150 flasks with 6 ml DMEM GlutaMAX (+10 % FCS, Na-Pyruvate, 1 % Penicillin/ Streptomycin, 50 µg/ml, Gentamycin 50 µg/ml) for several days to allow the tissue pieces to adhere to the surface and fibroblasts to spread out. Cells were checked every day to exclude bacterial contamination. After 3 to 7 days, the fibroblasts started to grow out from the tissue and additional medium was added (5 – 10 ml). The obtained cells were treated as usual with a medium change twice a week. At a confluence around 80 to 90 %, the cells were detached and either frozen (see 3.1.3) for long-term storage or expanded in several T150 flasks with a seeding density of $6x10^5$ cells for 5 to 7 days.

### 3.1.7 Isolation and passaging of organoids from human lung tissue

To isolate organoids from human lung tissue the protocol from the Clevers lab was used and adjusted (Drost & Clevers, 2018). In brief, the tissue was measured, weighed and inflamed or necrotic regions were excluded. The rest of the tissue was minced using a scalpel and digested in 10 mg/ml collagenase for one hour at 37 °C in Advanced DMEM F12 medium. The reaction was stopped by adding FCS (2 % of final volume). Afterwards, the tissue pieces were sheared using a serological pipette and glass-pipettes over 3 to 4 steps. To check for organoids in the different fractions 10 µl drops were pipetted on a petri dish and observed under a light microscope. Fractions containing organoids were pooled centrifuged and washed with medium. The pellet was then resuspended in a mixture of medium and Matrigel® (1:1) and plated in 24 well plate 3 to 4 drops per well. After 20 min of solidification at 37 °C 300 µl of medium were added per well. For the exact media composition, see Table 8.

## 3.2 Preparation of human microphysiologic 3D tumour models

The here used microphysiologic 3D tumour models show a tissue-like structure compared to standard 2D cell culture, because the cells are seeded on a biological collagen scaffold. Previous work could already prove the significance of those models (Stratmann *et al.*, 2014; Göttlich *et al.*, 2016; Nietzer *et al.*, 2016; Baur *et al.*, 2019).

### 3.2.1 Manufacturing of the porcine matrix

For the establishment of human microphysiologic 3D tumour models a specific matrix called SISmuc (small intestine submucosa with preserved mucosa) is used. It is prepared using standard operating protocols (SOP) as published before (Linke *et al.*, 2007; Schanz *et al.*, 2010; Stratmann *et al.*, 2014; Göttlich *et al.*, 2016). The matrix is generated from porcine jejunal segments of young pigs (German landrace, local supplier). The animals used for organ removal were not bred specifically for research purposes, but were obtained from a local supplier who is breeding animals for slaughter.

Prior to surgery, the pigs were sedated and injected with heparin to prevent coagulation of blood in the blood vessels. After injection of T61, death of the animal was ensured and the organ removal was started. All explantations were in compliance with the German Animal Protection Laws (§4 Abs. 3) and all animals received humane care in compliance with the guidelines by the FELASA, WHO and FDA (WHO-TRS978 Annex3 und FDA-OCTGT Preclinical Guidance) after approval from our institutional animal protection board (registration reference number #2532-2-12, Ethics Committee of the District of Unterfranken, Würzburg, Germany).

To extract the SISmuc matrix an artery was cannulated and flushed with isotonic saline solution containing 10 U/ml heparin. Then, the associated vein was cut open to allow for a flow through.

The intestine was then extracted still connected to its vascular tree. For the decellularisation process the intestinal lumen was emptied from remaining faeces and rinsed with $PBS^-$ for several times. The preserved artery was connected to a flask containing $PBS^-$ and rinsed via a peristaltic pump. Afterwards, several steps of $PBS^-$ containing P/S and sodium desoxycholate solution of the lumen and the vascular system overnight ensured the complete removal of porcine cells. To ensure that the vasculature was not destroyed during the procedure a pressure of 50 mmHg in the beginning and 80 mmHg in the end was not exceeded. Then, the vascular tree was pulled off and the remaining scaffold was cut into pieces of 10 cm length. To improve the removal of porcine DNA, a DNAse digestion was performed. As the scaffold has to be sterile for its final use in cell culture experiments, it was sterilised by gamma sterilisation with 25 kG (BFF Sterilisationsservice GmBH). For quality control of the scaffold, samples were stained with Feulgen (remaining DNA) and Haematoxylin and Eosin (remaining cells). In addition, an assay to detect gallic acid was performed which provides information about the residues of the sodium desoxycholate.

### 3.2.2 Preparation of microphysiologic 3D tumour models

For the setup of a Microphysiologic 3D tumour model the SISmuc was placed between two specific rings (=cell crowns) so that it can be used like a trans-well model. The outer ring has small feet to allow for medium contact (1.5 ml) from the bottom, while the inner ring can hold up to 1 ml cell specific medium. These cell crowns are available made from metal and from a polyetheretherketone (PEEK) material, which is a biocompatible plastic. The PEEK allows for optical analysis without distracting light (e.g. luminescence measurements). In addition, a turnable cell crown is available to allow cell seeding from both sides made from polylactic acid (PLA) by 3D printing. For insertion of the SISmuc into the cell crowns a piece of matrix is placed flat in a sterile Petri dish and cut open so that the luminal side is facing upwards. Then, small pieces were cut out an placed between the two rings of a cell crown, as published before (Göttlich *et al.*, 2016). In the end, the former luminal side of the intestine is facing upwards and the basolateral side is facing downwards. Cell crowns with SISmuc were placed into 12-well-cell culture-plates and filled with cell specific medium. For a monoculture, $1x10^5$ cells of respective cell type were seeded in 500 µl of cell specific medium. To set up co-cultures, $1x10^5$ cells per cell type were used in 250 µl mixed medium. If an endothelial barrier was included $3x10^5$ endothelial cells were seeded on the basolateral side 3 days before any additional cell type. After seeding, the models were placed in the incubator at 37 °C for 2 h to let the cells attach and the medium to flow to the lower part of the cell crown. Afterwards, medium was adjusted to 2.5 ml total volume.

### 3.2.3 Static and semi-dynamic culture of the microphysiologic 3D tumour models

To establish a tumour-like-structure the models can be cultured in different ways. The simplest way is the static culture. After about 10 to 11 days, a tissue like homeostasis where treatments can be performed for 3 to 7 days is reached. The medium was changed every 2 to 3 days until the treatment was started. To achieve increased generation of tissue in the model also a semi-dynamic culture is possible, where the tumour models were placed on an orbital shaker at 100 rpm. This method enables for an increase in cell number as well as increased cell growth and tissue generation. The treatment period started at day 10 or 11 for up to 7 days. For assays from the supernatant, a medium change was performed 24 h before and directly prior to adding the CAR T cells. In case of co-cultures, the medium change was performed 48 h prior to CAR T cell treatment to keep possible secreted factors within the culture. During treatment with CAR T cells 210 µl medium was sampled and refilled every 24 hours with an additional exchange of 500 µl on day 2 or 3. For co-cultures, a mixture of both cell specific media was used.

### 3.2.4 Dynamic culture of the microphysiologic 3D tumour models

It is also possible to perform dynamic cultures with the microphysiologic 3D tumour models by using an established flow bioreactor system. For CAR T cell treatment the already published set up was used engaging one circuit for one tumour model (Nietzer *et al.*, 2016). As an endothelial barrier was established in this work, this set up had to be adjusted. Therefore, two circuits were incorporated separating the side with endothelial cells from the tumour cell site (Figure 4). The models were set up as described earlier (see 3.2.2 and 3.2.3). To allow for adherence of the cells they were kept under static conditions for 3 days and then placed in the bioreactor chamber. This chamber was then connected to a medium reservoir containing 45 ml of cell specific medium that was further connected to a peristaltic roller pump at a speed of 3 rpm providing a media flow of 2.5 ml/min. Medium was changed every 7 days. After 14 days of dynamic culture, treatment was applied. The medium flow assured a continuous supply of fresh medium and allowed for optimal waste disposal. With this technique, it is possible to generate a larger tumour cell mass than under static conditions and to mimic the blood flow. According to the treatment medium was changed 48 h or 24 h before CAR T cell administration. For sampling the medium, a port was incorporated into the tubing system to allow for sterile sampling. Upon addition of T cells, the medium reservoir was placed on a magnetic stirrer to allow T cells to enter the tubing system rather than sinking to the bottom of the medium reservoir. Treatment with CAR T cells was performed up to 14 days. For long-term treatment, a medium change was performed every 7 days. T cells were collected by centrifugation for 5 min at 300 *xg* and resuspended in fresh medium. For analysis of cytokines and for the apoptosis measurement the supernatant was sampled every 24 h of treatment. After the whole culture time, the microphysiologic 3D tumour models were extracted from the reactor chamber and either prepared for paraffin embedding (see 3.6.1.) or placed in plastic cell crowns for the BLI-based luminescence measurements (see 3.3.4).

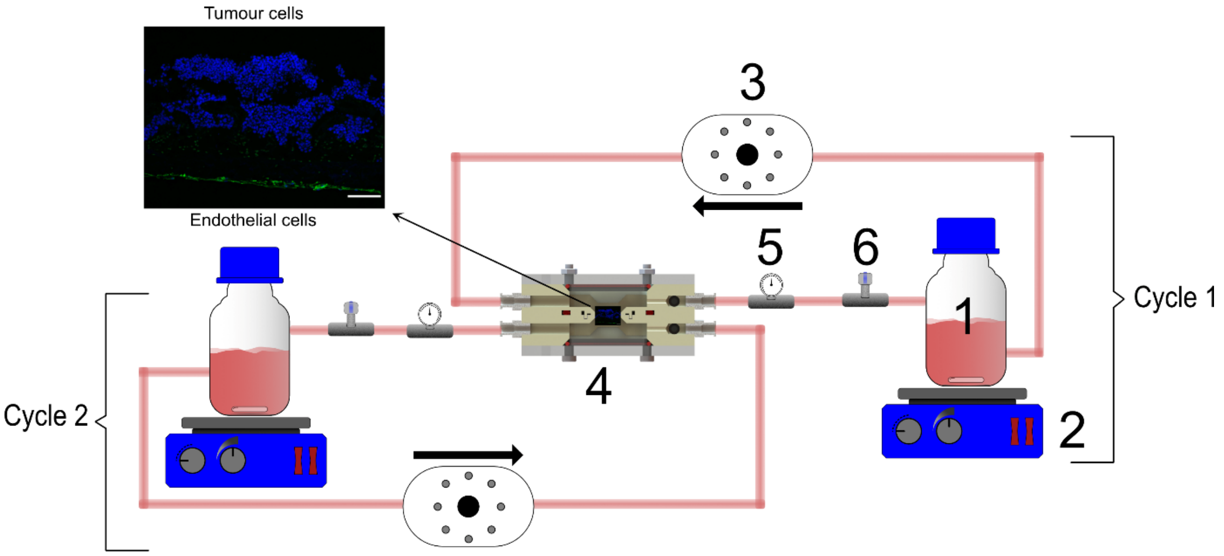

**Figure 4. Dynamic culture of microphysiologic 3D tumour models containing an endothelial cell layer with two separate circulations.**

(1): medium reservoir; (2): magnetic stirrer; (3): peristaltic roller pump; (4): bioreactor chamber containing the tumour model; (5) pressure dome; (6) sampling port. The same applies for both cycles. Cycle 1 is providing media flow for the tumour cells on the mucosal side, while cycle 2 is supplying the endothelial cells on the submucosal side.

### 3.2.5 Treatment with ROR1-specific CAR T cells

The ROR1-specific CAR T cells used during this work were produced and kindly provided by Dr Lars Wallstabe and Dr Razieh Monjezi from the group of Prof Michael Hudecek at the University Hospital Würzburg (Medizinische Klinik II).

In brief, $CD4^+$ and $CD8^+$ T cells were isolated and activated using anti CD3/CD28 beads. Transduction was either performed using a lentiviral vector for experiments with standard ROR1 CAR T cells as already described (Wallstabe *et al.*, 2018) or with Sleeping Beauty based gene transfer using a minicircle DNA in case of the gene-edited ROR1 CAR T cells as described by Monjezi *et al.* (Monjezi *et al.*, 2017).

In case of lentiviral transduction the vectors included a single-chain variable fragment derived from either the rabbit anti–human ROR1 mAb R12 or the mouse anti–human ROR1 mAb 2A2, a short IgG4-Fc hinge or long IgG4-Fc hinge-$C_H2$-$C_H3$ spacer, a CD28 transmembrane domain, and a signalling module of 4-1BB_CD3ζ or CD28_CD3ζ (Wallstabe, Göttlich, Nelke, Kühnemundt *et al.*, 2019).

For transduction with Sleeping Beauty based gene transfer using a minicircle DNA the CAR cassette included CAR cassette comprised a scFv derived from the anti-human ROR1 mAb R12 ($V_H$-linker-$V_L$), a short IgG4-Fc hinge spacer, 4-1BB and CD3ζ signalling domains. Furthermore, gene-edited CAR T cells carried gene knock-outs for either the PD-1 gene (PKO), TGF-β-receptor (TKO) or a combination of both. Additionally, unaltered wildtype (WT) ROR1 CAR T cells were used (Monjezi *et al.*, 2017; Stüber *et al.*, 2020).

In each cassette, the CAR transgene is separated by a T2A element from a truncated epidermal growth factor receptor (EGFRt) as transfection and depletion marker. The cell subsets positive for EGFR were enriched by immunomagnetic selection using biotin-conjugated anti-EGFR mAB and streptavidin microbeads. Before functional testing of the respective CARs the CAR T cells were expanded. If not otherwise stated, ROR1 CAR T cells carried R12 epitope with a short IgG4-Fc hinge spacer, and a 4-1BB_CD3ζ signalling module were used.

### 3.2.6 Treatment with $G_{D2}$-specific CAR T cells

As the SISmuc provides a unique support structure to the cells also sarcoma cells can be grown on the here presented matrix. To establish a model of Ewing sarcoma, the specific cell lines SK-ES1 and MS-EwS-4 were seeded on the SISmuc as described in 3.2.2 and 3.2.3. To target the sarcoma cells, the surface marker $G_{D2}$ was used which is upregulated upon addition of the drug GSK126. The GSK126 is a small molecule EZH2 inhibitor, which was administered in the medium reservoir at a dose of 12 µM or 4 µM per model depending on the cell line. After induction of $G_{D2}$ for 14 days, treatment of $G_{D2}$-specific CAR T cells ($30\times10^6$ per model) was performed for 5 days including stimulation with 50 U/ml IL-2. At the end of treatment, the tumour model was extracted from the bioreactor, fixed in formalin and embedded in paraffin. Supernatant was collected, frozen and used for further analysis.

## 3.3 Analysis parameters of microphysiologic 3D tumour models

To assess the efficacy of a treatment and the robustness of a model, different read out parameters were used. To characterise the condition of tumour cells, apoptosis, cell viability and specific tumour cell lysis were measured. In addition, CAR T cells were analysed using flow cytometry.

### 3.3.1 Flow cytometry analysis of T cells and fibroblasts

To analyse activation and function of ROR1-specific CAR T cells before and after contact with tumour cells they were characterised via flow cytometry by Dr Lars Wallstabe or Dr Razieh Monjezi. As $CD4^+$ and $CD8^+$ T cells were used during most experiments those markers were used for the first gate (after setting the lymphocyte gate). Afterwards viable cells were detected via 7AAD. Activation of T cells was assessed via the surface markers CD69$^+$, CD25$^+$ and PD-1$^+$. For the analysis, a FACS CANTO II (BD) was used.

In addition, to check if stromal cells express ROR1, which could result in an on-target of-tumour effects, tumour-associated fibroblasts were tested for the expression of ROR1. As a positive marker, CD80 was used.

### 3.3.2 Measurement of cell viability with MTT assay

Because the method to culture the microphysiologic 3D tumour models on an orbital shaker is relatively new, the cell viability had to be tested in order to decide how long the culture is stable. MTT is short for (3-(4, 5-dimethylthiazol-2-yl)-2, 5-diphenyltetrazolium bromide, which is reduced to an insoluble formazan inside of viable cells and turns from yellow to purple during the reaction. This reaction is due to NADPH- dependent enzymes found in the mitochondria of viable cells. Therefore, the amount of formazan is directly proportional to the amount of viable cells. To perform the MTT assay a solution of 5 mg/ml was prepared in cell specific medium and added to the cell crowns. After incubation for 3 hours at 37 °C the formazan was eluted using acidified isopropanol containing 0,01 N sodium chloride. To allow for complete removal of the purple formazan salt the elution was performed in three steps, each using 1 to 2 ml of acidified isopropanol over a period of 2 hours until the SISmuc was completely white. Afterwards, 200 µl of the solution containing the eluted formazan was measured in a spectrophotometer at 570 nm with a reference wavelength of 630 nm. Values obtained at the different wavelengths were subtracted and background value of an empty matrix was subtracted from each value. Values were plotted as optical density [OD].

### 3.3.3 Measuring the apoptosis of epithelial cells

To assess the efficacy of treatment on epithelial cells - the tumour cells - within the microphysiologic 3D tumour models, the M30 Cytodeath™ Enzyme-linked Immunosorbent Assay (ELISA) was used. It specifically measures the apoptosis of epithelial cells as its antibodies are directed against the Neopitope K18-Asp396-NE of caspase 9-cleaved-cytokeratin 18 (ccK18), which is found only in epithelial cells but not in mesenchymal cells. To allow for treatment evaluation over the whole treatment period supernatants from either cell crowns or bioreactor experiments were obtained every 24 h during the whole treatment period. The assay was conducted according to the manufacturer's instructions and all samples were run in duplicates. In brief, samples were thawed and diluted to fit in the range of the provided standards. Of each sample or standard solution 25 µl were pipetted in duplicates into the wells of a pre coated 96-well plate provided with the Kit. To each well 75 µl of diluted M30 CytoDeath™ Horseradish Peroxidase (HRP) Conjugate was added. After 4 hours of incubation (RT, 300 rpm on an orbital shaker), the supernatant was discarded and the well plates were manually washed 5 times with provided washing buffer. Afterwards, 200 µl of TMB substrate was added to each well and the plate was stored in the dark to protect the light sensitive substrate. After 20 minutes, the stop solution was added to each well and measurements were performed at 450 nm in a spectrophotometer (TECAN). For data analysis, the Software Origin 9.6 was used to calculate a sigmoidal standard curve from the provided standards. With this standard curve, the amount of ccK18 was calculated in Unit/l.

### 3.3.4 Measurement of specific tumour cell lysis via bioluminescence intensity-based assay in the In Vivo Imaging System

Most of the here used tumour cells are of epithelial origin and express cytokeratin 18, therefore, the M30 CytoDeath™ ELISA is an effective way to assess the efficacy of a specific treatment on the apoptosis of tumour cells. Often cells change their morphology when they gain invasive traits and become more mesenchymal. In this case, the M30 epitope is lost and its measurements becomes less conclusive. For those cell lines, as well as, for a visualisation of the treatment effect and model quality a protocol for the *in vivo* Imaging System (IVIS) of the company Bruker was established as it can quantify bioluminescence intensity (BLI). The IVIS is mostly known for the visualisation of the tumour burden in animal studies. To perform a measurement of microphysiologic 3D tumour models in the IVIS, luciferase transduced cell lines were used. As those cells harbour the luciferase gene, viable cells will emit light upon luciferin addition. The procedure is described in the following chapter.

For the measurement of a tumour model, 5 µl luciferin (stock 10 mg/ml) were added to the inner part of the cell crown and carefully mixed. Images were acquired within 1 hour after luciferin administration. Measurements were performed prior to CAR T cell administration (as day 0) and depending on the experiment on day 3, 5 and 7 and always at the end of experiment prior fixation. The emitted light was measured and quantified using the Bruker MI SE software. The mean/photon value per square millimetre (P/sec/mm/sq) was used to assess luminescence intensity. With these values, either the cell reduction or the specific lysis was calculated as follows: Cell reduction was calculated as the difference of the luminescence intensity measured in the same cell crown before and after the treatment. Cell reduction is presented in percent and calculated from mean photon intensity. Specific lysis was calculated via the difference of a treated sample to the values of mean photon intensity to respective controls, which received control T cells. Specific lysis is shown in percent.

## 3.4 Cytokine ELISA

To assess the activation of CAR T cells during treatment, IL-2 and IFN-γ ELISAs were performed according to the manufacturer’s protocol (BioLegend). The procedure is briefly described as follows:

To get an overview of the T cell activation during the treatment period supernatants were obtained after 6 hours of CAR T cell application and every 24 hours during the treatment and stored at -20 °C. All samples were measured in duplicates. One day prior to assay conduction the 96-well (half area, high binding, Corning) were coated with the respective antibody solution. For assay execution plates were washed 4 times with supplied washing buffer using an ELISA washer and unspecific binding sites were blocked to reduce unspecific antibody binding by the application of 200 µl Assay Diluent A for 1 h at RT. During this time, sample dilutions were prepared to fit in the range of the standards. After incubation, Assay Diluent A was removed and the 100 µl of the standards or the samples were added to the well-plate and incubated for 2 hours at RT on an orbital shaker (600 rpm). Afterwards, the plates were washed as mentioned above and 100 µl of detection antibody was added and incubated for 1 h at RT on the shaker. Then, plates were washed again and 100 µl of Avidin-HRP solution was added and incubated for 30 min at RT on the orbital shaker. After incubation with Avidin-HRP solution plates were washed again and for the detection 100 µl of TMB Substrate was added. After 20 minutes, the reaction was stopped using 100 µl Stop solution and absorbance was measured at 450 nm in a spectrophotometer (Tecan).

## 3.5 Human XL Cytokine Proteome Profiler™ Array

For the quantification of cytokines in co-culture models, a Human XL Proteome Profiler™ Array (R&D Systems, ARY022B) was used. The assay allows the detection of 105 different cytokines simultaneously. The cytokines are bound to a nitrocellulose membrane and can be incubated with cell culture supernatants. The assay was performed according to the manufacturer's protocol and is briefly described as follows:

The supernatants were taken from untreated tumour models after maturation and stored at -80°C. This allowed the determination of cytokines present at the start of CAR T cell therapy. For the assay, the membranes were equilibrated and blocked against unspecific binding for 1 h at RT on a rocking platform shaker using Array Buffer 6 as blocking agent. Then, 250 µl of the respective cell culture supernatant samples were diluted in 1250 µl Array Buffer 6, pipetted on the membranes and incubated over night at 4°C on a rocking platform shaker. After incubation, the membranes were placed in individual plastic containers with 20 ml of provided washing buffer. Three washing steps were performed using 10 ml washing buffer each. Next, the membranes were incubated with 30 µl of the Detection-Antibody-Cocktail in 1.5 ml of Array Buffer 4/6 at RT for 1 h and washed again as described. Detection was performed using 2 ml of the provided Streptavidin-HRP Solution. Finally, images were acquired via chemiluminescence using an Imaging station (Biozym). Images were taken at respective time points between 1 and 10 minutes. For the final analysis, images were processed with ImageJ.

## 3.6 Histological and immunofluorescence staining of paraffinised samples

As the here described microphysiologic 3D tumour models are based on a biological scaffold a tissue-like structure is achieved and methods known from clinical pathology such as immunofluorescence or histological stainings were used to evaluate the tumour models.

### 3.6.1 Fixation and paraffin embedding of samples

At the end of an experiment, the models were washed in pre-warmed $PBS^+$ to remove medium residues as well as dead cells. Afterwards, 4 % PFA solution was used to perform fixation for 2 h at RT. After fixation, the seeded area of the matrix was excised, placed between filter papers and placed into an embedding cassette for further processing using an embedding machine running the following programme:

*Table 18. Programme for embedding tumour models into paraffin using an embedding machine*

| Step | Solution | Time [h] |
|---|---|---|
| Removal of Fixation agent | Deionized Water | 1 |
| Dehydration with ascending ethanol content | Ethanol 50 % | 1 |
| | Ethanol 70 % | 1 |
| | Ethanol 80 % | 1 |
| | Ethanol 96 % | 1 |
| | Isopropyl I | 1 |
| | Isopropyl II | 1 |
| Substitution of alcohol in tissue by xylene | Isopropyl: Xylene (1:1) | 1 |
| | Xylene I | 1 |
| | Xylene II | 1 |
| Substitution of xylene in tissue by paraffin | Paraffin I | 1.5 |
| | Paraffin II | 1.5 |

### 3.6.2 Deparaffination and Rehydration of samples

To perform an (immuno) histological staining with the embedded samples they have to be sliced into 3 to 5 µm thin slices using a sliding microtome and transferred onto glass slides. To ensure strong adherence to the glass slides, coated slides were used with either Superfrost® (for H&E staining) - or Polylysine-coating (for IF staining). The sections were dried at 37 °C over night in a drying oven. Prior to staining, the paraffin was removed by melting at 60 °C in a drying oven followed by incubation in xylene and rehydration as described in the following table:

*Table 19: Deparaffination and rehydration protocol for staining procedure*

| Step | Solution | Time [Min] |
|---|---|---|
| Deparaffination | Xylene I | 10 |
| | Xylene II | 10 |
| Dehydration with ascending ethanol content | Ethanol I 96 % | Dipping 3x |
| | Ethanol II 96 % | Dipping 3x |
| | Ethanol 70 % | Dipping 3x |
| | Ethanol 50 % | Dipping 3x |
| | Deionised Water | Washed until free from disturbances |
| Substitution of alcohol in tissue by xylene | Isopropyl: Xylene (1:1) | 1 |
| | Xylene I | 1 |
| | Xylene II | 1 |
| Substitution of xylene in tissue by paraffin | Paraffin I | 1.5 |
| | Paraffin II | 1.5 |

Afterwards, (immuno) histological staining was performed.

### 3.6.3 Haematoxylin and Eosin Staining

Haematoxylin and Eosin (H&E) staining is a basic histological staining also often performed with specimen of cancer patients to assess the morphology of the cells and the tissue. As it is a relatively easy protocol as well as a cheap way to analyse tissues it is used to analyse the tumour models first to determine the quality of the respective model, indicated by cell density, cell morphology and also for a first evaluation of treatment efficacy.

Haematoxylin is an oxidised version of haematein using a metal cation e.g. aluminium as a mordant. This complex is positively charged and interacts with negatively charged or basophil cell compartments such as the nucleus harbouring negatively charged nucleic acids from the DNA. The staining solution has a low pH turning the cell nuclei brown in the first step. By using tap water for several minutes, the pH is changed and the Haematoxylin-complex turns blue.

In contrast to this, Eosin is an anionic acidic dye. It is charged negatively and reacts with positively charged or acidophilic compartments of the cell such as the cytoplasm. Those compartments appear pink. The staining was performed according the following protocol:

*Table 20. Haematoxylin and Eosin staining protocol*

| Step | Solution | Time [Min] |
|---|---|---|
| Staining of basophilic structures | Haematoxylin, acidic (Meyer) | 6 |
| Rinsing | Deionised Water | Until clear |
| Blueing of Haematoxylin | Tap Water | 5 |
| Staining of acidophilic structures | Eosin solution 1 % | 6 |
| Rinsing | Deionised Water | Until clear |
| Dehydration | Ethanol 70 % | Dipping 3x |
| | Ethanol 96 % | 2 |
| | Isopropyl I | 5 |
| | Isopropyl II | 5 |
| | Xylene I | 5 |
| | Xylene II | 5 |

After staining, the samples were mounted using Entellan® - an organic embedding medium for preservation.

### 3.6.4 Immunofluorescence staining

In addition to histological stainings, immunofluorescence stainings offer the possibility to evaluate the here described tumour models with different antibodies. The protocol was performed according to an SOP, which is described in brief as follows: After deparaffinisation and rehydration, antigen-retrieval was performed for 20 min in boiling citrate buffer with pH 6. Then, the glass slides were transferred to deionised water and a liquid blocker pen was used to create a defined area for the antibody solution. The slides were washed using PBS$^-$ +0,05 % Tween as a washing buffer for 5 min and blocked with 5 % donkey serum using an antibody dilution buffer for 20 min. After removal of blocking solution, the primary antibody was added in a 1:100 dilution. The samples were incubated over night at 4 °C in a humidity chamber. The next day, the slides were washed with washing buffer three times (5 min in a cuvette on a shaker) prior to incubation with the secondary antibody. The secondary antibody was added in a 1:400 dilution in antibody dilution solution (DCS) for 1 h at RT. Afterwards, three washing steps were performed. For mounting, Fluoromount-G™ containing DAPI (4′, 6-diamidino-2-phenylindole) was used, which also acted as counterstaining for the nuclei. For all used primary and secondary antibodies, see materials part 2.7.

### 3.6.5 Determination of cell proliferation rate

In addition to cell viability, calculation of the proliferation rate in the tumour models is a useful tool to check for quality and stability of the models. To assess the proliferation rate an immunofluorescence staining using an antibody against Ki67 was used (see 3.6.4 for staining protocol). Ki67 is a protein present in cells during active phases of the cell cycle (G1, S, G2, and mitosis) while it is absent in quiescent cells (G0). To quantify the amount of proliferating cells 5 - 6 images per tumour model were acquired using a digital microscope (BZ-9000, Keyence) and an objective with a 20-fold magnification. The number of Ki67 and DAPI positive cells was counted using the cell counter tool in the software ImageJ. For quantification, the following equation was used to calculate the number of Ki67-positive cells compared to the total number of DAPI-positive cells:

$$Proliferation\ Index = \frac{number\ of\ Ki67 - positive\ cells}{total\ cell\ number} x\ 100\ \%$$

To analyse DAPI$^+$ cells automatically the following ImageJ macro was used:

```
              requires("1.45s");
 dir = getDirectory("Choose a Directory ");
 //setBatchMode(true);
 count = 0;
              print("\\Clear");
              countFiles(dir);
              n = 0;
              processFiles(dir);

              selectWindow("Log");
              saveAs("Text",dir+"_Results.xls");

              close("*");

              if (isOpen("ROI Manager")) {
              selectWindow("ROI Manager");
              run("Close");
              }
              if (isOpen("Results")) {
              selectWindow("Results");
              run("Close");
              }
              if (isOpen("Log")) {
              selectWindow("Log");
              run("Close");
              }


  function countFiles(dir) {
    list = getFileList(dir);

    for (i=0; i<list.length; i++) {
        if (endsWith(list[i], "/"))
            countFiles(""+dir+list[i]);
        else
            count++;
    }
}

function processFiles(dir) {

    list = getFileList(dir);
    for (i=0; i<list.length; i++) {
        if (endsWith(list[i], "/"))
            processFiles(""+dir+list[i]);
        else {
           showProgress(n++, count);
           path = dir+list[i];
           processFile(path);
        }
    }
}

function processFile(path) {
     if (endsWith(path, "CH1.TIF")) {
      open(path);
```

```
        name = getTitle;
        //print(name);
        run("Properties...", "channels=1 slices=1 frames=1 unit=µM pixel_width=0.53 pixel_height=0.53 voxel_depth=0.53 global");
                        run("8-bit");
                        run("Enhance Contrast", "saturated=0.35");
                        setAutoThreshold("Default dark");
                        //run("Threshold...");
                        //setThreshold(11, 255);
                        setOption("BlackBackground", true);
                        run("Convert to Mask");

                        //run("Watershed");
                        run("Adjustable Watershed", "tolerance=0.3");
                        run("Analyze Particles...", "size=10-Infinity show=Overlay display exclude clear add");

                        //ROI Manager speichern
                        roidir = dir + "ROI_";
                        if (isOpen("ROI Manager")) {
                                selectWindow("ROI Manager");
                                roiManager("save",roidir+name+".zip");
                                //print(roidir+name+"_ROI.zip");
                                nROIs = roiManager("count");
                                run("Close");
                        }
                                print(name);
                                print(nROIs);
                                saveAs("Results",dir+name+".xls");

      }
  }
```

### 3.6.6 Statistical analysis

Statistical analysis was performed for n ≥ 3 independent experiments. For analysis Prism Software (Graphpad, V.7 and 9) was used. One-way analysis of variance (ANOVA) was used with a CI of 95 %. Tukey’s correction was applied. For significance p-values <0.05 were considered.

# 4. Results

The microphysiologic 3D tumour models have been proven useful for the evaluation of a variety of different therapy strategies mainly chemotherapy and targeted therapy (Göttlich *et al.*, 2016; Nietzer *et al.*, 2016; Göttlich *et al.*, 2018; Baur *et al.*, 2019). Therefore, the aim of this work was to extrapolate them for the evaluation of cellular immunotherapies and to improve them accordingly.

In this context, this work is divided in three parts, where first, the scale of assessment as well as improvements of the models are shown. This encompasses the evaluation of different culture modalities to enable long-term stability with preserved throughput of the microphysiologic 3D tumour models and the extension of the SISmuc matrix for the culture of non-epithelial cancers like melanoma and sarcoma. Microphysiologic 3D tumour models were then applied to evaluate $G_{D2}$-targeting CAR T cells. Additionally, primary lung (tumour) tissue was used to isolate primary cells for the implementation into the microphysiologic 3D tumour models in order to represent aspects of the TME. Characterisation of these stromal-enriched tumour models followed to assess the presence of CAFs. Furthermore, A commonly used *in vivo*-imaging technique (IVIS) based on bioluminescence intensity (BLI), known from animal experiments, was applied which represented a time-efficient monitoring and evaluation of the tumour models during culture and treatment time.

Second, the sensitivity of the microphysiologic 3D tumour models was assessed by testing differently designed ROR1 CAR T cells in order to demonstrate that CAR T cell efficacy strongly depends on the CAR design.

In the third part, ROR1 CAR T cells were evaluated in the improved microphysiologic 3D tumour models by challenging the T cells with long-term antigen exposure, an alternative route of application, as well as with the incorporated aspects of the TME, represented by stromal enrichment with CAFs and TGF-β administration. With this, it should be investigated if incorporated TME-aspects increase the predictive value by recapitulation of the immunosuppressive effects.

## 4.1 Scale of assessment and improvement of the microphysiologic 3D tumour models to determine anti-tumour efficacy

To improve the microphysiologic 3D tumour models, the following chapter concentrates on different culture conditions and the exploration towards non-epithelial cancer cells on the SISmuc matrix. Furthermore, lung (tumour) biopsies were utilised as a source of primary cells, which were implemented and characterised in stromal-enriched microphysiologic 3D tumour models. A BLI-based *in vivo* imaging was applied as a new read-out method. Afterwards, Ewing's sarcoma models were engaged to assess $G_{D2}$-targeting CAR T cells. Together, this should improve the microphysiologic 3D tumour models for the evaluation of cellular immunotherapies with regards towards TME-aspects respectively.

### 4.1.1 Semi-static and dynamic culture conditions lead to improved tumour tissue architecture

To generate the microphysiologic 3D tumour models described here, the biological scaffold SISmuc was used and seeded with tumour cells. The main approach in this work was the use of tumour models for lung adenocarcinoma and TNBC to test and optimise CAR T cell therapy in the context of the microenvironment in solid cancers. Therefore, the well-established tumour cell lines A549 (lung) and MDA-MB-231 (breast) were used. To reach a long and stable culture time of the models in addition to a high throughput capacity, different culture conditions were applied: static, semi-static and dynamic. During static culture, tumour models are cultured in a trans-well-like fashion in 12-well plates with standard cell culture conditions. For semi-static culture, models were placed on an orbital-shaker with 100 rpm. Dynamic culture engages a specific bioreactor setting, where continuous media flow was applied.

During static culture, the MDA-MB-231 cells grew scattered within the matrix (Fig. 5 A), while A549 cells grew in a distinct monolayer and filled crypts with only a few cells scattered within deeper layers of the matrix (Fig. 5 D). Dynamic culture induced an extensive cell growth in both cell lines (Fig. 5 C & F) with larger cell aggregates on top of the SISmuc. Additionally, MDA-MB-231 cells invaded and remodelled the mucosal part of the matrix, while A549 cells filled the crypts of the intestinal structure.

Semi-static models showed improved tissue generation for both cell lines (Fig. 5 MDA-MB-231: (B); A549: (E)) compared to static culture. The MDA-MB-231 cells scattered even more throughout the mucosal layer with invasive cells at the border of mucosa and submucosa (indicated by black arrows). A549 cells increased strongly in cell number when grown semi-statically, leading to a thickening of the cell layer on top of the mucosa. This generated a multilayer of cells instead of a monolayer under static conditions. The A549 also started to scatter throughout the matrix and grew at the border of mucosa and submucosa, as indicated by the left black asterisks in Figure 5 E. Furthermore, the cell aggregates found in the crypts of the intestinal structure were enlarged. Taken together, the semi-static culture led to a larger tumour cell number with increased invasion while the throughput of the static culture was maintained. It, therefore, provided a new option as an intermediate culture modality to perform testing with an increased tissue generation than static culture and a higher throughput than dynamic culture.

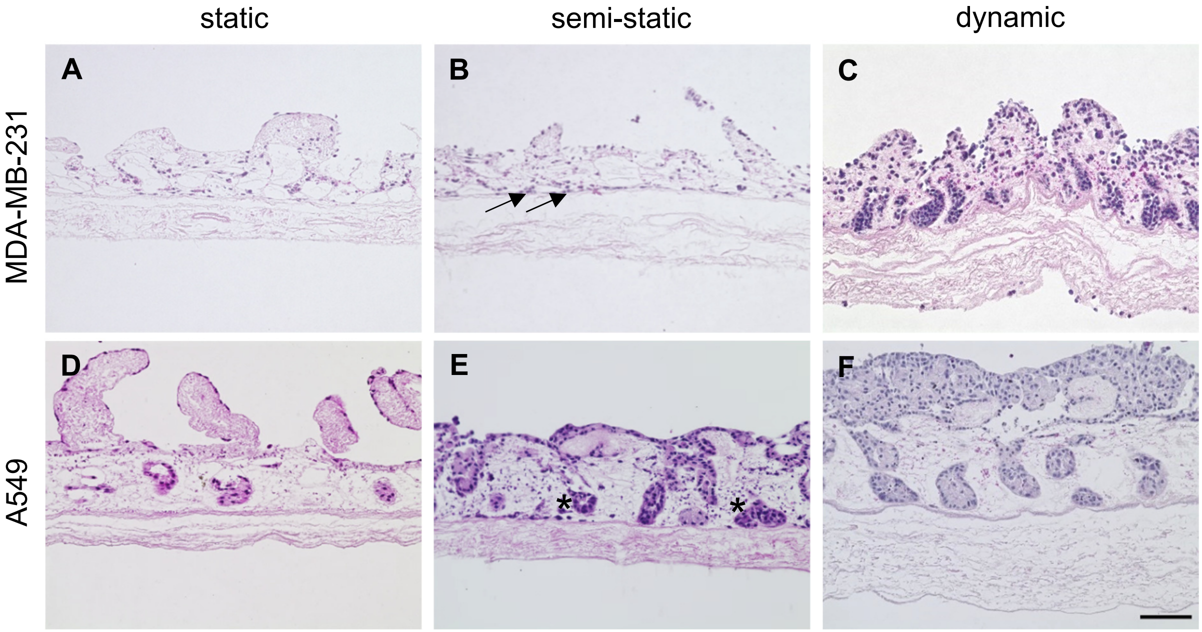

**Figure 5. Different culture modalities for the enhancement of tumour tissue generation in microphysiologic 3D lung and breast tumour models.**

H&E stainings of SISmuc tumour model paraffin sections. (A – C): MDA-MB-231 (TNBC) cells and (D - F): A549 (lung adenocarcinoma) grown either statically (A, D), semi-statically (B, E) or dynamically (C, F) in a bioreactor system for 14 days. Tumour tissue generation increased from static to dynamic culture, with more invasive cells scattered throughout the matrix. Arrows indicate cells, which invaded into the matrix and asterisks indicate large tumour cell aggregates. Dr Lena Nelke kindly provided the sample from image C. Scale bar indicates 100 µm.

### 4.1.2 Semi-static culture mediates long-term tissue homeostasis of microphysiologic 3D lung tumour models

As described before, the semi-static culture enabled an enhanced tissue formation of the tumour cells compared to the static culture, while also allowing for a large number of models compared to the dynamic culture. This bridges the gap between previously described methods of static and dynamic culture. To use a standardisable model, it was necessary to determine the time, during which models reach a homeostasis-like state and can be used for treatment testing. During the treatment period, the cells within the model need to show – similar to a living tissue in homeostasis - a stable proliferation, high viability and a steady and low apoptosis-level. These parameters were assessed for the lung tumour cell lines A549 over a period of 28 days under semi-static culture conditions (Fig. 6).

Until day 7 (Fig. 6 A), a monolayer of lung tumour cells formed on top of the matrix and a stable and comparable cell morphology was reached from day 10 onwards. However, an increase in cell number was observed until day 13, which stabilised a (Fig. 6 B to G). This was also reflected in the quantification of DAPI$^+$ cells (Fig. 6 J), as well as, indicated by a stable proliferation index from day 10 to day 28 (Fig. 6 K). Apoptosis was measured using the M30 CytoDeath™ ELISA to find the baseline of apoptosis (Fig. 6 H). The results of apoptosis measurement supported the findings of DAPI$^+$ cell counting and the proliferation index as a lower amount was measured until day 10 and no strong increase was observed until the end of culture. In addition, the MTT test revealed the stability of the model from day 10 to day 28 as it illustrates a stable cell viability (Fig. 6 I).

Notably, analysis of morphology, apoptosis and proliferation revealed a homeostatic stage between day 10 and 28 of the semi-static microphysiologic 3D lung tumour model as the analysed parameters did not show strong fluctuations. Consequently, during this time, treatment can be applied and no influences of internal variance are expected to impair treatment evaluation.

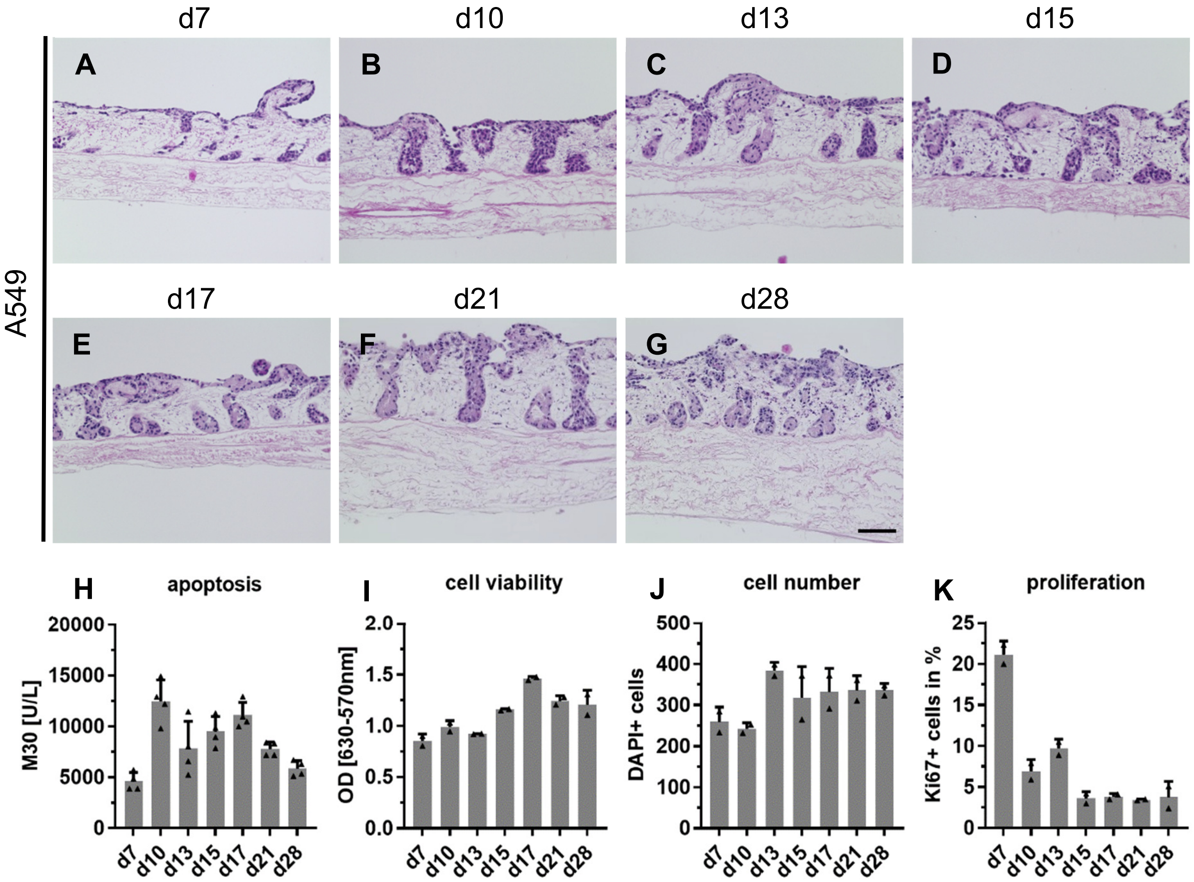

**Figure 6. Analysis of morphology and homeostasis of semi-static microphysiologic 3D lung tumour models**

H&E stainings of semi-static tumour model paraffin sections containing the lung adenocarcinoma cell line A549 (A - G) as well as analysis of apoptosis (M30 CytoDeath™ ELISA) (H) and cell viability via MTT (I). Cell number and proliferation index (J, K) were evaluated from immunofluorescence stainings.

(A - G): On day 7 fewer tumour cells grew within the model and a thinner cell layer formed. From day 10 onwards, a comparable tumour cell growth with a multi-layered cell mass on top of the matrix and filled crypt structures formed. Scale bar indicates 100 µm. (H): Apoptosis was measured from the supernatant. Data is shown in [U/L] of M30 per cell crown. At day 7 a low apoptosis occurred, which increased at day 10. From day 10 onwards, apoptosis level remained within the same range. (I): OD-values were normalised to a reference wavelength 630 nm and a reference cell crown without cells. Cell viability did not decrease throughout the whole culture time. (J): Total cell number was estimated by counting DAPI positive cells per microscopy slide (5 images per model, 2 cell crowns from n=1) and increased until day 13. After day 13 a stable number around 300-400 cells per image frame was determined. (K): Proliferation Index was estimated by counting Ki67$^+$ cells in comparison to the total amount of DAPI$^+$ cells (5 images per model, 2 cell crowns from 1 experiment). After day 7 the Proliferation Index dropped from 21 % to 4 % until day 15. Data is presented as arithmetic mean of 2-4 cell crowns ±SD. n=1 experiment.

### 4.1.3 The SISmuc matrix in the microphysiologic 3D tumour models supports growth of different solid tumours including carcinomas and sarcomas

The microphysiologic 3D tumour models described in the previous chapters represent TNBC and lung adenocarcinoma. Carcinoma cell lines benefit from the basement membrane of the SISmuc matrix as epithelial cells are naturally anchored to it and overcome it during invasion. As it is also important to enable the analysis of non-epithelial cancers, it will be demonstrated, if the SISmuc supports the differences of various tumour entities. Hence, it was assessed whether the collagen-rich matrix SISmuc is also applicable to non-epithelial tumours like sarcomas or melanomas and could serve as a universal matrix. As comparison cell lines, that have already been established on the matrix before are shown to give an overview of differences in cell growth.

Differences in cell morphology as well as growth pattern in different tumour models were revealed on the SISmuc matrix (Fig 7). Here, the tumour models were cultured either for 14 days under static conditions or for 17 to 19 days under dynamic conditions.

Under static conditions, the lung adenocarcinoma cell line HCC827 (Fig. 7 A) established a monolayer on top of the SISmuc, while breast (Fig. 7 B), colon (Fig. 7 C) and skin cancer cells (Fig. 7 D), grew scattered on the mucosal surface. In addition, they filled the crypt structures of the former intestine.

Stronger differences became visible under dynamic conditions. Here, the sarcoma cell line SK-ES-1 (Fig. 7 H) showed strong cell growth with single cells loosely attached and invasive cells below the basement membrane-structure, indicated by black arrows. The breast cancer cell lines MCF-7 (Fig. 7 F) and the colorectal cancer cell line SW480 (Fig. 7 G) formed cell aggregates on top of the villi structures in addition to loosely attached single cells. These aggregates also appeared larger in MCF-7 cells (Fig. 7 F, black arrow). Additionally, the cells grew scattered within the mucosal part indicating an invasive growth pattern comparable to colorectal (Fig. 7 G) cancer cells. Comparison of static and dynamic culture indicates that the invasive phenotype is more pronounced when tumour cell lines are grown dynamically. Consequently, the SISmuc matrix supported the tissue formation of non-epithelial cancers demonstrated here for sarcoma and melanoma.

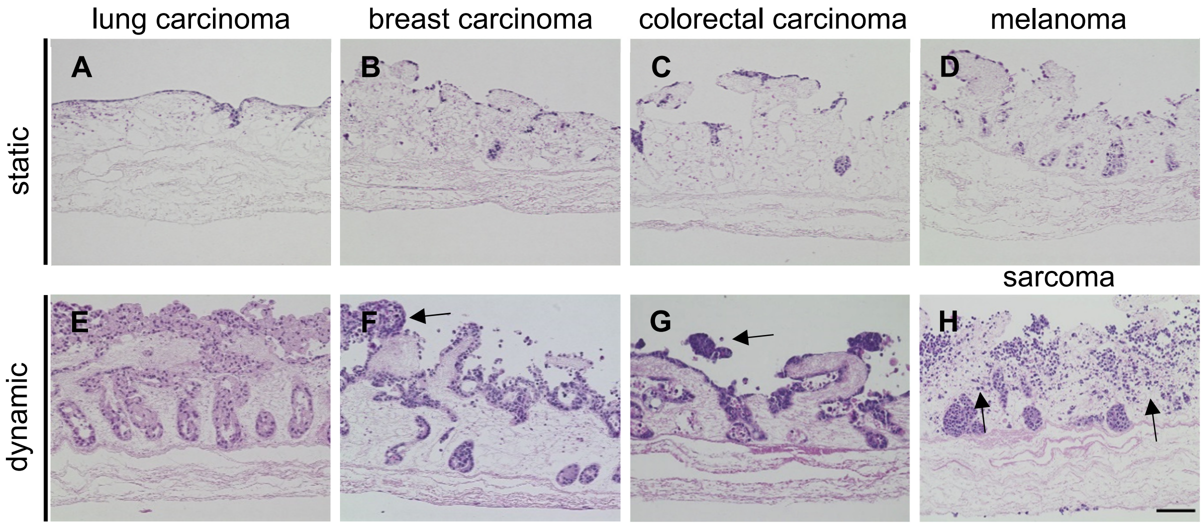

**Figure 7. The SISmuc matrix supports growth of different tumour types beyond the context of epithelial cancer.**

H&E stainings of paraffin sections from different tumour models on the SISmuc: lung (HCC827), breast (MCF-7), colorectal (HROC87), melanoma (SK-MEL-28), sarcoma (SK-ES-1). (A – D): Static tumour models are shown. HCC827 cells grew in a tight monolayer, while MCF-7, HROC87 and SK-MEL-28 cells filled the crypt structures and formed smaller tumour cell aggregates on top of the matrix. (E - H): Dynamic tumour models are shown. MCF-7 and HROC87 cells formed large tumour cell aggregates (indicated by black arrows in F&G), which were loosely attached to the matrix. SK-ES1 cells grew loosely attached and scattered within the mucosal part of the matrix (indicated by black arrows). Scale bar indicates 100 µm.

### 4.1.4 Isolation and implementation of patient-derived cells to represent aspects of the TME in the microphysiologic 3D tumour models

To include components of the TME, which can influence therapy outcome, stromal cells native from lung tumour tissue, were isolated to establish a protocol. Those fibroblasts were then added together with tumour cells to produce stromal-enriched microphysiologic 3D tumour models to represent aspects of the TME. To achieve this, lung tumour biopsies, as well as healthy lung tissue were used and as a control, fibroblasts from skin biopsies were isolated.

For isolation of fibroblasts from the biopsies, the tissue was minced and digested with collagenase. The fibroblasts began growing from the tissue fragments after 1 to 2 weeks following isolation (Fig. 8 A to C). Here, the tissue pieces without any cells are shown, solely single non-adherent cells are visible in the medium (Fig. 8 A). After one week of culture (Fig. 8 B), long and stretched cells started to grow out from the floating tissue fragments (black arrow). After two weeks of culture (Fig. 8 C), the fibroblasts started to grow in associated clusters and larger amounts grew from the tissue fragments (indicated by black arrows).

The cell suspension obtained from the collagenase digestion could also be used further for the isolation of primary tumour cells, which revealed an epithelial morphology (Fig. 8 D). Only a few attempts of isolating primary tumour cells were successful, resulting in a small number of cells. Unfortunately, tumour cells could not be kept in culture for longer periods.

The isolated and expanded fibroblasts were cultured under standard cell culture conditions and implemented in the tumour models after expansion. Simultaneously, fibroblasts were obtained from different donors. To represent stromal cells from different tumour stages, fibroblasts from a primary tumour site (primCAF, Fig. 8 G) and from a metastatic site (metCAF; Fig. 8 H) were isolated. As a healthy control, human lung fibroblasts (hLF) were also isolated from healthy parts of lung biopsies and are shown in Figure 8 F. All lung-derived fibroblasts showed a spindle-shaped cell morphology with small cell nuclei. For comparison, primary human dermal fibroblasts (hDF) were used, which were isolated from foreskin biopsies (Fig. 8 E). In comparison to lung-derived fibroblasts, they were shorter and showed larger cell nuclei. Hence, the cell morphology of skin fibroblasts clearly differed from the morphology of lung tissue fibroblasts.

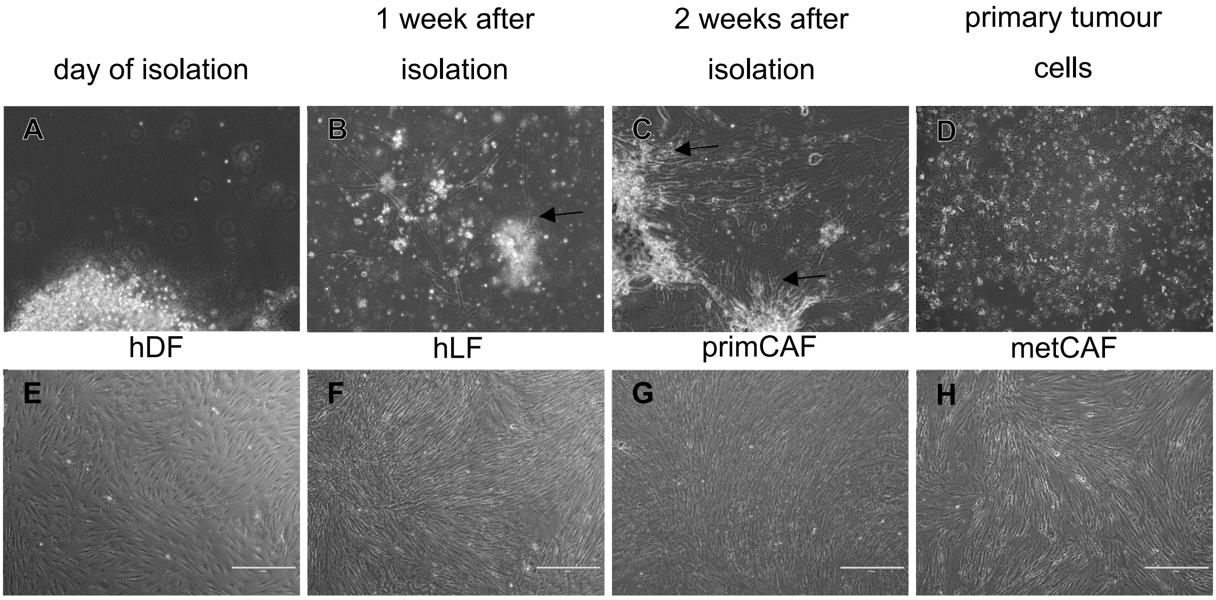

**Figure 8. Overview of fibroblast-outgrowth from lung tumour biopsies and fibroblasts during maintenance culture.**

(A - C): Bright field images of the outgrowth of fibroblasts from lung tissue over 2 weeks. At the day of isolation, no cells were present at the border of the tissue fragments. One week after isolation, the first cells started to grow from the tissue fragments. After two weeks, islets of fibroblast cells started to form. Black arrows indicate stretched cells. (D - H): Bright field images of primary cells in maintenance culture after 1 – 2 passages. (D): primary tumour cells in passage 1 isolated from lung tumour biopsies are shown and depict a distinct polygonal shape. (E): Primary human dermal fibroblasts (hDF) isolated from foreskin biopsies. (F): Human lung fibroblasts (hLF) isolated from healthy biopsies. (G): Cancer fibroblasts isolated from a primary lung tumour site (primCAF). (H): Cancer fibroblasts isolated from a metastatic lung tumour site (metCAF). All fibroblasts showed the distinct branched cytoplasm and elongated cell shape. hDF showed larger nuclei and were shorter compared to the other fibroblasts derived from lung tissue. Scale bars indicate 400 µm. Representative images from one donor are shown.

In addition to single cells, the isolation of organoids from lung tumour tissue has recently been established by the Clevers Lab (Sachs *et al.*, 2019). There, it was shown to be feasible to isolate and promote organoids from patient tissue, which are genetically stable for several months. As the isolation of primary tumour cells was rarely successful during this work, the published protocol by Sachs *et al.* was used and modified for organoid generation. To isolate organoids, the lung tumour tissue was digested and sheared via different steps, and organoids were collected. In the end, all elutions, which contained organoids were pooled and seeded into Matrigel® droplets. This enabled culture of organoids from a healthy lung biopsy for up to 30 days (Figure S1) and from a small cell lung carcinoma (SCLC) for 26 days (Fig. 9). The organoids formed within one day after isolation and the characteristic core region became visible (Fig. 9, indicated by black arrows). The size, shape and core structure were used to monitor the organoids. Loss of shape and the distinct core region were indicators for aberrant or stalled growth. If both of these was observed the organoids were discarded. With this protocol, it was possible to maintain the organoid structures for nearly a month, which was equally true for healthy and tumour lung organoids. During this time, the organoids were splitted roughly once a week. Expansion and longer maintenance were not possible and not all isolations lead to stable organoids. From 5 isolations, 3 allowed establishment of organoids, but none of those 3 were possible to expand to larger numbers for later use. Organoids from healthy lung tissue did not differ in shape or size compared to tumour-derived organoids.

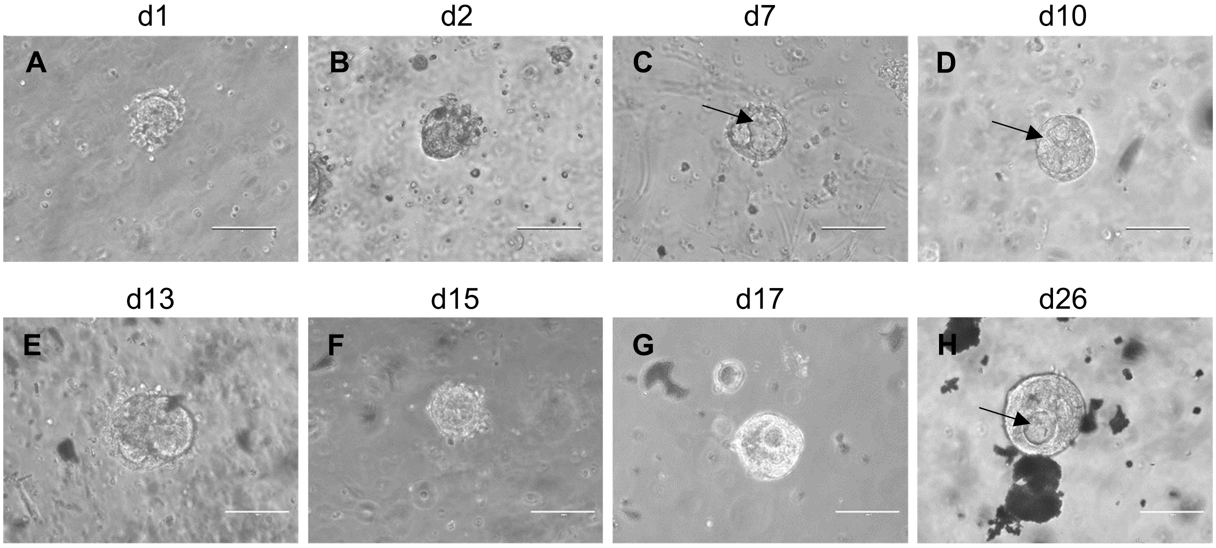

**Figure 9. Organoids derived from small cell lung cancer tissue.**

(A - H): Bright field images of organoids from a SCLC patient biopsy from the lung, cultured in Matrigel® droplets one day after isolation until 26 days post-isolation. All organoids showed a distinct organoid core region. Black arrows indicate distinct core regions of the organoids. Scale bars indicate 100 µm. Representative images from one donor are shown.

To adjust the microphysiologic 3D tumour models presented here to more *in vivo*-like conditions, the aim of this work was to implement primary cells from the tumour microenvironment into the models to represent parts of the TME. The TME consists of many different cell types such as immune cells, fibroblasts and endothelial cells. Since the main aim of this work was to study cellular immunotherapies in the microphysiologic 3D tumour models, endothelial cells were of a particular interest. They are involved in angiogenesis and drug trafficking, as well as immunomodulation. They represent the entryway for immune cells into the tissue and are important for immune cell diapedesis. Additionally, they should extend the SISmuc matrix and, therefore, tumour models as an additional cell type and TME-aspect. To include endothelial cells into the models, cells from foreskin biopsies were used as they are easy to obtain, isolate and maintain in culture. In addition, Human Umbilical Vein Endothelial Cells (HUVECs) were used, which also served as a source of endothelial cells.

To allow for a standardisable set up of the tumour models with implemented endothelial cells, a new cell crown was developed, that is turnable and allows cell seeding on both sides (Fig. 10 A). In white, a cell crown produced by 3D printing (PLA material) is shown which was equally suitable for the use during cell culture experiments as the cell crowns in brown made from polyether ether ketone (PEEK). Experiments with different tumour cell lines allowed establishment of tumour models with an intact endothelial cell layer for lung (Fig. 10 B), breast (Fig. 10 C) and colorectal (Fig. 10 D) carcinoma. In addition, it was equally possible to establish and maintain an endothelial monolayer under static (Fig. 10 B & C) and dynamic (Fig. 10 D) conditions. To implement the endothelial cell layer under dynamic conditions, a novel bioreactor setting was created with two distinct cycles (Figure 4). For the generation of a monolayer, the endothelial cells were seeded 3 days prior the tumour cells. The H&E staining (Fig. 10 B) showed a tight alignment of endothelial cells (black arrows) on the basolateral site and HCC827 lung tumour cells on the luminal site. To characterise the endothelial cells phenotypically, the tumour models containing MCF-7 breast cancer cells (Fig. 10 C) and HROC87 colorectal cancer cells (Fig. 10 D) together with endothelial cells were stained for the endothelial marker CD31. The alignment of the CD31$^+$ cells (white arrows) indicated an endothelial cell layer in both models.

Taken together, it was feasible to incorporate endothelial cells into the microphysiologic 3D tumour models of different tumour types, presented here for breast, lung and colorectal cancer. The endothelial cells formed a monolayer, confirmed by CD31 staining and H&E staining. Parts of these data were also successfully published in the journal "*Alternatives to Animal Experimentation*" with equally contributing co-authorship (Kühnemundt *et al.*, 2020).

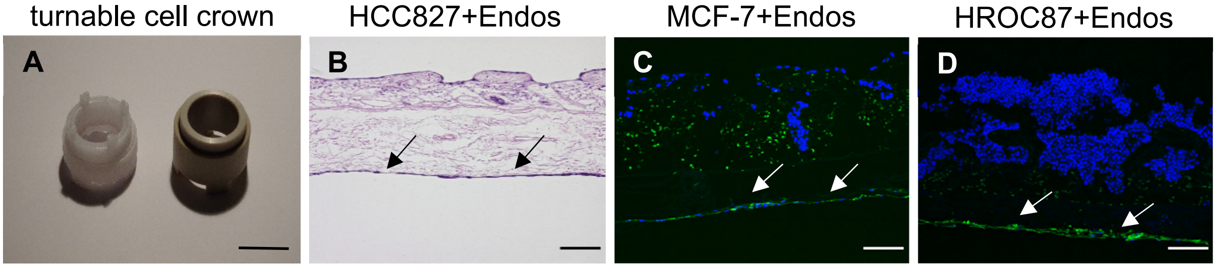

**Figure 10. Implementation of endothelial cells into different microphysiologic 3D solid tumour models.**

(A): Newly designed cell crown, which was 3D printed (left, white) and conventional cell crown (right, brown) made from PEEK. The new cell crown allows easy culture of cells on both sides of SISmuc. Scale bar indicates 1 cm. (B): H&E staining of a static tumour model containing the human lung cancer cell line HCC827 together with HUVECs. HCC827 cells formed a monolayer on the mucosal side of the matrix, while endothelial cells formed a monolayer on submucosal side, which is indicated by black arrows. (C & D): Immunofluorescence staining against CD31 (green) of a static tumour model containing the human breast cancer cell line MCF-7 or a dynamic tumour model containing human colorectal cancer cells HROC87 together with primary microvascular endothelial cells isolated from skin biopsies. Nuclei are counterstained with DAPI (blue). Tumour cells grew on the mucosal side and within the crypt structure while endothelial cells formed a layer on the basal site of the matrix. Representative images of n=3. Scale bars indicate 100 µm in images B - D. Image A adapted from (Kühnemundt *et al.*, 2020).

To study effects of fibroblasts on CAR T cell therapy and to enrich the microphysiologic 3D tumour models with aspects of the TME, the aim of this work was to implement primary fibroblasts from lung (tumour) tissue into lung tumour models to create stromal-enriched microphysiologic 3D tumour models, which should increase their predictive value. To achieve this, the primary fibroblasts described in 4.1.4 were used.

Fibroblasts derived from dermal biopsies (e.g. foreskin) had been incorporated into the tumour models before and an interaction with the tumour cells and an equal distribution throughout the matrix was shown (Nietzer *et al.*, 2016). To assess if the fibroblasts differ depending on the tissue used for isolation, cells from healthy or tumorous lung tissue were isolated. Additionally, fibroblasts from a primary tumour site (primCAF) and a metastatic tumour site (metCAF) were used.

Co-cultures containing different fibroblasts together with A549 lung adenocarcinoma cells were assessed via H&E staining (Fig. 11 A - D) and immunofluorescence staining (Fig. 11 E - H) to evaluate cell morphology and to distinguish mesenchymal and epithelial cells, respectively. H&E staining of semi-static co-cultures revealed a comparable tumour cell mass on top of the matrix with flattened villi surrounded by tumour cells independent of incorporated fibroblast. The co-culture containing metCAFs (Fig. 11 D) showed a stronger remodelling effect of the fibroblasts as the villi structures were not pronounced at the end of culture. Since an evaluation of fibroblast density and arrangement is not possible from an H&E staining, an immunofluorescence staining for the epithelial marker pan-cytokeratin (green) and vimentin (red) was performed, where PCK was specifically expressed by tumour cells and vimentin by fibroblasts. Here, hDF (Fig. 11 E), primCAFs (Fig. 11 G) and metCAFs (Fig. 11 H) were equally distributed and grew in comparable densities in the tumour models. The co-culture containing the hLF (Fig. 11 F) showed fewer fibroblasts. The morphology of the fibroblasts (see magnified images, white arrows); however, was comparable between all different fibroblasts, as spindle-shaped cells with small nuclei were present.

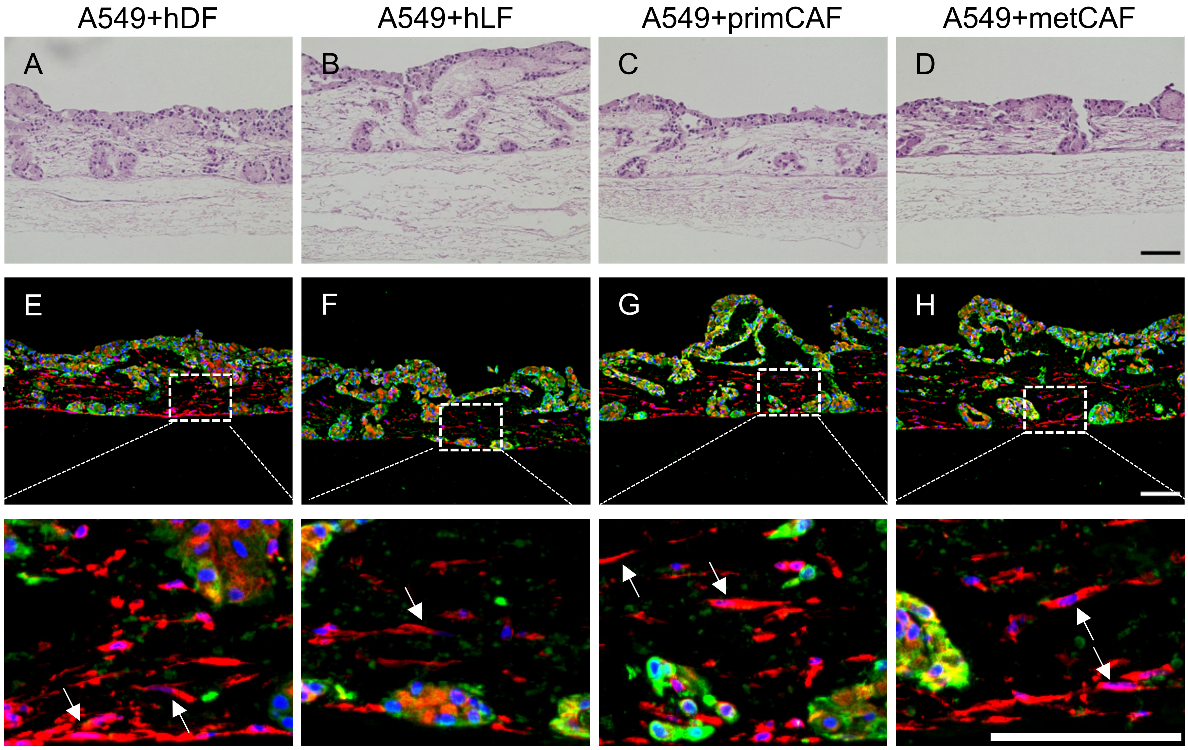

**Figure 11. Fibroblasts derived from different primary tissues form stromal-enriched microphysiologic 3D tumour models together with lung tumour cells.**

A549 lung tumour cells were co-cultured together with different types of primary fibroblasts under semi-static conditions for 14 days and analysed in paraffin sections. Fibroblasts were isolated from either human skin tissue (human dermal fibroblasts = hDF), human lung tissue (human lung fibroblasts = hLF), human lung tumour tissue from a primary tumour (primCAFs) or human lung tumour tissue from metastatic tumour (metCAFs). (A - D): H&E staining of respective models revealed comparable cell growth, while metCAFs induced stronger flattening of the villi structures. (E - H): Immunofluorescence staining for Pan-cytokeratin (green) and vimentin (red) of the respective models is shown. Tumour cells were positive for the cytoskeleton marker PCK (green), while fibroblasts expressed the mesenchymal marker vimentin (red). Fibroblasts from healthy lung tissue showed decreased cell density. Comparable tissue architecture formed independent of incorporated fibroblast type. Representative images of n=2 independent experiments. Nuclei are counterstained with DAPI (blue). Scale bars indicate 100 µm.

Taken together, it was feasible to incorporate different types of fibroblasts into the microphysiologic 3D tumour models, which all grew in a comparable architecture within the matrix compartment beneath the basement membrane. This enables the production of stromal-enriched microphysiologic 3D tumour models with aspects of the TME, which are further organotypical for lung (tumour) tissue.

### 4.1.5 Phenotypic analysis confirms CAF phenotype of implemented primary fibroblasts from lung tissue

To determine if CAF populations are present within the stromal-enriched microphysiologic 3D tumour models, several markers were tested during this work. The visualisation of fibroblast activation (FAP, α-SMA) together with a general mesenchymal marker vimentin (VIM) was assessed via immunofluorescence staining. Analysis of fibroblast-associated makers was performed for dynamic and semi-static stromal-enriched lung tumour (A549) models to study how comparable the new culture modality was in terms of cell morphology and tissue generation when fibroblasts were included. Additionally, stromal-enriched microphysiologic 3D models with TNBC cells (MDA-MB-231) and metCAFs were analysed. Of note, all CAF-related stainings were performed once (n=1).

At first, the general mesenchymal marker vimentin (red) and the CAFs specific marker α-SMA (green) were assessed in semi-dynamic models (Fig. 12 A) and dynamic models (Fig. 12 B). In chapter 4.1.4 different fibroblast sources were described, which were successfully incorporated into the tumour models. As the metCAFs were the fibroblasts, that grew especially well on the SISmuc and were derived from a metastatic tumour-site, they were further characterised within microphysiologic 3D A549 lung tumour models.

A549 cells showed a large tumour cell mass on top of the matrix and also filled crypts (Fig. 12 DAPI$^+$-cells, blue, 1st row) under semi-static and dynamic conditions, which was more pronounced in the dynamic model (Fig. 12, right). Fibroblasts indicated by positive VIM-expression were evenly distributed throughout the whole matrix and spread into the submucosal part when cultured dynamically (Fig. 12, red, 3rd row). The marker α-SMA (Fig. 12, green, 2nd row) was expressed in the cytoplasm and cytosol by most A549 lung tumour cells and by a subpopulation of fibroblasts in both culture conditions. The marker expression was associated with fibroblasts, as these stromal cells show a distinct stretched morphology and grow in the submucosal compartment (Fig. 12, overlay and magnification), while A549 are mainly located on top off the mucosal compartment. Hence, the presence of CAFs is indicated inside the microphysiologic 3D tumour model.

Collectively, the presence of α-SMA$^+$ populations within a stromal-enriched microphysiologic 3D lung tumour model is the first indicator that activated fibroblasts could be integrated.

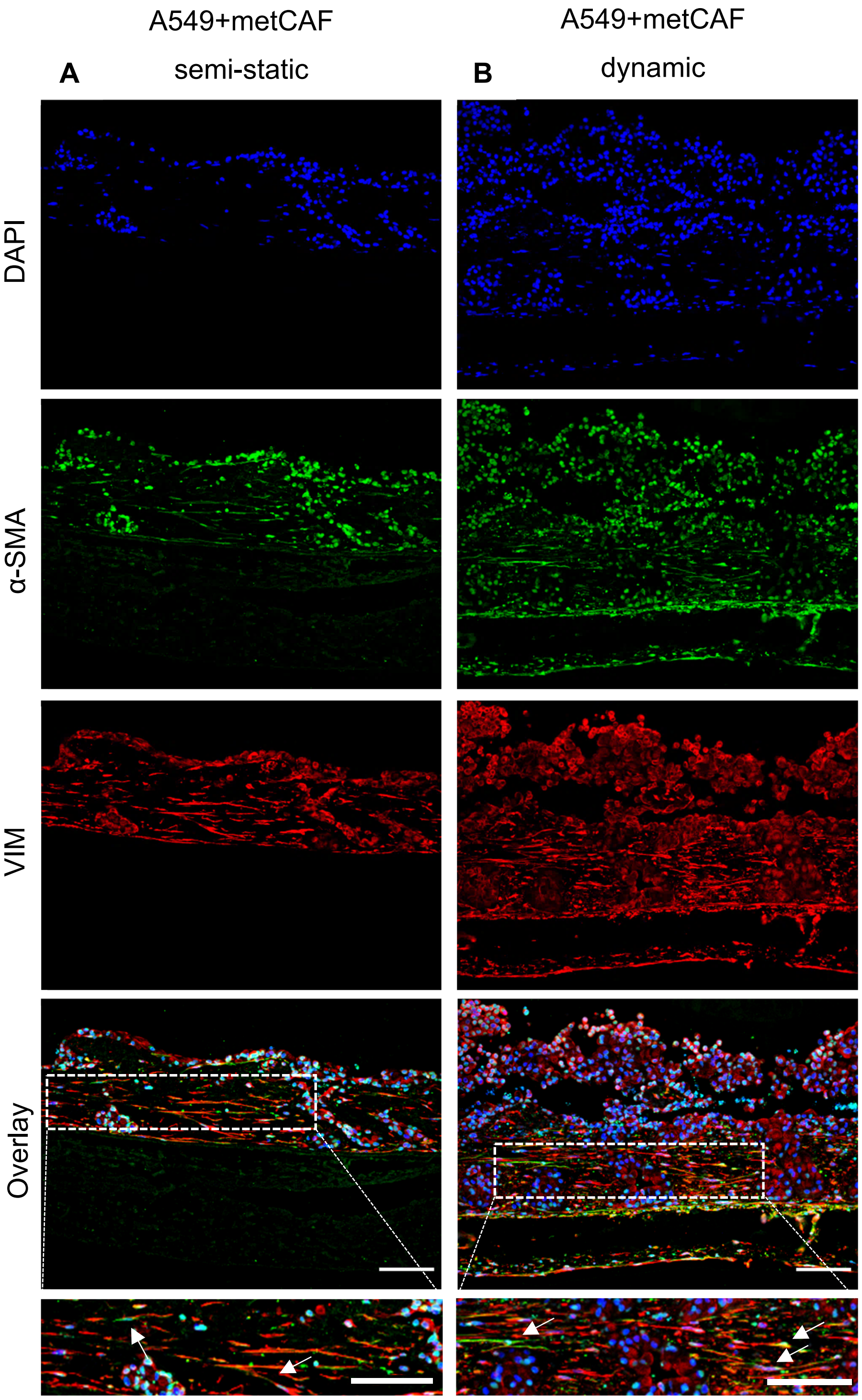

**Figure 12. Characterisation of stromal-enriched microphysiologic 3D lung tumour models with the CAF-associated marker α-SMA.**

(A & B): Immunofluorescence stainings of paraffin sections from semi-static or dynamic tumour models containing A549 cells and metCAFs. Staining was directed against α-SMA (green), VIM (red). Nuclei are counterstained with DAPI (blue). Arrows in magnified images indicate stretched fibroblast cells, which were positively stained for α-SMA and VIM. Scale bars indicate 100 µm.

To extend the use of the isolated fibroblasts from lung tumour specimens and further assess whether the non-organotypic cell context would influence marker expression, stromal-enriched microphysiologic 3D breast tumour models were established with MDA-MB-231 cells and metCAFs from lung biopsies (Fig S2). Again, semi-static models were compared to dynamic models. This time, TGF-β was also administered to evaluate its effect on CAFs and tumour cells. MDA-MB-231 cells reflect a more advanced and aggressive type of cancer with a tendency to metastasise.

Semi-static (Fig. S2 A & B) and dynamic (Fig. S2 C) models were analysed via immunofluorescence staining for the mesenchymal marker VIM (red) and the CAF marker α-SMA. Depending on the culture conditions, the models differed in cell density, as dynamic models also showed cell growth throughout the submucosal layer (Fig. S2 C), which was not observed in semi-static models, independent of TGF-β administration (Fig. S2 A & B). Here, cells also grew scattered and invasive but did not exceed the mucosal part of the SISmuc. Expression of both markers occurred in nearly all cells homogenously, making the discrimination of fibroblasts and tumour cells nearly impossible. Furthermore, as nearly all cells showed a similar morphology, distinction was difficult (Fig. S2, Overlay, 4th row and magnifications). Nonetheless, arrows in magnified images indicate stretched cells positively stained for α-SMA and VIM in all models, which could indicate CAFs. Expression of α-SMA seemed to occur not only within the nuclei, but also in the cytoplasm to some extent. Addition of TGF-β did not alter α-SMA expression or cell growth.

Collectively, these stainings indicated that MDA-MB-231 cells express the marker α-SMA in the nucleus and in the cytoplasm. However, the presence of CAFs was not confirmed as the characteristic stretched cell shape of fibroblasts was difficult to distinguish from the elongated MDA-MB-231 cells. Therefore, it was difficult to clearly define CAFs inside the stromal-enriched microphysiologic 3D TNBC model.

The verification of one marker for a heterogeneous cell population like CAFs is far from sufficient, especially since α-SMA can also be found in other types of fibroblasts or mesenchymal cells. Other markers, which have been described in CAFs were tested accordingly in the same models. One of those markers is fibroblast activation protein (FAP), which can be found in CAFs within the stroma in solid cancers (Zeltz *et al.*, 2020).

In stromal-enriched microphysiologic 3D lung tumour models, fibroblasts located in the lower part of the matrix showed homogenous expression of FAP in semi-static (Fig. 13 A) and dynamic (Fig. 13 B) models. White arrows pointing towards stretched cells located at the border of mucosa and submucosa indicate fibroblasts positive for FAP. In addition, some clusters of the A549 cells located at the border of the cell clusters were positive for FAP in dynamic models (Fig. 13 B). In semi-static models, FAP expression was more homogenously distributed than in the dynamic model (Fig 13 A). The expression of FAP in A549 cells could indicate an EMT, which would be in line with the partial VIM expression of A549 cells that was observed (e.g. Fig. 12).

For stromal-enriched microphysiologic 3D breast tumour models (Fig. S3), a homogenous expression of FAP was found in all cells, especially in the semi-dynamic models (Fig. S3 A & B). In the dynamic models (Fig. S3 C), parts of the cells, where the mucosa and submucosa connect, did not show uniform FAP expression. The attempt to distinguish GFP-expressing tumour cells from the fibroblasts failed as the GFP antibody was not specific in this case and was expressed by all cells in models with A549 and MDA-MB-231 cells (data not shown). Therefore, the origin of the FAP$^+$ cells could not be assigned when breast cancer cells were cocultured with fibroblasts. However, no differences were observed upon supplementation with TGF-β, indicating that it does not alter FAP expression. This also confirmed the observation from the α-SMA staining.

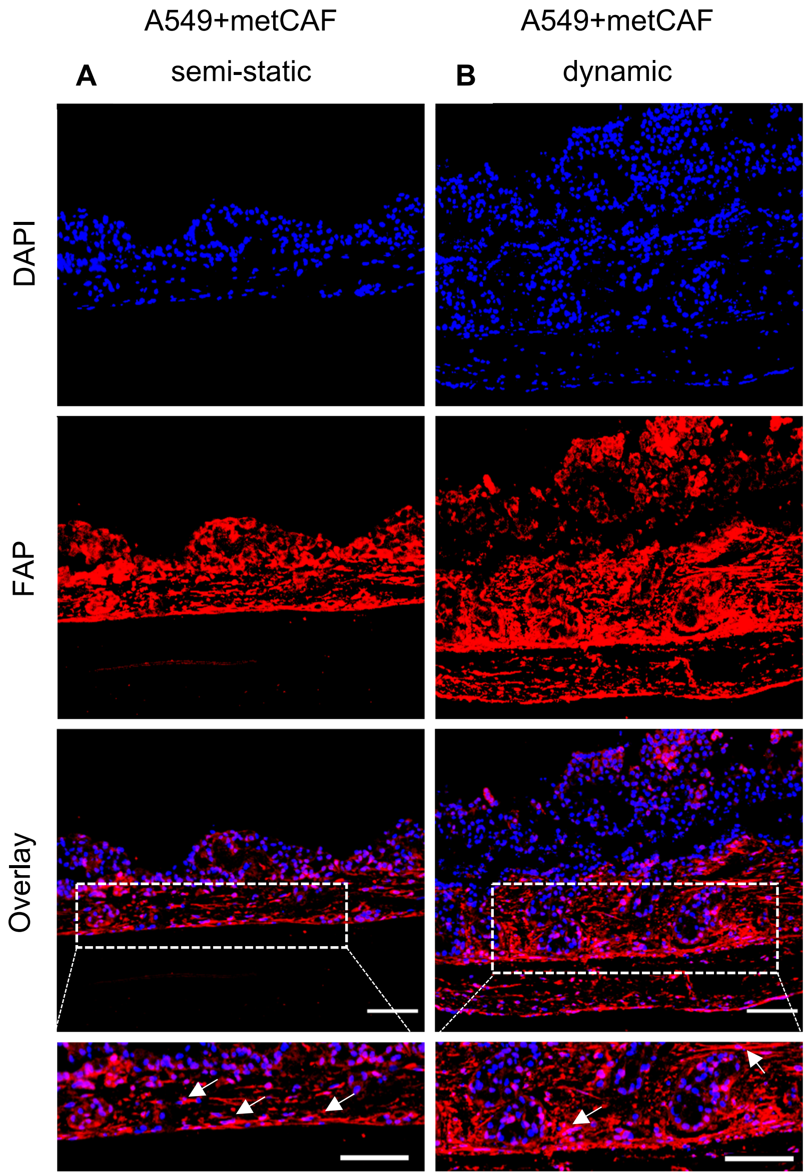

**Figure 13. Characterisation of stromal-enriched microphysiologic 3D lung tumour models with the CAF-associated marker FAP.**

(A & B): Immunofluorescence staining of paraffin sections from semi-static or dynamic tumour models containing A549 cells and metCAFs. Staining was directed against FAP (red). Nuclei are counterstained with DAPI (blue). Arrows in magnified images indicate stretched fibroblast cells, which were positively stained for FAP. Scale bars indicate 100 µm.

Taken together, the staining of FAP further supports that CAFs could be incorporated in the microphysiologic 3D tumour models, especially in the lung tumour model.

Considering the role of fibroblasts within the connective tissue and especially during the desmoplastic reaction in carcinomas, they are mainly responsible for the remodelling of ECM structures. This can be mediated by different enzymes like hyaluronidases, collagenases or matrix metalloproteases. In the context of cancer and CAFs, the matrix metalloproteases 2 and 9 (MMP-2 and MMP-9) have been described as important mediators of matrix remodelling and initiators of metastasis formation (Kalluri & Zeisberg, 2006; Nurmik *et al.*, 2020). Both can be secreted either by tumour cells or by CAFs. To estimate whether the stromal enrichment of the tumour models leads to increased MMPs within the model, MMP-2 and 9 were assessed with an immunofluorescence staining, which is shown in Figure S4 (MMP-2) and 14 (MMP-9).

Since tumour cells are also able to secrete MMPs, a dynamic monoculture of A549 was compared to co-cultures containing either primCAFs or metCAFs. To compare tissue structure, a native lung adenocarcinoma sample served as control. To confirm whether the secretion is located in areas of tumour cell masses or fibroblasts, the mesenchymal marker vimentin was counterstained as it is strongly expressed by fibroblasts. MMP-2 (Fig. S4, green) staining showed scattered signals throughout all samples (Fig. S4 I, J, K, L). MMP-2 was located primarily in cell clusters within crypt structures in the A549 monoculture (Fig. S4 I, white arrows) and showed no distinct pattern in co-culture with primCAFs (Fig. S4 J). The signals in the co-culture containing metCAFs indicate a distinct expression, where fibroblasts are normally located (Fig. S4 K, white arrows). The native tissue showed expression within tumour cell islets (Fig. S4 L, white arrows) and a homogenous signal throughout the mesenchymal (VIM$^+$) cells, as well as in epithelial cell clusters (DAPI$^+$, VIM$^-$).

Consequently, the expression of MMP-2 indicated that A549 cells produce ECM remodelling enzymes, which can be supported by stromal enrichment, especially when using metCAFs. The addition of metCAFs also favoured an organised tissue architecture, which closely resembled the *in vivo* situation.

The MMP-9 staining (Fig. 14) of dynamic lung (A549) tumour models showed stronger signals for all groups compared to the MMP-2. The A549 monoculture (Fig. 14 I) revealed a comparable pattern as the MMP-2, with scattered signals, especially in tumour cell clusters in crypt structures. In stromal-enriched (Fig. 14 J & K) models, uniform MMP-9 expression throughout the fibroblast-containing parts of the matrix was present (indicated by white arrows). The native tissue (Fig. 14 L & P) showed diffuse overall expression with distinct MMP-9$^+$ cell clusters amongst tumour cells and stromal cells (Fig. 14 P, indicated by white arrows). It was also described previously that MMP-2 is often produced by tumour cells, while MMP-9 is mostly derived from stromal cells (Taguchi *et al.*, 2014).

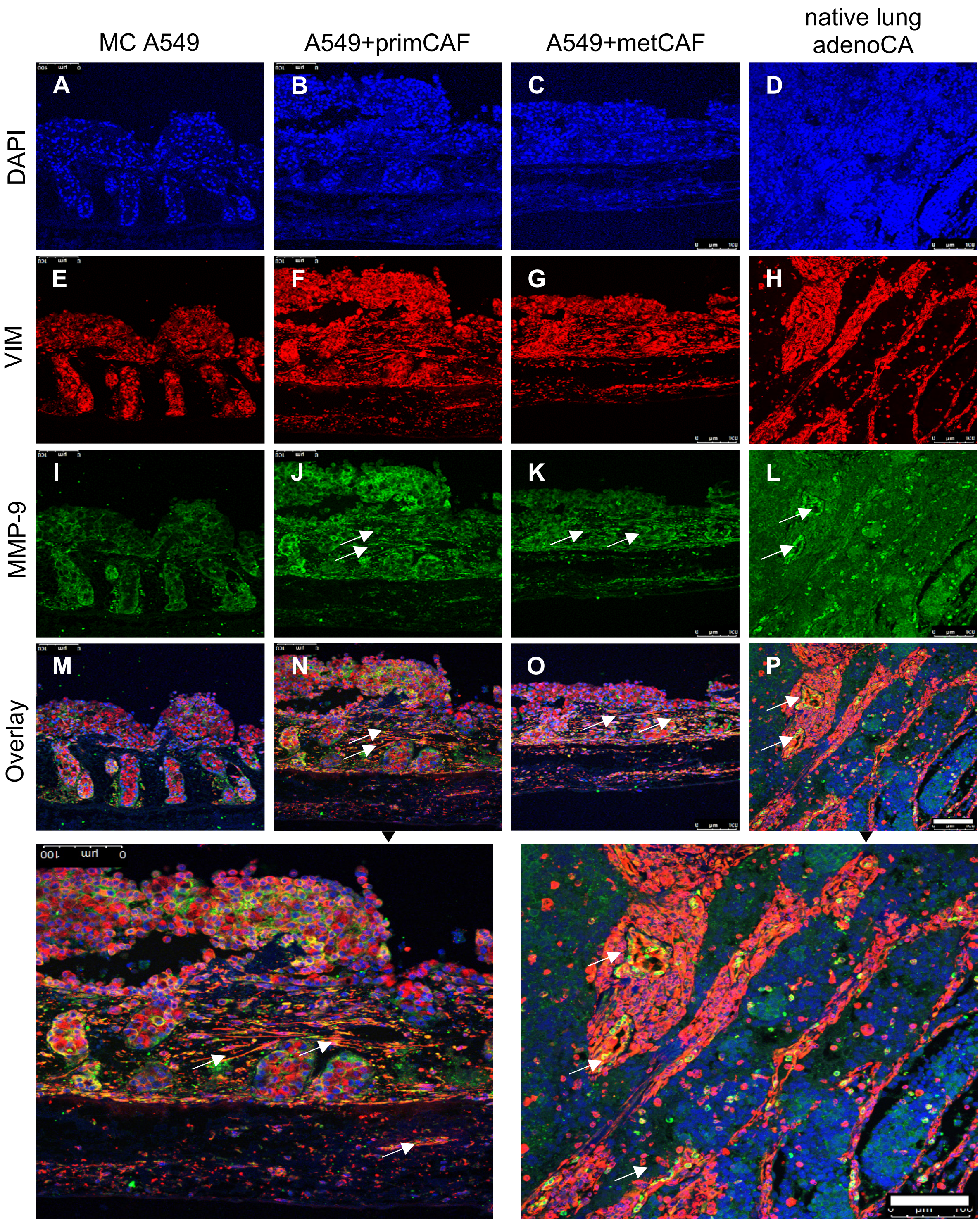
MC A549
A549+primCAF
A549+metCAF
native lung adenoCA
DAPI
VIM
MMP-9
Overlay
A
B
C
D
E
F
G
H
I
J
K
L
M
N
O
P
0 µm 100

**Figure 14. Characterisation of stromal-enriched microphysiologic 3D lung tumour models with the CAF-associated marker MMP-9.**

(A - P): Immunofluorescence staining of paraffin sections from dynamic tumour models containing A549 cells alone or in combination with either primCAFs or metCAFs. In addition, a biopsy of a lung adenocarcinoma was stained. Staining was performed against VIM (red) and MMP-9 (green). Nuclei were counterstained with DAPI (blue). White arrows indicate cells stained positive for MMP-9. Monoculture of A549 cells as well as co-cultures showed MMP-9 expression. The co-cultures showed distinct positive cells within the tumour cell mass and in fibroblast dense areas. Scale bars indicate 100 µm.

Taken together, the combination of MMP-2 and MMP-9 stainings revealed that ECM remodelling enzymes are present in the microphysiologic 3D tumour models and in an extended amount in stromal-enriched microphysiologic 3D tumour models. The architecture of lung tumour models containing primCAFs and metCAFs appeared similar. However, the combination with metCAFs led to a more compact structure, while models containing primCAFs appeared looser and thicker in diameter. These results illustrate that it is feasible to generate stromal-enriched microphysiologic 3D tumour models on the SISmuc, which closely resemble the native tissue architecture while also showing distinct patterns of CAF markers and associated ECM remodelling proteins.

In addition to ECM modifying proteins like MMPs, the effects of CAFs within the TME are mediated by secreted cytokines. This way, they can affect immune cells as well as cancer cells and modulate therapy outcome.

To further asses which cytokines are produced within the stromal-enriched microphysiologic 3D tumour models, a Multiplex (Human XL Proteome Profiler™) assay was performed, which analyses 105 proteins per sample simultaneously (Fig. 15 and Tab. S1). This method was used to evaluate cytokine secretion in stromal-enriched microphysiologic 3D models containing either A549 (CC A549) or MDA-MB-231 (CC MDA) cells. Additionally, a metCAF (MC metCAF fibroblasts) alone was assessed to examine the baseline of cytokine production of the fibroblasts. Semi-static models were established and supernatants were sampled after 48 h to allow for cytokine accumulation.

Quantification of the spots was not possible due to variations in references spots. The results were visually divided in the three groups: high, medium and low (Table S1), but discussion was only performed independently of this grading. Cytokines were associated in a Venn-diagram to find correlations between the different groups (Fig. 15). Here, 8 similarities were found, that were present in all cultures and 8, that were shared between both co-cultures. To understand mechanisms and differences, literature research was conducted to bring the measured markers into context.

Markers present in all samples are associated with metastasis in lung and breast cancer and EMT. Moreover, CAF-associated markers were found as well as markers involved in inflammation and promotion of CAF phenotype. Similarities in the samples containing both tumour cell types and fibroblasts are associated with cancer progression, matrix remodelling, angiogenesis and immunosuppression. Fibroblasts alone showed markers for CSC formation, TGF-β pathway interactions, angiogenesis and migration. Co-culture of fibroblasts and A549 tumour cells revealed stroma-signalling and EMT association. MDA-MB-231 cells together with fibroblasts indicated association with immunomodulatory and inflammatory effects, invasion and angiogenesis.

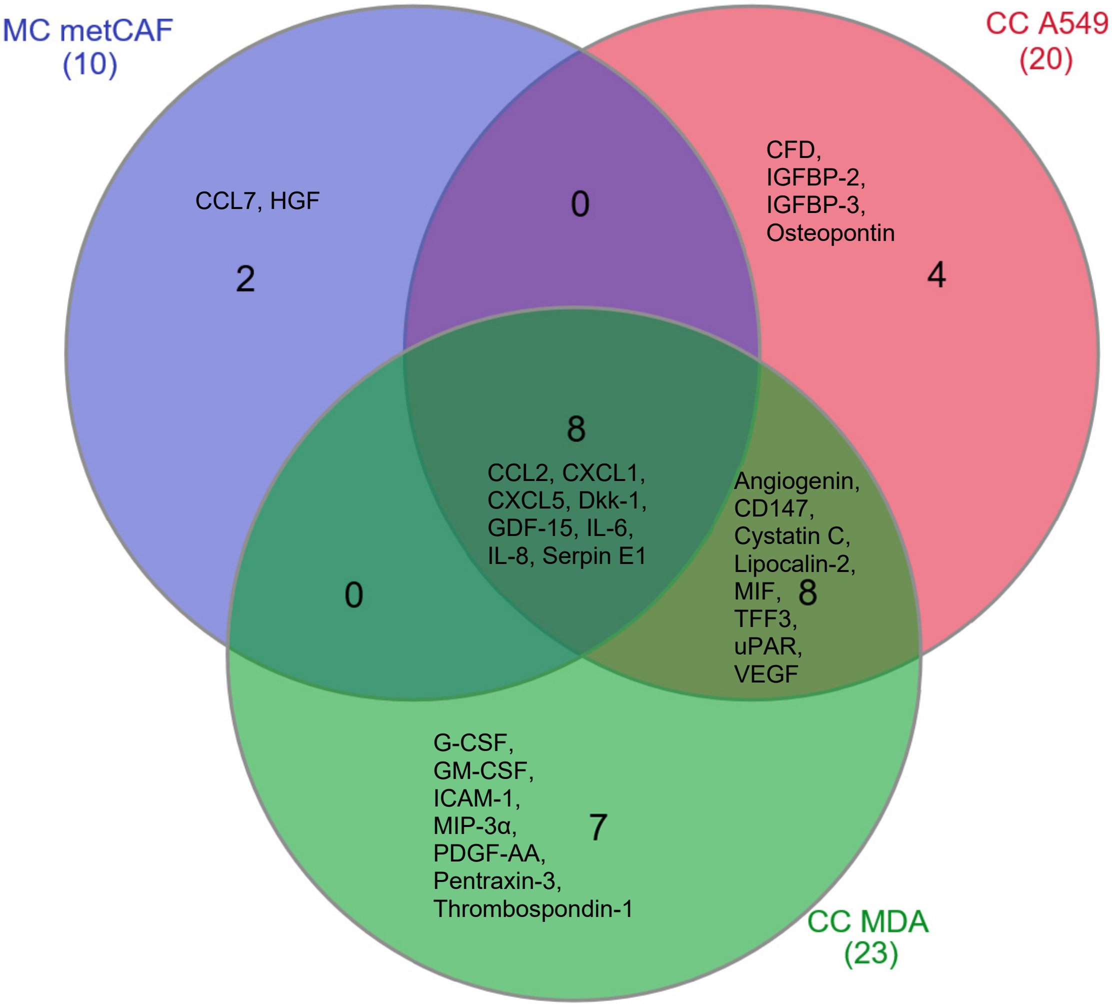

**Figure 15. Multiplex Analysis using a Proteome Profiler™ assay to analyse secreted cytokines in microphysiologic 3D tumour models containing lung tumour-derived fibroblasts alone or in combination with either A549 or MDA-MB-231 cells.**

Semi-static tumour models including either metCAF alone (=MC metCAF) or in combination with either A549 (=CC A549) or MDA-MB-231 (=CC MDA) cells were cultured for 10 days and supernatant was collected after 48 h. Medium alone served as control. Proteome Profiler™ (Human XL Cytokine Array) was used for analysis. Detailed information of array coordinates is provided in Table S1 and Figure S8. N=1.

### 4.1.6 Microphysiologic 3D sarcoma models can be sensitised for $G_{D2}$-targeting CAR T cells

As shown at the beginning in chapter 4.1.3, the SISmuc matrix allows the modelling of not only carcinomas but also sarcomas. To assess treatment options for Ewing’s sarcoma, microphysiologic 3D sarcoma models were established under dynamic conditions. So far, treatment options for Ewing’s sarcoma are limited, but it has been shown that the surface marker $G_{D2}$ could be a promising target for future therapies. $G_{D2}$ is heterogeneously expressed on sarcoma cells; therefore, a $G_{D2}$–targeting therapy would not target all tumour cells equally. However, studies could show that $G_{D2}$ can be upregulated when the epigenetic modulator GSK126 is administered prior to treatment, making Ewing’s sarcoma cells susceptible for $G_{D2}$-directed treatment. To target $G_{D2}$ expressing sarcoma cells, $G^{D2}$ CAR T cells were produced and kindly provided by Dr Kailayangiri (Kailayangiri *et al.*, 2012; Kailayangiri *et al.*, 2017).

The CAR T cells were tested in dynamic models using the cell lines MS-EwS-4 and SK-ES-1. This added the additional challenges of active adherence from the media flow to the immune cells. The models were maturated for 14 days under dynamic conditions and GSK126 was administered for the duration of the whole culture time to induce homogenous $G_{D2}$ expression. At day 14 $G_{D2}$ targeting CAR T cells were administered and treatment was performed for 5 days.

MS-EwS-4 cells (Fig. 16 A) grew loosely attached, while SK-ES-1 cells (Fig. 16 B) grew in large clusters on top of the matrix and filled the preserved crypt structures. Flow cytometry of re-isolated cells from the SISmuc revealed $G_{D2}$ expression in both cell lines after GSK126 administration for 14 days in the dynamic system. In SK-ES-1 (Fig. 16 B) cells a 4 µM dose was sufficient, while MS-EwS-4 (Fig. 16 A) required treatment with 12 µM. Treatment with $G_{D2}$ CAR T cells for 5 days reduced cell numbers of SK-ES-1 cells compared to the control (Fig. 16 C). Some of these results were successfully published in the Journal “*Molecular Therapy*” (Kailayangiri *et al.*, 2019).

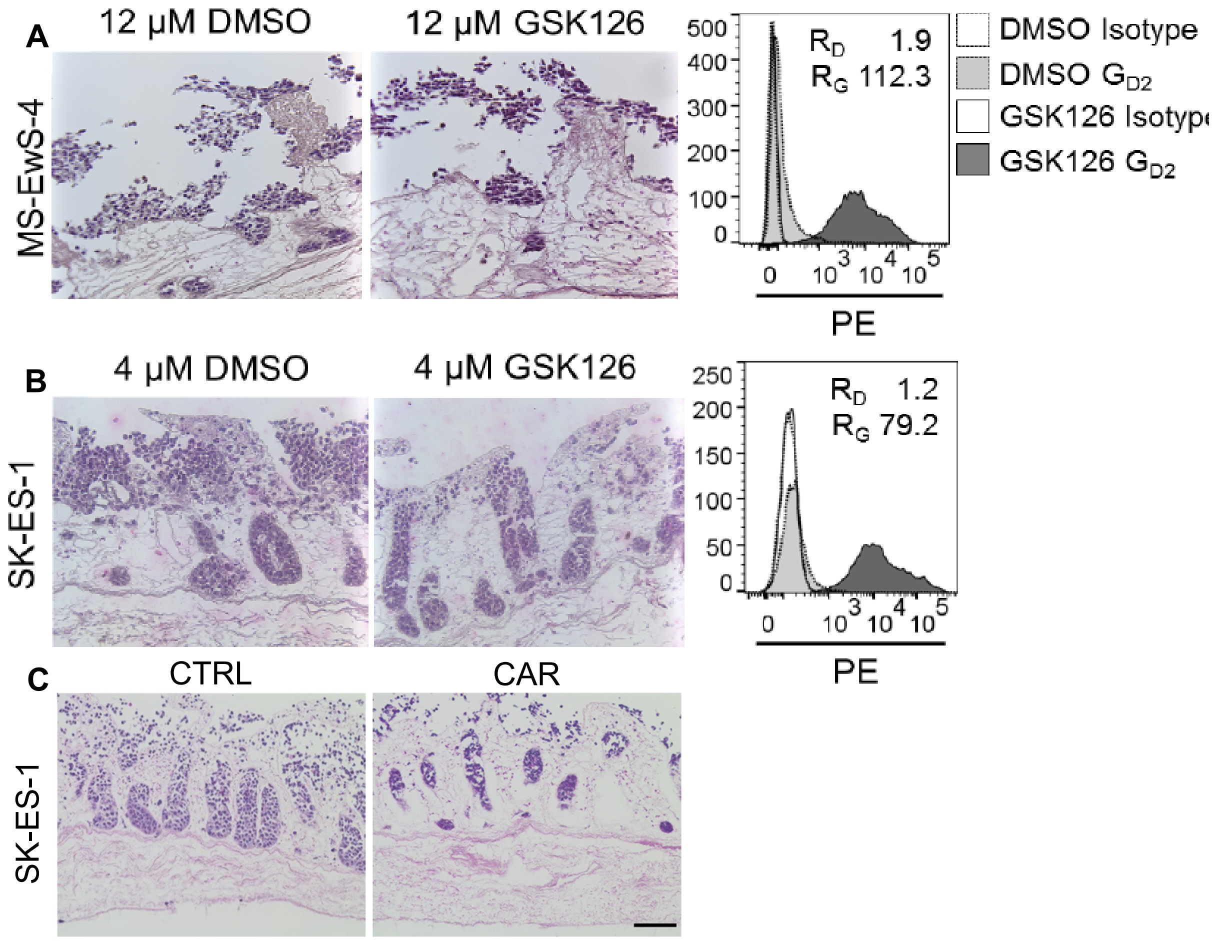

**Figure 16. G$_{D2}$ expression can be induced in Ewing's sarcoma cells and sensitises them for G$_{D2}$ CAR T cells.**

Microphysiologic 3D sarcoma models with either MS-EwS-4 or SK-ES-1 cells were cultured under dynamic conditions and treated with indicated concentrations of GSK126 for 14 days. On day 14, treatment was administered in terms of 30x10$^{6}$ G$_{D2}$ CAR T cells or Control T cells for 5 days. H&E stainings were performed on paraffin embedded tissue sections. (A & B): H&E stainings of models containing either MS-EwS-4 or SK-ES-1 cells after 14 days of indicated GSK126 administration. Equal amounts of DMSO served as Control. G$_{D2}$ surface expression was quantified by flow cytometry and confirmed for both cell lines after re-isolation from the SISmuc. (C): H&E stainings of models containing SK-ES-1 cells treated with G$_{D2}$ CAR T cells for 5 days after induction of G$_{D2}$ for 14 days. G$_{D2}$ CAR T cells led to a reduction of tumour cells compared to the Control. Representative images from one T cell donor are shown. N=1. Scale bar indicates 100 µm. Figure adapted from (Kailayangiri *et al.*, 2019).

Taken together, microphysiologic 3D tumour models representing Ewing's sarcoma can be utilised for the evaluation of cellular immunotherapeutic approaches with G$_{D2}$-targeting CAR T cells and demonstrated that G$_{D2}$-expression can be induced, sensitising inhomogeneous subpopulations for G$_{D2}$ CAR T cell treatment

### 4.1.7 Non-invasive bioluminescence-based measurement enhances analysis in microphysiologic 3D tumour models

Evaluation and visualisation of tumour burden in mice is easily performed by *in vivo* imaging based on bioluminescence intensity (BLI), which relies on the reaction between luciferase-expressing tumour cells and the substrate luciferin. Upon this reaction, light is emitted, which is detected by a sensitive camera incorporated in an *in vivo* imaging system (IVIS).

The challenge during this work was to assess, if this method could be applied to the microphysiologic 3D tumour models. This would allow time-efficient serial monitoring and evaluation of tumour cell growth and treatment efficacy without model destruction and consequently increase the scale of assessment.

To generate stable and homogenous luciferase-expression the cell lines A549 and MDA-MB-231 were transfected with a vector containing the *firefly-luciferase* gene. These cells were produced and kindly provided by Dr Lars Wallstabe. Static microphysiologic 3D tumour models were produced and treated with ROR1 CAR T cells for 3 days. Measurements were performed before CAR T cell administration and at the end of treatment.

Tumour models were treated either with $1x10^5$ (equal amounts $CD4^+$ and $CD8^+$) ROR1 CAR T cells (CAR), non-transduced control T cells (NT) or left untreated in cell specific media (CTRL). To evaluate background signal of luciferin application, an empty cell crown was supplemented with luciferin (empty). 5 µl (1 mg/ ml) luciferin were administered into the inner compartment of the cell crown.

Tumour models, that received control T cells showed distinct tumour cell distribution for A549 (Fig. 17 A) and MDA-MB-231 (Fig. 17 B) cells. A549 cells filled the crypt structure and formed a monolayer, while MDA-MB-231 cells grew scattered throughout the matrix. After 3 days of CAR T cell treatment (CAR), only a few cells remained on the SISmuc (Fig. 17 C & D). Measurement showed equally distributed cells where no treatment was administered (CTRL) or Control T cells were added (NT). This is equally true for A549 and MDA-MB-231 models. CAR T cell-treated models showed comparable cell distribution as well as cell reduction for A549 (Fig. 17 E) and MDA-MB-231 (Fig. 17 F) cells. Quantification of bioluminescence intensity can be calculated in different ways. The easiest way to assess whether different tumour cells can be compared to each other and how treatment affects tumour cells is the photon intensity. This value is detected by the IVIS and represents the photons per second over the surface area (P/sec/mm/sq). Those values were within the same range for both tested cell lines, with around $8.2x10^6$ (A549) and $9.6x10^6$ (MDA-MB-231) P/sec/mm/sq (Fig. 17 G). To quantify treatment efficacy, the calculation of either cell reduction or specific lysis can be performed. Cell reduction is the difference of photon intensity of one cell crown before and after treatment on itself. Cell lysis is calculated as difference to the respective control - either as specific lysis to control T cells or as total lysis to the untreated control. Here, the specific lysis is shown after 3 days of treatment with 1x$10^5$ ROR1 CAR T cells (Fig. 17 H). Specific lysis of A549 and MDA-MB-231 cells was comparable with 38 % in MDA-MB-231 and 42 % in A549 models. This indicated that both cell lines are equally susceptible for ROR1 CAR T cell therapy.

So far, the main read-out to assess therapy efficacy was the M30 CytoDeath™ ELISA, which measures apoptosis from the supernatant via cytokeratin 18. This is released by different epithelial cells upon apoptosis induction (Fig. S5). The effect of ROR1 CAR T cells on tumour cell apoptosis was dose dependent but much lower due to the mesenchymal characteristics of the MDA-MB-231 cells. Even when 1x$10^6$ ROR1 CAR T cells were added, the MDA-MB-231 cells showed a maximal fold-change of apoptosis of 4 (24 h), while A549 cells showed a fold-change of 14.5 (24 h). As MDA-MB-231 cells are more mesenchymal, they are less sensitive towards M30 CytoDeath™ ELISA, which becomes especially clear when compared to more epithelial A549 cells. To overcome this obstacle, the BLI-based IVIS measurement was demonstrated as a suitable method to measure treatment efficacy independent of epithelial cell status.

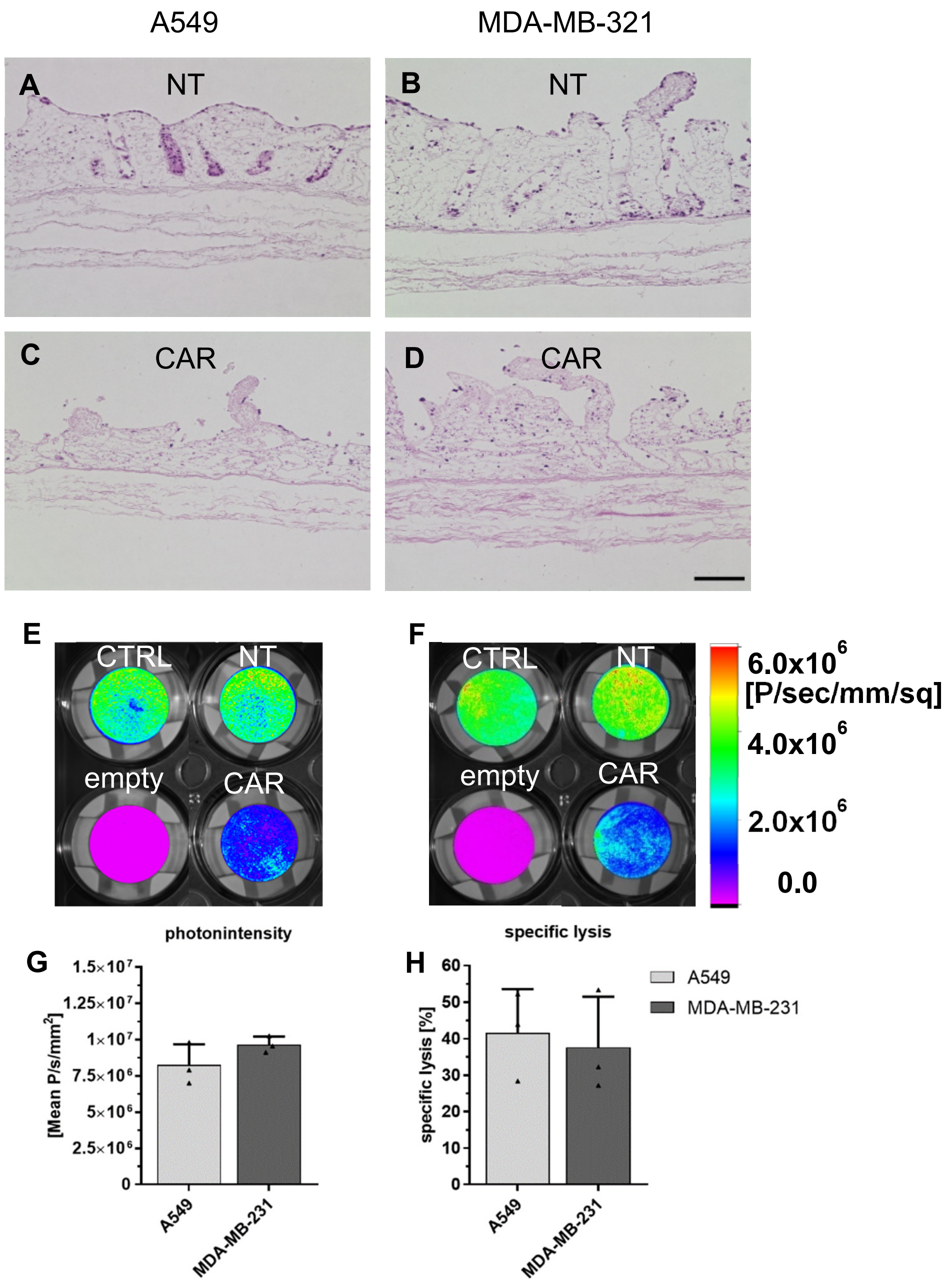

**Figure 17. BLI-based measurement enables quantification of treatment efficacy with ROR1 CAR T cells for epithelial and mesenchymal microphysiologic 3D tumour models.**

Static tumour models containing A549 or MDA-MB-231 cells were established and treated with $1x10^5$ ROR1 CAR T cells (equal amounts $CD4^+$ and $CD8^+$) for 3 days. Models were either treated with ROR1 CAR T cells (CAR), non-transduced control T cells (NT) or left untreated (CTRL). As a background control, an empty SISmuc was used (empty). (A - D): H&E staining of paraffin sections from tumour models containing either A549 or MDA-MB-231 tumour cells were treated with control T cells or ROR1 CAR T cells. Tumour cells were reduced in CAR treated models for both cell lines. Scale bar indicated 100 µm. (E & F): Luminescence was measured in the *in vivo* imaging system (IVIS) after 5 µl (1 mg/ ml) luciferin administration. ROR1-specific CAR T cell treatment led to a reduction in photon intensity. Scale indicates $P/s/mm^2$ (Photon intensity). (G): Quantification of luminescence intensity for untreated models. An intensity of $8.2x10^6$ $P/s/mm^2$ was reached for A549 cells and of $9.6x10^6$ $P/s/mm^2$ for MDA-MB-231 cells. (H): Specific lysis compared to non-transduced T cells was calculated and is illustrated in percent. A specific lysis of 42 % was reached for A549 and of 38 % for MDA-MB-231 cells. Data are presented as arithmetic mean of 3 cell crowns ± SD. n=1 experiment with 1 T cell donor.

### *Interim Summary*

The aim of this chapter was to improve the microphysiologic 3D tumour models in order to increase the predictive value for cellular immunotherapies by implementation of TME-aspects, long-term homeostasis and application of the SISmuc matrix to represent melanoma and sarcoma in addition to epithelial cancers. Additionally, a novel read-out method was established based on BLI.

Semi-static culture supported long-term tissue homeostasis for at least 28 days in lung cancer models. Utilisation of patient biopsies allowed isolation of fibroblasts and endothelial cells, which were successfully implemented into the tumour models in order to reflect parts of the TME as stromal enrichment, as well as endothelial cell layer. Furthermore, isolation of primary lung organoids was demonstrated as a proof-of-principle. Characterisation of the fibroblasts confirmed them as CAFs regarding their marker expression (FAP, α-SMA, MMP-2, MMP-9) and secretory phenotype (e.g. CCL2, CXCL1, IL-6). Testing of $G_{D2}$-specific CAR T cells in microphysiologic 3D models of Ewing's sarcoma supports the possibility to sensitise Ewing's sarcoma cells for $G_{D2}$-targeting therapy. In order to improve read-out parameters that comprises assessment of model quality, visualisation of the tumour tissue and analysis of treatment efficacy, serial bioluminescence intensity-based *in vivo* imaging was successfully established as a novel read-out parameter.

## 4.2 Analysis of different ROR1 CAR T cell designs in microphysiologic 3D tumour models reveals differences in efficacy

To reach a strong efficacy against tumour cells and improve therapy outcome with a CAR T cell approach, different factors must be considered regarding CAR design. Components of the CAR, like costimulatory domain, spacer length and the selection of suitable targeting domain have a strong influence on CAR T cell performance *in vitro* and *in vivo*.

To assess whether the microphysiologic 3D tumour models for breast (MDA-MB-321) and lung (A549) cancer are suitable and sensitive enough to evaluate the performance of differently designed CAR T cells and to explore that anti-tumour function depends on the CAR design, ROR1 CAR T cells were tested, which differ in spacer, targeting domain and costimulation. Experiments were performed using static tumour models. To evaluate the efficacy of the different CAR T cells, cytokines like IL-2 and IFN-γ were measured to analyse T cell activation. In addition, M30 CytoDeath™ ELISA was performed in order to measure the apoptosis of the tumour cells mediated by the CAR T cells. Furthermore, BLI-based measurements were conducted.

### 4.2.1 ROR1 CAR T cells with 4-1BB or CD28 costimulatory domain are equally potent in microphysiologic 3D tumour models

Since the first CAR T cell was described in the 1980s, different generations of CAR T cells followed. One difference between the generations involves the costimulatory domains, which mediate activation of the CAR T cells. A CAR T cell from the first generation only harbours the 3ζ domain without any costimulation. CARs from the second generation, which are also mainly used in approved CAR T cell products as well as clinical studies, can include additional costimulatory domains such as CD28 or 4-1BB. These domains favour CAR T cell expansion, function, persistence and antitumor activity. So far, it is known that CAR T cells from the second generation can induce superior anti-tumour effects compared to CAR T cells from the first generation and different costimulatory domains have been shown to be effective. The here tested costimulatory domains CD28 and 4-1BB have demonstrated strong influence on persistence and longevity of the CAR T cells (Weinkove *et al.*, 2019).

To assess whether the microphysiologic 3D tumour models are suitable to evaluate differences of CD28 and 4-1BB costimulation compared to missing costimulation, ROR1 CAR T cells with the high affinity R12 targeting domain were administered. The CARs contained either only the 3ζ domain (R12sh3z) or an additional costimulatory domain, here CD28 (R12sh28_3z) or 4-1BB (R12sh4-1BB_3z). CAR T cell ($CD8^+$ only) treatment was administered for 72 h in different concentrations ($5x10^3$, $2.5x10^4$, $1x10^6$) in static tumour models containing MDA-MB-231 (Fig. S6) or A549 (Fig. 20) cells.

H&E staining for breast tumour models (Fig. S6) showed the characteristic scattered cell growth with no tumour cell reduction at all concentrations for control T cells (Fig. S6 A). R12sh3z CAR T cells induced a slight tumour cell reduction at the concentration $2.5x10^4$ and nearly complete tumour cell removal when $1x10^6$ CAR T cells were administered (Fig. S6 B). R12sh4-1BB_3z CAR T cells showed a comparable pattern with fewer tumour cells at the $2.5x10^4$ concentration and nearly no remaining cells at the $1x10^6$ concentration (Fig S6 C). R12sh28_3z CAR T cells only removed cells in the group with the highest concentration (Fig. S6 D). Cell reduction and specific lysis, from BLI-based measurements (Fig. S6 E & F), indicate that the lowest concentration of all CAR T cells induced no tumour cell reduction, while $2.5x10^4$ administered CAR T cells led to 12 % and 11 % reduction for R12sh3z and R12sh28_3z CAR T cells. When $1x10^6$ CAR T cells were administered, 71 % and 73 % of the tumour cells were removed for both CAR T cells with costimulation and 61 % for R12sh3z CAR T cells. Specific lysis (Fig. S6 F) confirms these tendencies. Here, the R12sh28_3z CAR T cells induced the highest specific lysis with 36 % ($5x10^3$), 48 % ($2.5x10^4$) and 83 % ($1x10^6$). However, no large differences occurred between the constructs at all concentrations.

Testing of the same ROR1 CAR T cells in lung tumour models (Fig. 18 A - D) revealed a disruption of the tumour cells on the SISmuc when $1x10^6$ control T cells were administered, while the other concentrations of control T cells did not show this effect. Between the differently designed CAR T cells, it could be observed that all were able to disrupt the tumour cell layer at the $2.5x10^4$ concentration. When one million CAR T cells were applied, this resulted in nearly complete cell removal from all tumour cells independently of CAR design.

BLI-based measurements revealed small differences between the different CAR T cells as the cell reduction (Fig. 18 E) indicated a tumour cell increase for the R12sh3z CAR T cells at the lowest concentration, which was not observed for the other designs. When $2.5x10^4$ CAR T cells were added, the R12sh28_3z CAR induced the highest cell reduction with 24 %, while other CAR T cells did not affect tumour cell reduction. After administration of 1 million CAR T cells with either 4-1BB or CD28 costimulation, 91 % (R12sh4-1BB) and 87 % (R12sh28_3z) of lung tumour cells were removed, while the CAR T cells without costimulation removed 78 %. The specific lysis (Fig. 18 F) confirmed a trend towards stronger efficacy of the R12sh28_3z CAR T cells as it induced a specific lysis of 26 % ($5x10^3$), 45 % ($2.5x10^4$) and 92 % ($1x10^6$). The R12sh4-1BB CAR T cells led to a specific lysis of 15 % ($5x10^3$), 23 % ($2.5x10^4$) and 93 % ($1x10^6$). The R12sh3z CAR T cells could not induce specific lysis when $5x10^3$ cells were added, but induced specific lysis of 31 % for the $2.5x10^4$ concentration and 89 % for $1x10^6$ administered CAR T cells.

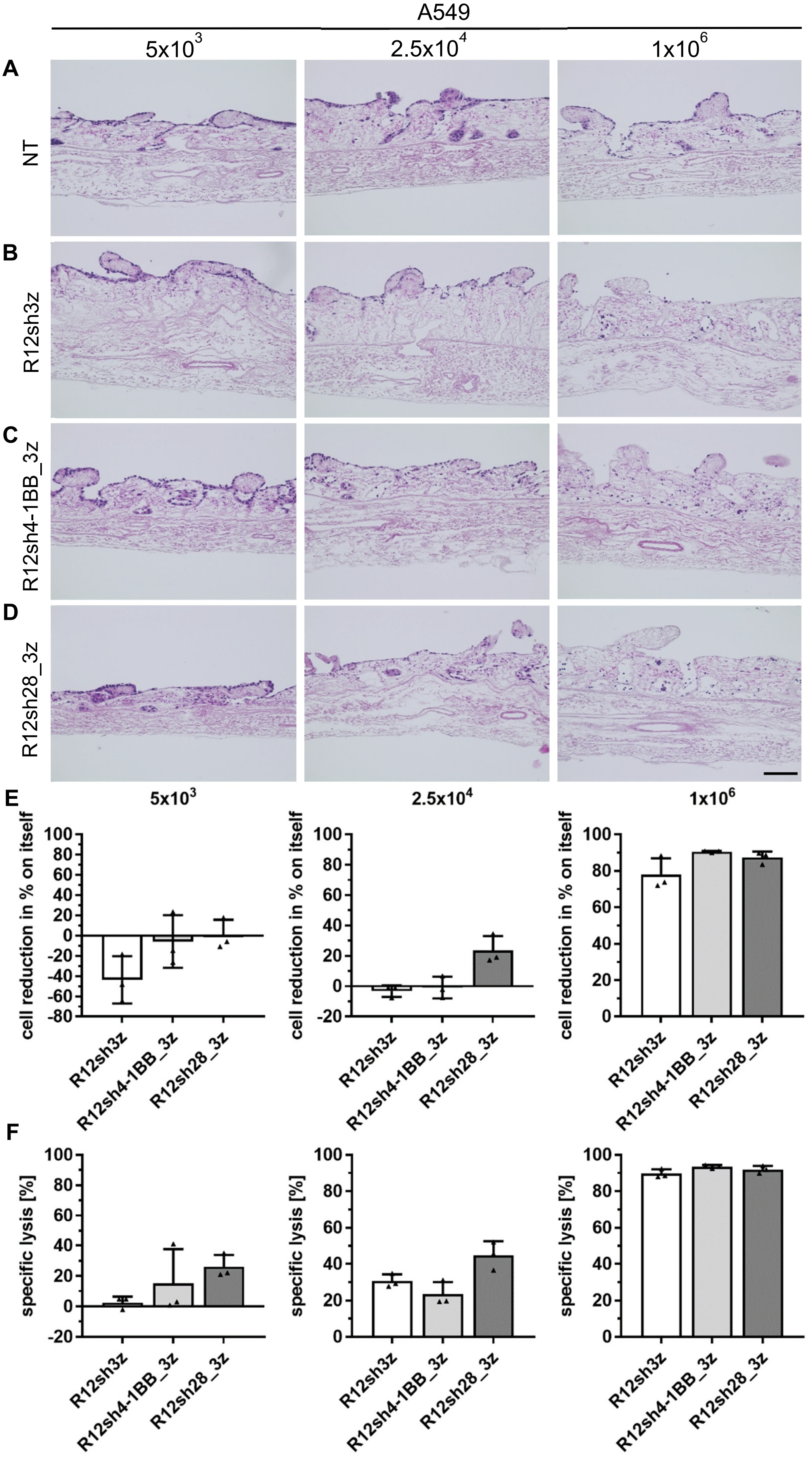
A549
5x10^3
2.5x10^4
1x10^6
A
NT
B
R12sh3z
C
R12sh4-1BB_3z
D
R12sh28_3z
E
5x10^3
2.5x10^4
1x10^6
cell reduction in % on itself
R12sh3z
R12sh4-1BB_3z
R12sh28_3z
F
specific lysis [%]
R12sh3z
R12sh4-1BB_3z
R12sh28_3z

**Figure 18. ROR1 CAR T cells with different costimulatory domains reduce tumour cells in static microphysiologic 3D lung tumour models with comparable efficacy.**

Static tumour models containing A549 cells were established and treated with three different concentrations ($5\times10^3$, $2.5\times10^4$, $1\times10^6$) of $CD8^+$ ROR1 CAR T cells for 3 days. ROR1 CAR T cells contained either no costimulatory domain (R12sh3z), a 4-1BB costimulatory domain (R12sh4-1BB_3z) or a CD28 costimulatory domain (R12sh28_3z). Models were treated either with ROR1 CAR T cells (CAR) or non-transduced control T cells (NT). (A – D): H&E staining of paraffin sections from tumour models containing A549 revealed a strong reduction of tumour cells when the highest concentration of CAR T cells was administered, while moderate effects occurred with $2.5\times10^4$ CAR T cells. Scale bar indicates 100 µm. (E & F): Quantification of specific lysis or cell reduction was performed via luminescence intensity signal. Specific lysis and cell reduction revealed highest specific lysis for the CD28 costimulatory domain when $2.5\times10^4$ CAR T cells were administered, while the highest CAR T cell concentration induced comparable levels of lysis and reduction for all administered CAR T cells. Data are presented as arithmetic mean of 3 cell crowns ± SD. n=1 experiment with 1 T cell donor.

Taken together, the ROR1 CAR T cells compared here from the first and second generation could reduce tumour cells and induced specific lysis in microphysiologic 3D lung and breast cancer models in a concentration dependent manner. However, conclusive results in MDA-MB-231 models were not observed. Differences on A549 cells were only moderate between the different CAR T cells, with a trend of stronger anti-tumour efficacy when CD28 costimulation was incorporated. Later higher concentrations of CAR T cells were used to improve anti-tumour effects for the low and medium concentration.

### 4.2.2 ROR1 CAR T cells with a higher affinity targeting domain lead to superior anti-tumour efficacy in microphysiologic 3D lung tumour models

Another factors, which influences CAR T cell performance and efficacy is the choice of the targeting domain. These domains are derived from monoclonal antibodies (mAbs) and mediate the binding to the specific antigen on the tumour cell surface, which can vary in affinity and avidity.

For ROR1 CAR T cells, previous *in vitro* and *in vivo* experiments have shown that the high affinity targeting domain R12 mediates superior anti-tumour efficacy compared to the low affinity targeting domain 2A2 (Hudecek *et al.*, 2013). To assess whether these results can be reproduced in the microphysiologic 3D lung tumour models, ROR1 CAR T cells with the different targeting domains were tested. CAR T cells carried 4-1BB costimulatory domain either with the 2A2 (low affinity) targeting domain or with the R12 (high affinity) targeting domain. Both were administered for 72 h in the static microphysiologic 3D lung tumour models containing A549 cells. As described previously, three different concentrations of $CD8^+$ ROR1 CAR T cells were administered. Considering the small effects with the doses $5x10^3$ and $2.5x10^4$, higher doses in terms of $5x10^4$ (low) and $2.5x10^5$ (medium) CAR T cells were applied.

H&E staining revealed no effect of control T cells (Fig. 19 A) on the tumour cells independent of CAR T cell concentration. The ROR1 CAR T cell with the low affinity targeting domain 2A2 (Fig. 19 B) induced tumour cell reduction for $2.5x10^5$ and $1x10^6$ administered CAR T cells, but not for $5x10^4$ applied CAR T cells. The highest concentration of 2A2 CAR T cells removed nearly all tumour cells, leaving only scattered cells on the SISmuc, and the medium concentration did not remove cells from the crypt structures but removed them from the model surface. The ROR1 CAR cells with the high affinity targeting domain R12 (Fig. 19 C) already disrupted the tumour cell layer at the lowest concentration and removed tumour cells from crypt structures when $2.5x10^5$ CAR T cells were added. At the highest concentration, nearly all tumour cells were eradicated. In the BLI-based measurements (Fig. 19 D) both tested CAR T cells, independent of affinity, caused increasing levels of cell reduction with increasing CAR T cell number, while the ROR1 CAR T cell with the R12 targeting domain showed a higher cell reduction at low (29 %>23 %) and medium (78 %>70 %) concentration. Cell reduction upon administration of 1 million CAR T cells was nearly identical with over 97 % (2A2) and 95 % (R12). Results for the specific lysis showed similar results supporting this trend, indicating that ROR1 CAR T cells with the high affinity targeting domain R12 could be superior to CAR T cells with the low affinity 2A2 targeting domain.

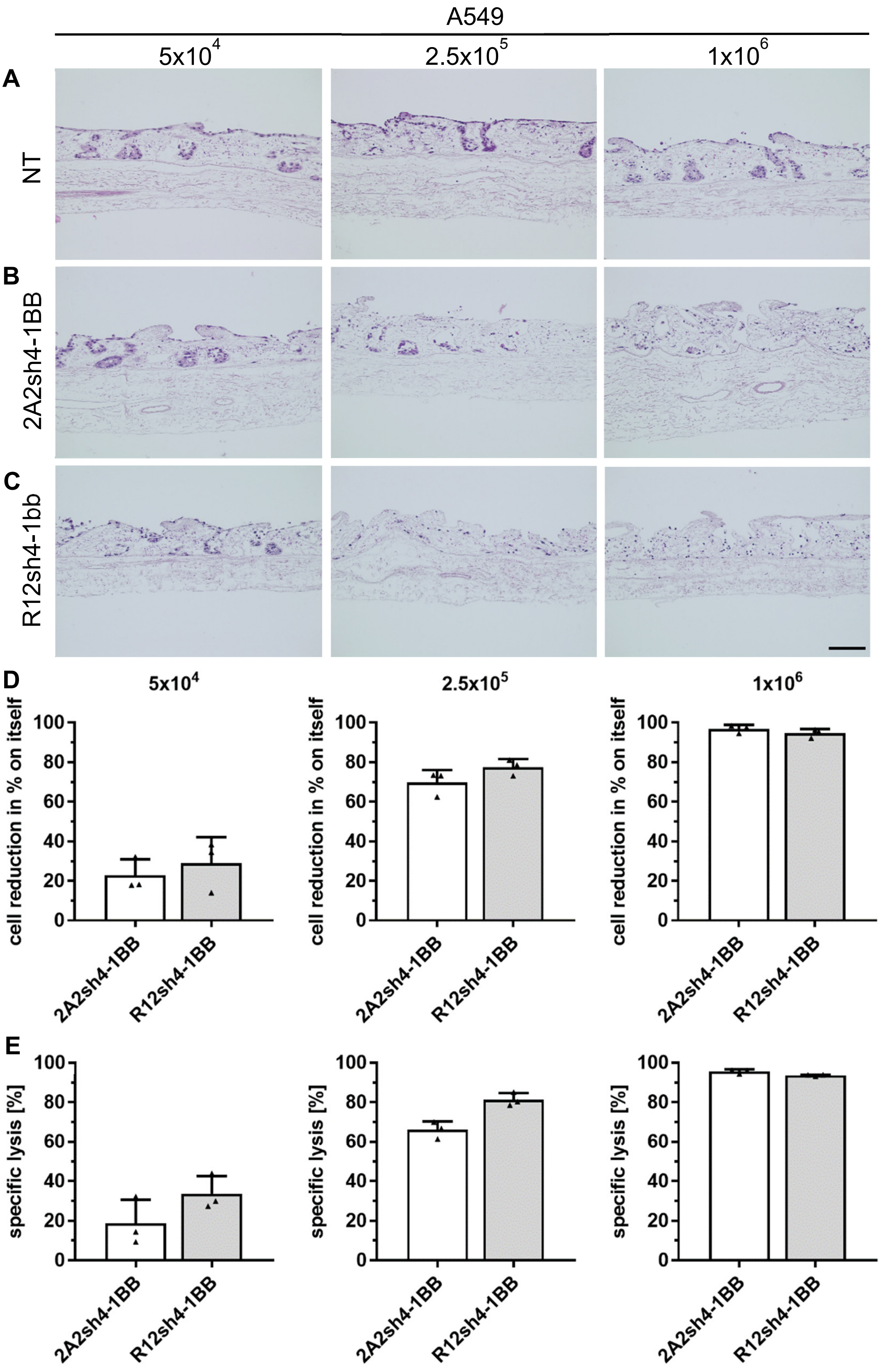
A549
5x10^4
2.5x10^5
1x10^6
A
NT
B
2A2sh4-1BB
C
R12sh4-1bb
D
5x10^4
2.5x10^5
1x10^6
cell reduction in % on itself
0
20
40
60
80
100
2A2sh4-1BB
R12sh4-1BB
E
specific lysis [%]
0
20
40
60
80
100
2A2sh4-1BB
R12sh4-1BB

**Figure 19. ROR1 CAR T cells remove lung tumour cells effectively dependent on targeting domain affinity in static microphysiologic 3D lung tumour models.**

Static tumour models containing A549 cells were established and treated with three different concentrations ($5\times10^4$, $2.5\times10^5$, $1\times10^6$) of $CD8^+$ ROR1 CAR T cells for 3 days. ROR1 CAR T cells contained either a low affinity targeting domain (2A2) or a high affinity targeting domain (R12) together with a 4-1BB costimulation. Models were treated either with ROR1 CAR T cells (CAR) or non-transduced control T cells (NT). (A – D): H&E staining of paraffin sections from tumour models containing A549 revealed a strong reduction of tumour cells when the high concentration of CAR T cells was administered for the 2A2 and the R12 targeting domain, while moderate effects occurred with $2.5\times10^4$ CAR T cells, which was more pronounced in the CAR T cells with R12 targeting domain. Scale bars indicate 100 µm. (E & F): Quantification of specific lysis and cell reduction was performed via BLI-based measurements. The CAR T cells with the R12 targeting domain induced higher tumour cell reduction and specific lysis for the low and medium concentration. Data are presented as arithmetic mean of 3 cell crowns ± SD. n=1 experiment with 1 T cell donor.

Since the results of the H&E staining and the BLI-based measurements indicated only a trend that the CAR T cells with the R12 targeting domain are superior to ROR1 CAR T cells carrying 2A2 targeting domain, apoptosis measurements, as well as cytokine release and flow cytometry data were assessed. Here, cytokine ELISA regarding IL-2 and IFN-γ and flow cytometry can reveal differences in activation of the different ROR1 CAR T cells.

Apoptosis measurements (Fig. 20 A) showed that R12 ROR1 CAR T cells induced higher tumour cell apoptosis for $5x10^4$ administered cells, which peaked after 48 h. Medium concentrations showed similar tendencies but without strong differences between 2A2 and R12. Here the medium concentration induced a 10-fold increase at 48 h for R12 ROR1 CAR T cells and an 8-fold increase for 2A2 CAR T cells. Apoptosis for $1x10^6$ administered CAR T cells appeared similar. This indicates higher anti-tumour efficacy of the CAR T cells with R12 targeting domain at lower CAR T cell concentrations.

IFN-γ levels (Fig. 20 B) were higher for CAR T cells with R12 targeting domain compared to 2A2 targeting domain in all administered concentrations but especially at low and medium concentrations. Here, secretion peaked at the 24 h time point (4000 pg/ml > 2000 pg/ml). In terms of IL-2 secretion (Fig. 20 C), the R12 ROR1 CAR T cells also secreted higher amounts compared to 2A2 ROR1 CAR T cells. This was true for all administered concentrations, where secreted IL-2 peaked 6 h after treatment start in R12 ROR1 CAR T cells. Differences were especially high in the low and medium concentrations (2500 pg/ml > 1000 pg/ml (low) and 9000 pg/ml > 5000 pg/ml (medium)). In addition, the activation markers CD25 and CD69 were assessed by flow cytometry (Fig. 20 D) with CAR T cells, which were sampled from the medium after the 72 h treatment period. Here, 98 % of all T cells were positive for both marker in the models receiving R12 ROR1 CAR T cells while 93 % were positive in the models with 2A2 CAR T cells. This indicated higher amounts of activated T cells amongst CAR T cells with the R12 targeting domain.

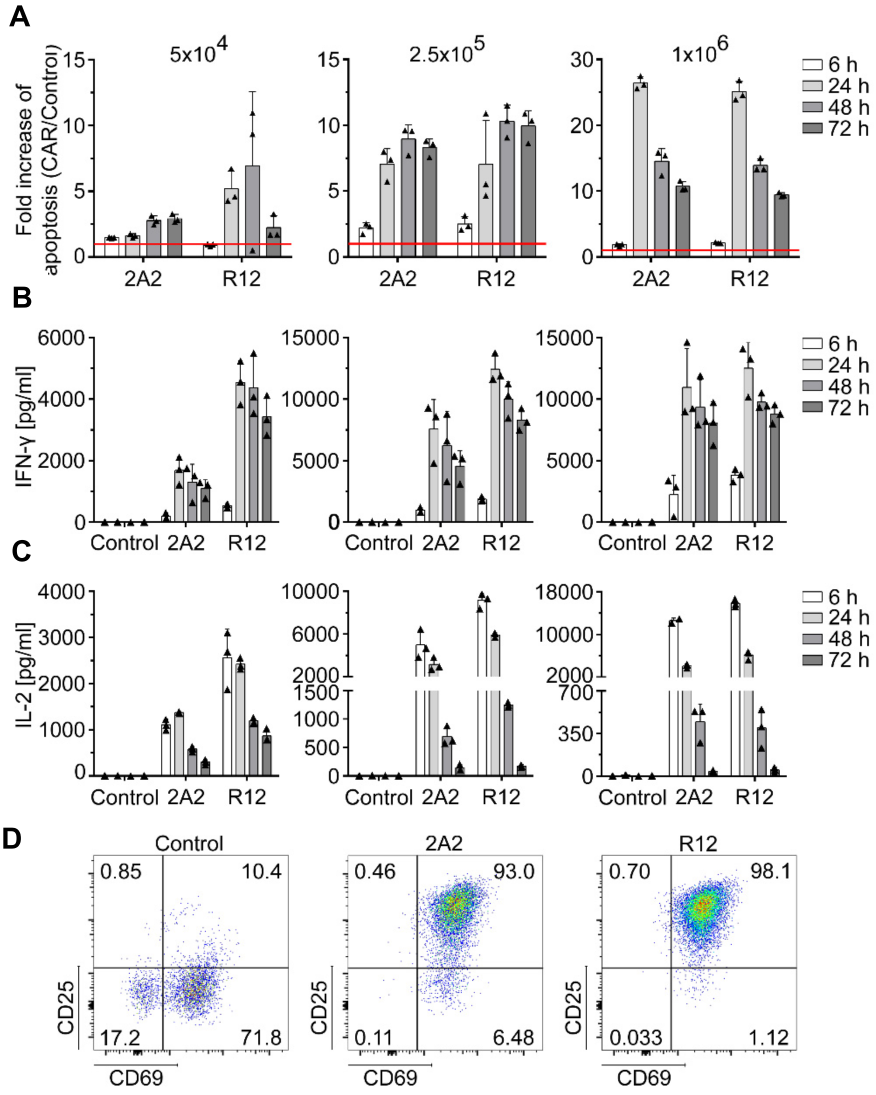

**Figure 20. ROR1 CAR T cells induce apoptosis and become activated dependent on targeting domain affinity in static microphysiologic 3D lung tumour models.**

Static tumour models containing A549 cells were established and treated with three different concentrations ($5\times10^4$, $2.5\times10^5$, $1\times10^6$) of $CD8^+$ ROR1 CAR T cells for 72 h. ROR1 CAR T cells contained either a low affinity targeting domain (2A2) or a high affinity targeting domain (R12) together with a 4-1BB costimulatory domain. Models were treated either with ROR1 CAR T cells (CAR) or non-transduced control T cells (NT). (A): Quantification of apoptosis was performed by M30 CytoDeath™ ELISA with samples from the supernatant at the indicated time points. Values are presented as fold change compared to the same dose of control T cells (red line). CAR T cells with the R12 targeting domain induced higher apoptosis at the low concentration. Data are presented as arithmetic mean of 3 cell crowns ± SD. n=1 experiment with 1 T cell donor. (B & C): ELISA-based quantification of IFN-γ and IL-2 secretion with samples from the supernatant at the indicated time points. R12 ROR1 CAR T cells secreted higher levels of IL-2 and INF-γ at all administered concentrations. Data are presented as arithmetic mean of 3 cell crowns ± SD. n=1 experiment with 1 T cell donor. (D): Expression of CD25 and CD69 on $CD8^+$ ROR1 CAR T cells and control T cells at the end of the 72-hour treatment. One representative plot of 3 cell crowns from n=1 experiment with 1 T cell donors is shown. Figure is adapted from (Wallstabe, Göttlich, Nelke, Kühnemundt *et al.*, 2019).

These results indicate that ROR1 CAR T cells with R12 targeting domain promote stronger anti-tumour efficacy implied by BLI-based measurements and the histological analysis but especially by cytokine secretion. Together, they support previous findings that ROR1 CAR T cells with R12 targeting show higher anti-tumour efficacy compared to 2A2 targeting domain (Hudecek *et al.*, 2013). Parts of these data were successfully published in the "*Journal of Clinical Investigatio*n" with an equally contributing co-authorship (Wallstabe, Göttlich, Nelke, Kühnemundt *et al.*, 2019).

### 4.2.3 ROR1 CAR T cell efficacy depends on specific spacer design

The design of the extracellular spacer, which is located between the transmembrane domain and the extracellular domain, influences the efficacy of a CAR by mediating the flexibility of the receptor towards the antigen. A receptor targeting a more membrane-proximal region of the epitope can preferably bind when combined with a long spacer. For a receptor, which binds at a membrane-distal region of the epitope, a short spacer can favour efficacy (Hudecek *et al.*, 2013; Hudecek *et al.*, 2015). To test the sensitivity of microphysiologic 3D tumour models, ROR1 CAR T cells with optimal and suboptimal spacer combination were applied. ROR1 CAR T cells with 2A2 mAb combined with either a short or a long spacer domain were administered in three different concentrations to static microphysiologic 3D lung tumour models containing A549 cells. The 2A2 mAb targets a membrane-distal region of the ROR1 antigen and, therefore, CAR T cells with a short spacer should perform more effectively.

H&E staining of models receiving control T cells (Fig. 21 A) did not show reduction of tumour cells. The CAR T cells with a short spacer domain (Fig. 21 B) reduced the tumour cells drastically upon administration of medium and high CAR T cell concentrations, with only scattered cells left on the matrix. 2A2 long (Fig. 21 C) induced tumour cell reduction, but tumour cells in crypt structures remained for medium and high concentrations. BLI-based measurements revealed comparable tumour cell reduction (Fig. 21 E) of both CAR T cell designs for low and medium concentrations $5x10^4$ (33 %) and $2.5x10^5$ (short: 55 %; long: 57 %). When one million CAR T cells were added, strong tumour cell reduction was observed with 80 % reduction induced by the CAR T cells with the short spacer and 66 % by the CAR T cells with the long spacer. This tendency was only partly reflected by specific tumour cell lysis (Fig. 21 F). No specific lysis was measured for 2A2 short at the lowest administered concentration. 2A2 long revealed minor tumour cell increase when $5x10^4$ CAR T cells were added. For the medium concentration 46 % cell lysis was induced by 2A2short and 35 % by 2A2long. The highest concentration induced a specific lysis of 74 % for 2A2short and of 45 % for 2A2long.

M30 CytoDeath™ ELISA was performed measuring the apoptosis of the rather epithelial tumour cells A549 (Fig. 21 G). Regarding tumour cell apoptosis no significant differences were revealed between the ROR1 CAR T cells with the long and the short spacer. Both induced a maximum of 4-fold (48 h) increase at the lowest administered concentration of CAR T cells and a 13- to 14-fold (24 h and 48 h) increase at the highest concentration. In presence of the medium concentration a small difference in apoptosis induction occurred. The peak of apoptosis induced by 2A2short was measured with 10-fold (48 h) and for 2A2long with 9-fold (6 h). The data from apoptosis measurements could not show conclusively if one spacer combination works more effectively.

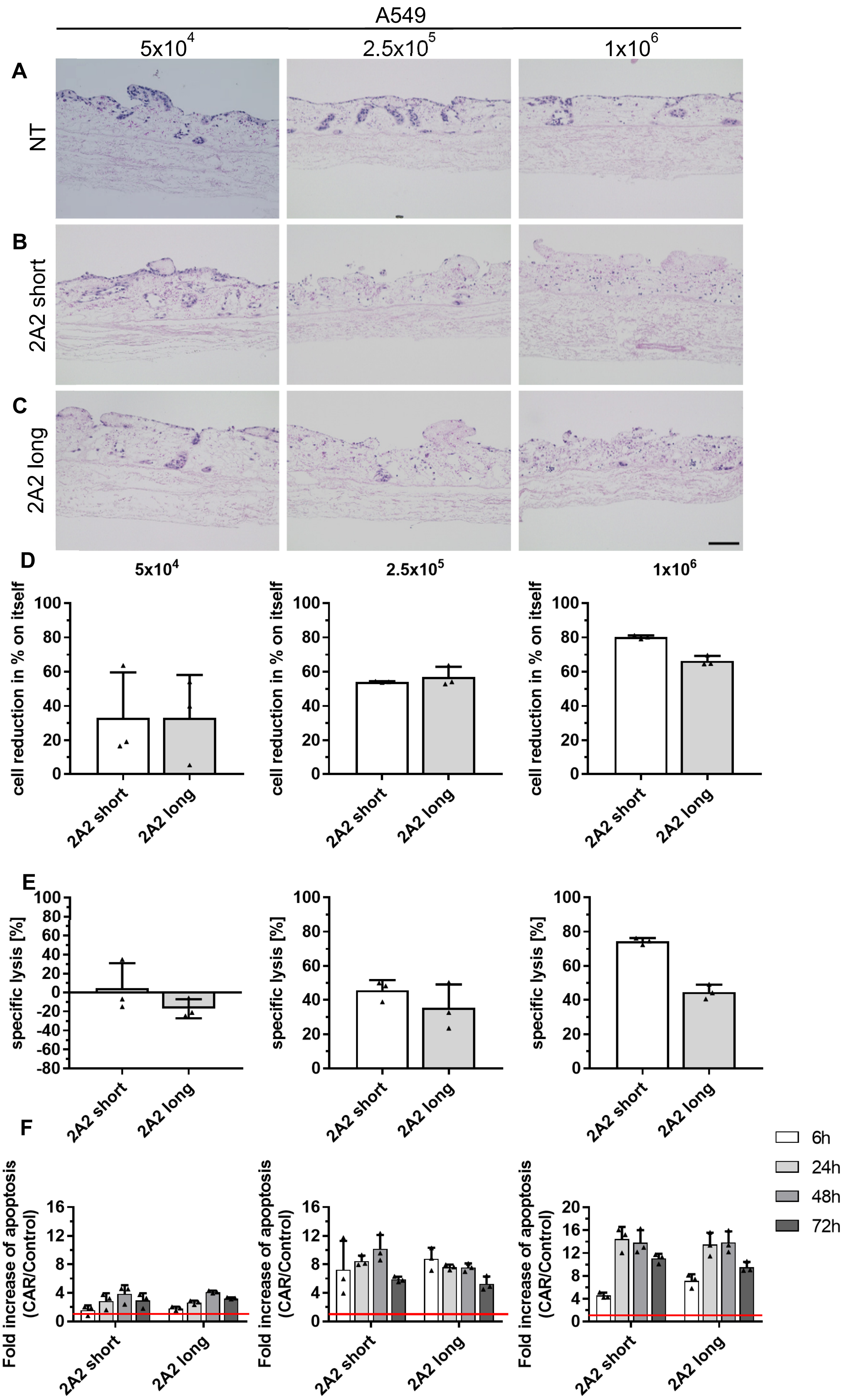
A549
5x10^4
2.5x10^5
1x10^6
A
NT
B
2A2 short
C
2A2 long
D
5x10^4
2.5x10^5
1x10^6
cell reduction in % on itself
0
20
40
60
80
100
2A2 short
2A2 long
E
specific lysis [%]
-80
-60
-40
-20
0
20
40
60
80
100
2A2 short
2A2 long
F
Fold increase of apoptosis (CAR/Control)
0
4
8
12
16
20
2A2 short
2A2 long
6h
24h
48h
72h

**Figure 21. ROR1 CAR T cells with 2A2 and a short spacer show a trend to reduce tumour cells more effectively in static microphysiologic 3D lung tumour models compared to a long spacer.**

Static tumour models containing A549 cells were established and treated with three different concentrations ($5\times10^4$, $2.5\times10^5$, $1\times10^6$) of CD8$^+$ ROR1 CAR T cells for 3 days. ROR1 CAR T cells contained a low affinity 2A2 targeting domain and either a short (IgG4-Fc hinge) or long (IgG4-Fc hinge-CH2-CH3) spacer domain. Models were treated either with ROR1 CAR T cells (CAR) or non-transduced control T cells (NT). (A - C): H&E staining of paraffin sections from tumour models containing A549 induced a disruption of the tumour cell layer at the lowest administered CAR T cell concentration for both designs. At higher concentrations 2A2short removed nearly all tumour cells, while 2A2long left behind tumour cells within the crypt structures. Scale bar indicates 100 µm. (E & D): Quantification of specific lysis or cell reduction was performed via luminescence signal intensity encompassing the entire model surface. 2A2short revealed higher specific lysis at all administered concentrations when compared to 2A2long. This effect was not confirmed by the cell reduction. (F): Apoptosis was measured with M30 CytoDeath™ ELISA from supernatants collected at the indicated time points and is presented as fold-change compared with the same dose of control T cells (red line). Low and high dose treatment revealed no difference between the two designs, while the administration of $2.5\text{x}10^5$ CAR T cells led to a maximum of a 10-fold increase (48 h) for 2A2short and an 8-fold (24 h) for 2A2long. Data are presented as arithmetic mean of 3 cell crowns ± SD. n = 1 experiment with 1 T cell donor.

To evaluate further if the ROR1 CAR T cells with 2A2 targeting domain and long or short spacer performed differently, cytokine concentrations for IFN-γ and IL-2 were measured via ELISA from samples of the supernatant at the indicated time points. Here, IFN-γ concentrations (Fig. 22 A) of 2A2short were higher in all administered CAR T cell concentrations compared to 2A2long. Peak concentrations of IFN-γ always occurred 24 h after treatment start. Amounts of IFN-γ increased drastically with increasing CAR T cell numbers and was higher for 2A2short compared to 2A2long with 1000 pg/ml > 650 pg/ml ($5\text{x}10^4$), 3750 pg/ml > 1500 pg/ml ($2.5\text{x}10^5$) and 10,000 pg/ml > 3000 pg/ml ($1\text{x}10^6$). A comparable tendency was observed for the concentrations of IL-2 (Fig. 22 B) secreted by 2A2short, where peak concentrations were reached at 24 h for the lowest (2500 pg/ml) and at 6 h for the medium (6000 pg/ml) and high (12500 pg/ml) administered CAR T cell concentrations. In comparison IL-2 concentrations in 2A2long peaked always at 6 h with 1250 pg/ml (low), 2100 pg/ml (medium) and 1400 (high) measured concentrations.

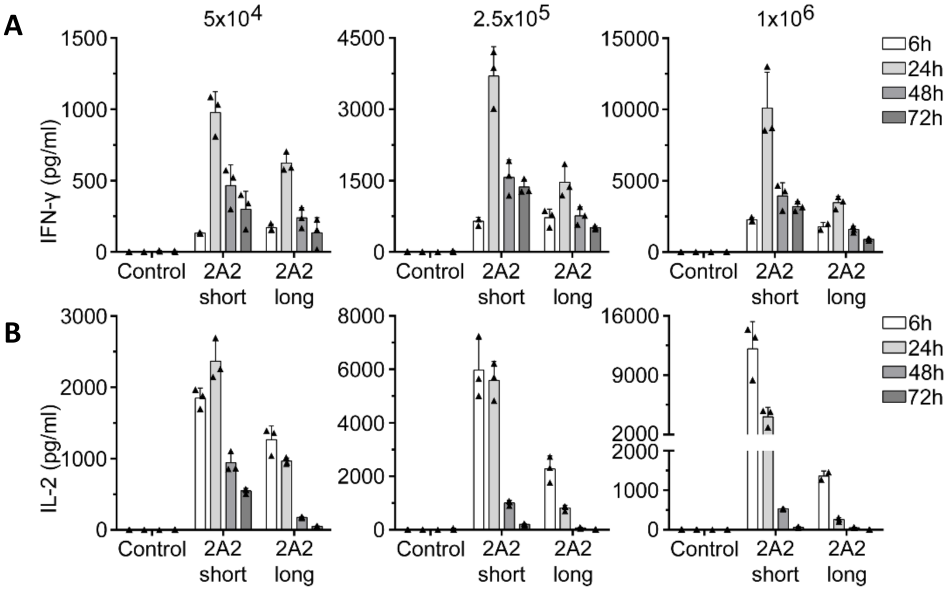

**Figure 22. Spacer design of ROR1 CAR T cells affects anti-tumour function in microphysiologic 3D lung cancer models.**

Static tumour models containing A549 cells were established and treated with three different concentrations ($5\times10^4$, $2.5\times10^5$, $1\times10^6$) of $CD8^+$ ROR1 CAR T cells for 3 days. ROR1 CAR T cells contained a low affinity 2A2 targeting domain and either a short (IgG4-Fc hinge) or long (IgG4-Fc hinge-CH2-CH3) spacer domain. Models were treated either with ROR1 CAR T cells (CAR) or non-transduced control T cells (NT). (A & B): ELISA-based quantification of IFN-γ and IL-2 concentrations from supernatants sampled at the indicated time points. ROR1 CAR T cells with the short spacer secreted higher levels of IFN-γ at all administered concentrations, which peaked at 24h. IL-2 levels were also higher for 2A2short at all concentrations and peaked after 6h ($5x10^4$) or 24h ($2.5x10^5$ and $1x10^6$). Data are presented as arithmetic mean of 3 cell crowns from n=1 experiment + SD with 1 T cell donor. Figure is adapted from (Wallstabe, Göttlich, Nelke, Kühnemundt *et al.*, 2019).

Collectively, the trend indicated by H&E staining and BLI-based measurements was reflected by the amounts of activating cytokines secreted by the ROR1 CAR T cells and supports that the 2A2 is superior when combined with a short spacer domain. Parts of these results were also successfully published in the "*Journal of Clinical Investigation"* with equally contributing co-authorships (Wallstabe, Göttlich, Nelke, Kühnemundt *et al.*, 2019).

### *Interim Summary*

Consequently, it was shown that different costimulatory domains induced similar anti-tumour function when administered in suboptimal concentrations. However, a tendency of ROR1 CAR T cells with CD28 costimulation towards stronger anti-tumour efficacy was shown. Comparison of ROR1 CAR T cells with differences in affinity of the targeting domain revealed that a higher affinity indeed induces stronger anti-tumour efficacy. Regarding spacer design, it was shown that the 2A2 epitope targeting a membrane-distal region of ROR1 performed better when combined with a short spacer, which demonstrated that targeting domains have specific spacer requirements. Therefore, the microphysiologic 3D tumour models demonstrated a high sensitivity, which showed that anti-tumour function depends on CAR design. With this, they are suitable to distinguish optimally and suboptimally designed CAR T cells.

## 4.3 Effects of TME-aspects on ROR1 CAR T cells posed by implementation of TGF-β and CAF enrichment

Solid tumours present a variety of obstacles for immunotherapies, which is also indicated by the lack of results in the clinic. Among these barriers present in solid tumours are physiological barriers, indicated by a tight matrix and ECM-association mediated by stromal cells and immunological barriers posed by the secretion profile of the TME. These factors limit entry and efficacy of the CAR T cells and further reduce their ability to eradicate a tumour (Martinez & Moon, 2019; Mhaidly & Mechta-Grigoriou, 2020; Nazemi & Rainero, 2020).

In order to analyse if the hostile TME hindering CAR T cell efficacy *in vivo* can be recapitulated in the microphysiologic 3D tumour models, aspects of the TME were implemented and their effects on ROR1 CAR T cell efficacy were assessed in this work. Implementation of TME-aspects was performed by stromal enrichment with CAFs and supplementation with TGF-β.

Evaluation of effects mediated by TME-aspects on ROR1 CAR T cells encompasses modulation of TGF-β signalling and stromal enrichment represented by CAFs in semi-static and dynamic models. Furthermore, long-term treatment for 14 days in dynamic tumour models as well as an alternative route of CAR T cell application mimicking direct injection were assessed and improved gene-edited ROR1 CAR T cells were investigated. The latter are gene-edited CAR T cells with knock-outs of specific exhaustion-associated genes in order to reduce their susceptibility towards effects from the hostile TME that are present in solid tumours.

### 4.3.1 TGF-β-receptor inhibition augments ROR1 CAR T cell function

One key player in the context of TNBC is TGF-β, which can be secreted by stromal fibroblasts, macrophages, neutrophils, regulatory T cells, and platelets within the tumour tissue. This is especially important as TGF-β can strongly inhibit tumour-infiltrating T cells.

To address the question if inhibition of TGF-β can augment the efficacy of ROR1 CAR T cells microphysiologic 3D breast tumour models, containing the invasive MDA-MB-231 cell line, were used. To mediate TGF-β inhibition and to interfere with the TGF-β signalling, the highly selective and competitive TGF-β-receptor I kinase inhibitor SD-208 was chosen. It is easily orally bioavailable and could be proven safe and efficient for different tumour entities in the clinic (Uhl *et al.*, 2004).

Here, static microphysiologic 3D models containing the TNBC tumour cell line MDA-MB-231 were treated for 5 days with a dose of $1x10^5$ $CD8^+$- ROR1 CAR T cells. To study TGF-β-mediated influences on the CAR T cells 10 ng/ml TGF-β was administered. The effect should then be abrogated by addition of 1 µM SD-208.

BLI-based measurements (Fig 23 A) revealed strong tumour cell reduction in all groups treated with ROR1 CAR T cells except where TGF-β was applied. Quantification (Fig. 23 B) of those datasets revealed reduced tumour cell lysis in TGF-β-treated models with around 35 %. While SD-208 application alone led to 70 % specific lysis and untreated CAR T cells induced 65 % specific lysis. In addition, tumour cell apoptosis was measured using the M30 CytoDeath™ ELISA (Fig. S7). Here, no differences in apoptosis occurred between the groups or over time.

Analysis of the cytokines IFN-γ and IL-2, which indicate T cell activation, was normalised to untreated (w/o) CAR T cells and is shown as fold-increase (Fig. 23 C). This showed reduced secretion of both cytokines when TGF-β alone or the combination with SD-208 was administered. SD-208 alone led to an increase of IL-2 over the treatment period, which peaked at day 5. Additionally, PD-1 expression on the CAR T cells was analysed using flow cytometry (Fig. 23 D), indicating a higher proportion of PD-1⁺ cells when TGF-β was administered. Collectively, these results demonstrate that SD-208 can augment ROR1 CAR T cell function in microphysiologic 3D breast cancer models. Parts of the results have successfully been published in the "*Journal for Immunotherapy of Cancer"* (Stüber *et al.*, 2020).

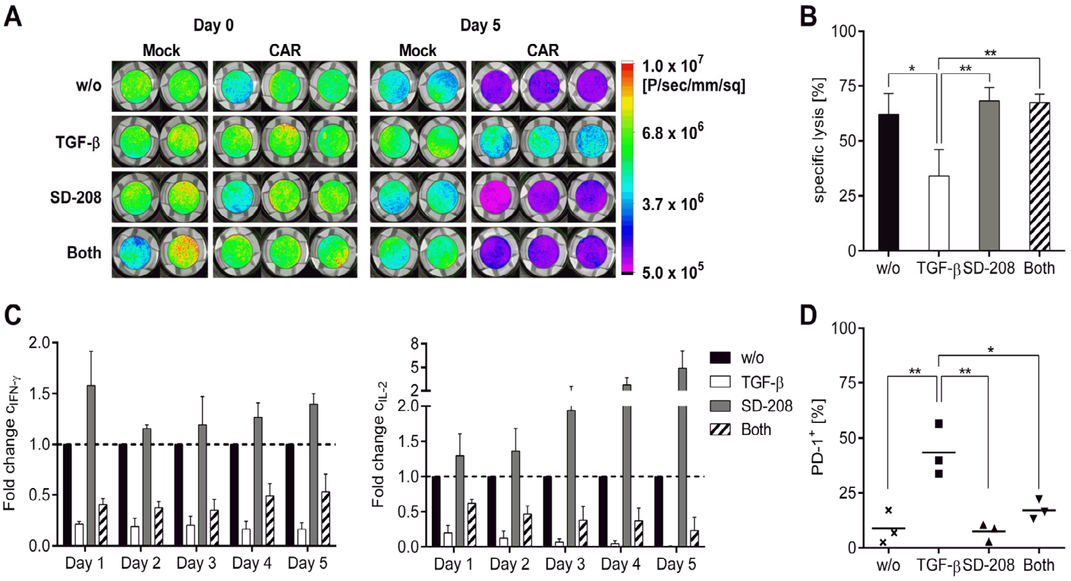

**Figure 23. Effects of TGF-β and the TGF-β receptor inhibitor SD-208 on specific lysis, cytokine secretion and PD-1 expression of $CD8^+$ ROR CAR T cells on static microphysiologic 3D TNBC models.**

Static models containing MDA-MB-231 tumour cells were treated for 5 days with $5 \times 10^5$ $CD8^+$ non-transduced control T cells (Mock) or ROR1 CAR T cells. Models were cultured either in standard cell specific medium or with additional 10 ng/ml TGF-β and/or 1 µM SD-208. (A): Images from BLI-based measurements show bioluminescence signals from viable tumour cells of different groups before CAR T cell administration (d0) and after end of treatment period (d5). A stronger signal was observed when TGF-β was present. Images for one representative T cell donor are shown. (B): Quantification of photon intensity over the model surface area revealed a reduction in tumour cell burden encompassing the entire surface of the cell crowns. Values were normalised to respective control groups containing Mock cells. Specific lysis was reduced when TGF-β was present. (C): IFN-γ and IL-2 concentrations were measured by ELISA from the supernatant at the indicated time points and compared to untreated T cells. Values are illustrated as fold change. TGF-β supplementation led to reduced cytokine secretion. (D): T cells were collected from the supernatant at day 5 and analysed for viability (7-Aminoactinomycin$^-$) and the surface marker CD45. From that, the proportion of PD-1$^+$ cells was calculated, which was increased in TGF-β-treated models. Data shown are mean values ± SD from three independent experiments with $^*p<0.05$, $^{**}p<0.01$, $^{***}p<0.001$, $^{****}p<0.0001$ by one-way analysis of variance, ns=not significant. Image adapted from (Stüber *et al.*, 2020).

### 4.3.2 Efficacy of ROR1 CAR T cells is retained in the presence of CAFs

The addition of TGF-β can represent effects of the TME and, therefore, reduced efficacy of ROR1 CAR T cells. To investigate effects of implemented CAFs and analyse possible immunosuppressive effects or the generation of a physical barrier on CAR T cell therapy, CAFs from human lung (tumour) and skin biopsies (see 4.1.4) were implemented to form organotypic stromal-enriched microphysiologic 3D lung tumour models. This should increase their predictive value due to higher *in vivo*-comparability. A549 lung tumour cells were combined with different fibroblasts, which were either isolated from skin biopsies or lung tissue. Here, A549 monocultures served as controls and were compared to co-cultures containing either hDFs, healthy hLFs or fibroblasts from a primary lung tumour tissue (primCAF) or a metastatic tumour site (metCAF) from the lung. To preserve the throughput, that is achieved by static culture, but also to increase tissue generation, semi-static cultures on an orbital shaker were prepared and treated for 5 days with ROR1 CAR T cells. $1 \times 10^5$ or $2 \times 10^5$ ROR1 CAR T cells were administered containing equal amounts of $CD4^+$ and $CD8^+$ cells. Non-transduced T cells served as control (NT) in addition to untreated controls (CTRL).

H&E staining (Fig. 24) indicated that A549 tumour cells grew in multiple layers on top of the matrix and within preserved crypt structure in the untreated groups as well as in the presence of control T cells. Only the metCAF containing co-culture (Fig. 24 Q) formed a more compressed structure with flattened villi. After 5 days of treatment with $1 \times 10^5$ CAR T cells, all groups (Fig. 24 C, G, K, O, S) showed reduced tumour cell numbers with abrogated tumour cell layers in top of the matrix. Tumour cell reduction was especially pronounced in the co-culture containing hDFs (Fig. 24 G) as this is the only group, where tumour cells within the crypt structures were eliminated by the lower CAR T cell concentration. When 2x10$^5$ ROR1 CAR T cells were administered for 5 days, more tumour cells were removed in equal amounts in all groups (Fig. 24 D, H, L, P, T). Here, cell clusters within crypt structures were also reduced. Again, the group containing hDFs showed an even stronger effect with no visible tumour cells left after treatment (Fig. 24 H).

To assess differences in tumour cell lysis quantitatively, BLI-based measurements were performed (Fig. 24 U). After 5 days of treatment with 1x10$^5$ ROR1 CAR T cells a specific lysis of 40-50 % (MC: 47 %; CC hLF: 47 %; CC primCAF: 45 %; CC metCAF: 54 %) was induced in all groups except for the co-culture containing hDFs, where it was higher with 62 %. When a concentration of 2x10$^5$ ROR1 CAR T cells was applied, around 80 % specific lysis occurred in all groups (MC: 85 %; CC hLF: 87 %; CC primCAF: 82 %; CC metCAF: 88 %), while again, the co-culture containing hDFs showed a slightly higher specific lysis with 93 %. Taken together, this shows that the fibroblasts used here did not inhibit ROR1 CAR T cell efficacy, but dermal fibroblasts showed a trend to enhance efficacy marginally.

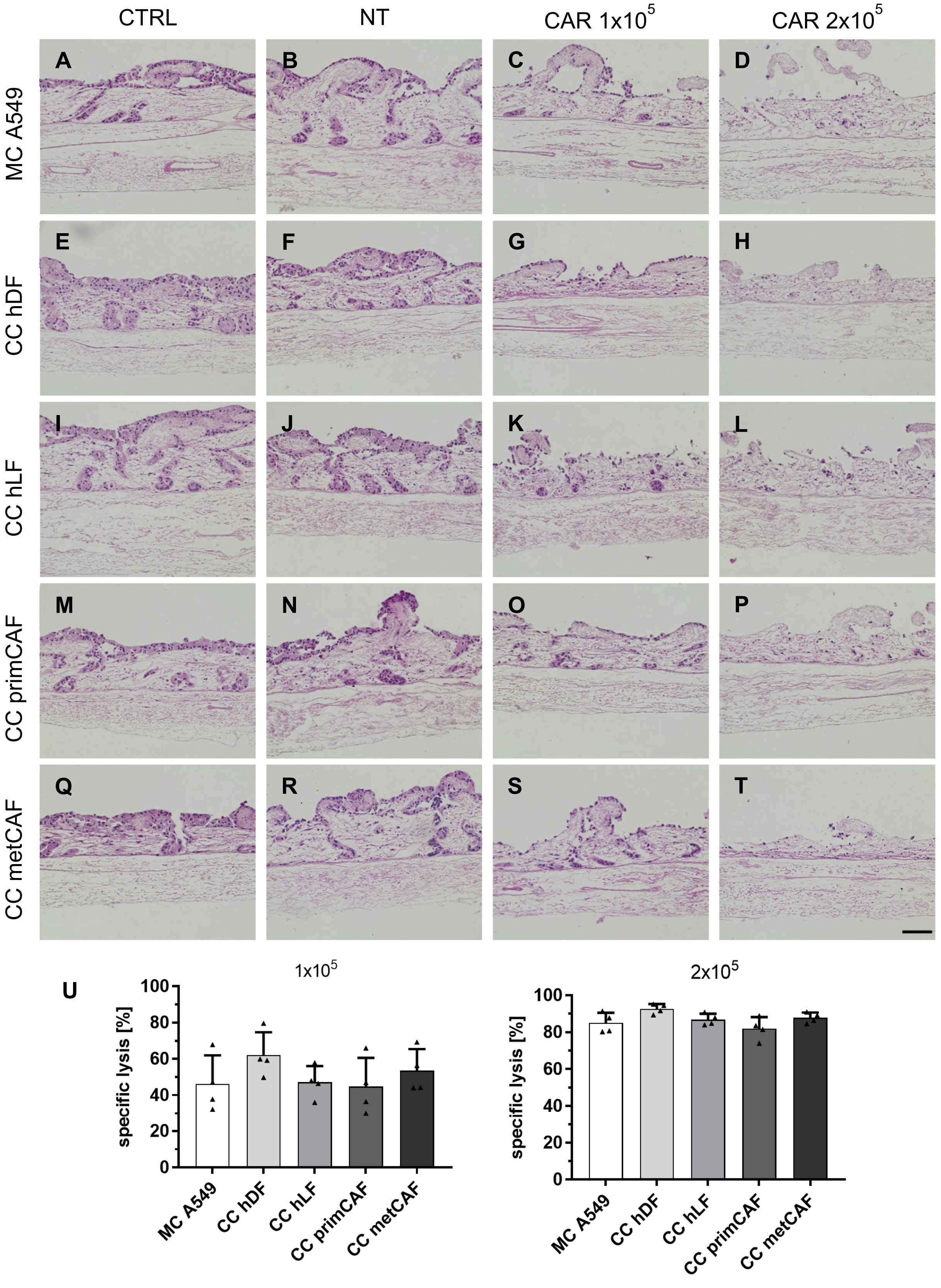
CTRL
NT
CAR 1x10^5
CAR 2x10^5
MC A549
CC hDF
CC hLF
CC primCAF
CC metCAF
A
B
C
D
E
F
G
H
I
J
K
L
M
N
O
P
Q
R
S
T
U
1x10^5
2x10^5
specific lysis [%]
0
20
40
60
80
100
MC A549
CC hDF
CC hLF
CC primCAF
CC metCAF

**Figure 24. Effect of ROR1 CAR T cells on different stromal-enriched semi-static microphysiologic 3D lung tumour models.**

A549 lung tumour cells were co-cultured together with different types of fibroblasts under semi-static conditions and treated for 5 days with either $1x10^5$ or $2x10^5$ (equal amounts $CD4^+$ and $CD8^+$) ROR1 CAR T cells or respective non-transduced control T cells (NT). Fibroblasts from different donor tissues were incorporated into the microphysiologic 3D lung tumour models from either human skin tissue (human dermal fibroblasts = hDF), human lung tissue (human lung fibroblasts = hLF), human lung tumour tissue from a primary tumour (primCAFs) or human lung tumour tissue from metastatic tumour (metCAFs). (A - T): H&E staining of formalin-fixed paraffin sections from stromal-enriched microphysiologic 3D tumour models. Tumour cells did not show altered cell morphology when cultured with different fibroblast types. CAR T cell efficacy was not changed by the presence of fibroblasts and led to reduction of tumour cells depending on administered CAR T cell concentration. Scale bar indicates 100 µm. Images from one representative T cell donor are shown. (U): Specific lysis calculated from BLI-based measurements is shown in percent, which was calculated to respective control T cells. Only models containing hDFs showed 10 % higher increase of specific lysis than the other co-cultures. Data shown are mean values ± SD from n=2 independent experiments. 2 T cell donors.

To further visualise tissue architecture and distinguish tumour cells from fibroblasts specifically, additional staining is needed. Therefore, immunofluorescence staining was performed with the epithelial marker PCK (green), indicating tumour cells, and the mesenchymal marker VIM (red), staining fibroblasts (Fig. 25). With this, it is also possible to investigate if fibroblasts get lost during ROR1 CAR T cell treatment. In the control groups, an organised tissue architecture became visible with larger $PCK^+$ tumour cell clusters on top of the matrix and within preserved crypt structures, while $VIM^+$ fibroblasts always grew in the submucosal part between the tumour cells. Co-cultures containing hLFs showed the lowest amount of fibroblasts (Fig. 25 I) within the control groups. However, CAFs derived from primary (Fig. 25 M) or metastatic (Fig. 25 Q) lung tumour or fibroblasts derived from skin tissue (Fig. 25 E) were present in large numbers and showed an *in vivo*-like tissue architecture (see Figure 26, right site). Staining of models treated with $1x10^5$ CAR T cells confirmed the results of the H&E staining as co-cultures containing hDFs (Fig. 25 G) did show reduced tumour cells especially in residing crypt structures, in contrast to all other groups after CAR T cell treatment. In addition, hLFs and metCAFs seemed to reduce in number (Fig. 25 K, S). The removal of nearly all tumour cells observed in the H&E staining (Fig. 24) also became visible when $2x10^5$ ROR1 CAR T cells were administered to co-cultures containing hDFs (Fig. 25 H). Fibroblast architecture and number stayed unaltered after treatment with $2x10^5$ ROR1 CAR T cells in all groups, except in co-cultures with hLFs, where the fibroblasts were reduced. Comparable amounts of tumour cells were removed by CAR T cell treatment in the monoculture (Fig. 25 D) as well as in the co-cultures containing, hLFs, primCAFs or metCAFs (Fig. 25 L, P, T).

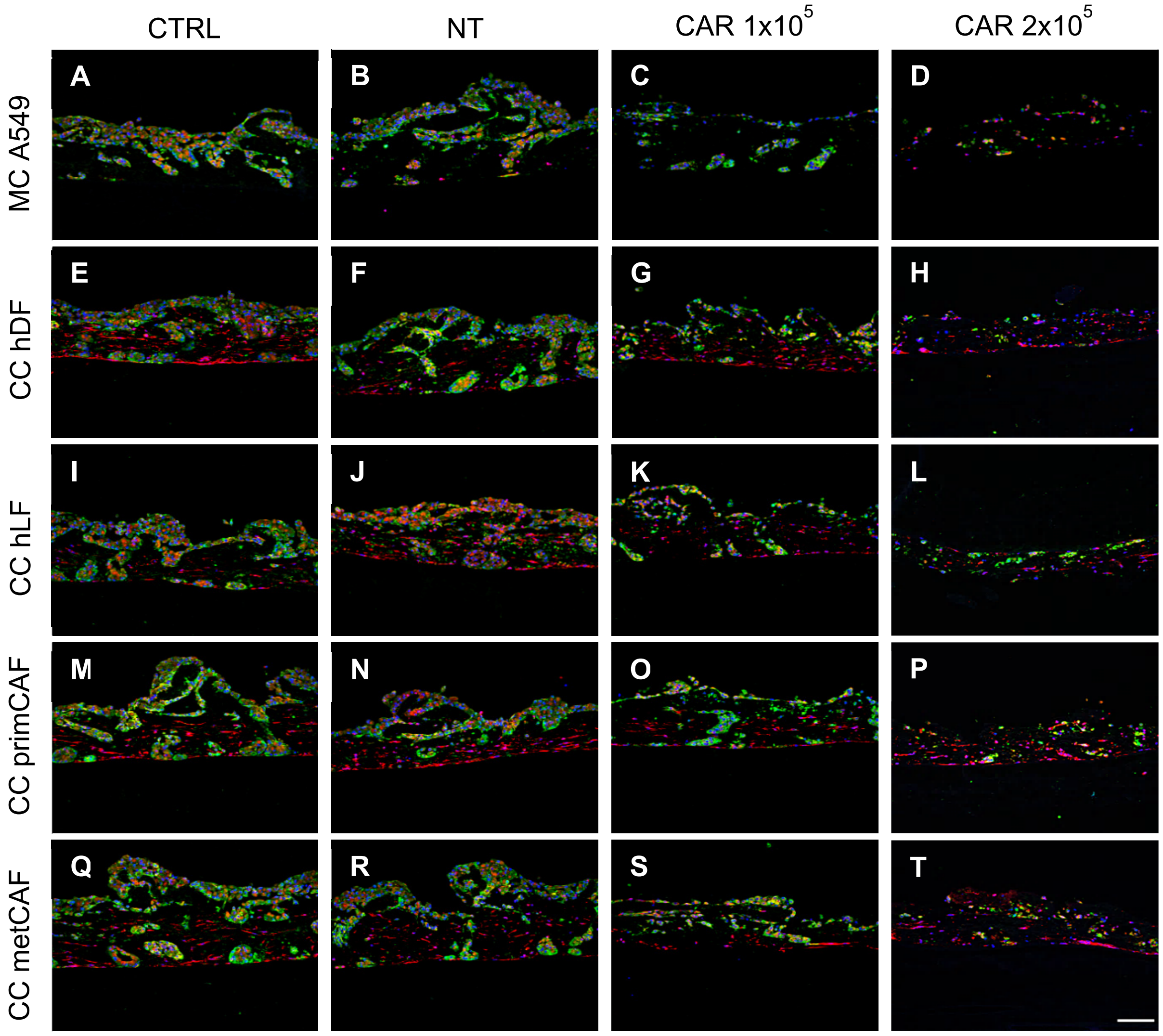

**Figure 25. Effect of ROR1 CAR T cells on stromal-enriched semi-static microphysiologic 3D lung tumour models.**

A549 lung tumour cells were co-cultured together with different types of fibroblasts under semi-static conditions and treated for 5 days with either 1x$10^5$ or 2x$10^5$ (equal amounts CD$4^+$ and CD$8^+$) ROR1 CAR T cells or respective non-transduced control T cells (NT). Fibroblasts from different donor tissues were incorporated into the microphysiologic 3D lung tumour models from either human skin tissue (human dermal fibroblasts = hDF), human lung tissue (human lung fibroblasts = hLF), human lung tumour tissue from a primary tumour (primCAFs) or human lung tumour tissue from metastatic tumour (metCAFs). (A - T): Immunofluorescence staining for the epithelial marker PCK (green) and the mesenchymal marker vimentin (red) of paraffin fixed sections. Tumour cells were positively stained with the epithelial marker PCK, while fibroblasts were positive for the mesenchymal marker vimentin. Fibroblasts always grew in the submucosal part of the SISmuc and did not seem largely affected by CAR T cell treatment. Nuclei are counterstained with DAPI (blue). Scale bar indicates 100 µm. Images from one representative T cell donor are shown. N=2.

Collectively, these results confirmed a successful establishment of semi-static stromal-enriched microphysiologic 3D lung tumour models suitable for ROR1 CAR T cell administration. Only stromal cells derived from healthy lung tissue and metCAFs were slightly diminished after treatment. However, ROR1 CAR T cells retained their anti-tumour function in the presence of implemented CAFs. Only implementation of stromal cells derived from skin biopsies showed a tendency to increase CAR T cell efficacy in this setting, which was not found to be statistically significant.

To further increase tissue generation and cell growth of stromal-enriched microphysiologic 3D lung tumour models, they can be cultured in an established bioreactor system. This can also help to analyse further, if implemented CAFs are reduced upon ROR1 CAR T cell administration. Dynamic culture has been shown to increase tumour cell mass significantly compared to static models. Furthermore, it includes additional stimuli to the cells like media flow, which also serves as an efficient way for waste removal. This culture condition also poses additional challenges to the CAR T cells, as they must actively migrate from the media flow to reach the tumour cells and to mediate specific killing. It also represents most accurately a common way of application in patients, as CAR T cells are mainly applied via intravenous infusion.

Therefore, CAFs from either a primary lung tumour site (primCAFs) or from a metastatic lung tumour site (metCAFs) were combined with A549 on the SISmuc to produce dynamic stromal-enriched microphysiologic 3D lung tumour models. These models were used to assess whether differences can be observed regarding ROR1 CAR T cell efficacy in the presence of CAFs when additional challenges are posed to the CAR T cells as presented in dynamic conditions.

Mature tumour models were established for 14 days under dynamic conditions and then treated with $10x10^6$ ROR1 CAR T cells (equal amounts $CD4^+$ & $CD8^+$) for 5 days. For control groups, models were either left untreated (CTRL) or the same number of control T cells (NT) was applied. To assess whether CAFs behave differently when isolated from lower or higher grade tumour, two sets of CAFs were used. Additionally, A549 monocultures were included and served as a control.

H&E staining showed that tumour models grew in an organised architecture and increasing cell masses were established in all untreated controls (Fig. 26 A, D, G). Tumour cells grew in large aggregates on top of the matrix and filled the conserved crypt structures of the SISmuc. Models with different fibroblasts showed comparable cell growth with stretched cells within the mucosal as well as the submucosal layer of the matrix, which indicates fibroblasts. When metCAFs (Fig. 26 G) were incorporated, they invaded the matrix stronger than primCAFs (Fig. 26 D). Control T cells did not reduce tumour cells in all groups (Fig. 26 B, E, H). ROR1 CAR T cell treated models (Fig. 26 C, F, I) showed equally disrupted tumour cell clusters and reduced tumour cells. In terms of tissue architecture, the stromal-enriched models appeared more comparable to a patient’s biopsy of a lung adenocarcinoma (Fig. 26 K). They showed large tumour cell clusters surrounded by stromal cells, while a healthy lung biopsy (Fig. 26 J) revealed smaller cell numbers and characteristic holes between the cells.

Immunofluorescence staining for the epithelial marker PCK (green) and the mesenchymal marker VIM (red) revealed the organisation of distinct cells on the matrix (Fig. 26 L - V). Tumour cells appeared in larger clusters with mainly PCK$^{+}$ cells, while VIM$^{+}$ fibroblasts grew throughout the membrane between the tumour cells. This was true for both fibroblast types. The immunofluorescence staining confirmed that control T cells did not reduce tumour cell numbers in all groups (Fig. 26 M, P, S). Furthermore, fibroblasts were not affected, neither by the control T cells nor by the ROR1 CAR T cells. All groups showed comparable amounts of VIM$^{+}$ cells. After 5 days of ROR1 CAR T cell treatment tumour cell clusters on top of the matrix were diminished, while those within crypt structures remained unaltered. This was observed for A549 monocultures (Fig. 26 N), co-culture with primCAFs (Fig. 26 Q), as well as co-cultures with metCAFs (Fig. 26 T), indicating no differences in tumour cell reduction in the presence of CAFs. A comparison of the stromal-enriched microphysiologic 3D lung tumour models to the patient biopsy of a lung adenocarcinoma (Fig. 26 V) and a healthy lung biopsy (Fig. 26 U) confirmed their organised tissue architecture and increased cell growth. The native tissue and the models showed distinct clusters of tumour cells (green) surrounded by stromal cells (red).

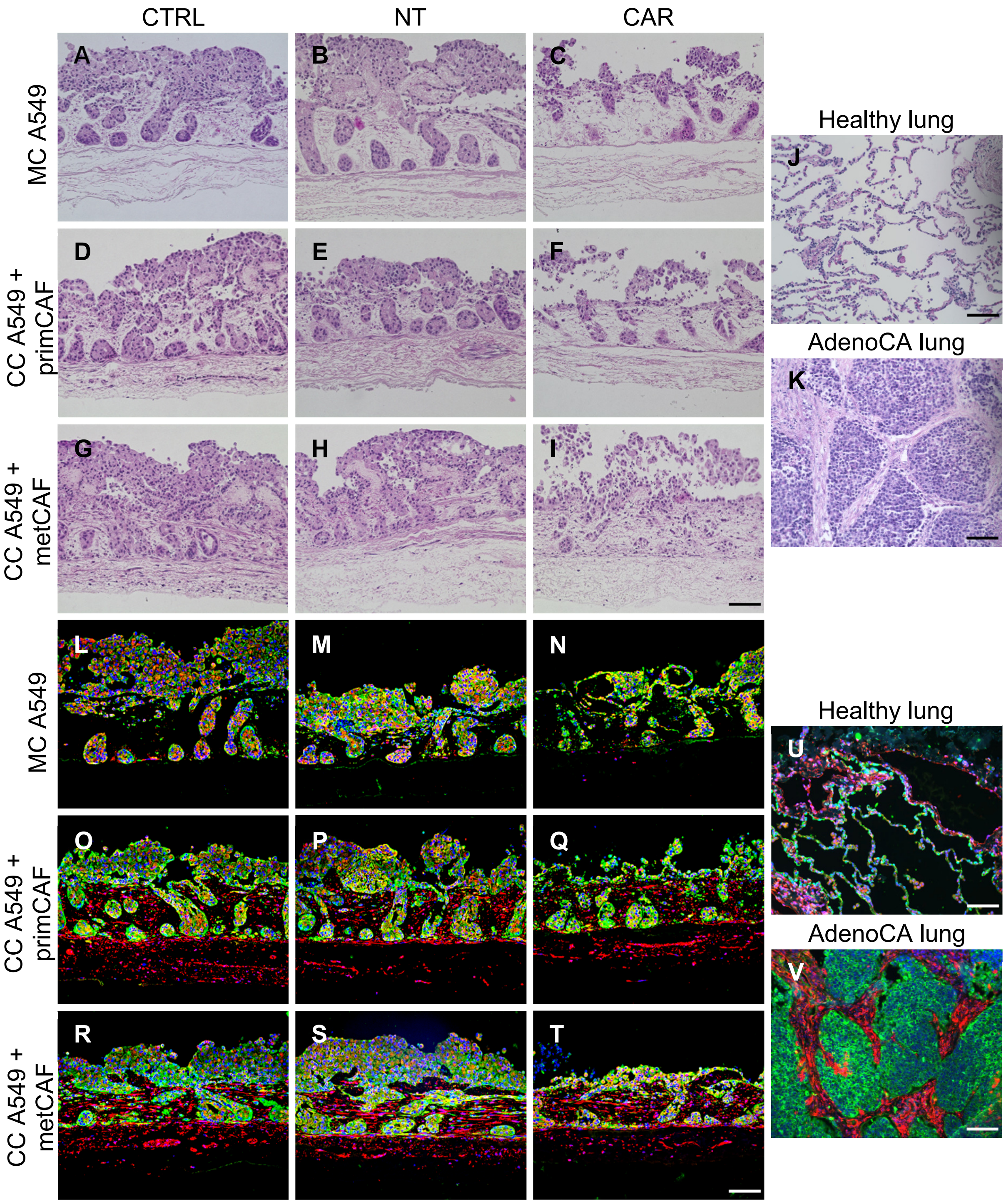
CTRL
NT
CAR
MC A549
CC A549 + primCAF
CC A549 + metCAF
A
B
C
D
E
F
G
H
I
Healthy lung
J
AdenoCA lung
K
MC A549
CC A549 + primCAF
CC A549 + metCAF
L
M
N
O
P
Q
R
S
T
Healthy lung
U
AdenoCA lung
V

**Figure 26. Effect of ROR1 CAR T cell therapy on CAF-enriched dynamic microphysiologic 3D lung tumour models.**

A549 lung tumour cells were co-cultured together with either primCAFs or metCAFs under dynamic conditions and treated for 5 days with $10 \times 10^6$ (equal amounts of $CD4^+$ and $CD8^+$) non-transduced control T cells (NT), ROR1 CAR T cells (CAR) or left untreated (CTRL). For comparison, respective architecture of native lung tissue is shown. (A - K): H&E staining of formalin-fixed paraffin sections of dynamic tumour models showed no cell reduction in control groups. Administration of CAR T cells led to disruption of tumour cell masses on top of the SISmuc matrix. Comparison to native tissue revealed relevant tissue architecture within dynamic tumour models. (L - V): Immunofluorescence staining of formalin-fixed paraffin section of dynamic tumour models against PCK (green) and vimentin (red). All samples revealed large $PCK^+$ tumour cell clusters on top of the matrix as well as filled crypt structures. $VIM^+$ cells were present, surrounding the filled crypts, indicating fibroblasts. In comparison to the native tissue, this revealed an *in vivo*-like organisation of the tumour models comparable to the native lung-adenocarcinoma. Nuclei are counterstained with DAPI (blue). Scale bars indicate 100 µm. Representative images from one T cell donor are shown. N=3. 3 T cell donors.

These results indicate that the stromal-enriched microphysiologic 3D lung tumour models with CAFs from lung tissue are able to generate an *in vivo*-comparable architecture when cultured under dynamic conditions. However, the tumour cell reduction did not vary between mono- and co-cultures when ROR1 CAR T cells were applied. Furthermore, reduction of fibroblasts upon CAR T cell administration, as it was partly observed in semi-static models, could not be confirmed.

To quantify efficacy of ROR1 CAR T cell-mediated killing, BLI-based measurements and M30 CytoDeath™ ELISA were performed (Fig. 27). Specific lysis did not indicate differences between mono- and co-cultures as all showed a specific lysis around 40 % (MC A549: 42 %; CC primCAF: 42 %; CC metCAF: 39 %). M30 CytoDeath™ ELISA measurements from the supernatant, obtained via a sampling port every 24 h during treatment time, did not show a strong increase in apoptosis over time. Only for the co-culture with primCAFs a significant increase of apoptosis was measured compared to monoculture on day 1 (5-fold increase to 3-fold increase) after CAR T cell administration. Co-cultures containing metCAFs showed a maximum of apoptosis on day 2 with 4-fold, which continuously decreased after that. Additionally, a decrease of apoptosis can be observed for all groups from day 3 to day 5.

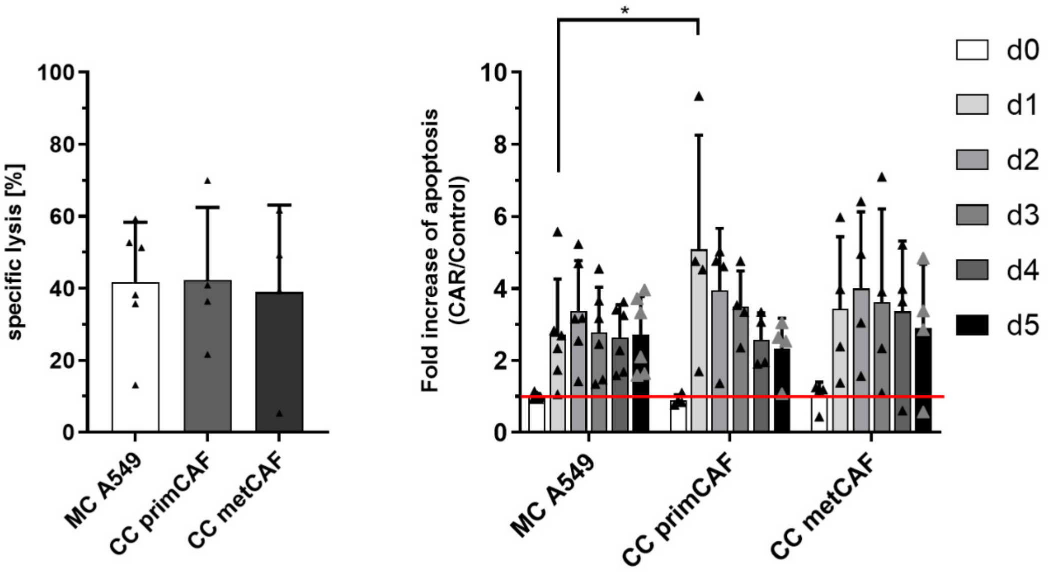

**Figure 27. Tumour cell apoptosis and specific lysis did not reveal immunosuppressive properties of stromal enrichment with cancer-associated fibroblasts.**

A549 lung tumour cells were co-cultured together with either primCAFs or metCAFs under dynamic conditions and treated for 5 days with 10x10$^6$ (equal amounts of CD4$^+$ and CD8$^+$) non-transduced control T cells (NT), ROR1 CAR T cells (CAR) or left untreated (CTRL). (A): Specific lysis was calculated from the tumour models using BLI-based measurements at the end of the 5 day-treatment period. No significant difference was measured between the mono- and co-cultures. (B): Apoptosis of epithelial tumours cells was analysed using the M30 CytoDeath™ ELISA at the indiacted time points. Samples were obtained every 24 h during treatment time via a port system. No significant difference occurred between the different groups, only presence of primCAFs induced significantly higher apoptosis compared to the MC at day 1. Data shown are mean values ± SD from 3 independent experiments with *p<0.05, **p<0.01, ***p<0.001, by one-way analysis of variance. 3 T cell donors.

As no significant reduction in specific lysis or tumour cell apoptosis was revealed in co-cultures compared to tumour cell monocultures, ROR1 CAR T cells seem to retain anti-tumour function in the presence of stromal enrichment with CAFs.

### 4.3.3 Alternative route of administration of ROR1 CAR T cells leads to strong anti-tumour efficacy

So far, influences on ROR1 CAR T cell treatment by implemented stromal components was not observed and tumour cell lysis was not affected by incorporated CAFs. Since one reason could be that the contact of tumour-, stromal- and CAR T cells was not optimal, a new approach was tested. Here, a Sandwich-co-culture model was established to increase tissue generation and proximity of the different cell types without the additional difficulties and limited throughput of a bioreactor culture. Additionally, CAR T cells could be injected directly into the models, presenting direct application into tumour tissue as an alternative application route. Intratumoural application of CAR T cells into solid tumours could overcome limited trafficking of CAR T cells to tumour sites and increase efficacy. This strategy is also currently assessed in clinical trials for several solid malignancies (Khan *et al.*, 2019). Therefore, models were used to analyse whether direct injection of CAR T cells would lead to increased efficacy or stronger influence of stromal enrichment.

To establish these models, semi-static stromal-enriched microphysiologic 3D tumour models containing either TNBC (MDA-MB-231) or lung tumour (A549) cells together with metCAFs were combined after tissue maturation and ROR1 CAR T cells were injected.

H&E staining (Fig. 28) of the Sandwich-models show the generated tissues. To perform intratumoural injection, the CAR T cells were applied via injection in 200 µl cell specific medium into the gap between both combined models. To assess whether the injection process itself would damage the models either no injection was performed (CTRL) or cell specific media was injected (Media). For CAR T cell treatment, either 2x10$^5$ non-transduced control T cells (NT) or ROR1 CAR T cells (CAR) were injected. Here, equal amounts of CD4$^+$ and CD8$^+$ ROR1 CAR T cells were administered. Untreated controls showed a strong cell association with a dense and compact structure (Fig 28 A & E). This was also true for the media injection (Fig. 28 B & F). In general, models containing MDA-MB-231 cells were less compact to models with A549 cells. When control T cells were applied, a slight cell reduction A549 (Fig. 28 G) occurred, which was not observed in the MDA-MB-231 (Fig. 28 C) models. CAR T cell administration reduced the cell number drastically for A549 (Fig. 28 H) and MDA-MB-231 (Fig. 28 D) models. Here, MDA-MB-231 cells showed a reduction especially on top of the mucosal layer, while cells closer to the border between mucosal and submucosal layer were still present and tightly associated. A549 models revealed a strong cell reduction throughout the submucosal layer, while cell clusters in the crypt structures were preserved. For a quantification of CAR T cell efficacy, BLI-based measurements were performed (Fig. 28 I). Here, cell reduction is indicated on the left and specific tumour cell lysis on the right site. Both revealed a stronger effect on A549 cells with 68 % of tumour cell reduction and 52 % of specific lysis, compared to MDA-MB-231 cells with a cell reduction of 42 % and a specific tumour cell lysis of 40 % when 2x10$^5$ ROR1 CAR T cells were injected.

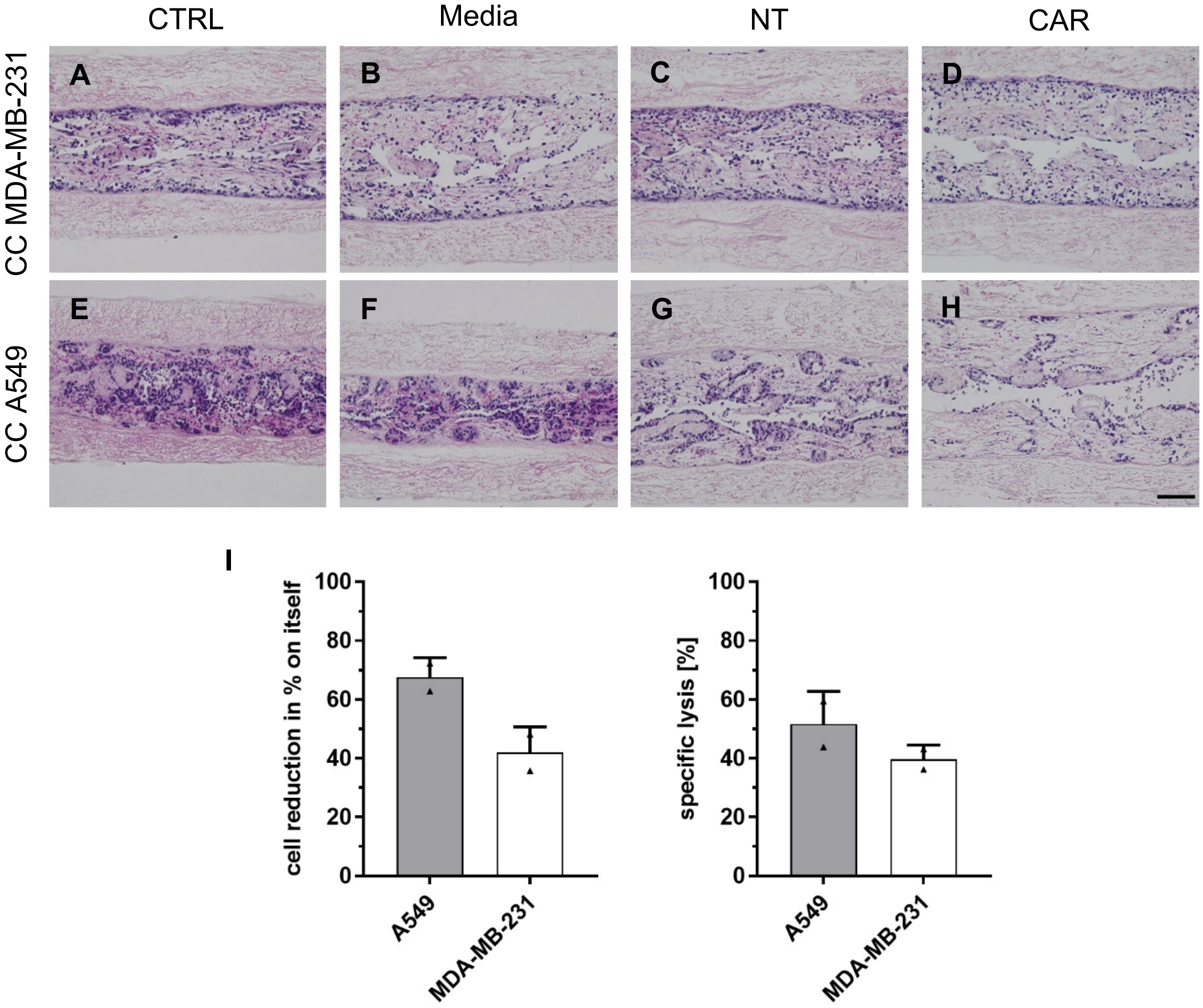

**Figure 28. Effect of injected ROR1 CAR T cells into CAF-enriched microphysiologic 3D Sandwich-models containing MDA-MB-231 or A549 tumour cells.**

Stromal-enriched Sandwich-models containing indicated tumour cells together with metCAFs were cultured under semi-static conditions and treated for 3 days with $2x10^5$ (equal amounts $CD4^+$ and $CD8^+$) non-transduced control T cells (NT), ROR1 CAR T cells (CAR), left untreated (CTRL) or only assay-specific media was injected (Media). Treatment was applied via injection of the T cells in 200 µl into the cleft between the models. (A - H): H&E staining of formalin-fixed paraffin sections of microphysiologic 3D Sandwich tumour models. CAR T cell treatment reduced tumour cell burden in breast and lung tumour models equally, while the injection process did not damage model integrity Scale bars indicate 100 µm. (I): Cell reduction and specific lysis calculated from BLI-based measurements is shown in percent. Tumour cell burden was stronger reduced in A549 models compared to MDA-MB-231 models. Data shown are mean values ± SD from two cell crowns. n=1. 1 T cell donor.

With this, a fourth way to culture the microphysiologic 3D tumour models was established, generating tightly associated stromal-enriched microphysiologic 3D tumour models for lung and breast cancer. Additionally, it was possible to represent intratumoural application of CAR T cells to solid tumours as alternative route of application.

### 4.3.4 ROR1 CAR T cells mediate anti-tumour efficacy during long-term application *in vitro*

The previous findings indicate that treatment with ROR1 CAR T cells is effective in microphysiologic 3D lung tumour models regardless of stromal enrichment. However, a substantial tumour cell mass stayed present on the SISmuc and was not removed within the treatment time of 5 days. To assess if a longer time of ROR1 CAR T cell application would improve tumour cell killing, dynamic models containing A549 lung tumour cells were established. Here, $10x10^6$ (equal parts $CD4^+$ and $CD8^+$) ROR1 CAR T cells were administered for 14 days after model maturation under dynamic conditions.

H&E staining (Fig. 29) of lung tumour models revealed the distinct tumour cell clusters on top of the SISmuc with seeded crypt structures (Fig. 29 A - F). Here, only control T cells (NT) or ROR1 CAR T cells (CAR) were administered. Control T cells (Fig. 29 A - C) did not reduce tumour cells compared to CAR T cells (Fig. 29 D - F). More tumour cells were removed by the ROR1 CAR T cells after 9 days of treatment (Fig. 29 E) compared to 4 days of treatment (Fig. 29 D). After 14 days of CAR T cell treatment, a comparable amount of tumour cells was left as after 9 days of treatment. However, some tumour cells invaded deeper into the matrix structure, as indicated by black arrows (Fig. 29 F). Furthermore, the models were more compact after 14 days of CAR T cell treatment, which was not observed in the respective control.

Immunofluorescence staining for PCK (green) and VIM (red) confirmed model structure and tissue architecture, as well as a compacter model structure after 14 days of treatment

(Fig. 29 G - L). Models receiving control T cells did not show tumour cell reduction, while CAR T cell treatment reduced tumour cell clusters mainly until day 4 (Fig. 29 J). Only minor changes occurred between day 9 (Fig. 29 K) and 14 (Fig. 29 L) of CAR T cell treatment. Again, tumour cells revealed invasive growth throughout the matrix, which was not as pronounced as in the H&E staining, as PCK showed a high background staining.

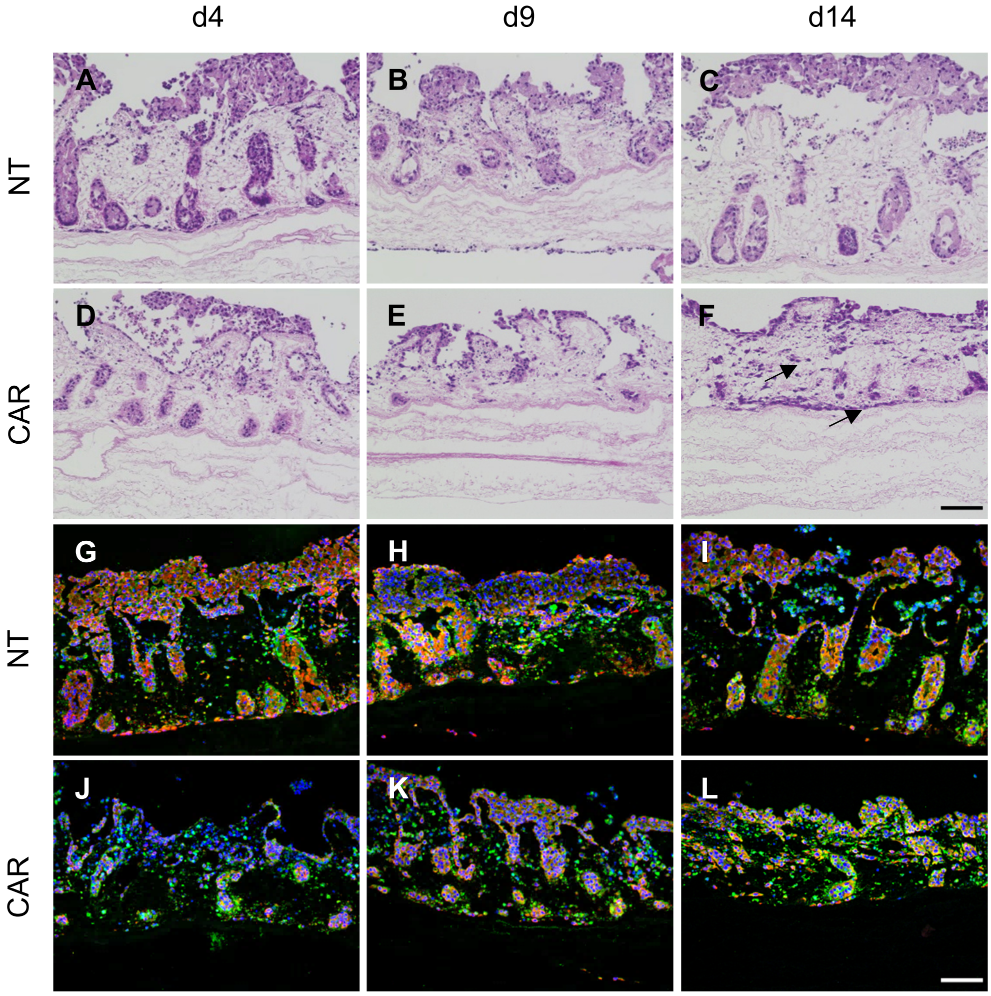

**Figure 29. Effect of long-term treatment with ROR1 CAR T cells on dynamic microphysiologic 3D lung tumour models containing A549 cells.**

Tumour models containing A549 cells were cultured under dynamic conditions and treated for 4, 9 or 14 days with $10x10^6$ (equal amounts of $CD4^+$ and $CD8^+$) non-transduced control T cells (NT) or $ROR1^+$ CAR T cells (CAR). (A - F): H&E staining of formalin-fixed paraffin sections of respective models showed no tumour cell disruption in control groups and a reduced cell mass in treated groups. After 14 days of treatment tumour cells showed invasive growth indicated by black arrows. (G - L): Immunofluorescence staining of formalin-fixed paraffin sections of respective models against Pan-cytokeratin (green) and vimentin (red) revealed large $PCK^+$ tumour cell clusters on top of the matrix as well as in filled crypt structures. Nuclei are counterstained with DAPI (blue). Scale bars indicate 100 µm. Representative images from 1 T cell donor are shown. N=1.

After treatment for up to 14 days, tumour cells remained on top of the matrix and in residing crypt structures. This raised the question if those remaining cells were altered by the administered treatment and specifically long-term culture. One way tumour cells can escape treatment is the loss of the targeted antigen, in this case ROR1. To assess this, ROR1 was stained via immunofluorescence (data not shown). However, ROR1 was difficult to visualise and only an indistinct staining was observed.

Furthermore, cancer stem cells (CSCs) are discussed to resist treatment and later induce metastasis or relapse. Here, CD44 was described in other studies for CSCs in lung cancer (Su *et al.*, 2016; Zhou *et al.*, 2021). To investigate whether the A549 cells in the microphysiologic 3D lung tumour models have traits of CSCs and if changes in proliferation occurred, the cancer stem cell marker CD44 and the proliferation marker Ki67 were investigated.

CD44 was homogenously expressed in all A549 cells after 4 days when control T cells were administered (Fig. 30 A). After 9 and 14 days (Fig. 30 B & C) homogenous expression mainly shifted to tumour cell clusters deep in the crypt structures or into larger cell masses on top of the membrane, while the rest only showed indistinct signals. The same pattern became visible in models after 4 and 9 days of ROR1 CAR T cell treatment (Fig. 30 D & E), where even more tumour cells showed inhomogeneous CD44 staining in residing crypt structures compared to the control. However, after 14 days of CAR T cell treatment, invading tumour cells became positive for CD44 (Fig. 30 F) and a homogenous CD44 expression occurred again in all tumour cells. To highlight this difference between control and CAR T cells, magnified images are shown on the right site. Here, the strong and homogenous CD44 staining is present in larger areas of the ROR1 CAR T cell treated model and in fewer areas in the control.

In addition to stem cell markers, the proliferation marker Ki67 was stained (Fig. 30 G - L). Models treated with control T cells only showed Ki67 expression in few cells (Fig. 30 G - I). The same was true for the ROR1 CAR T cell treated models after 4 and 9 days of treatment (Fig. 30 J & K). However, treatment with ROR1 CAR T cells for 14 days induced expression of Ki67 in a larger number of A549 tumour cells. To underline this difference, magnified images are shown on the right from the 14-day control and CAR T cell treated model.

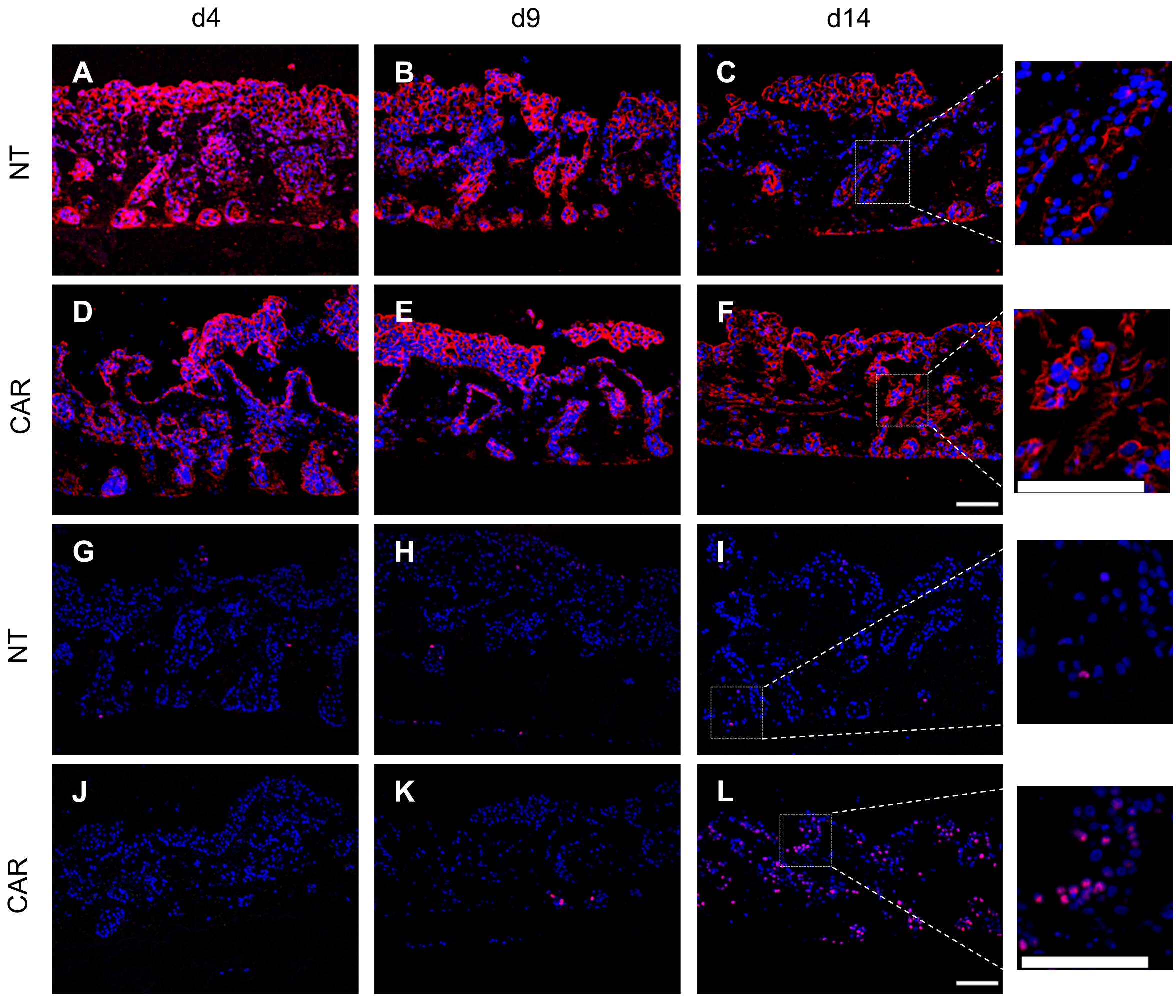

**Figure 30. Effects on stem cell marker expression and proliferation in dynamic microphysiologic 3D lung tumour models after long-term treatment with ROR1 CAR T cells.**

Tumour models containing A549 cells were cultured under dynamic conditions and treated for 4, 9 or 14 days with $10x10^6$ (equal amounts of $CD4^+$ and $CD8^+$) non-transduced control T cells (NT) or $ROR1^+$ CAR T cells (CAR). (A - F): Immunofluorescence staining of formalin-fixed paraffin sections of respective models against the tumour stem cell marker CD44 (red) revealed homogenous expression after 14 days of ROR1 CAR T cell culture in invasive cells. (G - L): Immunofluorescence of the proliferation marker Ki67 (magenta) indicated that the amount of $KI67^+$ cells increased when treated for 14 days with ROR1 CAR T cells. Nuclei are counterstained with DAPI (blue). Scale bars indicate 100 µm. Representative images from 1 T cell donor are shown. N=1.

Collectively, these findings indicate that long-term treatment of two weeks with ROR1 CAR T cells did not reduce tumour cell burden of the microphysiologic 3D lung tumour models further compared to shorter treatment periods. However, it led to invasive tumour cells, confirmed by H&E staining, which was supported by stainings of distinct mesenchymal and epithelial markers, as well as a homogenous CD44 expression. Additionally, prolonged CAR T cell treatment induced tumour cell proliferation, which was not observed when control T cells were applied for the same duration of time.

### 4.3.5 Improved gene-edited ROR1 CAR T cells lacking PD-1 and TGF-β receptor induce superior anti-tumour efficacy in the presence of TGF-β and CAF enrichment in microphysiologic 3D breast tumour models

The previous experiments indicate that immunosuppressive effects can be induced by the addition of TGF-β to the microphysiologic 3D tumour models. However, implementation of CAFs could not reduce ROR1 CAR T cell efficacy in lung tumour models. Therefore, the effects of TGF-β were combined with CAF enrichment in the following experiments to assess if this combination reflects additional immunomodulatory aspects of the TME. Here, metCAFs described in 4.1.4 were incorporated into tumour models containing TNBC cells (MDA-MB-231) to achieve stromal enrichment. The TNBC cell line MDA-MB-231 used here grows more invasively on the SISmuc, therefore, represents a more advanced tumour stage. This increases the challenge towards applied CAR T cells, because the target cells are not as accessible as in lung tumour models with A549 cells. This could also change the influence of the implemented CAFs on CAR T cell therapy because the stromal cells might associate differently. Furthermore, phenotypic analysis of CAFs in CC with MDA-MB-231 cells revealed association with immunomodulatory and inflammatory effects respectively. The preceding data also demonstrates that conventional ROR1 CAR T cells are unable to remove all tumour cells from the microphysiologic 3D models independent of stromal enrichment.

To overcome immunomodulatory effects of TGF-β and to improve CAR T cell efficacy, different gene-edited ROR1 CAR T cells were used for the following experiments. These CAR T cells were genetically edited to include knock-outs (KO) of the genes for PD-1 or the TGF-β receptor. Additionally, a ROR1 CAR T cell was edited to lack both receptors. These KO ROR1 CAR T cells were designed, produced and kindly provided by Dr Razieh Monjezi. The genetic alterations should make the CAR T cells less susceptible for immunosuppression posed by CAFs and tumour cells and by supplemented TGF-β.

To test whether the different gene-edited ROR1 CAR T cells differ in their anti-tumour effects, semi-static stromal-enriched microphysiologic 3D breast tumour models were established and treated with $5 \times 10^4$ ROR1 CAR T cells (equal amounts $CD4^+$ and $CD8^+$) for 7 days. Different gene-edited ROR1 CAR T cells are termed as follows: wild type=ROR1 CAR T cell without gene knock-outs = WT, PD-1 KO = PKO, TGF-β receptor KO = TKO and KO of both genes is termed DKO. As control, models were left untreated (CTRL) or non-transduced control T cells were applied (Mock). Cell specific medium was supplemented with 10 ng/ml of TGF-β.

Images of the BLI-based measurements (Fig. 31 A) indicated a reduction of tumour cells for all different gene-edited ROR1 CAR T cells, but the group treated with WT CAR T cells showed higher signal intensity indicating more remaining tumour cells, and TKO as well as DKO revealed increased, but comparable tumour cell reduction. Quantification of those images and calculation of specific lysis (Fig. 31 B) confirmed tumour cell lysis within all CAR T cell treated groups, with around 40 to 50 % specific lysis after 3 days (WT: 43 %; PKO: 40 %; TKO: 53 %; DKO: 55 %). After 5 days of treatment, the groups receiving TKO and DKO CAR T cells showed a significant increase in specific lysis up to 58 % for TKO and 61 % for DKO, while WT and PKO did not reveal any increase compared to day 3. A similar trend became visible after 7 days of ROR1 CAR T cell application, where WT and PKO treated models still revealed a lysis of 41 % and 43 %, while TKO and DKO treated models induced an increase of specific lysis up to 62 % for TKO and up to 69 % for DKO, which was statistically significant.

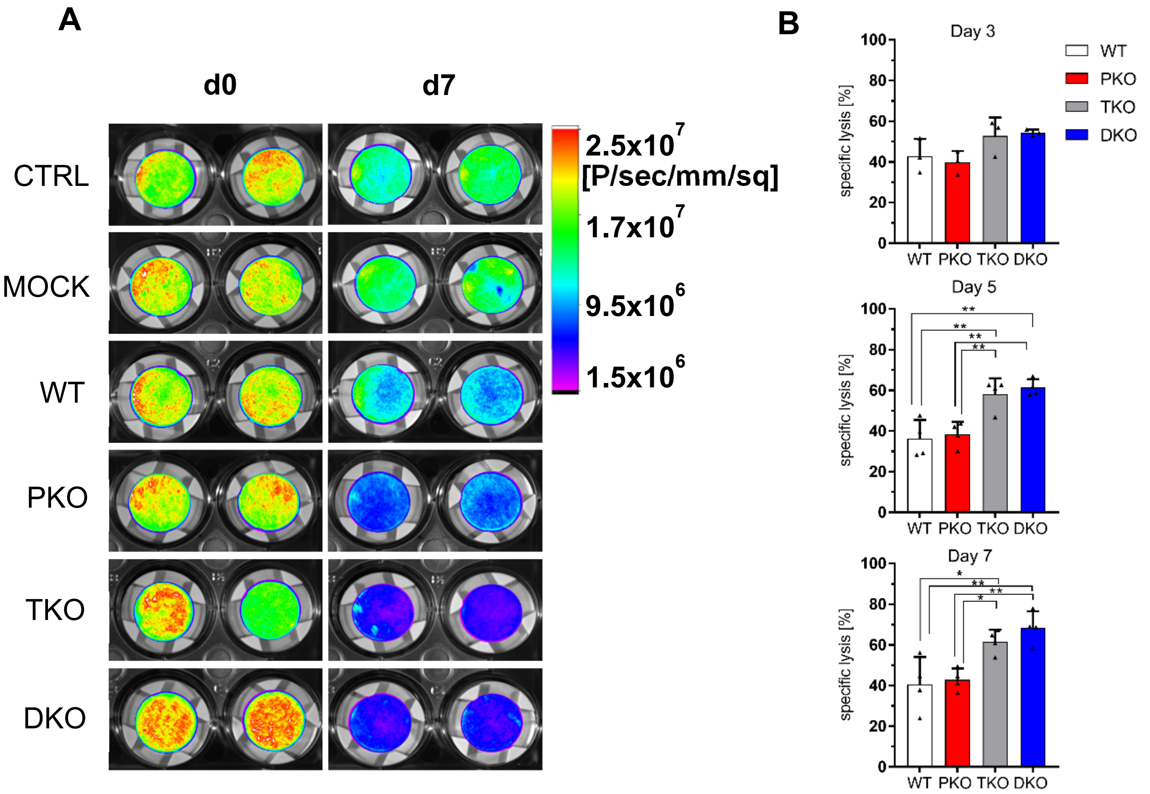

**Figure 31. Gene-edited ROR1 CAR T cells lacking TGF-β receptor and PD-1 mediate increased tumour cell lysis in invasive stromal-enriched microphysiologic 3D tumour models visualised by BLI-based imaging.**

Tumour models contained MDA-MB-231 breast cancer cells together with primCAFs and were cultured under semi-static conditions. On day 10, $5x10^4$ (equal amounts $CD4^+$ and $CD8^+$) different ROR1 CAR T cells were applied for 7 days. Models received either non-transduced control T cells (MOCK) or different gene-edited ROR1 CAR T cells (CAR) or were left untreated (CTRL). Different gene-edited ROR1 CAR T cells are termed as follows: (WT) wild type=ROR1 CAR T cell without gene knock-out (KO), (PKO) PD-1 KO, (TKO) TGF-β receptor KO, (DKO) KO of PD-1 KO and TGF-β receptor KO. Medium was supplemented with 10 ng/ml TGF-β. (A): Luminescence was measured encompassing the entire model surface. Images depicting the bioluminescence signal from viable tumour cells on day 0 and day 7 for one representative T cell donor. Scale indicates $P/s/mm^2$ (Photon intensity). Images for one representative T cell donor are shown. TKO and DKO show strongest signal reduction amongst all groups. (B): Reduction in tumour cell burden based on the bioluminescence signal encompassing the entire surface of the model normalised to the signal of mock cells. TKO and DKO induced increased specific lysis especially after 7 days of treatment time. Data shown are mean values ± SD from four independent experiments with $^*p<0.05$, $^{**}p<0.01$, $^{***}p<0.001$, $^{****}p<0.0001$ by one-way analysis of variance, ns=not significant. 4 T cell donors.

To assess differences in ROR1 CAR T cell invasion and number within the treated tumour models, immunofluorescence staining for the leukocyte marker CD45 (green) and the matrix specific marker collagen IV (red) was performed. Furthermore, immunofluorescence images were quantified either counting $DAPI^+$ cells to reveal differences in cell number or counting $CD45^+$ cells to investigate differences in T cell invasion and activation amongst the different gene-edited ROR1 CAR T cells.

Images (Fig. S9 A) revealed $CD45^+$ CAR T cells in all groups. Furthermore, CAR T cells were active, which was evaluated by their stretched and enlarged morphology. To emphasise this, magnified images are shown below, white arrows indicating $CD45^+$ CAR T cells. Quantification of $DAPI^+$ cells (Fig. S9 B) revealed no significant variations of general cell number on the tumour models between the different gene-edited CAR T cells, but Mock-treated models showed a slight increase in $DAPI^+$ cells. Counting of $CD45^+$ compared to the total cell number (Fig. 32 A) indicated that a higher percentage of CAR T cells was present in the groups treated with TKO (9 %) or DKO (8 %) CAR T cells compared to WT (7 %) and PKO (5 %). Even though, these differences were not statistically significant they indicate the potency of the administered gene-edited ROR1 CAR T cells. Many active T cells migrated and invaded deep into the tumour tissue even at the low administered cell number of 50.000 CAR T cells per tumour model.

To assess activation of the different gene-edited ROR1 CAR T cells during treatment, PD-1 expression was evaluated at the end of treatment via flow cytometry (Fig. 32 B). As TGF-β is described to have a stronger effect on resting $CD8^+$ T cells, $CD4^+$ and $CD8^+$ CAR T cells were evaluated separately. $CD8^+$ ROR1 CAR T cells from WT and TKO were found to have a significantly higher percentage of PD-1⁺, with 46 % in the WT and 30 % in the TKO cells compared to 4 % in PKO and 3 % in DKO. However, a comparable pattern was found in the CD4⁺ subset. Here, 89 % of WT CAR T cells were positive for PD-1 and 55 % of TKO CAR T cells. In the groups containing PKO and DKO CAR T cells, only 12 % were found to express PD-1 for PKO and 10 % for DKO, which was also found to be statistically significant.

In addition, the activating cytokines IFN-γ, IL-2, TNF-α and IL-4 were measured by ELISA. Therefore, supernatant was sampled during the treatment period and is depicted for day 3 and day 7 (Fig. 32 C & D). Here, TKO and DKO CAR T cells showed significantly higher secretion of IFN-γ, IL-2, and TNF-α and IL-4 after 3 days. This was also true after 7 days of treatment within the stromal-enriched microphysiologic 3D breast tumour models. TKO and DKO ROR1 CAR T cells secreted significantly higher amount of IFN-α and IL-4. DKO ROR1 CAR T cells also secreted significantly higher amounts of TNF-α. However, secretion of IL-2 was strongly reduced in all groups after 7 days in the tumour models.

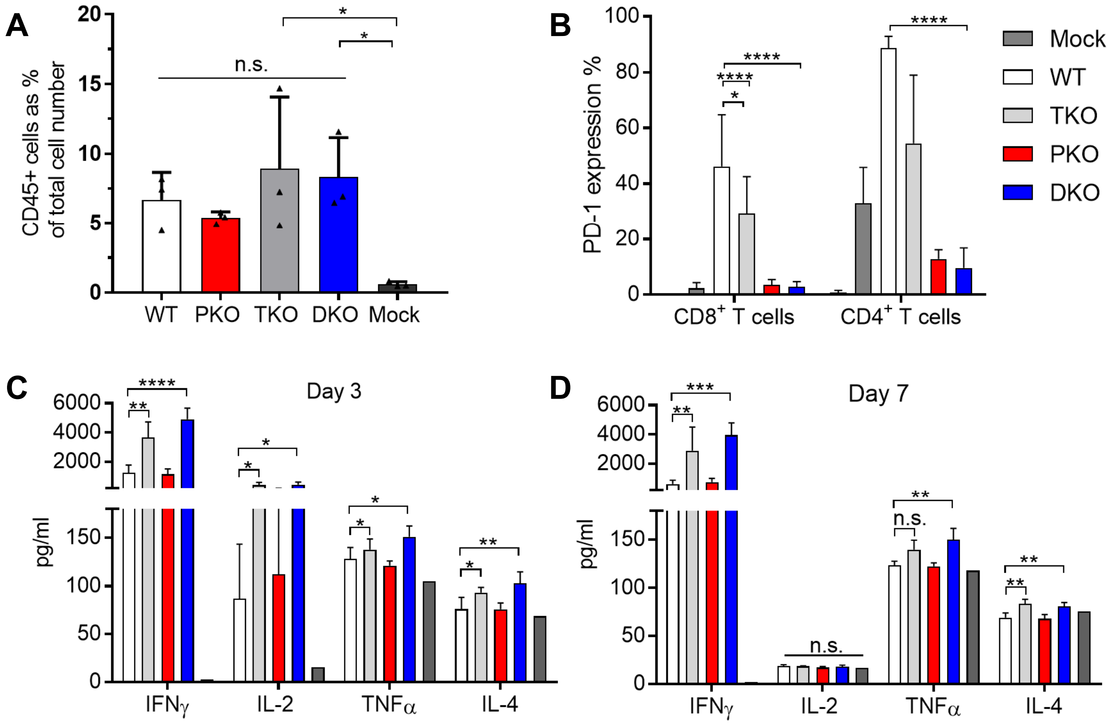

**Figure 32. Cytokine secretion of different gene-edited ROR1 CAR T cells after encountering CAF-enriched microphysiologic 3D breast tumour models for 3 to 7 days.**

Tumour models contained MDA-MB-231 breast cancer cells together with primCAFs and were cultured under semi-static conditions. On day 10, $5x10^4$ (equal amounts $CD4^+$ and $CD8^+$) different ROR1 CAR T cells were applied for 7 days. Models received either non-transduced control T cells (MOCK) or different gene-edited ROR1 CAR T cells (CAR) or were left untreated (CTRL). Different gene-edited ROR1 CAR T cells are termed as follows: (WT) wild type=ROR1 CAR T cell without gene knock-out, (PKO) PD-1 KO, (TKO) TGF-β receptor KO, (DKO) KO of PD-1 KO and TGF-β receptor KO. Media was supplemented with 10 ng/ml TGF-β (A): ELISA-based analysis of the activating cytokines interferon (IFN-γ) and interleukin 2 (IL-2), tumour necrosis factor-alpha (TNF-α) and interleukin 4 (IL-4) in cell supernatant at indicated time points. Concentrations are shown as fold-increase to mock control T cells. DKO ROR1 CAR T cells revealed significant higher amounts of IFNγ, TNFα and IL-4. (B): Proportion of $PD\text{-}1^+$ cells from living (7-Aminoactinomycin$^-$) and $CD45^+$ cells collected from the supernatant on day 7. Data shown are mean values ± SD from four independent experiments with $^*p<0.05$, $^{**}p<0.01$, $^{***}p<0.001$, $^{****}p<0.0001$ by one-way analysis of variance, ns=not significant. 4 T cell donors.

Consequently, it was shown that ROR1 CAR T cells without TGF-β receptor and PD-1 remain efficient after encountering a microphysiologic 3D TNBC cancer model for 7 days, which included immunosuppressive effects of TGF-β and CAF enrichment. Lack of either PD-1 or TGF-β receptor already improved CAR T cell function compared to WT ROR1 CAR T cells.

### *Interim Summary*

In order to assess important TME-aspects, which can impair CAR T cell therapy in solid tumours different approaches were studied in microphysiologic 3D tumour models with regard to the physical and immunological barrier of the TME to evaluate if this increases the predictive value of the models. Application of different approaches revealed that CAF enrichment alone did not impair ROR CAR T cell function in semi-static and dynamic culture of lung tumour models. Additionally, long-term treatment of ROR1 CAR T cells for 14 days did not improve therapy outcome in dynamic lung tumour models. However, microphysiologic 3D tumour models could present an alternative application route as a proof-of-principle in a sandwich-model, which allowed direct injection into the tumour tissue. Pharmacological intervention of immunosuppressive effects posed by TGF-β showed that the TGF-β-receptor inhibitor SD-208 augmented ROR1 CAR T cell efficacy. Combination of CAF enrichment and immunosuppressive effects represented by TGF-β administration revealed that gene-editing of exhaustion-associated genes led to an improved ROR1 CAR T cell product. Especially, lack of the PD-1 gene and the TGF-β-receptor gene together improved ROR1 CAR T cell efficacy and shielded them against effects from the hostile TME, partly reflected here by TGF-β and CAF enrichment.

# 5. Discussion

In the present work, defined microphysiologic 3D *in vitro* models for solid tumours were improved and characterised to apply them for the evaluation of cellular immunotherapies. This encompasses advances with regard to: (i) throughput and homeostasis (ii) entities (iii) TME-aspects (iv) BLI-based analysis comparable to animal studies, and (v) bioreactors, in order to offer preclinical testing with increased predictive value for cellular immunotherapies.

These aspects address the need for advanced tumour models, which can improve the high attrition rates that occur during drug development, especially in the field of oncology (Hutchinson & Kirk, 2011). During the last years, the field of immunotherapies expanded, therefore preclinical tumour models need to fit the special requirements of preclinical drug testing of those approaches. The models have to support in-depth analysis of the large variety of novel therapy approaches like cancer vaccines, adoptive T cell therapy and checkpoint inhibitors, as they require analysis beyond cytotoxicity. These approaches need distinct evaluation such as analysis of immune cells and cytokines. This is also of particular importance as adoptive cellular therapy with CAR T cells still lacks efficacy in solid tumours and can benefit from improved preclinical testing (Martinez & Moon, 2019; Marofi *et al.*, 2021).

So far, new therapy approaches are mainly tested in 2D cell culture and animal studies. In 2D cell culture cells are grown in a simplified way and lack anchorage to a matrix (Edmondson *et al.*, 2014). However, growth behaviour of cells strongly depends on their environment as shown by Mina Bissel already 40 years ago. This stresses the importance of extracellular matrix (ECM) and stromal components as factors of the tumour microenvironment to study cellular behaviour (Bissell, 1981; Bissell *et al.*, 2003). Therefore, 3D models like the microphysiologic 3D tumour models, presented here, can address the shortcomings of 2D cell culture as they provide a collagen-rich ECM, lead to organised tissue-like structures and show proliferation rates more comparable to the *in vivo* situation (Nietzer *et al.*, 2016). In this work, especially long-term homeostasis of several weeks and TME-aspects were addressed.

In addition to 2D cell culture, animal models, are commonly used for preclinical testing, which reflect a more complex tissue context, but specifically xenografts lack human stroma and tumour inoculation occurs ectopically (Hylander *et al.*, 2013; Wegner, 2017; Srivastava *et al.*, 2021). As animal studies also raise ethical concerns the principle of “3R” including reduction, refinement and replacement formulated by Russell and Burch in 1959 (Russell & Burch, 1992; Hughes & Health, JH Bloomberg School of Public, 2020) enforced the development of alternative test systems.

3D cell culture and tissue engineering can address this need as they can produce models, which allow 3D tissue generation with increased validity *in vitro* compared to standard 2D cell culture. Especially organoids and spheroids are being widely studied. However, spheroids are limited to spheroid-forming cell lines (Sant & Johnston, 2017) and organoids can have low success rates (Dijkstra *et al.*, 2020). Therefore, additional test systems are required.

In this work, importance of the TME was addressed by isolation of cells from primary (tumour) tissue for implementation into the microphysiologic 3D tumour models and the use of the SISmuc matrix was applied for a variety of tumour entities. TME-aspects were incorporated by CAF enrichment and TGF-β supplementation and especially CAFs were characterised. BLI-based *in vivo* imaging was introduced to enable serial and time-efficient online-evaluation of model quality and treatment efficacy and a two-circuit bioreactor was realised supporting microphysiologic 3D tumour models with an endothelial cell layer. Furthermore, the models were cultured under static, semi-static and dynamic conditions. Semi-static culture prolonged tissue-homeostasis over a long-term period of several weeks while being less elaborate than bioreactors and preserving the throughput of static culture. Additionally, an alternative route of application mimicking direct injection of CAR T cells into the tumour tissue was established. Together, these aspects improved the microphysiologic 3D tumour models respectively.

The microphysiologic 3D tumour models were applied in order to analyse their sensitivity towards differently designed CAR T cells, which differed in targeting domain, spacer length and costimulation. Then, effects of the implemented TME-aspects on the CAR T cells were analysed in order evaluate whether physical and immunological barriers were present. For these experiments, different ROR1 CAR T cells were analysed in microphysiologic 3D tumour models (TNBC, lung cancer) as ROR1 has been described as a suitable target for several malignancies including triple negative breast cancer (TNBC) and lung cancer. Here, pharmacological intervention by TGF-β receptor inhibition and improvement of the ROR1 CAR T cells by distinct gene-editing were analysed as approaches to improve anti-tumour efficacy of the ROR1 CAR T cells respectively.

## 5.1 Scale of assessment and improvement of the microphysiologic 3D tumour models to determine anti-tumour efficacy

Improvements of the microphysiologic 3D tumour models encompassed application of semi-static culture conditions, which supported tissue homeostasis in semi-static tumour models for at least 28 days reflecting long-term tissue stability compared to 2D cell culture. This bridges the gap between static and dynamic culture. The SISmuc matrix also demonstrated feasibility to support several entities like sarcoma and melanoma in addition to epithelial cancers. Incorporation of TME-aspects from primary tissues was successful; confirming achieved stromal enrichment with CAFs and first trials of lung organoid isolation. Application of these models proved that Ewing's sarcoma models can be sensitised for $G_{D2}$-targeting CAR T cell therapy and application of serial BLI-based imaging was established successfully as new time-efficient read-out method.

### 5.1.1 Semi-static culture mediates long-term tissue homeostasis of microphysiologic 3D lung tumour models

For the generation of microphysiologic 3D tumour models, cells are implemented on a natural collagen-rich matrix derived from chemically decellularised porcine jejunum, called SISmuc. The SISmuc provides a basement membrane and its collagen structure has been proven useful for several tissue engineering approaches and implantation (Stratmann *et al.*, 2014; Steinke *et al.*, 2015). So far, epithelial cancers have been established on the SISmuc, but in this work development of microphysiologic 3D models of non-epithelial cancers was achieved. As collagen is the main ECM-component in human tissue it is conceivable that non-epithelial cancer cells also produce organised tissues on the SISmuc as shown here for melanoma and sarcoma cells (Cen *et al.*, 2008; Balasubramanian *et al.*, 2013). Thus, in this work application of the SISmuc matrix in the microphysiologic 3D tumour models was extended, leading to increased tumour entities that can be modelled, respectively. This demonstrated the versatility of the SISmuc matrix in the microphysiologic 3D tumour models and proved that the SISmuc supports a variety of cancer types.

The microphysiologic 3D lung tumour models have been described before with two different culture modalities, either static in the incubator or dynamic in a bioreactors (Göttlich *et al.*, 2016; Nietzer *et al.*, 2016). With this, a higher throughput was feasible when static culture was applied, or an increased tissue generation was initiated by dynamic culture. However, dynamic culture only provides a low throughput and handling remains elaborate. As a standardisable test system needs to be feasible in a relatively high throughput while benefiting from enhanced tissue generation, semi-static culture conditions were applied. Improved growth of breast cancer models has been demonstrated before on an orbital shaker (Nelke, 2019). Therefore, this promising technique should be further expandend. Lung tumour models were cultured on an orbital shaker, here named semi-static culture, which led to increased tumour cell growth and a comparable tissue architecture as the dynamic culture. In addition, it preserves the throughput of static culture. Tumour cells formed enhanced tumour tissue-like architecture *in vitro* with stable apoptosis, cell viability, cell number and cell proliferation, indicating a state of tissue homeostasis (Rué & Martinez Arias, 2015). This state is reached after 10 days of semi-static culture and the models remain stable for at least 28 days as shown for A549 lung tumour cells. Therefore, they represent long-term stability especially in comparison to 2D cell culture. Semi-static culture prolongs previously described culture time from 21 days of static models. Hence, it allows for treatment periods of approximately 18 days from previously feasible 10 days without the need of bioreactors. Even longer culture could be conceivable but was not demonstrated yet. These effects are most likely mediated through a continuous mixing of the medium, which leads to better nutrient supply that is also observed in the bioreactor. Application of shaker culture has also been described to improve generation of iPSC-derived organoids (Lee *et al.*, 2020). Furthermore, oxygen content within the medium has shown to influence mesenchymal stem cells and could also affect cancer cell growth respectively (Yeatts *et al.*, 2013).

Of note, tissue homeostasis is especially important for drug testing as it determines the window by which the model does not influence the therapy by inconsistency. A stable and relatively low level of proliferation, as it is shown in the microphysiologic 3D tumour models presented here, allows a standardisable efficacy determination of drug effects (Edmondson *et al.*, 2014). The low proliferation index observed in the microphysiologic 3D tumour models is more comparable than 2D cell culture to the *in vivo* situation of patients, where it has been described, for example, with 25.8 % for lung adenocarcinoma (Warth *et al.*, 2014). Long-term model stability and tissue homeostasis is most likely achieved due to the matrix structure as the ECM is an important factor of the latter (Nelson & Bissell, 2006). This demonstrates that long-term culture is feasible under semi-static culture conditions. This is an additional improvement particularly valuable for the evaluation of cellular immunotherapies as this bridges the gap between short-term assays from 2D cell culture and elaborate and expensive animal studies.

### 5.1.2 Utilisation of lung tumour biopsies for primary cell isolation

Tumour cell lines are the main cell source to produce standardisable, reproducible, and relatively cost-effective tumour models. They are feasible in culture for a long time, and maintenance and propagation are easy. However, cell lines raise different concerns. They are often cultured for several decades and are often genetically drifted from the original tumour. This is discussed especially with regard to the large set of lung cancer cell lines (Gazdar *et al.*, 2010). Furthermore, they do not represent the heterogeneity, which is found in patients and cross-contaminations between different tumour cell lines are a common problem (Lucey *et al.*, 2009; Lorsch *et al.*, 2014). The use of primary cells derived from patient biopsies gains increasing attention as they can represent heterogeneity and a closer resemblance of the patient’s physiology. To improve the microphysiologic 3D tumour models, tumour and stromal cells were isolated from tissue biopsies of lung tumour patients. For this, resected lung tissue was obtained from the University clinic in Magdeburg (collaboration Prof T. Walles). However, isolation of tumour cells was not sufficiently achieved in this work. Isolation was performed combining enzymatic digestion and manual disruption. However, fibroblasts overgrew cultures rapidly or epithelial cell were not present in the first place. Quatromoni *et al*. showed that successful isolation of tumour cells from lung tumour material is difficult to establish and a fine balance of different enzymes and mechanical disruption is mandatory for successful cell isolation. Additionally, isolation protocols need adjustments, because tumour cell isolation via collagenase alone was insufficient. Here, a combination with elastase could improve isolation yield, as elastin is prominent in the ECM of lung tumours and was described by others for improved tissue digestion (Quatromoni *et al.*, 2015).

Due to logistic reasons, the biopsies were obtained the day after resection, which influences cell viability and reduces the number of viable cells that can be isolated from the tissue, with that, reducing the yield of viable cells after isolation. Therefore, depletion of dead cells and cell debris needs to be performed in future experiments (Reichard & Asosingh, 2019). In general, it was shown by Ferry-Galow *et al.* that the percentage of tumour content within a biopsy is relatively low, which additionally reduces the chances of successful tumour cell isolation (Ferry-Galow *et al.*, 2018). Additionally, optimal media constitution can influence cellular outgrowth, as fibroblasts overgrow other cell types rapidly, if suboptimal medium is used. Here, the addition of cancer-specific growth factors could improve isolation yield as this also promotes growth in lung cancer organoids, where medium is adjusted to the specific signalling pathways in the respective tissue (Drost & Clevers, 2018; Sachs *et al.*, 2019). Furthermore, isolated cells were grown under standard 2D cell culture conditions in polystyrene flasks leading to culture conditions where cells lack a suitable substrate or matrix for optimal anchorage. This could lead to limited cell expansion, indicating the importance of ECM supporting again the advantages of 3D cell culture (Kapałczyńska *et al.*, 2018). This goes in line with previous findings where decellularised matrices also promoted the growth of iPSCs (Berger *et al.*, 2020).

The isolation of single tumour cells was rarely successful and inefficient. Therefore, an isolation protocol for organoids was adapted as they present a promising tool for preclinical research (Drost & Clevers, 2018). Organoids are structured cell clusters that can be generated from tissue of different organs and from cancer tissue. Here, several different cell types can be preserved and genomic stability is maintained over several months as stated by Sachs *et al.* (Sachs *et al.*, 2019). With this, they can overcome previous problems from single-cell-based isolations as they preserve cell-cell contacts, grow in ECM-droplets and the medium is more defined. Hence, cell-isolates from fresh tissues can be produced. The culture of organoids, however, is elaborate and the medium needs specific supplementation with growth factors. Furthermore, organoids are implemented in Matrigel®. The latter is discussed as a non-defined influence on the cells as the composition is not completely revealed (Panek *et al.*, 2018). Additionally, the success rate of organoid isolation differs tremendously as Dijkstra *et al*. achieved only in 17 % pure NSCLC organoids even though they processed >70 samples. Sachs *et al*. obtained lung cancer organoids in 28 % (n=28) of the isolations but only, if needle biopsies of metastatic tumours were available. For other biopsy types, a success rate was not defined, but overgrowth of tumour organoids by normal organoids is suspected to occur frequently. In contrast Li *et al*. demonstrated an impressive success rate of 80 % for lung adenocarcinoma-derived organoids, but only evaluated 15 samples (Sachs *et al.*, 2019; Dijkstra *et al.*, 2020; Li *et al.*, 2020).

In this work, the generation of organoids was successful in 3 out of 5 samples, which resembles relatively low sample number. Additionally, not all processed samples were derived from cancer tissue. However, expansion and maintenance were limited and no organoids could be cryopreserved for later experiments. As medium constitution is especially important for successful organoid culture, the supplementation could be inadequate for the distinct biopsy. Sachs *et al*. also stated this and were not successful in expanding tumour organoids by adapting medium supplementation. Due to the high diversity of mutated signalling pathways in lung cancer, sufficient media constitution remains difficult (Chen *et al.*, 2014; Sachs *et al.*, 2019). Therefore, inadequate maintenance of organoids is most likely a result of the medium composition. Again, the relatively late isolation start could also be the reason for reduced cell viability, reducing success rate even further. It could not be excluded whether the obtained organoids comprise tumour organoids specifically. In addition, organoids from normal tissue could have overgrown tumour organoids and stalled in their growth as the medium composition was adapted towards cancer cell metabolism.

However, organoids can be a useful tool to isolate tumour cells from patient biopsies by preserving tissue context in future studies, when tissue becomes available directly after resection and medium composition can be adapted towards patient-specific mutational burden when this information is available.

### 5.1.3 The SISmuc supports incorporation of an endothelial cell barrier and phenotypic analysis confirms CAF phenotype of implemented primary fibroblasts from lung tissue

Even though primary tumour cells could not be utilised for implementation into the microphysiologic 3D tumour models until now, isolation of other primary cell types was successful. In addition to tumour cells, the hostile tumour microenvironment influences therapies and tumour progression. Here, especially cancer-associated fibroblasts (CAFs) are important as they are a major part of the TME and can mediate physical and immunological barriers within the tumour which influences therapy outcome of cellular immunotherapy (Anderson *et al.*, 2017; LeBleu & Kalluri, 2018).

To incorporate these aspects and with this increase the predictive value of the microphysiologic 3D tumour models, fibroblasts were isolated from patient biopsies and implemented into the models. So far, only fibroblasts from skin biopsies (hDF) were incorporated into the microphysiologic 3D tumour models. Here, a strong association of fibroblasts and colorectal cancer cells formed indicating that the SISmuc matrix promotes tumour-stroma interactions (Nietzer *et al.*, 2016).

Dermal fibroblasts present a stable cell source and are easily available; however, they are not organotypical for the tumour models presented here and are often isolated from young children, which do not represent the typical cancer patient for lung and breast cancer. Therefore, fibroblasts were outgrown from healthy lung and lung tumour tissue and were investigated in an organotypical surrounding by co-culturing them with lung tumour cells (A549). Additionally, co-cultures with TNBC (MDA-MB-231) cells were used as they represent a more advanced tumour stage and, therefore, possibly associate differently with the stroma cells. The focus was to analyse whether implemented fibroblasts could be identified as CAF-specific populations, which then should reflect aspects from the hostile TME.

Characterisation of stromal-enriched microphysiologic 3D lung tumour models revealed an organised tumour tissue-like architecture with large tumour cell masses on top of the matrix and in preserved crypt structures, with fibroblasts pervading in the submucosal part. Tissue architecture was comparable to native lung adenocarcinoma tissue, when lung tumour-derived fibroblasts were incorporated under dynamic conditions and no morphologic differences occurred between fibroblasts from cancer patients and hDFs on the SISmuc matrix. Both represented a comparable growth verified by immunofluorescence and H&E staining. Healthy lung fibroblasts and metCAFs, however, seemed to reduce upon ROR1 CAR T cell administration when cultured together with A549 cells und semi-static conditions, which was not confirmed under dynamic conditions. Therefore, vanished fibroblasts are rather due to variances in the staining and variances within the respective tumour model than due to CAR T cell administration. The previously described interplay and remodelling of the SISmuc by tumour cells and fibroblasts (Nietzer *et al.*, 2016) was not observed. Stromal-enriched microphysiologic 3D breast tumour models revealed strong invasion of cells, where fibroblasts and cancer cells showed similar morphology.

Cancer-associated fibroblasts are an important cell type in solid tumours, which can influence tumour promotion and therapy outcome (Ziani *et al.*, 2018). Nonetheless, the origin of CAFs within a tumour is not completely defined yet. They can derive from a variety of healthy cells by the influence of cancer cells. Here, for instance, healthy tissue fibroblasts can become active and obtain a CAF phenotype (Anderberg & Pietras, 2009; Kalluri, 2016; LeBleu & Kalluri, 2018; Ziani *et al.*, 2018; Yoshida, 2020).

Fibroblasts can change marker expression when they are activated or obtaining a CAF-phenotype and several markers have been postulated to distinguish CAFs from normal fibroblasts. To analyse whether incorporated fibroblasts show a CAF phenotype, several markers were analysed such as α-SMA, which is associated with fibroblast activation and FAP, which is found in CAFs specifically. CAFs can show ECM remodelling properties, therefore, MMP-2 and- 9 were analysed as they also have been described in context of CAFs (Kalluri & Zeisberg, 2006; Nurmik *et al.*, 2020).

Expression of α-SMA was confirmed in fibroblasts and A549 tumour cells, which is a first hint towards activated fibroblast subpopulations. Alpha-SMA expression in tumour cells is associated with epithelial to mesenchymal transition (EMT) and mesenchymal cell traits (Ohbayashi *et al.*, 2014; Yıldırım *et al.*, 092017). Partly mesenchymal cell populations are present in A549 cells, especially when cultured on the SISmuc in the presence of an ECM (Wallstabe, Göttlich, Nelke, Kühnemundt *et al.*, 2019). Regarding influences of the ECM, especially fibrotic matrices can increase α-SMA expression in A549 lung tumour cells (Chen *et al.*, 2017). These findings are in line with the FAP expression, which was observed in A549 cells on top of the matrix in addition to FAP$^{+}$ fibroblasts populations and has been described previously (Puré & Blomberg, 2018). Alpha-SMA and FAP expressing cells were also found in stromal-enriched microphysiologic 3D breast tumour models. However, tumour cells and stromal cells were not distinguishable as MDA-MB-231 cells revealed expression of all stained markers. Expression of αSMA and FAP in MDA-MB-231 cells has been reported before, especially when co-cultured with CAFs (Jia *et al.*, 2014; Porretti *et al.*, 2014). As CAFs have matrix-remodelling properties, MMPs were also described to characterise them. The matrix-remodelling enzymes MMP-2 and -9 were found in close proximity to the fibroblast populations and in A549 cells, which is especially true for MMP-9. Expression of MMP-2 and -9 was described before in A549 cells and is associated with invasiveness and EMT (Xu *et al.*, 2014; Merchant *et al.*, 2017).

As mentioned above, FAP, αSMA and MMP-2/-9 are applicable to characterise CAFs, therefore, these data confirm that at least populations of CAFs were implemented into the tumour models or developed during culture together with tumour cells. Consequently, used fibroblasts can be termed CAFs. However, additional markers are necessary to confirm this especially in stromal-enriched microphysiologic 3D breast cancer models.

To assess whether a more invasive cell type and administration of TGF-β would change association with the fibroblasts, CAFs were co-cultured with MDA-MB-231 breast cancer cells as they represent a more advanced and more invasive cancer cell type when grown on the SISmuc. Additionally, stromal-enriched microphysiologic 3D breast tumour models were treated with TGF-β I as this has been described to promote CAF formation (Calon *et al.*, 2014; Erdogan & Webb, 2017).

Surprisingly, supplementation with TGF-β did not alter cell growth, even though this was shown in the microphysiologic 3D tumour model for other cell lines, where invasive tumour cell growth was induced in HCC827 lung cancer cells upon TGF-β administration (Göttlich *et al.*, 2016). Sun *et al.* demonstrated, that TGF-β could induce EMT and invasion in MDA-MB-231 cells when 5 ng/ml were administered (Sun *et al.*, 2019). Controversially, absence of further invasion of MDA-MB-231 towards TGF-β addition has also been described before (Mur *et al.*, 1998; Lynch *et al.*, 2001). In this work, 10 ng/ml TGF-β I was administered and cell growth was determined via IF and H&E staining. MDA-MB-231 cells grew invasive independently of TGF-β and did not further invade upon TGF-β administration. It is possible that invasion by TGF-β administration can not be increased, because the collagen matrix already promotes invasive cell growth. This goes in line with previous findings, where matrix and ECM stiffness have shown tremendous effects on metastatic growth of breast cancer cells (Acerbi *et al.*, 2015). Consequently, it is conceivable that the influence of the SISmuc matrix outperforms the effects of TGF-β, and already extensive invasion of MDA-MB-231 cells occurs without TGF-β supplementation. Characterisation of fibroblast-association was impossible due to previously discussed antibody staining and morphological similarities. Therefore, effects on implemented fibroblasts mediated by TGF-β administration can neither be confirmed nor excluded.

In order to assess whether the interaction of CAFs differs when co-cultured with A549 or MDA-MB-231 cells and if a CAF phenotype is promoted in the tumour models, as well as if immunomodulatory cytokines are present, a multiplex Proteome Profiler™ assay was performed, analysing 105 secreted cytokines simultaneously from supernatants of the respective stromal-enriched microphysiologic 3D tumour models after maturation.

The assay revealed 8 distinct markers, which were shared between all groups or between co-cultures. Additionally, 2 markers were selectively found in fibroblast monoculture, while A549 CC revealed 4 and CC MDA showed 7 that were detected in each sample exclusively. Literature research revealed distinct function of the markers.

Here, markers that are found in all samples are associated with metastasis in breast and lung cancer e.g. CCL2 (Liubomirski *et al.*, 2019), CXCL5 (Zhang *et al.*, 2020). CCL2 is also associated with EMT, when secreted by cancer cells (Yoshimura, 2018). CXCL5 expressed by CAFs is also described to promote PD-L1 expression (Li & Zhou *et al.*, 2019). Furthermore, cytokines associated with CAFs were found, like CXCL1, which can be secreted by cancer cells and induces CAF phenotype (Wang *et al.*, 2017). Additionally, Dickkopf-1 (DKK-1) and GDF-15 are associated with CAFs, while DKK-1 is especially secreted in CAFs of breast cancer (Sadlonova *et al.*, 2009; Bruzzese *et al.*, 2014). Interestingly, IL-6 was present in all groups, which is secreted by CAFs of an inflammatory phenotype (Wu *et al.*, 2017; Barrett & Puré, 2020). Additionally, Serpin E1 is associated with a CAF phenotype as it has been observed in higher levels within CAFs after TGF-β stimulation (Santi *et al.*, 2018). Furthermore, markers associated with the recruitment of myeloid cells in the context of breast cancer were present, like IL-8 (Barrett & Puré, 2020) and DKK-1 (D'Amico *et al.*, 2016). IL-8 is also described to promote cancer stem cell niches together with IL-6 (Fiori *et al.*, 2019).

Consequently, the markers that were present in all tested models identify a baseline of the tumour microenvironment present in the tumour models, which indicate that the SISmuc and the CC promote CAF growth, and immune cell interaction could indeed occur supporting an immunological barrier. As CCL7 and HGF were found in the monoculture of fibroblasts this confirms that, they are not only generated by the presence of cancer cells but also by fibroblasts alone. This indicated that CAFs are directly isolated from the tumour tissue or generated by 3D culture on the SISmuc matrix. Additionally, CSC growth is promoted on the SISmuc, as well as invasive traits for cancer cells, as it was also shown in Kühnemundt *et al.* (Kühnemundt *et al.*, 2020).

For the markers present in both tumour cell containing co-cultures similar associations were found as Cystatin C is associated with cancer progression and invasion (Završnik *et al.*, 2017) as well fibroblast activation (Allinen *et al.*, 2004). Comparable actions are found for TFF3 and uPAR, which also promote metastasis formation and inhibition of apoptosis in cancer cells (Ahmed *et al.*, 2012; Mahmood *et al.*, 2018). Lipocalin-2 and CD147 show similar effects, but with stronger association to matrix remodelling as both are described to increase or modulate MMP-production in cancer cells and stromal fibroblasts. (Yan *et al.*, 2005; Santiago-Sánchez *et al.*, 2020). Markers in co-cultures were strongly associated with angiogenesis and immunosuppression. For instance Angiogenin, VEGF, Lipocalin-2, MIF are all promoting angiogenesis either expressed by tumour cells or CAFs (Fukumura *et al.*, 1998; Miyake *et al.*, 2015; Guda *et al.*, 2019; Santiago-Sánchez *et al.*, 2020). Additionally, immunosuppressive functions can be mediated by MIF and VEGF (Balogh *et al.*, 2018; Yang *et al.*, 2018). These findings confirm that a microenvironment is present in the microphysiologic 3D tumour models that can support CAF populations and represents aspects of immunosuppression. Interestingly, aspects of angiogenesis are promoted when cancer cells are present. This indicates that cultures, which contain tumour cells together with CAFs would favour endothelial cell growth. This could further lead to a more complex tumour models when endothelial cells are not only combined with tumour cells alone.

Lastly, several markers were only found in each group alone. Co-culture of CAFs with A549 cells showed markers, which have been secreted or associated with CAFs and promote cancer progression, motility and invasion like Osteopontin (Castello *et al.*, 2017; Fiori *et al.*, 2019). Osteopontin can also be found in tumour cells, especially A549 and lung fibroblasts, if stressed and lead to increased migration (Fong *et al.*, 2009; Kato *et al.*, 2014). IGFBP-2 can act stimulatory and as a signalling between cancer and stromal cells (Thomas & Radhakrishnan, 2019), while IGFBP-3 is found in cancer cells with aggressive characteristics and also plays a crucial role in fibroblasts to myofibroblast differentiation (Pickard & McCance, 2015; Tas *et al.*, 2016). Additionally, complement-associated factors like Complement Factor D were found, which is described to influence tumour-associated macrophages and EMT (Hamilton *et al.*, 2016; Zhang *et al.*, 2019).

In the microphysiologic 3D tumour models containing MDA-MB-231 cells together with CAFs, especially markers associated with an invasiveness and metastasis formation in breast cancer were present, like G-CSF, ICAM-1, MIP-3α, PDGFR-AA, Thrombospondin-1, Pentaxin-3 (Carvalho *et al.*, 2005; Rosette *et al.*, 2005; Yee *et al.*, 2009; Osuala & Sloane, 2014; Giacomini *et al.*, 2018; Liu *et al.*, 2020). Pentraxin-2 is especially associated with bone-metastasis formation and cancer stem-cell induction, which is not surprising, as MDA-MB-231 can metastasise into the bone in *in vivo* experiments and metastatic sub-clones are available (Wright *et al.*, 2016). G-CSF, GM-CSF, PDGF-AA and Thrombospondin-1 are also associated with stromal fibroblasts and can activate and promote stromal interaction, as well as CAF activation, and favour CAF formation (Bretscher *et al.*, 2000; Kazerounian *et al.*, 2008; Bremnes *et al.*, 2011; Liu *et al.*, 2020). Interestingly, discussed markers also showed strong association with immunosuppressive actions. Here, G-CSF, GM-CSF and MIP-3α have been described to promote immunomodulation, where G-CSF and MIP-3α are especially associated with macrophages, while G-CSF also promotes angiogenesis (Hollmén *et al.*, 2016; Hong, 2016; Korbecki *et al.*, 2020). ICAM-1 was found in MDA-MB-231 CC alone, which mediates several actions specifically in breast cancer. It is described as pro-inflammatory cytokine, which can promote invasion and metastasis and mediates the interaction between the tumour and the immune system, if expressed by cancer cells. Additionally, it can mediate immune-escape and influence leukocyte transmigration (Kotteas *et al.*, 2014; Figenschau *et al.*, 2018).

Lastly, CAFs alone expressed CCL7 and HGF, which are both associated with invasion, migration and malignancy, as well as CSC formation, where CCL7 can be secreted by CAFs and is associated with the TGF-β pathway (Bremnes *et al.*, 2011; Liu *et al.*, 2016; Fiori *et al.*, 2019; Lee & Cho, 2020). Furthermore, HGF can promote angiogenesis, induce cancer cell invasion and can be secreted by fibroblasts (Grugan *et al.*, 2010; Ding *et al.*, 2018). Presence of these markers hint again towards a CAF phenotype. Furthermore, the SISmuc matrix supports CAF growth independent of cancer cell co-culture.

Consequently, findings from the literature research imply, that A549 tumour cells exhibit stronger effects on stroma-signalling and EMT, while MDA-MB-231 cells associate more strongly with immunomodulatory and inflammatory effects, invasion and angiogenesis. However, both cell lines indicate support of CAFs by their secretory phenotype, which is also true for the SISmuc matrix alone.

Of note, the markers discussed here were analysed from the supernatant of semi-static models, but quantification of the respective signals was not possible, because strong differences occurred in the controls. Therefore, markers where only discussed as generally present or not, without respect to intensity. To analyse those markers quantitatively, larger amounts of media need to be assessed or ELISA for distinct markers can be conducted. However, the findings give a first hint towards the composition of the present soluble aspects of the hostile tumour microenvironment and further generate supporting evidence for successful CAF implementation.

In addition to fibroblasts, several other cell types are present in the TME. Here, endothelial cells are especially interesting as they are part of the vasculature, which mediates nutrient supply but also the entry of immune cells (Filippi, 2016). Furthermore, they secrete important signalling molecules and influence drug response (Meurette & Mehlen, 2018; Gubbiotti *et al.*, 2020).

To represent parts of the vasculature and allow immune cell diapedesis within the microphysiologic 3D tumour models, endothelial cells were isolated from skin tissue and implemented in the models of different tumour cell entities. To achieve this, a newly developed cell crown produced by 3D printing was successfully applied as it provides the advantage of feasible cell seeding and culture from both sides. For dynamic culture, a special bioreactor set-up was applied with two separated cycles enabling specific administration of substances or cells to either the tumour cell site or the endothelial cell layer. Endothelial cells were combined with breast, lung and colorectal cancer cancers cells and formed a distinct monolayer, which remained stable under static and dynamic conditions. The endothelial cell layer was confirmed by CD31-staining and showed a tight monolayer, which formed on the submucosal part of the SISmuc. The incorporation of an endothelial layer in the microphysiologic 3D tumour models encompasses several advantages compared to other endothelial 3D cell culture models, like trans-well plates, as it provides direct contact of the endothelial cells to the ECM, which is an important modulator of endothelial cell signalling (Fukuhara *et al.*, 2009). In addition to the ECM-anchorage, molecules secreted by tumour cells can influence endothelial cell growth, which goes in line with the results of the multiplex proteome assay, where angiogenesis-associated factors were present when tumour cells and CAFs were cultured on the SISmuc. The establishment of an endothelial cell layer improves future testing of immunotherapies as it reflects additional aspects of the TME.

### 5.1.4 Microphysiologic 3D sarcoma models can be sensitised for $G_{D2}$-targeting CAR T cells

The main aim of this work was the use of the microphysiologic 3D tumour models for cellular immunotherapies. In cooperation with the group of Dr. Rossig (University Hospital Münster), the treatment of Ewing's sarcoma with $G_{D2}$ CAR T cells was investigated. Ewing's sarcoma is an aggressive form of bone or soft tissue cancer, which intrinsically lacks suitable target antigens (Grünewald *et al.*, 2018; Knott *et al.*, 2019). It was assessed whether microphysiologic 3D tumour models can recapitulate Ewing's sarcoma *in vitro* and, therefore, can be utilised for immunotherapy testing with $G_{D2}$-targeting CAR T cells. However, the surface marker $G_{D2}$ is normally expressed inhomogenously on Ewing's sarcoma cells, but can become a promising target as its expression is inducible by EZH2 inhibition mediated by GSK126 (Kailayangiri *et al.*, 2017). It was confirmed in this work, that a multi-layered microphysiologic 3D Ewing's sarcoma model was established and re-isolated Ewing's sarcoma cells expressed $G_{D2}$ after administration of GSK126 for about 2 weeks (Kailayangiri *et al.*, 2019). Furthermore, treatment with $G_{D2}$ CAR T cells upon $G_{D2}$-induction indicated tumour-cell reduction in first experiments. With this, it was shown that the microphysiologic 3D tumour models provide a versatile tool to study immunotherapies in the context of a non-epithelial-derived Ewing's sarcoma (Kailayangiri *et al.*, 2019).

### 5.1.5 Non-invasive bioluminescence-based measurement enhances analysis in microphysiologic 3D tumour models

Microphysiologic 3D tumour models need read-out methods that are applicable in a high throughput while still being time-efficient, in order to evaluate novel immunotherapeutic approaches effectively. As the microphysiologic 3D tumour models form tissue-like constructs, a bioluminescence intensity (BLI)-based *in vivo* imaging method was established during this work, which allows evaluation of CAR T cell efficacy and model quality in order to expand the scale of assessment and increase the predictivity of the models accordingly.

The establishment of a protocol for luminescence-based measurements provides a rapid and sensitive read-out to analyse the microphysiologic 3D tumour models (McCaffrey *et al.*, 2003). Advantages are that it can visualise treatment efficacy and tumour growth during culture time (Close *et al.*, 2011). Additionally, the method is relatively cheap with regard to the chemicals required (McCaffrey *et al.*, 2003; Close *et al.*, 2011; Tung *et al.*, 2016).

Cancer cells often encompass heterogenic cell populations and tumour cells can gain invasive traits by undergoing EMT, which influences marker expression. This became especially evident when apoptosis measurements were performed to evaluate treatment efficacy based on M30 CytoDeath™ ELISA. The latter relies on cytokeratin 18 expression of the tumour cells as a cleaved epitope of this cytoskeletal protein is released in the cell culture supernatant upon apoptosis. Here, the tumour cell lines A549 and MDA-MB-231, equally susceptible for ROR1-targeting therapy, showed different levels of apoptosis, which was contradictory to immunohistochemical stainings, which indicated equal effects and tumour cell reduction of both tumour cell lines upon ROR1 CAR T cell therapy. MDA-MB-231 showed nearly no increase in apoptosis detected by M30 CytoDeath™ ELISA, whereas A549 revealed strong apoptosis levels. The same was observed during studies, where effects of TGF-β and the blocking of its action with the TGF-β receptor inhibitor SD-208 did not induce increasing apoptosis over time in MDA-MB-231 cells, even though cytokine measurements revealed T cell activation. The reason for this is that MDA-MB-231 cells strongly express vimentin accompanied by decreasing cytokeratin expression, indicating a mesenchymal phenotype especially when cultured under 3D conditions (Vuoriluoto *et al.*, 2011; Pal *et al.*, 2019; Wallstabe, Göttlich, Nelke, Kühnemundt *et al.*, 2019). Low to zero levels of cytokeratin 18 have been described in MDA-MB-231 cells (Bühler & Schaller, 2005). The combination of the strong mesenchymal phenotype together with the 3D surrounding of the SISmuc matrix supports and increases this phenotype. This goes in line with the data from the multiplex proteome analysis revealing cytokines associated with invasiveness and EMT when MDA-MB-231 are present. Although, MDA-MB-231 still express epithelial markers to some extend when grown on SISmuc matrix (Wallstabe, Göttlich, Nelke, Kühnemundt *et al.*, 2019), the expression of fibroblast-associated markers also supports the strong mesenchymal phenotype. Consequently, MDA-MB-231-cells withdraw themselves partially from M30 CytoDeath™ ELISA analysis. This influences sensitivity and applicability of the M30 CytoDeath™ ELISA for this cell line and, therefore, a new read-out parameter was needed, which would quantify treatment efficacy independent of EMT-marker expression. Furthermore, quality evaluation during culture of microphysiologic 3D tumour models needs to be feasible, since until now only end-point measurements after formalin-fixation or by MTT-test were available to analyse cell density and cell distribution. Therefore, a technique commonly used to visualise and quantify tumour burden in animal experiments was adapted for application in the tumour models.

To achieve this, *firefly*-luciferase transduced tumour cells were used for further experiments and a protocol for BLI-based measurements was established. Here, luciferin is administered and upon reaction with viable cells, light is emitted which is detected by a sensitive camera in an *in vivo* imaging system (IVIS) (Marques & Esteves da Silva, 2009). The camera detecting the light quantifies this by measuring emitted photons over the surface area. With this, it is possible to evaluate cell distribution and density integrating the complete model surface. As the transduction is independent of EMT-status, both cell lines used here (A549 and MDA-MB-231) were confirmed to be equally sensitive to administered ROR1 CAR T cells, mirroring the findings from H&E stainings and cytokine measurements. Analysis of BLI in microphysiologic 3D models of TNBC proved quantitatively that SD-208 can restore ROR1 CAR T cell function upon TGF-β administration supporting cytokine analysis (Stüber *et al.*, 2020). Establishment of BLI-based *in vivo* imaging extends the scale of assessment and improves the microphysiologic 3D tumour models. It demonstrates that the tissue-like structure, which is formed on the SISmuc matrix, enables application of distinct techniques commonly used in animal studies.

However, the use of transfected cells is mandatory to facilitate luminescence, which is easily achieved in cell lines, which are accessible transfection hosts. As mentioned before, generating microphysiologic 3D tumour models with patient-specific directly isolated tumour cells is highly interesting. Stable viral transfection of primary cells can be challenging. To overcome this, other cell tracking methods could be utilised, which are not based on stable transfection, because the IVIS-device also enables visualisation of fluorescence intensities (Iyer *et al.*, 2009; Sapudom *et al.*, 2017).

## 5.2 Analysis of different ROR1 CAR T cell designs in microphysiologic 3D tumour models reveals differences in efficacy

In order to determine their sensitivity, microphysiologic 3D tumour models representing TNBC and lung cancer were applied to analyse the efficacy of differently designed ROR1 CAR T cells. Here, they proved that anti-tumour function of CAR T cells depends on their design, which was shown for spacer, targeting domain and costimulation. This demonstrates the sensitivity of the microphysiologic 3D tumour models for candidate selection. Additionally, the feasibility of long-term studies was demonstrated in dynamic microphysiologic 3D lung tumour models in order to evaluate ROR1 CAR T cell efficacy in the presence of large tumour cell masses for 14 days. A novel sandwich-culture modality was established, which enables direct injection as an alternative route for the application of cellular immunotherapies in addition to administration via the medium flow.

### 5.2.1 Anti-tumour function depends on CAR design

The main aim of this work was to enable standardisable efficacy testing of CAR T cells in the microphysiologic 3D tumour models and to demonstrate their sensitivity accordingly. Currently, the potency of CAR T cells is assessed in either conventional 2D cell culture or animal models. Problems occur, because 2D cell culture lacks complexity with easy antigen exposure and high effector to target cell ratios for CAR T cells, which does not reflect the situation in the patient. In animal models, mainly murine xenograft models, a more complex tissue generation occurs naturally. However, inoculation is often performed ectopically and, therefore, lacks architecture and phenotype of the human tumour (Wegner, 2017; Srivastava *et al.*, 2021). In order to provide a suitable preclinical model with increased predictive value for CAR T cell testing the microphysiologic 3D tumour models were engaged and further improved as already mentioned. Sensitivity of the respective models was evaluated by application of differently designed ROR1 CAR T cells. Here, CAR T cells differed in either costimulatory domain, spacer length or receptor affinity in order to determine if the microphysiologic 3D tumour models can distinguish between optimal and suboptimal CAR design and to demonstrate that anti-tumour function depends on it.

Static microphysiologic 3D tumour models containing either breast cancer (MDA-MB-231) or lung cancer (A549) cells were treated with ROR1 CAR T cells, either including the CD28 or 4-1BB costimulatory domain. Additionally, a first-generation CAR without costimulation was applied. Experiments resulted in a trend in A549 and MDA-MB-231 tumour models, where costimulation with CD28 indicated favourable results. However, low differences were observed, which could be the result of inadequate CAR T cell concentrations. Furthermore, treatment period of 72 h might be insufficient and longer periods need to be assessed, because costimulation with CD28 is associated with faster tumour cell elimination, while 4-1BB mediated long-term persistence in previous studies (Weinkove *et al.*, 2019). Surprisingly, the construct without costimulatory domain induced comparable results to CAR T cells with either CD28 or 4-1BB costimulation, although it is known that second generation CAR T cells are indeed superior to designs from the first generation due to their costimulation (Boroughs *et al.*, 2019). These results can be attributed to the short treatment time, as well as the relatively low tumour cell number, that is present in static tumour models. Nevertheless, this is the first hint that microphysiologic 3D tumour models can distinguish different CAR designs.

For future testing of different CAR designs, higher CAR T cell concentrations should be administered, which was realised in the experiments discussed below, where CAR T cells with different spacer and antibody-domains were analysed.

The administered number of ROR1 CAR T cells was increased by a factor of 10 to induce results that are more distinct. With this adaptation, the comparison of two targeting domains with different affinities (R12 = high affinity; 2A2 = low affinity) was performed in static microphysiologic 3D lung tumour models. Here, H&E staining and BLI-based measurements indicated favourable results for the R12 ROR1 CAR T cells, which represents the high affinity targeting domain compared to lower affinity in 2A2 ROR1 CAR T cells. To further analyse these tendencies, apoptosis and cytokine, as well as flow cytometry data were acquired and confirmed superior performance of R12 ROR1 CAR T cells as they secreted higher amounts of the activating cytokines IFN-γ and IL-2 and induced higher apoptosis in A549 tumour cells during the 72 h treatment period. In addition, more CAR T cells expressed the activation markers CD25 and CD69 (Wallstabe, Göttlich, Nelke, Kühnemundt *et al.*, 2019). Of note, CAR T cells with high affinity will indeed induce faster tumour cell lysis due to faster kinetics as reported by others (Yang *et al.*, 2011; Baskar *et al.*, 2012). Moreover, these findings go in line with previous studies, where the affinity of R12 was favourable, which supports its relevance for continuous preclinical and clinical development (Hudecek *et al.*, 2013; Berger *et al.*, 2015). The study presented here, evaluated a relatively short treatment period of 72 h and no effects of the respective ROR1 CAR T cells over weeks or months were monitored. However, due to high affinity and strong activation, R12 ROR1 CAR T cells could be more susceptible for dysfunction and ultimately exhaustion. Therefore, the 2A2 targeting domain with lower affinity could also lead to promising results when monitored extensively as it could reduce adverse effects due to lower activation (Park *et al.*, 2017; Ghorashian *et al.*, 2019). Thus, a combination treatment is conceivable, where CAR T cells with a high affinity targeting domain (e.g. R12) would induce strong anti-tumour response and CAR T cells with lower affinity targeting domain (e.g. 2A2) would mediate low anti-tumour activity in the first place but persist in the patient while still activated. Combinations of distinct CAR T cell populations could lead to an improved combinatory CAR T cell product with different costimulatory domains, promoting fast tumour cell eradication and longer persistence. Such experiments could be realised in semi-static or dynamic tumour models, where long-term treatment for at least 14 days is feasible.

As a third approach, ROR1 CAR T cells with the low affinity targeting domain 2A2 combined with different spacer lengths were compared in static microphysiologic 3D lung tumour models. The extracellular spacer domain is located between the transmembrane and the extracellular domain and influences the flexibility of the receptor towards the antigen. When a receptor is targeting a more membrane-proximal region of the epitope, a long spacer can preferably bind and mediate efficient tumour cell lysis. For a receptor, which is binding to a membrane-distal region of the epitope, a short spacer can favour efficacy. As the 2A2 targeting domain binds to a membrane-distal region of the ROR1-antigen, it can mediate favourable anti-tumour efficacy when combined with a short spacer (Hudecek *et al.*, 2015). A tendency towards stronger anti-tumour efficacy occurred in H&E stainings and BLI-based measurements. Apoptosis measurements did not show large differences, indicating that they are not sensitive enough for this type of assessment. Cytokine-secretion, on the other hand, revealed that higher concentrations of the activating cytokines IL-2 and IFN-γ were released by the 2A2 ROR1 CAR T cells with a short spacer (Wallstabe, Göttlich, Nelke, Kühnemundt *et al.*, 2019). This confirmed previous findings, where 2D cell culture experiments, as well as animal studies revealed, that the 2A2 targeting domain works best when combined with a short spacer domain and that a suitable spacer design has to be conducted with great care (Hudecek *et al.*, 2015; Jayaraman *et al.*, 2020).

Consequently, the microphysiologic 3D tumour models demonstrated that they are a highly sensitive and enable discrimination of optimal and suboptimal ROR1 CAR T cell designs and that anti-tumour function depends on the latter. To increase sensitivity and to challenge CAR T cells further, semi-static or dynamic tumour models could be engaged in the future for candidate selection, as they present tissue-like architecture with increased tumour cell numbers compared to static tumour models. Additionally, they provide stability and treatment window for longer periods, which could uncover additional effects such as T cell exhaustion and long-term performance of the CAR T cells.

### 5.2.2 Long-term treatment and alternative route of administration of ROR1 CAR T cells leads to strong anti-tumour efficacy

In order to evaluate whether longer treatment periods can improve tumour cell reduction, ROR1 CAR T cell efficacy was assessed over 14 days. So far, limited anti-tumour effects were observed in microphysiologic 3D lung and breast tumour models, as tumour cell removal was not complete after 72 h of ROR1 CAR T cell treatment. Only application of a high dose led to full tumour cell eradication. Dynamic lung tumour models (A549) were treated with ROR1 CAR

T cells (R12sh4-1BB-3z) up to 14 days. Strong reduction of tumour cells was observed after 4 days, which became stagnant until the end of treatment. After 2 weeks of ROR1 CAR T cell application, tumour cells started to invade into deeper layers of the SISmuc matrix. The tumour stem cell maker CD44 revealed increased homogenous expression after 14 days of CAR T cell administration, which was not observed in the control. This goes in line with upregulation of the proliferation marker Ki67, which also occurred upon long-term CAR T cell encounter, respectively. These findings indicate that ROR1 CAR T cells can reduce tumour cell burden even when challenged with large tumour cell masses in dynamic microphysiologic 3D tumour models. Further, they were able to adhere and migrate from the flow of the dynamic setup. However, tumour cell eradication was not achieved. These findings indicate that tumour cells could possibly evade from destruction by downregulation of ROR1, which was not confirmed (data not shown).

Moreover, expression patterns of CD44 and Ki67 indicate that tumour cells could have gained stem cell traits, because CD44 is defined as a cancer stem cell marker. Moreover, it is associated with increased proliferation in NSCLC (Hu *et al.*, 2018) and increased invasion (Batlle & Clevers, 2017). Especially ECM components can change stem cell marker expression, which would explain high intrinsic expression of CD44 when tumour cells are cultured on the SISmuc matrix (Nallanthighal *et al.*, 2019). Invasive growth of A549 cells is especially interesting as this was not observed before on the SISmuc matrix (Stratmann *et al.*, 2014; Göttlich *et al.*, 2016). Consequently, CSCs could evade destruction by CAR T cells or increased proliferation would induce regrowth of the tumour cell mass. Additionally, it is conceivable that ROR1 CAR T cells have entered a state of dysfunction or exhaustion after persisting tumour antigen encounter. Therefore, they could have been unable to eliminate the tumour cell mass completely. This is especially likely as dynamic tumour models challenge CAR T cells with an extensive tumour cell mass favouring T cell exhaustion (McLane *et al.*, 2019; Poorebrahim *et al.*, 2021). These results mirror observations from the clinic where only insufficient tumour control is achieved when solid tumours are treated with CAR T cell-based immunotherapies.

Combination of ROR1 CAR T cell treatment with checkpoint inhibitors could lead to favourable results and should be included in future studies. Moreover, additional doses of CAR T cells could improve therapy outcome or the combination with dasatinib could prevent CAR T cell exhaustion as it can modulate cytolytic activity of the CAR T cells and serve as an on-off-switch preventing exhaustion (Mestermann *et al.*, 2019). Here, preliminary studies have been performed in the microphysiologic 3D tumour models but the study design needs optimisation.

So far, the main application of CAR T cell therapy is mediated via intravenous infusion of the cells into the patient. This application mediates sufficient engraftment in haematological malignancies. However, curative effects for solid tumours are still missing. Here, engraftment and invasion of CAR T cells into the distinct tumour sites could be favoured when administered directly. Direct injection was already assessed for approaches against brain cancer, but is also discussed for several other solid cancers e.g. breast cancer (Tchou *et al.*, 2017; Khan *et al.*, 2019). In order to study this application method and to generate increasing tumour tissue architecture with close proximity of all cell types, a new culture modality was established during this work. Here, two mature semi-static stromal-enriched microphysiologic 3D tumour models were combined to produce sandwich-models leading to stronger tissue association, where ROR1 CAR T cells can then be administered by injection as alternative application route in addition to application via the medium flow. This was conducted as a proof-of principle for stromal-enriched TNBC (MDA-MB-231) and lung tumour models (A549).

H&E stainings and BLI-based measurements revealed strong anti-tumour effects in lung and breast cancer models. However, tumour cells persisted after CAR T cell therapy, recapitulating again the clinical situation. Consequently, it is feasible to perform direct injection into the microphysiologic 3D tumour sandwich models as an alternative application route in addition to application via the medium flow.

Taken together, long-term treatment window and direct injection represent additional improvements of the microphysiologic 3D tumour models making them particularly useful for the evaluation of cellular immunotherapies.

## 5.3 Effects of TME-aspects on ROR1 CAR T cells posed by implementation of TGF-β and CAF enrichment

Solid tumours have a complex tissue architecture with a hostile microenvironment represented by immunological (D'Aloia *et al.*, 2018; Li & Li *et al.*, 2019; Martinez & Moon, 2019) and physical barriers (Mhaidly & Mechta-Grigoriou, 2020), which can impair CAR T cell efficacy by its soluble, matrix and cellular components (Baker *et al.*, 2021). Therefore, these barriers needs to be reflected in the microphysiologic 3D tumour models in order to increase their predictive value. Hence, stromal enrichment and immunosuppression was realised in the microphysiologic 3D tumour models by implementation of CAFs and TGF-β, it was further studied whether this reflects barriers from the TME.

Application of TGF-β revealed that immunological barriers were incorporated and that blockade of TGF-β receptor augments ROR1 CAR T cell function. Successful stromal enrichment with CAFs alone, however, did not demonstrate presence of an immunological or physical barrier and did not impair ROR1 CAR T cell efficacy. Combination of stromal enrichment with CAFs and immunosuppressive effects with TGF-β showed that distinct gene-editing of exhaustion-related genes led to an improved ROR1 CAR T cell product, which withstands the represented aspects of the TME and mediates persisting anti-tumour effects for at least 7 days.

### 5.3.1 TGF-β-receptor inhibition augments ROR1 CAR T cell function

TGF-β is an important factor, which is secreted by different cells within the TME for instance cancer cells, stromal fibroblasts and macrophages. It is described to support metastasis formation, induces EMT in cancer cells, and is associated with a poor prognosis in TNBC (Baselga *et al.*, 2008; Papageorgis & Stylianopoulos, 2015). In the context of CAR T cell therapy its immunosuppressive actions are especially important, which strongly influence resting CD8$^+$ T cells and thereby reducing CAR T cell therapy efficacy (Cottrez & Groux, 2001).

To assess the action of TGF-β on CAR T cells in the context of TNBC, static microphysiologic 3D breast tumour models (MDA-MB-231) were treated with ROR1 CAR T cells under the presence of 10 ng/ml TGF-β. To intervene TGF-β mediated immunosuppressive actions a TGF-β-receptor I inhibitor (SD-208) was administered to evaluate whether this would abrogate inhibitory effects of TGF-β on ROR1 CAR T cells. SD-208 has been proven safe and effective in the clinic for different tumour entities. Furthermore, it is a highly selective and competitive inhibitor and, therefore, can positively influence therapy outcome (Uhl *et al.*, 2004).

ROR1 CAR T cells were challenged for 5 days in breast cancer models and results indicated that TGF-β indeed induced inhibition of lytic effects and reduced secretion of activation-related cytokines from CAR T cells. Additionally, surface expression of PD-1 was found in a higher proportion of CD8⁺ ROR1 CAR T cells, which can be associated with activation, but is also a sign of exhaustion, when T cell mediated lysis decreases. Addition of SD-208 abrogated these inhibitory effects of TGF-β and restored anti-tumour function as well as secretion of IFN-γ and IL-2 of ROR1 CAR T cells. In addition, expression of PD-1 was not increased upon SD-208 administration. Interestingly, SD-208 administration alone, without additional TGF-β led to increased cytokine secretion indicating favourable effects on CAR T cells without extensive TGF-β challenge. This goes in line with existing data of supporting effects of SD-208 in glioblastoma. Uhl *et al.* showed that infiltration of lymphocytes and T cells is increased and secretion of activating cytokines is upregulated upon SD-208 administration (Uhl *et al.*, 2004). Together, these results demonstrate that SD-208 is a valid option to abrogate immunosuppressive function of TGF-β and overcome T cell exhaustion, which was demonstrated in microphysiologic 3D breast tumour models. Here, microphysiologic 3D tumour models were also accepted as an alternative to animal experiments (Stüber *et al.*, 2020). Furthermore, treatment time was extended up to 5 days (from previously 3 days) in static tumour models indicating that longer periods of treatment can indeed be studied. However, anti-tumour effects are still insufficient as about 25 % of tumour cells remained after treatment. In the present study only CD8⁺ ROR1 CAR T cells were administered and combination with CD4⁺ T cells could be beneficial as it has been proven to increase anti-tumour effects by others (Sommermeyer *et al.*, 2016). The combination of CD8⁺ and CD4⁺ CAR T cells is also approved for clinical applications as it leads to favourable outcome (Stock *et al.*, 2019). In addition, CAR T cell numbers can be increased as only 50,000 CAR T cells were administered, which is a rather low concentration when applied into the microphysiologic 3D tumour models (Dasyam *et al.*, 2020).

### 5.3.2 Efficacy of ROR1 CAR T cells is retained in the presence of CAFs

Another factor that can influence administered CAR T cells in solid tumours are stromal cells as part of the hostile TME. In particular, CAFs can affect anti-tumour therapies. One way is as an immunological barrier by secretion of distinct factors such as TGF-β and IL-6. Another possibility is the formation of a physiological barrier via ECM modifications (Mhaidly & Mechta-Grigoriou, 2020; Nazemi & Rainero, 2020). These barriers posed by CAFs have been shown to influence T cells especially, (Baker *et al.*, 2021) and need to be studied during preclinical testing of CAR T cell approaches.

In order to assess if the incorporation of CAFs would form such barriers and represent immunomodulatory aspects from the TME, stromal-enriched microphysiologic 3D lung tumour models (A549) were treated for 5 days with ROR1 CAR T cells under semi-static or dynamic conditions. Quantification of anti-tumour efficacy did not indicate differences when lung tissue-derived fibroblasts were present. Only presence of hDFs led to a slight increase in anti-tumour effects mediated by ROR1 CAR T cells in semi-static lung tumour models, which however, was not statistically significant. Similar results, where no differences in anti-tumour efficacy occurred upon CAF presence, were observed in dynamic cultures of A549 and MDA-MB-231 models (data not shown), especially, because distinction of CAFs and tumour cells remained difficult when MDA-MB-231 cells were present. Analysis of implemented fibroblasts hinted towards a CAF phenotype indicated by marker expression and cytokine secretion, which is discussed in 4.1.5. Therefore, it was conceivable that they could influence CAR T cell efficacy, which however, was not confirmed by quantification of anti-tumour effects.

The observed tissue architecture in microphysiologic 3D lung tumour models revealed that tumour cells and fibroblasts grew in distinct niches, where tumour cells grew in preserved crypts and on top of the matrix, while fibroblasts enriched within the mucosal layer of the SISmuc. Even though this represents an *in vivo*-like tissue architecture, it could result in reduced influences of CAFs on CAR T cells. A549 tumour cells grew distinct from fibroblasts and, therefore, no direct physiological barrier was presented to the CAR T cells as they encounter a larger amount of tumour cells before reaching the fibroblasts. In dynamic models, CAR T cells could also attach and invade from the fibroblast-dense site, but as it is more likely that they rather attach to the site of the tumour model, where antigen-presenting tumour cells are present in a large number. However, CAR T cell administration could be modulated in future experiments to challenge CAR T cells with the possible barriers of fibroblasts first. With this, it could also be studied whether CAF populations are present, which actively reduce immune cell infiltration (Pickup *et al.*, 2014; Baker *et al.*, 2021).

The absence of effects on CAR T cell function in CAF-enriched models was especially surprising as the multiplex proteome analysis confirmed the presence of distinct cytokines (e.g. CXCL5, IL-6, MCP-1) in cocultures of tumour cells and CAFs, which have been described to act immunomodulatory on T cell especially (Baker *et al.*, 2021). As the quantification of cytokines was not possible, it is probable that concentrations of the distinct cytokines are insufficient to mediate effects on ROR CAR T cells. This is particularly likely in the bioreactor setting, where the medium volume is 18-fold higher compared to semi-static models. Measurements of single cytokine concentrations e.g. IL-6 could be performed in future experiments to analyse whether relevant concentrations are present and medium can be supplemented with immunosuppressive cytokines accordingly. Furthermore, distinct subtypes of CAFs have been described which can promote different functions (Costa *et al.*, 2018; Su *et al.*, 2018; Pereira *et al.*, 2019). Therefore, more detailed analysis of CAFs, within the microphysiologic 3D tumour models is required to understand if CAFs with immunomodulatory effects are present and if different subpopulations coexist.

### 5.3.3 Improved gene-edited ROR1 CAR T cells lacking PD-1 and TGF-β receptor induce superior anti-tumour efficacy in the presence of TGF-β and CAF enrichment in microphysiologic 3D breast tumour models

Previous experiments indicated that CAFs alone did not induce the formation of a physical barrier and also no immunosuppressive effects on ROR1 CAR T cells were observed in lung tumour models. However, addition of TGF-β resulted in immunosuppressive effects towards ROR1 CAR T cells in microphysiologic 3D TNBC models (Stüber *et al.*, 2020). Therefore, the immunological barrier represented by TGF-β and CAF enrichment were combined in CAF-enriched semi-static microphysiologic 3D breast tumour models. This could lead to activated or desmoplastic stroma, especially mediated by elevated levels of TGF-β (Bhowmick & Moses, 2005; Thomas & Radhakrishnan, 2019). It is further conceivable that the phenotypically more invasive MDA-MB-231 tumour cells could associate differently with the implemented CAFs, leading to additional challenges for the administered CAR T cells with decreased accessibility of the tumour cells.

As mentioned before, abrogating immunosuppressive effects via pharmacological intervention is a promising strategy to increase therapy efficacy of ROR1 CAR T cells in microphysiologic 3D tumour models for solid tumours, shown for breast cancer (Stüber *et al.*, 2020). Besides, specific gene-editing of the CAR T cells can make them less susceptible towards immunosuppressive effects. This can improve engraftment, efficacy and consequently therapy outcome in solid tumours as it was already shown for PSMA-targeting CAR T cells, which included a dominant negative TGF-β receptor II. Kloss *et al.* observed increased resistance towards exhaustion and long-term persistence tackling two main problems of CAR T cells in solid tumours (Kloss *et al.*, 2018).

In this work, 3 different gene-edited ROR1 CAR T cells for different exhaustion-related genes were assessed. Here, either the PD-1 receptor or the TGF-β receptor was depleted. In addition, a double knock-out lacking both receptors was investigated. These alterations should be favourable as PD-1 and TGF-β receptor are part of the inhibitory axis of T cells and normally lead to T cell exhaustion and consequently lack of therapy efficacy (Poorebrahim *et al.*, 2021). Experiments regarding gene-edited ROR1 CAR T cells were performed together with Dr Razieh Monjezi (AG Hudecek) who designed, produced, and provided the different KO ROR1 CAR T cells.

Gene-edited ROR1 CAR T cells were challenged in stromal-enriched semi-static microphysiologic 3D breast cancer models (MDA-MB-231) under additional TGF-β I administration (10 ng/ml).Therapy time was extended to 7 days. Of note, quantification of the pan-leukocyte marker CD45 indicated high invasion of gene-edited ROR1 CAR T cells lacking

TGF-β receptor, which demonstrates their strong capability to invade into the defined microphysiologic 3D breast tumour models.

Combination of stromal enrichment and TGF-β administration revealed that ROR1 CAR T cells lacking TGF-β and PD-1 receptors indeed showed strong anti-tumour efficacy and activation due to increased amounts of activation-associated cytokines (IFN-γ, IL-2; TNF-α, IL-4). Furthermore, they showed lower proportions of PD-1$^+$ cells for the CD4$^+$ and CD8$^+$ subset. In contrast, WT CAR T cells revealed a high percentage of PD-1-expressing cells, which in this case indicates signs of exhaustion due to reduced tumour cell lysis (Simon & Labarriere, 2017). Therefore, gene-edited cells lacking PD-1 and TGF-β receptor can be confirmed as the superior ROR1 CAR T cell product. However, editing of the single genes can already improve performance compared to the wildtype.

This demonstrates that genetic modification of exhaustion-associated genes can lead to extremely effective CAR T cells, which mediate strong anti-tumour efficacy even when challenged with TGF-β and CAFs. They are able to persist over a longer treatment period, without signs of dysfunction or exhaustion, which goes in line with other studies (Kloss *et al.*, 2018). To confirm lacking exhaustion; however, additional analyses are mandatory such as metabolic and genetic profiling (Wherry & Kurachi, 2015; Blank *et al.*, 2019). To increase anti-tumour effects even further, extension of the treatment time could be assessed in future experiments. Of note, gene-edited ROR1 CAR T cells were genetically modified using Sleeping Beauty-based gene transfer, which provides a better safety profile compared to lentiviral transduction, representing an additional advance towards an improved CAR T cell product (Monjezi *et al.*, 2017).

However, immunomodulatory effects were only achieved when TGF-β was administered in addition to CAFs in microphysiologic 3D TNBC models. CAF enrichment alone did not influence administered CAR T cells strongly (data not shown). As distinction of CAFs and MDA-MB-231 cells was hardly possible future studies are required in order to reveal tumour-stroma interactions and cytokine concentrations. Consequently, the aim to represent aspects from the hostile TME was partly reached, which needs additional attention with regard to interaction between CAFs, tumour cells and immune cells. However, microphysiologic 3D tumour models demonstrated their feasibility for candidate selection also for improved CAR T cell products

# 6. Conclusion

The present work encompasses several improvements of the microphysiologic 3D tumour models, which makes them particularly useful for the evaluation of cellular immunotherapies. It was shown that the SISmuc matrix in the microphysiologic 3D tumour models promotes tissue development of different tumour entities including carcinomas, sarcomas and melanomas. Here, Ewing's sarcoma models were sensitised for $G_{D2}$-targeting CAR T cells (Kailayangiri *et al.*, 2019). Different culture modalities were feasible, that support long-term homeostasis for at least 28 days with increased tissue generation of semi-static models compared to static models. The semi-static culture led to extended treatment window compared to static culture, while being less elaborate than bioreactors and, therefore, bridge the gap between static and dynamic culture. A novel culture modality was introduced, providing sandwich-models for direct injection into the tumour site as alternative application route for cellular immunotherapies. Furthermore, a novel bioreactor setting was applied to allow two separate circulations especially useful when endothelial cells are introduced and immune cell diapedesis is studied (Kühnemundt *et al.*, 2020). A new time-efficient read out parameter was established by using serial BLI-based *in vivo* imaging to visualise model quality and therapy efficacy, overcoming shortcomings of M30 CytoDeath™ ELISA-based apoptosis measurements and increasing the scale of assessment.

The use of primary cells was extensively studied by utilising patient biopsies from lung and skin for cell isolation. Stromal enrichment was achieved by implementation of fibroblasts from lung (tumour) tissue and endothelial cells, which grew in distinct niches on the SISmuc matrix, thereby reflecting aspects of the TME. Stromal enrichment represents TME-aspects within the microphysiologic 3D tumour models and an organised tumour tissue-like architecture was generated, which was comparable to native lung tumour tissue. Cancer-associated fibroblasts (CAFs) are an important cell type in the TME. Characterisation of the secretory profile indicated CAF-associated cytokines were present independently of tumour cells, and support of CAF phenotype was mediated in the presence of tumour cells, but also by the SISmuc matrix alone. Cellular marker expression of α-SMA, FAP and MMP-2/-9 also support that the tumour-isolated fibroblasts showed a CAF phenotype.

The co-culture with lung tumour cells revealed association with stroma signalling and EMT, while breast cancer cells promoted invasion, immunomodulation and angiogenesis. In addition, a protocol for lung organoid isolation was applied overcoming limited success of direct tumour cell isolation.

Taken together, microphysiologic 3D tumour models were improved by increasing long-term tissue-homeostasis for up to 28 days in less elaborate semi-static culture of lung tumour models, implementing TME-components and proved that epithelial and mesenchymal cancer can be modelled *in vitro* with high tissue generation. Furthermore, serial BLI-based *in vivo* imaging was applied increasing read-out comparability towards *in vivo* models as a time efficient analysis method. These findings demonstrate successful realisation of the first specific aim.

For the second specific aim, high sensitivity of microphysiologic 3D tumour models was confirmed. Here, optimal and sub-optimal designed ROR1 CAR T cells proved that anti-tumour function is depended on CAR design and that microphysiologic 3D tumour models are suitable for evaluation and candidate selection (Wallstabe, Göttlich, Nelke, Kühnemundt *et al.*, 2019). Long-term treatment was assessed successfully, for 14 days in dynamic lung tumour models. Addition of TGF-β represented immunosuppressive effects, which were abrogated by SD-208 addition, a specific TGF-β receptor inhibitor. Inhibition of TGF-β receptor augmented anti-tumour efficacy of ROR1 CAR T cells (Stüber *et al.*, 2020). Incorporation of CAFs as stromal enrichment in the microphysiologic 3D lung tumour models was successful, however, did not impair ROR1 CAR T cell efficacy and consequently could not confirm the presence of a physical or immunological barrier by CAF implementation alone.

Combination of semi-static conditions, together with CAF enrichment and immunosuppressive effects of TGF-β was applied to challenge improved gene-edited ROR1 CAR T cells lacking different exhaustion-associated genes. ROR1 CAR T cells without PD-1 and TGF-β receptor indeed favoured superior anti-tumour efficacy and overcame immunosuppressive effects present in solid tumours, demonstrated here for microphysiologic CAF-enriched 3D TNBC models. Therefore, specific aim 3 was partly achieved, as the physical barrier could not be confirmed nor excluded finally. However, the tumour models represent an increased predictive value as adverse effects on stromal cells can be monitored in lieu with anti-tumour effects.

Collectively, the microphysiologic 3D tumour models revealed that differences in efficacy of CAR T cells is depended on the CAR design and can be improved by pharmacological intervention and intelligent gene-editing and by this overcome effects posed by the hostile TME.

# 7. Outlook

In this work, several improvements of the microphysiologic 3D tumour models were achieved and high sensitivity of the microphysiologic 3D tumour models for differently designed CAR T cells was demonstrated. Implementation of TME-aspects was successful, whereas TGF-β mediated immunosuppression respectively, and CAFs led to stromal enrichment and *in vivo*-like tissue architecture. However, physical and immunological barriers could not be confirmed by CAFs alone. Nonetheless, CAF implementation is useful to analyse adverse effects of cellular immunotherapies on stromal cells. Together, this leads to an increase of the predictive value of the microphysiologic 3D tumour models and makes them particularly useful for the evaluation of cellular immunotherapies, but CAFs specifically need to be explored further in the tumour models. Here, it needs to be focussed on tumour-stroma interactions, in order to analyse whether the barriers of the hostile TME can be reflected by CAF enrichment. Additional interventions such as cytokine application or pre-activation of fibroblasts could be analysed (Casey *et al.*, 2008).

Characterisation of CAFs also needs further investigation. Here, cytokine concentrations from multiplex analysis should be quantified and single cell analysis could be performed to analyse subsets of fibroblasts that differ in marker expression and metabolism (Avagliano *et al.*, 2018; Costa *et al.*, 2018; Su *et al.*, 2018; Pereira *et al.*, 2019). Furthermore, additional CAF-related markers should be confirmed and interaction of CAFs and T cells could be studied further (Baker *et al.*, 2021). This should then reveal why no effects on ROR1 CAR T cell efficacy occurred when CAFs were present without TGF-β and could further show if administration of TGF-β does influences CAFs, which has not been studied in this work in detail.

CAF-enriched microphysiologic 3D tumour models also enable the analysis of CAF-targeting approaches, which have increased strongly during the last years (Baker *et al.*, 2021). Here, CAF-specific markers are often targeted in order to abrogate the hostile TME as it was shown for FAP$^{+}$ CAR T cells (Liu *et al.*, 2021). Relevant TME-targeting CAR T cells could be analysed in future studies in the CAF-enriched microphysiologic 3D tumour models in addition to targeting of tumour-specific antigens.

Additionally, other cellular components present in the TME should be incorporated to further increase complexity and by that increase the predictive value and represent influences posed on a therapy administered to solid tumours. Among those cells, macrophages are especially interesting, as they have been described to influence immunotherapies (Vitale *et al.*, 2019; Zhou *et al.*, 2020).

In addition to the TME, different aspects need attention and further exploration.

Isolation of lung/tumour organoids needs to be optimised by using tissue directly after surgery and adapting enzymatic digestion (Quatromoni *et al.*, 2015).

The application of the BLI-based imaging could be further expanded by combining different luciferases e.g. *gaussia* luciferase in order to analyse different cell populations (Lewandrowski *et al.*, 2014). Furthermore, this technique can be combined with other cell-tracking methods, which engage fluorescence as this can also be quantified in the IVIS device.

Further improvements regarding CAR T cell therapy for solid tumours are needed to mediate complete tumour cell removal. This can be performed with the gene-edited ROR1 CAR T cells by investigating longer treatment periods (> 7 days) and by application of an additional or increased dose of CAR T cells. In addition, intervention with checkpoint inhibitors could increase therapy response.

Other cellular immunotherapeutic approaches like NK-CAR cells can also be evaluated in the future, as they are also promising for solid tumours (Xie *et al.*, 2020). Additionally, analysis of the mutation background of the tumour cells in combination with infiltration of different immune cells could be studied (Kortlever *et al.*, 2017).

Currently, the microphysiologic 3D tumour models are engaged to explore other promising targets in solid tumours like integrin$\alpha_v\beta_3$ in melanoma models, which is targeted with CAR T cells. Integrin$\alpha_v\beta_3$ has been described as a target in several malignancies such as melanoma, breast and pancreatic cancer, but expression on CAFs and other cells from the TME was also shown. Integrin$\alpha_v\beta_3$-targeting CAR T cells have demonstrated high anti-tumour efficacy during *in vitro* an *in vivo* studies (Wallstabe *et al.*, 2018). Application of integrin$\alpha_v\beta_3$-targeting CAR T cells could abrogate parts of the hostile TME as well as tumour cells, which together could overcome the barriers present in solid tumours, leading to increased therapy outcome. Here, the CAF-enriched microphysiologic 3D tumour models can be applied in order to evaluate effects on cancer cells and on cells from the TME.

Collectively, the defined microphysiologic 3D tumour models are scalable, reproducible, standardisable and modular. They show an enhanced predictive value due to implemented TME-aspects and high sensitivity for the evaluation of CAR T cells. The microphysiologic 3D tumour models can contribute to the principles of “3R” and can be applied for translational research and preclinical testing, and are especially advantageous for evaluation and candidate selection of cellular immunotherapies.

# References

(2018) Tissue-engineered disease models. *Nature Biomedical Engineering*, 2(12), 879–880. Available from: https://doi.org/10.1038/s41551-018-0339-2.

Acerbi, I., Cassereau, L., Dean, I., Shi, Q., Au, A. & Park, C. et al. (2015) Human breast cancer invasion and aggression correlates with ECM stiffening and immune cell infiltration. *Integrative Biology : Quantitative Biosciences from Nano to Macro*, 7(10), 1120–1134. Available from: https://doi.org/10.1039/c5ib00040h.

Acloque, H., Adams, M.S., Fishwick, K., Bronner-Fraser, M. & Nieto, M.A. (2009) Epithelial-mesenchymal transitions: the importance of changing cell state in development and disease. *The Journal of Clinical Investigation*, 119(6), 1438–1449. Available from: https://doi.org/10.1172/JCI38019.

Ahmed, A.R.H., Griffiths, A.B., Tilby, M.T., Westley, B.R. & May, F.E.B. (2012) TFF3 is a normal breast epithelial protein and is associated with differentiated phenotype in early breast cancer but predisposes to invasion and metastasis in advanced disease. *The American Journal of Pathology*, 180(3), 904–916. Available from: https://doi.org/10.1016/j.ajpath.2011.11.022.

Akhurst, R.J. & Derynck, R. (2001) TGF- β signaling in cancer – a double-edged sword. *Trends in Cell Biology*, 11(11), S44-S51. Available from: https://doi.org/10.1016/S0962-8924(01)02130-4.

Allinen, M., Beroukhim, R., Cai, L., Brennan, C., Lahti-Domenici, J. & Huang, H. et al. (2004) Molecular characterization of the tumor microenvironment in breast cancer. *Cancer Cell*, 6(1), 17–32. Available from: https://doi.org/10.1016/j.ccr.2004.06.010.

Anderberg, C. & Pietras, K. (2009) On the origin of cancer-associated fibroblasts. *Cell Cycle (Georgetown, Tex.)*, 8(10), 1461–1462. Available from: https://doi.org/10.4161/cc.8.10.8557.

Anderson, K.G., Stromnes, I.M. & Greenberg, P.D. (2017) Obstacles Posed by the Tumor Microenvironment to T cell Activity: A Case for Synergistic Therapies. *Cancer Cell*, 31(3), 311–325. Available from: https://doi.org/10.1016/j.ccell.2017.02.008.

Annes, J.P., Munger, J.S. & Rifkin, D.B. (2003) Making sense of latent TGFbeta activation. *Journal of Cell Science*, 116(Pt 2), 217–224. Available from: https://doi.org/10.1242/jcs.00229.

Ardolino, L. & Joshua, A. (2019) Immune checkpoint inhibitors in malignancy. *Australian Prescriber*, 42(2), 62–67. Available from: https://doi.org/10.18773/austprescr.2019.012.

Avagliano, A., Granato, G., Ruocco, M.R., Romano, V., Belviso, I. & Carfora, A. et al. (2018) Metabolic Reprogramming of Cancer Associated Fibroblasts: The Slavery of Stromal

Fibroblasts. *BioMed Research International*, 2018, 6075403. Available from: https://doi.org/10.1155/2018/6075403.

Baghban, R., Roshangar, L., Jahanban-Esfahlan, R., Seidi, K., Ebrahimi-Kalan, A. & Jaymand, M. et al. (2020) Tumor microenvironment complexity and therapeutic implications at a glance. *Cell Communication and Signaling*, 18(1), 59. Available from: https://doi.org/10.1186/s12964-020-0530-4.

Baker, A.T., Abuwarwar, M.H., Poly, L., Wilkins, S. & Fletcher, A.L. (2021) Cancer-Associated Fibroblasts and T Cells: From Mechanisms to Outcomes. *The Journal of Immunology*, 206(2), 310–320. Available from: https://doi.org/10.4049/jimmunol.2001203.

Balakrishnan, A., Goodpaster, T., Randolph-Habecker, J., Hoffstrom, B.G., Jalikis, F.G. & Koch, L.K. et al. (2017) Analysis of ROR1 Protein Expression in Human Cancer and Normal Tissues. *Clinical Cancer Research : an Official Journal of the American Association for Cancer Research*, 23(12), 3061–3071. Available from: https://doi.org/10.1158/1078-0432.CCR-16-2083.

Balasubramanian, P., Prabhakaran, M.P., Sireesha, M. & Ramakrishna, S. (2013) Collagen in Human Tissues: Structure, Function, and Biomedical Implications from a Tissue Engineering Perspective. In: Abe, A., Kausch, H.-H., Möller, M. & Pasch, H. (Eds.) *Polymer Composites - Polyolefin Fractionation - Polymeric Peptidomimetics - Collagens.* Springer: Berlin, Heidelberg, pp. 173–206.

Balogh, K.N., Templeton, D.J. & Cross, J.V. (2018) Macrophage Migration Inhibitory Factor protects cancer cells from immunogenic cell death and impairs anti-tumor immune responses. *PLOS ONE*, 13(6), e0197702. Available from: https://doi.org/10.1371/journal.pone.0197702.

Barbazán, J. & Matic Vignjevic, D. (2019) Cancer associated fibroblasts: is the force the path to the dark side? *Current Opinion in Cell Biology*, 56, 71–79. Available from: https://doi.org/10.1016/j.ceb.2018.09.002.

Barrett, R. & Puré, E. (2020) Cancer-associated fibroblasts: key determinants of tumor immunity and immunotherapy. *Current Opinion in Immunology*, 64, 80–87. Available from: https://doi.org/10.1016/j.coi.2020.03.004.

Baselga, J., Rothenberg, M.L., Tabernero, J., Seoane, J., Daly, T. & Cleverly, A. et al. (2008) TGF-beta signalling-related markers in cancer patients with bone metastasis. *Biomarkers : Biochemical Indicators of Exposure, Response, and Susceptibility to Chemicals*, 13(2), 217–236. Available from: https://doi.org/10.1080/13547500701676019.

Baskar, S., Wiestner, A., Wilson, W.H., Pastan, I. & Rader, C. (2012) Targeting malignant B cells with an immunotoxin against ROR1. *MAbs*, 4(3), 349–361. Available from: https://doi.org/10.4161/mabs.19870.

Batlle, E. & Clevers, H. (2017) Cancer stem cells revisited. *Nature Medicine*, 23(10), 1124–1134. Available from: https://doi.org/10.1038/nm.4409.

Baur, F., Nietzer, S.L., Kunz, M., Saal, F., Jeromin, J. & Matschos, S. et al. (2019) Connecting Cancer Pathways to Tumor Engines: A Stratification Tool for Colorectal Cancer Combining Human In Vitro Tissue Models with Boolean In Silico Models. *Cancers*, 12(1). Available from: https://doi.org/10.3390/cancers12010028.

Berger, C., Bjørlykke, Y., Hahn, L., Mühlemann, M., Kress, S. & Walles, H. et al. (2020) Matrix decoded - A pancreatic extracellular matrix with organ specific cues guiding human iPSC differentiation. *Biomaterials*, 244, 119766. Available from: https://doi.org/10.1016/j.biomaterials.2020.119766.

Berger, C., Sommermeyer, D., Hudecek, M., Berger, M., Balakrishnan, A. & Paszkiewicz, P.J. et al. (2015) Safety of targeting ROR1 in primates with chimeric antigen receptor-modified T cells. *Cancer Immunology Research*, 3(2), 206–216. Available from: https://doi.org/10.1158/2326-6066.CIR-14-0163.

Bergin, A.R.T. & Loi, S. (2019) Triple-negative breast cancer: recent treatment advances. *F1000Research*, 8. Available from: https://doi.org/10.12688/f1000research.18888.1.

Bhowmick, N.A. & Moses, H.L. (2005) Tumor-stroma interactions. *Current Opinion in Genetics & Development*, 15(1), 97–101. Available from: https://doi.org/10.1016/j.gde.2004.12.003.

Bissell, M.J. (1981) The Differentiated State of Normal and Malignant Cells or How to Define a “Normal” Cell in Culture. In: Bourne, G.H., Danielli, J.F. & Jeon, K.W. (Eds.) *International Review of Cytology.* Academic Press, pp. 27–100.

Bissell, M.J. & Radisky, D. (2001) Putting tumours in context. *Nature Reviews Cancer*, 1(1), 46–54. Available from: https://doi.org/10.1038/35094059.

Bissell, M.J., Rizki, A. & Mian, I.S. (2003) Tissue architecture: the ultimate regulator of breast epithelial function. *Current Opinion in Cell Biology*, 15(6), 753–762. Available from: https://doi.org/10.1016/j.ceb.2003.10.016.

Blank, C.U., Haining, W.N., Held, W., Hogan, P.G., Kallies, A. & Lugli, E. et al. (2019) Defining 'T cell exhaustion'. *Nature Reviews Immunology*, 19(11), 665–674. Available from: https://doi.org/10.1038/s41577-019-0221-9.

Blobe, G.C., Schiemann, W.P. & Lodish, H.F. (2000) Role of transforming growth factor beta in human disease. *The New England Journal of Medicine*, 342(18), 1350–1358. Available from: https://doi.org/10.1056/NEJM200005043421807.

Borcherding, N., Kusner, D., Liu, G.-H. & Zhang, W. (2014) ROR1, an embryonic protein with an emerging role in cancer biology. *Protein & Cell*, 5(7), 496–502. Available from: https://doi.org/10.1007/s13238-014-0059-7.

Boroughs, A.C., Larson, R.C., Choi, B.D., Bouffard, A.A., Riley, L.S. & Schiferle, E. et al. (2019) Chimeric antigen receptor costimulation domains modulate human regulatory T cell function. *JCI Insight*, 5. Available from: https://doi.org/10.1172/jci.insight.126194.

Bremnes, R.M., Dønnem, T., Al-Saad, S., Al-Shibli, K., Andersen, S. & Sirera, R. et al. (2011) The role of tumor stroma in cancer progression and prognosis: emphasis on carcinoma-associated fibroblasts and non-small cell lung cancer. *Journal of Thoracic Oncology : Official Publication of the International Association for the Study of Lung Cancer*, 6(1), 209–217. Available from: https://doi.org/10.1097/JTO.0b013e3181f8a1bd.

Brentjens, R.J. & Curran, K.J. (2012) Novel cellular therapies for leukemia: CAR-modified T cells targeted to the CD19 antigen. *Hematology. American Society of Hematology. Education Program*, 2012, 143–151. Available from: https://doi.org/10.1182/asheducation-2012.1.143.

Brentjens, R.J., Davila, M.L., Riviere, I., Park, J., Wang, X. & Cowell, L.G. et al. (2013) CD19-targeted T cells rapidly induce molecular remissions in adults with chemotherapy-refractory acute lymphoblastic leukemia. *Science Translational Medicine*, 5(177), 177ra38. Available from: https://doi.org/10.1126/scitranslmed.3005930.

Bretscher, V., Andreutti, D., Neuville, P., Martin, M., Martin, F. & Lefebvre, O. et al. (2000) GM-CSF expression by tumor cells correlates with aggressivity and with stroma reaction formation. *Journal of Submicroscopic Cytology and Pathology*, 32(4), 525–533.

Breznik, B., Motaln, H. & Lah Turnšek, T. (2017) Proteases and cytokines as mediators of interactions between cancer and stromal cells in tumours. *Biological Chemistry*, 398(7), 709–719. Available from: https://doi.org/10.1515/hsz-2016-0283.

Bruzzese, F., Hägglöf, C., Leone, A., Sjöberg, E., Roca, M.S. & Kiflemariam, S. et al. (2014) Local and systemic protumorigenic effects of cancer-associated fibroblast-derived GDF15. *Cancer Research*, 74(13), 3408–3417. Available from: https://doi.org/10.1158/0008-5472.CAN-13-2259.

Bühler, H. & Schaller, G. (2005) Transfection of keratin 18 gene in human breast cancer cells causes induction of adhesion proteins and dramatic regression of malignancy in vitro and in vivo. *Molecular Cancer Research : MCR*, 3(7), 365–371. Available from: https://doi.org/10.1158/1541-7786.MCR-04-0117.

Calon, A., Tauriello, D.V.F. & Batlle, E. (2014) TGF-beta in CAF-mediated tumor growth and metastasis. *Seminars in Cancer Biology*, 25, 15–22. Available from: https://doi.org/10.1016/j.semcancer.2013.12.008.

Cancer (2020). Available from: https://www.who.int/news-room/fact-sheets/detail/cancer [Accessed 17 June 2020].

Carvalho, I., Milanezi, F., Martins, A., Reis, R.M. & Schmitt, F. (2005) Overexpression of platelet-derived growth factor receptor alpha in breast cancer is associated with tumour progression. *Breast Cancer Research*, 7(5), R788-95. Available from: https://doi.org/10.1186/bcr1304.

Casey, T.M., Eneman, J., Crocker, A., White, J., Tessitore, J. & Stanley, M. et al. (2008) Cancer associated fibroblasts stimulated by transforming growth factor beta1 (TGF-beta 1) increase invasion rate of tumor cells: a population study. *Breast Cancer Research and Treatment*, 110(1), 39–49. Available from: https://doi.org/10.1007/s10549-007-9684-7.

Castello, L.M., Raineri, D., Salmi, L., Clemente, N., Vaschetto, R. & Quaglia, M. et al. (2017) Osteopontin at the Crossroads of Inflammation and Tumor Progression. *Mediators of Inflammation*, 2017, 4049098. Available from: https://doi.org/10.1155/2017/4049098.

Cen, L., Liu, W., Cui, L., Zhang, W. & Cao, Y. (2008) Collagen tissue engineering: development of novel biomaterials and applications. *Pediatric Research*, 63(5), 492–496. Available from: https://doi.org/10.1203/PDR.0b013e31816c5bc3.

Chaignaud, B.E., Langer, R. & Vacanti, J.P. (2013) The History of Tissue Engineering Using Synthetic Biodegradable Polymer Scaffolds and Cells. In: Atala, A., Mooney, D.J., Arbor, A., Vacanti, J.P. & Langer, R. (Eds.) *Synthetic Biodegradable Polymer Scaffolds.* Birkhäuser Boston: Boston, MA, pp. 1–14.

Chen, C., Wang, Z.Y., Weng, J., Wang, Z.B., Mei, J. & Du, X.H. et al. (2017) Effect of two different acellular lung matrices on α-SMA expression in A549 cells. *Zhonghua yi xue za zhi*, 97(4), 303–307. Available from: https://doi.org/10.3760/cma.j.issn.0376-2491.2017.04.014.

Chen, Z., Fillmore, C.M., Hammerman, P.S., Kim, C.F. & Wong, K.-K. (2014) Non-small-cell lung cancers: a heterogeneous set of diseases. *Nature Reviews Cancer*, 14(8), 535–546. Available from: https://doi.org/10.1038/nrc3775.

Choi, B.D., Yu, X., Castano, A.P., Bouffard, A.A., Schmidts, A. & Larson, R.C. et al. (2019) CAR-T cells secreting BiTEs circumvent antigen escape without detectable toxicity. *Nature Biotechnology*, 37(9), 1049–1058. Available from: https://doi.org/10.1038/s41587-019-0192-1.

Choi, M.Y., Widhopf, G.F., Ghia, E.M., Kidwell, R.L., Hasan, M.K. & Yu, J. et al. (2018) Phase I Trial: Cirmtuzumab Inhibits ROR1 Signaling and Stemness Signatures in Patients with Chronic Lymphocytic Leukemia. *Cell Stem Cell*, 22(6), 951-959.e3. Available from: https://doi.org/10.1016/j.stem.2018.05.018.

Close, D.M., Xu, T., Sayler, G.S. & Ripp, S. (2011) In vivo bioluminescent imaging (BLI): noninvasive visualization and interrogation of biological processes in living animals. *Sensors (Basel, Switzerland)*, 11(1), 180–206. Available from: https://doi.org/10.3390/s110100180.

Costa, A., Kieffer, Y., Scholer-Dahirel, A., Pelon, F., Bourachot, B. & Cardon, M. et al. (2018) Fibroblast Heterogeneity and Immunosuppressive Environment in Human Breast Cancer.

*Cancer Cell*, 33(3), 463-479.e10. Available from: https://doi.org/10.1016/j.ccell.2018.01.011.

Cottrez, F. & Groux, H. (2001) Regulation of TGF-beta response during T cell activation is modulated by IL-10. *Journal of Immunology (Baltimore, Md. : 1950)*, 167(2), 773–778. Available from: https://doi.org/10.4049/jimmunol.167.2.773.

Courau, T., Bonnereau, J., Chicoteau, J., Bottois, H., Remark, R. & Assante Miranda, L. et al. (2019) Cocultures of human colorectal tumor spheroids with immune cells reveal the therapeutic potential of MICA/B and NKG2A targeting for cancer treatment. *Journal for Immunotherapy of Cancer*, 7(1), 74. Available from: https://doi.org/10.1186/s40425-019-0553-9.

Cowell, C.F., Weigelt, B., Sakr, R.A., Ng, C.K.Y., Hicks, J. & King, T.A. et al. (2013) Progression from ductal carcinoma in situ to invasive breast cancer: revisited. *Molecular Oncology*, 7(5), 859–869. Available from: https://doi.org/10.1016/j.molonc.2013.07.005.

Cserni, G., Chmielik, E., Cserni, B. & Tot, T. (2018) The new TNM-based staging of breast cancer. *Virchows Archiv*, 472(5), 697–703. Available from: https://doi.org/10.1007/s00428-018-2301-9.

da Silva, J.L., Dos Santos, A.L.S., Nunes, N.C.C., Moraes Lino da Silva, F. de, Ferreira, C.G.M. & Melo, A.C. de (2019) Cancer immunotherapy: the art of targeting the tumor immune microenvironment. *Cancer Chemotherapy and Pharmacology*, 84(2), 227–240. Available from: https://doi.org/10.1007/s00280-019-03894-3.

D'Aloia, M.M., Zizzari, I.G., Sacchetti, B., Pierelli, L. & Alimandi, M. (2018) CAR-T cells: the long and winding road to solid tumors. *Cell Death & Disease*, 9(3), 282. Available from: https://doi.org/10.1038/s41419-018-0278-6.

D'Amico, L., Mahajan, S., Capietto, A.-H., Yang, Z., Zamani, A. & Ricci, B. et al. (2016) Dickkopf-related protein 1 (Dkk1) regulates the accumulation and function of myeloid derived suppressor cells in cancer. *The Journal of Experimental Medicine*, 213(5), 827–840. Available from: https://doi.org/10.1084/jem.20150950.

D'Arcangelo, E., Wu, N.C., Cadavid, J.L. & McGuigan, A.P. (2020) The life cycle of cancer-associated fibroblasts within the tumour stroma and its importance in disease outcome. *British Journal of Cancer*, 122(7), 931–942. Available from: https://doi.org/10.1038/s41416-019-0705-1.

Dasyam, N., George, P. & Weinkove, R. (2020) Chimeric antigen receptor T-cell therapies: Optimising the dose. *British Journal of Clinical Pharmacology*, 86(9), 1678–1689. Available from: https://doi.org/10.1111/bcp.14281.

Dijkstra, K.K., Monkhorst, K., Schipper, L.J., Hartemink, K.J., Smit, E.F. & Kaing, S. et al. (2020) Challenges in Establishing Pure Lung Cancer Organoids Limit Their Utility for

Personalized Medicine. *Cell Reports*, 31(5), 107588. Available from: https://doi.org/10.1016/j.celrep.2020.107588.

Ding, X., Xi, W., Ji, J., Cai, Q., Jiang, J. & Shi, M. et al. (2018) HGF derived from cancer-associated fibroblasts promotes vascularization in gastric cancer via PI3K/AKT and ERK1/2 signaling. *Oncology Reports*, 40(2), 1185–1195. Available from: https://doi.org/10.3892/or.2018.6500.

Dongre, A. & Weinberg, R.A. (2019) New insights into the mechanisms of epithelial-mesenchymal transition and implications for cancer. *Nature Reviews Molecular Cell Biology*, 20(2), 69–84. Available from: https://doi.org/10.1038/s41580-018-0080-4.

Drost, J. & Clevers, H. (2018) Organoids in cancer research. *Nature Reviews Cancer*, 18(7), 407–418. Available from: https://doi.org/10.1038/s41568-018-0007-6.

Duma, N., Santana-Davila, R. & Molina, J.R. (2019) Non-Small Cell Lung Cancer: Epidemiology, Screening, Diagnosis, and Treatment. *Mayo Clinic Proceedings*, 94(8), 1623–1640. Available from: https://doi.org/10.1016/j.mayocp.2019.01.013.

Edmondson, R., Broglie, J.J., Adcock, A.F. & Yang, L. (2014) Three-dimensional cell culture systems and their applications in drug discovery and cell-based biosensors. *Assay and Drug Development Technologies*, 12(4), 207–218. Available from: https://doi.org/10.1089/adt.2014.573.

Elston, C.W. & Ellis, I.O. (1991) Pathological prognostic factors in breast cancer. I. The value of histological grade in breast cancer: experience from a large study with long-term follow-up. *Histopathology*, 19(5), 403–410. Available from: https://doi.org/10.1111/j.1365-2559.1991.tb00229.x.

Erdogan, B. & Webb, D.J. (2017) Cancer-associated fibroblasts modulate growth factor signaling and extracellular matrix remodeling to regulate tumor metastasis. *Biochemical Society Transactions*, 45(1), 229–236. Available from: https://doi.org/10.1042/BST20160387.

ESMO (2018) EMA Recommends Granting Marketing Authorisations for the First Two CAR T-cell Therapies in the EU. *ESMO,* 9 July. Available from: https://www.esmo.org/oncology-news/EMA-Recommends-Granting-Marketing-Authorisations-for-the-First-Two-CAR-T-cell-Therapies-in-the-EU [Accessed 24 June 2020].

EUR-Lex - 52020DC0016 - EN - EUR-Lex (2021). Available from: https://eur-lex.europa.eu/legal-content/EN/TXT/?qid=1581689520921&uri=CELEX:52020DC0016 [Accessed 19 February 2021].

*FDA* (2019) KYMRIAH (tisagenlecleucel), 5 April. Available from: https://www.fda.gov/vaccines-blood-biologics/cellular-gene-therapy-products/kymriah-tisagenlecleucel [Accessed 24 June 2020].

Ferry-Galow, K.V., Datta, V., Makhlouf, H.R., Wright, J., Wood, B.J. & Levy, E. et al. (2018) What Can Be Done to Improve Research Biopsy Quality in Oncology Clinical Trials? *Journal of Oncology Practice*, JOP1800092. Available from: https://doi.org/10.1200/JOP.18.00092.

Figenschau, S.L., Knutsen, E., Urbarova, I., Fenton, C., Elston, B. & Perander, M. et al. (2018) ICAM1 expression is induced by proinflammatory cytokines and associated with TLS formation in aggressive breast cancer subtypes. *Scientific Reports*, 8(1), 11720. Available from: https://doi.org/10.1038/s41598-018-29604-2.

Filippi, M.-D. (2016) Mechanism of Diapedesis: Importance of the Transcellular Route. *Advances in Immunology*, 129, 25–53. Available from: https://doi.org/10.1016/bs.ai.2015.09.001.

Fiori, M.E., Di Franco, S., Villanova, L., Bianca, P., Stassi, G. & Maria, R. de (2019) Cancer-associated fibroblasts as abettors of tumor progression at the crossroads of EMT and therapy resistance. *Molecular Cancer*, 18(1), 70. Available from: https://doi.org/10.1186/s12943-019-0994-2.

Fong, Y.-C., Liu, S.-C., Huang, C.-Y., Li, T.-M., Hsu, S.-F. & Kao, S.-T. et al. (2009) Osteopontin increases lung cancer cells migration via activation of the alphavbeta3 integrin/FAK/Akt and NF-kappaB-dependent pathway. *Lung Cancer*, 64(3), 263–270. Available from: https://doi.org/10.1016/j.lungcan.2008.09.003.

Foulkes, W.D., Smith, I.E. & Reis-Filho, J.S. (2010) Triple-negative breast cancer. *The New England Journal of Medicine*, 363(20), 1938–1948. Available from: https://doi.org/10.1056/NEJMra1001389.

Fukuhara, S., Sako, K., Noda, K., Nagao, K., Miura, K. & Mochizuki, N. (2009) Tie2 is tied at the cell-cell contacts and to extracellular matrix by angiopoietin-1. *Experimental & Molecular Medicine*, 41(3), 133–139. Available from: https://doi.org/10.3858/emm.2009.41.3.016.

Fukumura, D., Xavier, R., Sugiura, T., Chen, Y., Park, E.-C. & Lu, N. et al. (1998) Tumor Induction of VEGF Promoter Activity in Stromal Cells. *Cell*, 94(6), 715–725. Available from: https://doi.org/10.1016/S0092-8674(00)81731-6.

Gardner, R.A., Finney, O., Annesley, C., Brakke, H., Summers, C. & Leger, K. et al. (2017) Intent-to-treat leukemia remission by CD19 CAR T cells of defined formulation and dose in children and young adults. *Blood*, 129(25), 3322–3331. Available from: https://doi.org/10.1182/blood-2017-02-769208.

Gazdar, A.F., Girard, L., Lockwood, W.W., Lam, W.L. & Minna, J.D. (2010) Lung cancer cell lines as tools for biomedical discovery and research. *Journal of the National Cancer Institute*, 102(17), 1310–1321. Available from: https://doi.org/10.1093/jnci/djq279.

Ghorashian, S., Kramer, A.M., Onuoha, S., Wright, G., Bartram, J. & Richardson, R. et al. (2019) Enhanced CAR T cell expansion and prolonged persistence in pediatric patients with ALL treated with a low-affinity CD19 CAR. *Nature Medicine*, 25(9), 1408–1414. Available from: https://doi.org/10.1038/s41591-019-0549-5.

Giacomini, A., Ghedini, G.C., Presta, M. & Ronca, R. (2018) Long pentraxin 3: A novel multifaceted player in cancer. *Biochimica Et Biophysica Acta (BBA) - Reviews on Cancer*, 1869(1), 53–63. Available from: https://doi.org/10.1016/j.bbcan.2017.11.004.

Gibney, G.T., Kudchadkar, R.R., DeConti, R.C., Thebeau, M.S., Czupryn, M.P. & Tetteh, L. et al. (2015) Safety, correlative markers, and clinical results of adjuvant nivolumab in combination with vaccine in resected high-risk metastatic melanoma. *Clinical Cancer Research : an Official Journal of the American Association for Cancer Research*, 21(4), 712–720. Available from: https://doi.org/10.1158/1078-0432.CCR-14-2468.

Göttlich, C., Kunz, M., Zapp, C., Nietzer, S.L., Walles, H. & Dandekar, T. et al. (2018) A combined tissue-engineered/in silico signature tool patient stratification in lung cancer. *Molecular Oncology*, 12(8), 1264–1285. Available from: https://doi.org/10.1002/1878-0261.12323.

Göttlich, C., Müller, L.C., Kunz, M., Schmitt, F., Walles, H. & Walles, T. et al. (2016) A Combined 3D Tissue Engineered In Vitro/In Silico Lung Tumor Model for Predicting Drug Effectiveness in Specific Mutational Backgrounds. *Journal of Visualized Experiments : JoVE*, (110), e53885. Available from: https://doi.org/10.3791/53885.

Groeber, F., Schober, L., Schmid, F.F., Traube, A., Kolbus-Hernandez, S. & Daton, K. et al. (2016) Catch-up validation study of an in vitro skin irritation test method based on an open source reconstructed epidermis (phase II). *Toxicology in Vitro : an International Journal Published in Association with BIBRA*, 36, 254–261. Available from: https://doi.org/10.1016/j.tiv.2016.07.008.

Gross, G., Waks, T. & Eshhar, Z. (1989) Expression of immunoglobulin-T-cell receptor chimeric molecules as functional receptors with antibody-type specificity. *Proceedings of the National Academy of Sciences of the United States of America*, 86(24), 10024–10028. Available from: https://doi.org/10.1073/pnas.86.24.10024.

Grugan, K.D., Miller, C.G., Yao, Y., Michaylira, C.Z., Ohashi, S. & Klein-Szanto, A.J. et al. (2010) Fibroblast-secreted hepatocyte growth factor plays a functional role in esophageal squamous cell carcinoma invasion. *Proceedings of the National Academy of Sciences*, 107(24), 11026–11031. Available from: https://doi.org/10.1073/pnas.0914295107.

Grünewald, T.G.P., Cidre-Aranaz, F., Surdez, D., Tomazou, E.M., Álava, E. de & Kovar, H. et al. (2018) Ewing sarcoma. *Nature Reviews Disease Primers*, 4(1), 5. Available from: https://doi.org/10.1038/s41572-018-0003-x.

Gubbiotti, M.A., Buraschi, S., Kapoor, A. & Iozzo, R.V. (2020) Proteoglycan signaling in tumor angiogenesis and endothelial cell autophagy. *Seminars in Cancer Biology*, 62, 1–8. Available from: https://doi.org/10.1016/j.semcancer.2019.05.003.

Guda, M.R., Rashid, M.A., Asuthkar, S., Jalasutram, A., Caniglia, J.L. & Tsung, A.J. et al. (2019) Pleiotropic role of macrophage migration inhibitory factor in cancer. *American Journal of Cancer Research*, 9(12), 2760–2773.

Hamilton, G., Rath, B., Klameth, L. & Hochmair, M.J. (2016) Small cell lung cancer: Recruitment of macrophages by circulating tumor cells. *Oncoimmunology*, 5(3), e1093277. Available from: https://doi.org/10.1080/2162402X.2015.1093277.

Hanahan, D. & Weinberg, R.A. (2000) The Hallmarks of Cancer. *Cell*, 100(1), 57–70. Available from: https://doi.org/10.1016/S0092-8674(00)81683-9.

Hanahan, D. & Weinberg, R.A. (2011) Hallmarks of cancer: the next generation. *Cell*, 144(5), 646–674. Available from: https://doi.org/10.1016/j.cell.2011.02.013.

Hao, Y., Baker, D. & Dijke, P. ten (2019) TGF-β-Mediated Epithelial-Mesenchymal Transition and Cancer Metastasis. *International Journal of Molecular Sciences*, 20(11). Available from: https://doi.org/10.3390/ijms20112767.

Heberle, H., Meirelles, G.V., da Silva, F.R., Telles, G.P. & Minghim, R. (2015) InteractiVenn: a web-based tool for the analysis of sets through Venn diagrams. *BMC Bioinformatics*, 16, 169. Available from: https://doi.org/10.1186/s12859-015-0611-3.

Heczey, A., Louis, C.U., Savoldo, B., Dakhova, O., Durett, A. & Grilley, B. et al. (2017) CAR T Cells Administered in Combination with Lymphodepletion and PD-1 Inhibition to Patients with Neuroblastoma. *Molecular Therapy : the Journal of the American Society of Gene Therapy*, 25(9), 2214–2224. Available from: https://doi.org/10.1016/j.ymthe.2017.05.012.

Herbst, R.S., Heymach, J.V. & Lippman, S.M. (2008) Lung cancer. *The New England Journal of Medicine*, 359(13), 1367–1380. Available from: https://doi.org/10.1056/NEJMra0802714.

Hollmén, M., Karaman, S., Schwager, S., Lisibach, A., Christiansen, A.J. & Maksimow, M. et al. (2016) G-CSF regulates macrophage phenotype and associates with poor overall survival in human triple-negative breast cancer. *Oncoimmunology*, 5(3), e1115177. Available from: https://doi.org/10.1080/2162402X.2015.1115177.

Holmes, A., Brown, R. & Shakesheff, K. (2009) Engineering tissue alternatives to animals: applying tissue engineering to basic research and safety testing. *Regenerative Medicine*, 4(4), 579–592. Available from: https://doi.org/10.2217/rme.09.26.

Hong, I.-S. (2016) Stimulatory versus suppressive effects of GM-CSF on tumor progression in multiple cancer types. *Experimental & Molecular Medicine*, 48(7), e242. Available from: https://doi.org/10.1038/emm.2016.64.

Hu, B., Ma, Y., Yang, Y., Zhang, L., Han, H. & Chen, J. (2018) CD44 promotes cell proliferation in non-small cell lung cancer. *Oncology Letters*, 15(4), 5627–5633. Available from: https://doi.org/10.3892/ol.2018.8051.

Hudecek, M., Lupo-Stanghellini, M.-T., Kosasih, P.L., Sommermeyer, D., Jensen, M.C. & Rader, C. et al. (2013) Receptor affinity and extracellular domain modifications affect tumor recognition by ROR1-specific chimeric antigen receptor T cells. *Clinical Cancer Research : an Official Journal of the American Association for Cancer Research*, 19(12), 3153–3164. Available from: https://doi.org/10.1158/1078-0432.CCR-13-0330.

Hudecek, M., Schmitt, T.M., Baskar, S., Lupo-Stanghellini, M.T., Nishida, T. & Yamamoto, T.N. et al. (2010) The B-cell tumor-associated antigen ROR1 can be targeted with T cells modified to express a ROR1-specific chimeric antigen receptor. *Blood*, 116(22), 4532–4541. Available from: https://doi.org/10.1182/blood-2010-05-283309.

Hudecek, M., Sommermeyer, D., Kosasih, P.L., Silva-Benedict, A., Liu, L. & Rader, C. et al. (2015) The nonsignaling extracellular spacer domain of chimeric antigen receptors is decisive for in vivo antitumor activity. *Cancer Immunology Research*, 3(2), 125–135. Available from: https://doi.org/10.1158/2326-6066.CIR-14-0127.

Hughes, M. & Health, JH Bloomberg School of Public (2020) *The Principles of Humane Experimental Technique by W.M.S. Russell and R.L. Burch*. Available from: https://caat.jhsph.edu/principles/the-principles-of-humane-experimental-technique [Accessed 24 March 2021].

Hutchinson, L. & Kirk, R. (2011) High drug attrition rates--where are we going wrong? *Nature Reviews Clinical Oncology*, 8(4), 189–190. Available from: https://doi.org/10.1038/nrclinonc.2011.34.

Hylander, B.L., Punt, N., Tang, H., Hillman, J., Vaughan, M. & Bshara, W. et al. (2013) Origin of the vasculature supporting growth of primary patient tumor xenografts. *Journal of Translational Medicine*, 11(1), 110. Available from: https://doi.org/10.1186/1479-5876-11-110.

Inamura, K. (2017) Lung Cancer: Understanding Its Molecular Pathology and the 2015 WHO Classification. *Frontiers in Oncology*, 7, 193. Available from: https://doi.org/10.3389/fonc.2017.00193.

Iyer, R.K., Chui, J. & Radisic, M. (2009) Spatiotemporal tracking of cells in tissue-engineered cardiac organoids. *Journal of Tissue Engineering and Regenerative Medicine*, 3(3), 196–207. Available from: https://doi.org/10.1002/term.153.

Jayaraman, J., Mellody, M.P., Hou, A.J., Desai, R.P., Fung, A.W. & Pham, A.H.T. et al. (2020) CAR-T design: Elements and their synergistic function. *EBioMedicine*, 58, 102931. Available from: https://doi.org/10.1016/j.ebiom.2020.102931.

Jia, J., Martin, T.A., Ye, L. & Jiang, W.G. (2014) FAP-α (Fibroblast activation protein-α) is involved in the control of human breast cancer cell line growth and motility via the FAK pathway. *BMC Cell Biology*, 15(1), 16. Available from: https://doi.org/10.1186/1471-2121-15-16.

Jin, M.-Z. & Jin, W.-L. (2020) The updated landscape of tumor microenvironment and drug repurposing. *Signal Transduction and Targeted Therapy*, 5(1), 166. Available from: https://doi.org/10.1038/s41392-020-00280-x.

Kailayangiri, S., Altvater, B., Lesch, S., Balbach, S., Göttlich, C. & Kühnemundt, J. et al. (2019) EZH2 Inhibition in Ewing Sarcoma Upregulates GD2 Expression for Targeting with Gene-Modified T Cells. *Molecular Therapy : the Journal of the American Society of Gene Therapy*, 27(5), 933–946. Available from: https://doi.org/10.1016/j.ymthe.2019.02.014.

Kailayangiri, S., Altvater, B., Meltzer, J., Pscherer, S., Luecke, A. & Dierkes, C. et al. (2012) The ganglioside antigen G(D2) is surface-expressed in Ewing sarcoma and allows for MHC-independent immune targeting. *British Journal of Cancer*, 106(6), 1123–1133. Available from: https://doi.org/10.1038/bjc.2012.57.

Kailayangiri, S., Altvater, B., Spurny, C., Jamitzky, S., Schelhaas, S. & Jacobs, A.H. et al. (2017) Targeting Ewing sarcoma with activated and GD2-specific chimeric antigen receptor-engineered human NK cells induces upregulation of immune-inhibitory HLA-G. *Oncoimmunology*, 6(1), e1250050. Available from: https://doi.org/10.1080/2162402X.2016.1250050.

Kalluri, R. (2016) The biology and function of fibroblasts in cancer. *Nature Reviews Cancer*, 16(9), 582–598. Available from: https://doi.org/10.1038/nrc.2016.73.

Kalluri, R. & Zeisberg, M. (2006) Fibroblasts in cancer. *Nature Reviews. Cancer*, 6(5), 392–401. Available from: https://doi.org/10.1038/nrc1877.

Kapałczyńska, M., Kolenda, T., Przybyła, W., Zając̨zkowska, M., Teresiak, A. & Filas, V. et al. (2018) 2D and 3D cell cultures - a comparison of different types of cancer cell cultures. *Archives of Medical Science : AMS*, 14(4), 910–919. Available from: https://doi.org/10.5114/aoms.2016.63743.

Karvonen, H., Barker, H., Kaleva, L., Niininen, W. & Ungureanu, D. (2019) Molecular Mechanisms Associated with ROR1-Mediated Drug Resistance: Crosstalk with Hippo-YAP/TAZ and BMI-1 Pathways. *Cells*, 8(8). Available from: https://doi.org/10.3390/cells8080812.

Kato, A., Okura, T., Hamada, C., Miyoshi, S., Katayama, H. & Higaki, J. et al. (2014) Cell stress induces upregulation of osteopontin via the ERK pathway in type II alveolar epithelial cells. *PLOS ONE*, 9(6), e100106. Available from: https://doi.org/10.1371/journal.pone.0100106.

Kazerounian, S., Yee, K.O. & Lawler, J. (2008) Thrombospondins in cancer. *Cellular and Molecular Life Sciences : CMLS*, 65(5), 700–712. Available from: https://doi.org/10.1007/s00018-007-7486-z.

Khademhosseini, A. & Langer, R. (2016) A decade of progress in tissue engineering. *Nature Protocols*, 11(10), 1775–1781. Available from: https://doi.org/10.1038/nprot.2016.123.

Khan, J.F., Khan, A.S. & Brentjens, R.J. (2019) Chapter Eight - Application of CAR T cells for the treatment of solid tumors. In: Teplow, D.B. (Ed.) *Progress in Molecular Biology and Translational Science : Cancer Immunotherapy.* Academic Press, pp. 293–327.

Kim, M., Mun, H., Sung, C.O., Cho, E.J., Jeon, H.-J. & Chun, S.-M. et al. (2019) Patient-derived lung cancer organoids as in vitro cancer models for therapeutic screening. *Nature Communications*, 10(1), 3991. Available from: https://doi.org/10.1038/s41467-019-11867-6.

Kloss, C.C., Lee, J., Zhang, A., Chen, F., Melenhorst, J.J. & Lacey, S.F. et al. (2018) Dominant-Negative TGF-β Receptor Enhances PSMA-Targeted Human CAR T Cell Proliferation And Augments Prostate Cancer Eradication. *Molecular Therapy : the Journal of the American Society of Gene Therapy*, 26(7), 1855–1866. Available from: https://doi.org/10.1016/j.ymthe.2018.05.003.

Knott, M.M.L., Hölting, T.L.B., Ohmura, S., Kirchner, T., Cidre-Aranaz, F. & Grünewald, T.G.P. (2019) Targeting the undruggable: exploiting neomorphic features of fusion oncoproteins in childhood sarcomas for innovative therapies. *Cancer and Metastasis Reviews*, 38(4), 625–642. Available from: https://doi.org/10.1007/s10555-019-09839-9.

Korbecki, J., Grochans, S., Gutowska, I., Barczak, K. & Baranowska-Bosiacka, I. (2020) CC Chemokines in a Tumor: A Review of Pro-Cancer and Anti-Cancer Properties of Receptors CCR5, CCR6, CCR7, CCR8, CCR9, and CCR10 Ligands. *International Journal of Molecular Sciences*, 21(20). Available from: https://doi.org/10.3390/ijms21207619.

Kortlever, R.M., Sodir, N.M., Wilson, C.H., Burkhart, D.L., Pellegrinet, L. & Brown Swigart, L. et al. (2017) Myc Cooperates with Ras by Programming Inflammation and Immune Suppression. *Cell*, 171(6), 1301-1315.e14. Available from: https://doi.org/10.1016/j.cell.2017.11.013.

Kotteas, E.A., Boulas, P., Gkiozos, I., Tsagkouli, S., Tsoukalas, G. & Syrigos, K.N. (2014) The intercellular cell adhesion molecule-1 (icam-1) in lung cancer: implications for disease progression and prognosis. *Anticancer Research*, 34(9), 4665–4672.

Krook, M.A., Hawkins, A.G., Patel, R.M., Lucas, D.R., van Noord, R. & Chugh, R. et al. (2016) A bivalent promoter contributes to stress-induced plasticity of CXCR4 in Ewing sarcoma. *Oncotarget*, 7(38), 61775–61788. Available from: https://doi.org/10.18632/oncotarget.11240.

Krummel, M.F. & Allison, J.P. (1995) CD28 and CTLA-4 have opposing effects on the response of T cells to stimulation. *The Journal of Experimental Medicine*, 182(2), 459–465. Available from: https://doi.org/10.1084/jem.182.2.459.

Kühnemundt, J., Leifeld, H., Scherg, F., Schmitt, M., Nelke, L. & Schmitt, T. et al. (2020) Modular micro-physiological human tumor/tissue models based on decellularized tissue for improved preclinical testing. *ALTEX*. Available from: https://doi.org/10.14573/altex.2008141.

Kunnumakkara, A.B., Bordoloi, D., Sailo, B.L., Roy, N.K., Thakur, K.K. & Banik, K. et al. (2019) Cancer drug development: The missing links. *Experimental Biology and Medicine (Maywood, N.J.)*, 244(8), 663–689. Available from: https://doi.org/10.1177/1535370219839163.

Lakins, M.A., Ghorani, E., Munir, H., Martins, C.P. & Shields, J.D. (2018) Cancer-associated fibroblasts induce antigen-specific deletion of CD8 + T Cells to protect tumour cells. *Nature Communications*, 9(1), 948. Available from: https://doi.org/10.1038/s41467-018-03347-0.

Langhans, S.A. (2018) Three-Dimensional in Vitro Cell Culture Models in Drug Discovery and Drug Repositioning. *Frontiers in Pharmacology*, 9, 6. Available from: https://doi.org/10.3389/fphar.2018.00006.

Lanza, R.P. (2020) *Principles of tissue engineering*, 5th edition. Academic Press: London.

Lazzari, G., Nicolas, V., Matsusaki, M., Akashi, M., Couvreur, P. & Mura, S. (2018) Multicellular spheroid based on a triple co-culture: A novel 3D model to mimic pancreatic tumor complexity. *Acta Biomaterialia*, 78, 296–307. Available from: https://doi.org/10.1016/j.actbio.2018.08.008.

LeBleu, V.S. & Kalluri, R. (2018) A peek into cancer-associated fibroblasts: origins, functions and translational impact. *Disease Models & Mechanisms*, 11(4). Available from: https://doi.org/10.1242/dmm.029447.

Lee, J., Rabbani, C.C., Gao, H., Steinhart, M.R., Woodruff, B.M. & Pflum, Z.E. et al. (2020) Hair-bearing human skin generated entirely from pluripotent stem cells. *Nature*, 582(7812), 399–404. Available from: https://doi.org/10.1038/s41586-020-2352-3.

Lee, Y.S. & Cho, Y.B. (2020) CCL7 Signaling in the Tumor Microenvironment. In: Birbrair, A. (Ed.) *Tumor Microenvironment: The Role of Chemokines – Part A.* Springer International Publishing; Imprint: Springer: Cham, pp. 33–43.

Leitlinienprogramm Onkologie, L. (Ed.) (2018) *Interdisziplinäre S3-Leitlinie für die Diagnostik, Therapie und Nachsorge des Mammakarzinoms: Langversion 4.1, September 2018*, 4th edition. Zuckschwerdt: Germering.

Lewandrowski, G.K., Magee, C.N., Mounayar, M., Tannous, B.A. & Azzi, J. (2014) Simultaneous in vivo monitoring of regulatory and effector T lymphocytes using secreted

Gaussia luciferase, Firefly luciferase, and secreted alkaline phosphatase. *Methods in Molecular Biology (Clifton, N.J.)*, 1098, 211–227. Available from: https://doi.org/10.1007/978-1-62703-718-1_17.

Li, D., Li, X., Zhou, W.-L., Huang, Y., Liang, X. & Jiang, L. et al. (2019) Genetically engineered T cells for cancer immunotherapy. *Signal Transduction and Targeted Therapy*, 4(1), 35. Available from: https://doi.org/10.1038/s41392-019-0070-9.

Li, Z., Qian, Y., Li, W., Liu, L., Yu, L. & Liu, X. et al. (2020) Human Lung Adenocarcinoma-Derived Organoid Models for Drug Screening. *IScience*, 23(8), 101411. Available from: https://doi.org/10.1016/j.isci.2020.101411.

Li, Z., Zhou, J., Zhang, J., Li, S., Wang, H. & Du, J. (2019) Cancer-associated fibroblasts promote PD-L1 expression in mice cancer cells via secreting CXCL5. *International Journal of Cancer*, 145(7), 1946–1957. Available from: https://doi.org/10.1002/ijc.32278.

Linke, K., Schanz, J., Hansmann, J., Walles, T., Brunner, H. & Mertsching, H. (2007) Engineered liver-like tissue on a capillarized matrix for applied research. *Tissue Engineering*, 13(11), 2699–2707. Available from: https://doi.org/10.1089/ten.2006.0388.

Liu, G., Rui, W., Zhao, X. & Lin, X. (2021) Enhancing CAR-T cell efficacy in solid tumors by targeting the tumor microenvironment. *Cellular & Molecular Immunology*, 18(5), 1085–1095. Available from: https://doi.org/10.1038/s41423-021-00655-2.

Liu, J., Chen, S., Wang, W., Ning, B.-F., Chen, F. & Shen, W. et al. (2016) Cancer-associated fibroblasts promote hepatocellular carcinoma metastasis through chemokine-activated hedgehog and TGF-β pathways. *Cancer Letters*, 379(1), 49–59. Available from: https://doi.org/10.1016/j.canlet.2016.05.022.

Liu, L., Liu, Y., Yan, X., Zhou, C. & Xiong, X. (2020) The role of granulocyte colony-stimulating factor in breast cancer development: A review. *Molecular Medicine Reports*, 21(5), 2019–2029. Available from: https://doi.org/10.3892/mmr.2020.11017.

Liu, T., Han, C., Wang, S., Fang, P., Ma, Z. & Xu, L. et al. (2019) Cancer-associated fibroblasts: an emerging target of anti-cancer immunotherapy. *Journal of Hematology & Oncology*, 12(1), 86. Available from: https://doi.org/10.1186/s13045-019-0770-1.

Liubomirski, Y., Lerrer, S., Meshel, T., Rubinstein-Achiasaf, L., Morein, D. & Wiemann, S. et al. (2019) Tumor-Stroma-Inflammation Networks Promote Pro-metastatic Chemokines and Aggressiveness Characteristics in Triple-Negative Breast Cancer. *Frontiers in Immunology*, 10, 757. Available from: https://doi.org/10.3389/fimmu.2019.00757.

Lorsch, J.R., Collins, F.S. & Lippincott-Schwartz, J. (2014) Cell Biology. Fixing problems with cell lines. *Science (New York, N.Y.)*, 346(6216), 1452–1453. Available from: https://doi.org/10.1126/science.1259110.

Lucey, B.P., Nelson-Rees, W.A. & Hutchins, G.M. (2009) Henrietta Lacks, HeLa cells, and cell culture contamination. *Archives of Pathology & Laboratory Medicine*, 133(9), 1463–1467. Available from: https://doi.org/10.1043/1543-2165-133.9.1463.

Lynch, M.A., Petrel, T.A., Song, H., Knobloch, T.J., Casto, B.C. & Ramljak, D. et al. (2001) Responsiveness to transforming growth factor-beta (TGF-beta)-mediated growth inhibition is a function of membrane-bound TGF-beta type II receptor in human breast cancer cells. *Gene Expression*, 9(4-5), 157–171. Available from: https://doi.org/10.3727/000000001783992560.

Mahmood, N., Mihalcioiu, C. & Rabbani, S.A. (2018) Multifaceted Role of the Urokinase-Type Plasminogen Activator (uPA) and Its Receptor (uPAR): Diagnostic, Prognostic, and Therapeutic Applications. *Frontiers in Oncology*, 8, 24. Available from: https://doi.org/10.3389/fonc.2018.00024.

Majzner, R.G. & Mackall, C.L. (2019) Clinical lessons learned from the first leg of the CAR T cell journey. *Nature Medicine*, 25(9), 1341–1355. Available from: https://doi.org/10.1038/s41591-019-0564-6.

Malik, R., Lelkes, P.I. & Cukierman, E. (2015) Biomechanical and biochemical remodeling of stromal extracellular matrix in cancer. *Trends in Biotechnology*, 33(4), 230–236. Available from: https://doi.org/10.1016/j.tibtech.2015.01.004.

Marofi, F., Motavalli, R., Safonov, V.A., Thangavelu, L., Yumashev, A.V. & Alexander, M. et al. (2021) CAR T cells in solid tumors: challenges and opportunities. *Stem Cell Research & Therapy*, 12(1), 81. Available from: https://doi.org/10.1186/s13287-020-02128-1.

Marques, S.M. & Esteves da Silva, J.C.G. (2009) Firefly bioluminescence: a mechanistic approach of luciferase catalyzed reactions. *IUBMB Life*, 61(1), 6–17. Available from: https://doi.org/10.1002/iub.134.

Martinez, M. & Moon, E.K. (2019) CAR T Cells for Solid Tumors: New Strategies for Finding, Infiltrating, and Surviving in the Tumor Microenvironment. *Frontiers in Immunology*, 10, 128. Available from: https://doi.org/10.3389/fimmu.2019.00128.

Mason, C. & Dunnill, P. (2008) A brief definition of regenerative medicine. *Regenerative Medicine*, 3(1), 1–5. Available from: https://doi.org/10.2217/17460751.3.1.1.

Massagué, J., Seoane, J. & Wotton, D. (2005) Smad transcription factors. *Genes & Development*, 19(23), 2783–2810. Available from: https://doi.org/10.1101/gad.1350705.

Mayekar, M.K. & Bivona, T.G. (2017) Current Landscape of Targeted Therapy in Lung Cancer. *Clinical Pharmacology & Therapeutics*, 102(5), 757–764. Available from: https://doi.org/10.1002/cpt.810.

McCaffrey, A., Kay, M.A. & Contag, C.H. (2003) Advancing Molecular Therapies through In Vivo Bioluminescent Imaging. *Molecular Imaging*, 2(2), 153535002003031. Available from: https://doi.org/10.1162/15353500200303124.

McLane, L.M., Abdel-Hakeem, M.S. & Wherry, E.J. (2019) CD8 T Cell Exhaustion During Chronic Viral Infection and Cancer. *Annual Review of Immunology*, 37, 457–495. Available from: https://doi.org/10.1146/annurev-immunol-041015-055318.

Merchant, N., Nagaraju, G.P., Rajitha, B., Lammata, S., Jella, K.K. & Buchwald, Z.S. et al. (2017) Matrix metalloproteinases: their functional role in lung cancer. *Carcinogenesis*, 38(8), 766–780. Available from: https://doi.org/10.1093/carcin/bgx063.

Mestermann, K., Giavridis, T., Weber, J., Rydzek, J., Frenz, S. & Nerreter, T. et al. (2019) The tyrosine kinase inhibitor dasatinib acts as a pharmacologic on/off switch for CAR T cells. *Science Translational Medicine*, 11(499). Available from: https://doi.org/10.1126/scitranslmed.aau5907.

Meurette, O. & Mehlen, P. (2018) Notch Signaling in the Tumor Microenvironment. *Cancer Cell*, 34(4), 536–548. Available from: https://doi.org/10.1016/j.ccell.2018.07.009.

Mhaidly, R. & Mechta-Grigoriou, F. (2020) Fibroblast heterogeneity in tumor micro-environment: Role in immunosuppression and new therapies. *Seminars in Immunology*, 48, 101417. Available from: https://doi.org/10.1016/j.smim.2020.101417.

Misra, S., Moro, C.F., Del Chiaro, M., Pouso, S., Sebestyén, A. & Löhr, M. et al. (2019) Ex vivo organotypic culture system of precision-cut slices of human pancreatic ductal adenocarcinoma. *Scientific Reports*, 9(1), 2133. Available from: https://doi.org/10.1038/s41598-019-38603-w.

Miyake, M., Goodison, S., Lawton, A., Gomes-Giacoia, E. & Rosser, C.J. (2015) Angiogenin promotes tumoral growth and angiogenesis by regulating matrix metallopeptidase-2 expression via the ERK1/2 pathway. *Oncogene*, 34(7), 890–901. Available from: https://doi.org/10.1038/onc.2014.2.

Monjezi, R., Miskey, C., Gogishvili, T., Schleef, M., Schmeer, M. & Einsele, H. et al. (2017) Enhanced CAR T-cell engineering using non-viral Sleeping Beauty transposition from minicircle vectors. *Leukemia*, 31(1), 186–194. Available from: https://doi.org/10.1038/leu.2016.180.

Morgan, M.A. & Schambach, A. (2018) Engineering CAR-T Cells for Improved Function Against Solid Tumors. *Frontiers in Immunology*, 9, 2493. Available from: https://doi.org/10.3389/fimmu.2018.02493.

Morgan, R.A., Yang, J.C., Kitano, M., Dudley, M.E., Laurencot, C.M. & Rosenberg, S.A. (2010) Case report of a serious adverse event following the administration of T cells transduced with a chimeric antigen receptor recognizing ERBB2. *Molecular Therapy : the Journal of the American Society of Gene Therapy*, 18(4), 843–851. Available from: https://doi.org/10.1038/mt.2010.24.

Mur, C., Martínez-Carpio, P.A., Fernández-Montolí, M.E., Ramon, J.M., Rosel, P. & Navarro, M.A. (1998) Growth of MDA-MB-231 cell line: different effects of TGF-beta(1), EGF and estradiol depending on the length of exposure. *Cell Biology International*, 22(9-10), 679–684. Available from: https://doi.org/10.1006/cbir.1998.0306.

Naipal, K.A.T., Verkaik, N.S., Sánchez, H., van Deurzen, C.H.M., den Bakker, M.A. & Hoeijmakers, J.H.J. et al. (2016) Tumor slice culture system to assess drug response of primary breast cancer. *BMC Cancer*, 16, 78. Available from: https://doi.org/10.1186/s12885-016-2119-2.

Nakaya, Y. & Sheng, G. (2008) Epithelial to mesenchymal transition during gastrulation: an embryological view. *Development, Growth & Differentiation*, 50(9), 755–766. Available from: https://doi.org/10.1111/j.1440-169X.2008.01070.x.

Nallanthighal, S., Heiserman, J.P. & Cheon, D.-J. (2019) The Role of the Extracellular Matrix in Cancer Stemness. *Frontiers in Cell and Developmental Biology*, 7, 86. Available from: https://doi.org/10.3389/fcell.2019.00086.

Nashimoto, Y., Okada, R., Hanada, S., Arima, Y., Nishiyama, K. & Miura, T. et al. (2020) Vascularized cancer on a chip: The effect of perfusion on growth and drug delivery of tumor spheroid. *Biomaterials*, 229, 119547. Available from: https://doi.org/10.1016/j.biomaterials.2019.119547.

Nazemi, M. & Rainero, E. (2020) Cross-Talk Between the Tumor Microenvironment, Extracellular Matrix, and Cell Metabolism in Cancer. *Frontiers in Oncology*, 10, 239. Available from: https://doi.org/10.3389/fonc.2020.00239.

Nelke, L. (2019) *Establishment and optimization of 3-dimensional mamma carcinoma models for therapy simulation and drug testing*. Universität Würzburg. Available from: https://doi.org/10.25972/OPUS-17228.

Nelson, C.M. & Bissell, M.J. (2006) Of extracellular matrix, scaffolds, and signaling: tissue architecture regulates development, homeostasis, and cancer. *Annual Review of Cell and Developmental Biology*, 22, 287–309. Available from: https://doi.org/10.1146/annurev.cellbio.22.010305.104315.

Nietzer, S., Baur, F., Sieber, S., Hansmann, J., Schwarz, T. & Stoffer, C. et al. (2016) Mimicking Metastases Including Tumor Stroma: A New Technique to Generate a Three-Dimensional Colorectal Cancer Model Based on a Biological Decellularized Intestinal Scaffold. *Tissue Engineering. Part C, Methods*, 22(7), 621–635. Available from: https://doi.org/10.1089/ten.TEC.2015.0557.

Nurmik, M., Ullmann, P., Rodriguez, F., Haan, S. & Letellier, E. (2020) In search of definitions: Cancer-associated fibroblasts and their markers. *International Journal of Cancer*, 146(4), 895–905. Available from: https://doi.org/10.1002/ijc.32193.

Ohbayashi, M., Kubota, S., Kawase, A., Kohyama, N., Kobayashi, Y. & Yamamoto, T. (2014) Involvement of epithelial-mesenchymal transition in methotrexate-induced pulmonary fibrosis. *The Journal of Toxicological Sciences*, 39(2), 319–330. Available from: https://doi.org/10.2131/jts.39.319.

Okazaki, T. & Honjo, T. (2007) PD-1 and PD-1 ligands: from discovery to clinical application. *International Immunology*, 19(7), 813–824. Available from: https://doi.org/10.1093/intimm/dxm057.

Olson, J.L., Atala, A. & Yoo, J.J. (2011) Tissue engineering: current strategies and future directions. *Chonnam Medical Journal*, 47(1), 1–13. Available from: https://doi.org/10.4068/cmj.2011.47.1.1.

Osmani, L., Askin, F., Gabrielson, E. & Li, Q.K. (2018) Current WHO guidelines and the critical role of immunohistochemical markers in the subclassification of non-small cell lung carcinoma (NSCLC): Moving from targeted therapy to immunotherapy. *Seminars in Cancer Biology*, 52(Pt 1), 103–109. Available from: https://doi.org/10.1016/j.semcancer.2017.11.019.

Osuala, K.O. & Sloane, B.F. (2014) Many Roles of CCL20: Emphasis on Breast Cancer. *Postdoc Journal : a Journal of Postdoctoral Research and Postdoctoral Affairs*, 2(3), 7–16.

Pal, M., Chen, H., Lee, B.H., Lee, J.Y.H., Yip, Y.S. & Tan, N.S. et al. (2019) Epithelial-mesenchymal transition of cancer cells using bioengineered hybrid scaffold composed of hydrogel/3D-fibrous framework. *Scientific Reports*, 9(1), 8997. Available from: https://doi.org/10.1038/s41598-019-45384-9.

Panek, M., Grabacka, M. & Pierzchalska, M. (2018) The formation of intestinal organoids in a hanging drop culture. *Cytotechnology*, 70(3), 1085–1095. Available from: https://doi.org/10.1007/s10616-018-0194-8.

Papageorgis, P. & Stylianopoulos, T. (2015) Role of TGFβ in regulation of the tumor microenvironment and drug delivery (review). *International Journal of Oncology*, 46(3), 933–943. Available from: https://doi.org/10.3892/ijo.2015.2816.

Park, S., Shevlin, E., Vedvyas, Y., Zaman, M., Park, S. & Hsu, Y.-M.S. et al. (2017) Micromolar affinity CAR T cells to ICAM-1 achieves rapid tumor elimination while avoiding systemic toxicity. *Scientific Reports*, 7(1), 14366. Available from: https://doi.org/10.1038/s41598-017-14749-3.

Parker, J.S., Mullins, M., Cheang, M.C.U., Leung, S., Voduc, D. & Vickery, T. et al. (2009) Supervised risk predictor of breast cancer based on intrinsic subtypes. *Journal of Clinical Oncology*, 27(8), 1160–1167. Available from: https://doi.org/10.1200/JCO.2008.18.1370.

Pereira, B.A., Vennin, C., Papanicolaou, M., Chambers, C.R., Herrmann, D. & Morton, J.P. et al. (2019) CAF Subpopulations: A New Reservoir of Stromal Targets in Pancreatic Cancer. *Trends in Cancer*, 5(11), 724–741. Available from: https://doi.org/10.1016/j.trecan.2019.09.010.

Piccart-Gebhart, M.J., Procter, M., Leyland-Jones, B., Goldhirsch, A., Untch, M. & Smith, I. et al. (2005) Trastuzumab after adjuvant chemotherapy in HER2-positive breast cancer. *The New England Journal of Medicine*, 353(16), 1659–1672. Available from: https://doi.org/10.1056/NEJMoa052306.

Pickard, A. & McCance, D.J. (2015) IGF-Binding Protein 2 - Oncogene or Tumor Suppressor? *Frontiers in Endocrinology*, 6, 25. Available from: https://doi.org/10.3389/fendo.2015.00025.

Pickup, M.W., Mouw, J.K. & Weaver, V.M. (2014) The extracellular matrix modulates the hallmarks of cancer. *EMBO Reports*, 15(12), 1243–1253. Available from: https://doi.org/10.15252/embr.201439246.

Poltavets, V., Kochetkova, M., Pitson, S.M. & Samuel, M.S. (2018) The Role of the Extracellular Matrix and Its Molecular and Cellular Regulators in Cancer Cell Plasticity. *Frontiers in Oncology*, 8, 431. Available from: https://doi.org/10.3389/fonc.2018.00431.

Poorebrahim, M., Melief, J., Pico de Coaña, Y., L Wickström, S., Cid-Arregui, A. & Kiessling, R. (2021) Counteracting CAR T cell dysfunction. *Oncogene*, 40(2), 421–435. Available from: https://doi.org/10.1038/s41388-020-01501-x.

Porretti, J.C., Mohamad, N.A., Martín, G.A. & Cricco, G.P. (2014) Fibroblasts induce epithelial to mesenchymal transition in breast tumor cells which is prevented by fibroblasts treatment with histamine in high concentration. *The International Journal of Biochemistry & Cell Biology*, 51, 29–38. Available from: https://doi.org/10.1016/j.biocel.2014.03.016.

Proto, C., Ferrara, R., Signorelli, D., Lo Russo, G., Galli, G. & Imbimbo, M. et al. (2019) Choosing wisely first line immunotherapy in non-small cell lung cancer (NSCLC): what to add and what to leave out. *Cancer Treatment Reviews*, 75, 39–51. Available from: https://doi.org/10.1016/j.ctrv.2019.03.004.

Puré, E. & Blomberg, R. (2018) Pro-tumorigenic roles of fibroblast activation protein in cancer: back to the basics. *Oncogene*, 37(32), 4343–4357. Available from: https://doi.org/10.1038/s41388-018-0275-3.

Quatromoni, J.G., Singhal, S., Bhojnagarwala, P., Hancock, W.W., Albelda, S.M. & Eruslanov, E. (2015) An optimized disaggregation method for human lung tumors that preserves the phenotype and function of the immune cells. *Journal of Leukocyte Biology*, 97(1), 201–209. Available from: https://doi.org/10.1189/jlb.5TA0814-373.

Reichard, A. & Asosingh, K. (2019) Best Practices for Preparing a Single Cell Suspension from Solid Tissues for Flow Cytometry. *Cytometry. Part a : the Journal of the International Society for Analytical Cytology*, 95(2), 219–226. Available from: https://doi.org/10.1002/cyto.a.23690.

Rich, S., Seelig, M., Lee, H.M. & Lin, J. (1995) Transforming growth factor beta 1 costimulated growth and regulatory function of staphylococcal enterotoxin B-responsive

CD8+ T cells. *Journal of Immunology (Baltimore, Md. : 1950)*, 155(2), 609–618. Available from: https://www.jimmunol.org/content/155/2/609.long.

Rolfo, C., Caglevic, C., Santarpia, M., Araujo, A., Giovannetti, E. & Gallardo, C.D. et al. (2017) Immunotherapy in NSCLC: A Promising and Revolutionary Weapon. *Advances in Experimental Medicine and Biology*, 995, 97–125. Available from: https://doi.org/10.1007/978-3-319-53156-4_5.

Romano, S., Tufano, M., D'Arrigo, P., Vigorito, V., Russo, S. & Romano, M.F. (2020) Cell stemness, epithelial-to-mesenchymal transition, and immunoevasion: Intertwined aspects in cancer metastasis. *Seminars in Cancer Biology*, 60, 181–190. Available from: https://doi.org/10.1016/j.semcancer.2019.08.015.

Rosette, C., Roth, R.B., Oeth, P., Braun, A., Kammerer, S. & Ekblom, J. et al. (2005) Role of ICAM1 in invasion of human breast cancer cells. *Carcinogenesis*, 26(5), 943–950. Available from: https://doi.org/10.1093/carcin/bgi070.

Rué, P. & Martinez Arias, A. (2015) Cell dynamics and gene expression control in tissue homeostasis and development. *Molecular Systems Biology*, 11(1), 792. Available from: https://doi.org/10.15252/msb.20145549.

Russell, W.M.S. & Burch, R.L. (1992) *The principles of humane experimental technique*. UFAW: Potters Bar.

Sachs, N., Papaspyropoulos, A., Zomer-van Ommen, D.D., Heo, I., Böttinger, L. & Klay, D. et al. (2019) Long-term expanding human airway organoids for disease modeling. *The EMBO Journal*, 38(4). Available from: https://doi.org/10.15252/embj.2018100300.

Sadlonova, A., Bowe, D.B., Novak, Z., Mukherjee, S., Duncan, V.E. & Page, G.P. et al. (2009) Identification of molecular distinctions between normal breast-associated fibroblasts and breast cancer-associated fibroblasts. *Cancer Microenvironment*, 2(1), 9–21. Available from: https://doi.org/10.1007/s12307-008-0017-0.

Sahai, E., Astsaturov, I., Cukierman, E., DeNardo, D.G., Egeblad, M. & Evans, R.M. et al. (2020) A framework for advancing our understanding of cancer-associated fibroblasts. *Nature Reviews Cancer*, 20(3), 174–186. Available from: https://doi.org/10.1038/s41568-019-0238-1.

Sant, S. & Johnston, P.A. (2017) The production of 3D tumor spheroids for cancer drug discovery. *Drug Discovery Today. Technologies*, 23, 27–36. Available from: https://doi.org/10.1016/j.ddtec.2017.03.002.

Santi, A., Kugeratski, F.G. & Zanivan, S. (2018) Cancer Associated Fibroblasts: The Architects of Stroma Remodeling. *Proteomics*, 18(5-6), e1700167. Available from: https://doi.org/10.1002/pmic.201700167.

Santiago-Sánchez, G.S., Pita-Grisanti, V., Quiñones-Díaz, B., Gumpper, K., Cruz-Monserrate, Z. & Vivas-Mejía, P.E. (2020) Biological Functions and Therapeutic Potential of Lipocalin 2 in Cancer. *International Journal of Molecular Sciences*, 21(12). Available from: https://doi.org/10.3390/ijms21124365.

Santibañez, J.F., Quintanilla, M. & Bernabeu, C. (2011) TGF-β/TGF-β receptor system and its role in physiological and pathological conditions. *Clinical Science (London, England : 1979)*, 121(6), 233–251. Available from: https://doi.org/10.1042/CS20110086.

Sapudom, J., Waschke, J., Franke, K., Hlawitschka, M. & Pompe, T. (2017) Quantitative label-free single cell tracking in 3D biomimetic matrices. *Scientific Reports*, 7(1), 14135. Available from: https://doi.org/10.1038/s41598-017-14458-x.

Sato, Y., Tsuboi, R., Lyons, R., Moses, H. & Rifkin, D.B. (1990) Characterization of the activation of latent TGF-beta by co-cultures of endothelial cells and pericytes or smooth muscle cells: a self-regulating system. *The Journal of Cell Biology*, 111(2), 757–763. Available from: https://doi.org/10.1083/jcb.111.2.757.

Schanz, J., Pusch, J., Hansmann, J. & Walles, H. (2010) Vascularised human tissue models: a new approach for the refinement of biomedical research. *Journal of Biotechnology*, 148(1), 56–63. Available from: https://doi.org/10.1016/j.jbiotec.2010.03.015.

Schmidts, A. & Maus, M.V. (2018) Making CAR T Cells a Solid Option for Solid Tumors. *Frontiers in Immunology*, 9, 2593. Available from: https://doi.org/10.3389/fimmu.2018.02593.

Seoane, J. & Gomis, R.R. (2017) TGF-β Family Signaling in Tumor Suppression and Cancer Progression. *Cold Spring Harbor Perspectives in Biology*, 9(12). Available from: https://doi.org/10.1101/cshperspect.a022277.

Shafiee, A. & Atala, A. (2017) Tissue Engineering: Toward a New Era of Medicine. *Annual Review of Medicine*, 68, 29–40. Available from: https://doi.org/10.1146/annurev-med-102715-092331.

Shea, E.K.H., Koh, V.C.Y. & Tan, P.H. (2020) Invasive breast cancer: Current perspectives and emerging views. *Pathology International*, 70(5), 242–252. Available from: https://doi.org/10.1111/pin.12910.

Shi, M., Zhu, J., Wang, R., Chen, X., Mi, L. & Walz, T. et al. (2011) Latent TGF-β structure and activation. *Nature*, 474(7351), 343–349. Available from: https://doi.org/10.1038/nature10152.

Shi, Y. & Massagué, J. (2003) Mechanisms of TGF-β Signaling from Cell Membrane to the Nucleus. *Cell*, 113(6), 685–700. Available from: https://doi.org/10.1016/S0092-8674(03)00432-X.

Simon, S. & Labarriere, N. (2017) PD-1 expression on tumor-specific T cells: Friend or foe for immunotherapy? *Oncoimmunology*, 7(1), e1364828. Available from: https://doi.org/10.1080/2162402X.2017.1364828.

Sivakumar, R., Chan, M., Shin, J.S., Nishida-Aoki, N., Kenerson, H.L. & Elemento, O. et al. (2019) Organotypic tumor slice cultures provide a versatile platform for immuno-oncology and drug discovery. *Oncoimmunology*, 8(12), e1670019. Available from: https://doi.org/10.1080/2162402X.2019.1670019.

Sommermeyer, D., Hudecek, M., Kosasih, P.L., Gogishvili, T., Maloney, D.G. & Turtle, C.J. et al. (2016) Chimeric antigen receptor-modified T cells derived from defined CD8+ and CD4+ subsets confer superior antitumor reactivity in vivo. *Leukemia*, 30(2), 492–500. Available from: https://doi.org/10.1038/leu.2015.247.

Sontheimer-Phelps, A., Hassell, B.A. & Ingber, D.E. (2019) Modelling cancer in microfluidic human organs-on-chips. *Nature Reviews Cancer*, 19(2), 65–81. Available from: https://doi.org/10.1038/s41568-018-0104-6.

Specht, J.M., Lee, S., Turtle, C., Berger, C., Veatch, J. & Gooley, T. et al. (2018) Phase I study of immunotherapy for advanced ROR1+ malignancies with autologous ROR1-specific chimeric antigen receptor-modified (CAR)-T cells. *Journal of Clinical Oncology*, 36(5_suppl), TPS79-TPS79. Available from: https://doi.org/10.1200/JCO.2018.36.5_suppl.TPS79.

Srivastava, S., Furlan, S.N., Jaeger-Ruckstuhl, C.A., Sarvothama, M., Berger, C. & Smythe, K.S. et al. (2021) Immunogenic Chemotherapy Enhances Recruitment of CAR-T Cells to Lung Tumors and Improves Antitumor Efficacy when Combined with Checkpoint Blockade. *Cancer Cell*, 39(2), 193-208.e10. Available from: https://doi.org/10.1016/j.ccell.2020.11.005.

Steinke, M., Dally, I., Friedel, G., Walles, H. & Walles, T. (2015) Host-integration of a tissue-engineered airway patch: two-year follow-up in a single patient. *Tissue Engineering. Part a*, 21(3-4), 573–579. Available from: https://doi.org/10.1089/ten.tea.2014.0200.

St-Georges-Robillard, A., Cahuzac, M., Péant, B., Fleury, H., Lateef, M.A. & Ricard, A. et al. (2019) Long-term fluorescence hyperspectral imaging of on-chip treated co-culture tumour spheroids to follow clonal evolution. *Integrative Biology : Quantitative Biosciences from Nano to Macro*, 11(4), 130–141. Available from: https://doi.org/10.1093/intbio/zyz012.

Stock, S., Schmitt, M. & Sellner, L. (2019) Optimizing Manufacturing Protocols of Chimeric Antigen Receptor T Cells for Improved Anticancer Immunotherapy. *International Journal of Molecular Sciences*, 20(24). Available from: https://doi.org/10.3390/ijms20246223.

Stratmann, A.T., Fecher, D., Wangorsch, G., Göttlich, C., Walles, T. & Walles, H. et al. (2014) Establishment of a human 3D lung cancer model based on a biological tissue matrix combined with a Boolean in silico model. *Molecular Oncology*, 8(2), 351–365. Available from: https://doi.org/10.1016/j.molonc.2013.11.009.

Stüber, T., Monjezi, R., Wallstabe, L., Kühnemundt, J., Nietzer, S.L. & Dandekar, G. et al. (2020) Inhibition of TGF-β-receptor signaling augments the antitumor function of ROR1-

specific CAR T-cells against triple-negative breast cancer. *Journal for Immunotherapy of Cancer*, 8(1). Available from: https://doi.org/10.1136/jitc-2020-000676.

Su, J., Wu, S., Wu, H., Le Li & Guo, T. (2016) CD44 is functionally crucial for driving lung cancer stem cells metastasis through Wnt/β-catenin-FoxM1-Twist signaling. *Molecular Carcinogenesis*, 55(12), 1962–1973. Available from: https://doi.org/10.1002/mc.22443.

Su, S., Chen, J., Yao, H., Liu, J., Yu, S. & Lao, L. et al. (2018) CD10+GPR77+ Cancer-Associated Fibroblasts Promote Cancer Formation and Chemoresistance by Sustaining Cancer Stemness. *Cell*, 172(4), 841-856.e16. Available from: https://doi.org/10.1016/j.cell.2018.01.009.

Subklewe, M., Bergwelt-Baildon, M. von & Humpe, A. (2019) Chimeric Antigen Receptor T Cells: A Race to Revolutionize Cancer Therapy. *Transfusion Medicine and Hemotherapy : Offizielles Organ Der Deutschen Gesellschaft Fur Transfusionsmedizin Und Immunhamatologie*, 46(1), 15–24. Available from: https://doi.org/10.1159/000496870.

Sun, Y., Zhou, Q.-M., Lu, Y.-Y., Zhang, H., Chen, Q.-L. & Zhao, M. et al. (2019) Resveratrol Inhibits the Migration and Metastasis of MDA-MB-231 Human Breast Cancer by Reversing TGF-β1-Induced Epithelial-Mesenchymal Transition. *Molecules*, 24(6), 1131. Available from: https://doi.org/10.3390/molecules24061131.

Suzuki, Y., Yanagisawa, M., Ariga, T. & Yu, R.K. (2011) Histone acetylation-mediated glycosyltransferase gene regulation in mouse brain during development. *Journal of Neurochemistry*, 116(5), 874–880. Available from: https://doi.org/10.1111/j.1471-4159.2010.07042.x.

Taguchi, A., Kawana, K., Tomio, K., Yamashita, A., Isobe, Y. & Nagasaka, K. et al. (2014) Matrix metalloproteinase (MMP)-9 in cancer-associated fibroblasts (CAFs) is suppressed by omega-3 polyunsaturated fatty acids in vitro and in vivo. *PLOS ONE*, 9(2), e89605. Available from: https://doi.org/10.1371/journal.pone.0089605.

Tas, F., Bilgin, E., Tastekin, D., Erturk, K. & Duranyildiz, D. (2016) Serum IGF-1 and IGFBP-3 levels as clinical markers for patients with lung cancer. *Biomedical Reports*, 4(5), 609–614. Available from: https://doi.org/10.3892/br.2016.629.

Tchou, J., Zhao, Y., Levine, B.L., Zhang, P.J., Davis, M.M. & Melenhorst, J.J. et al. (2017) Safety and Efficacy of Intratumoral Injections of Chimeric Antigen Receptor (CAR) T Cells in Metastatic Breast Cancer. *Cancer Immunology Research*, 5(12), 1152–1161. Available from: https://doi.org/10.1158/2326-6066.CIR-17-0189.

The Nobel Prize in Physiology or Medicine 2018 (2020). Available from: https://www.nobelprize.org/prizes/medicine/2018/press-release/ [Accessed 24 June 2020].

Thomas, D. & Radhakrishnan, P. (2019) Tumor-stromal crosstalk in pancreatic cancer and tissue fibrosis. *Molecular Cancer*, 18(1), 14. Available from: https://doi.org/10.1186/s12943-018-0927-5.

Thomas, D.A. & Massagué, J. (2005) TGF-beta directly targets cytotoxic T cell functions during tumor evasion of immune surveillance. *Cancer Cell*, 8(5), 369–380. Available from: https://doi.org/10.1016/j.ccr.2005.10.012.

Tokarew, N., Ogonek, J., Endres, S., Bergwelt-Baildon, M. von & Kobold, S. (2019) Teaching an old dog new tricks: next-generation CAR T cells. *British Journal of Cancer*, 120(1), 26–37. Available from: https://doi.org/10.1038/s41416-018-0325-1.

Tran, T., Blanc, C., Granier, C., Saldmann, A., Tanchot, C. & Tartour, E. (2019) Therapeutic cancer vaccine: building the future from lessons of the past. *Seminars in Immunopathology*, 41(1), 69–85. Available from: https://doi.org/10.1007/s00281-018-0691-z.

Trapani, J.A. (2005) The dual adverse effects of TGF-beta secretion on tumor progression. *Cancer Cell*, 8(5), 349–350. Available from: https://doi.org/10.1016/j.ccr.2005.10.018.

Trujillo-de Santiago, G., Flores-Garza, B.G., Tavares-Negrete, J.A., Lara-Mayorga, I.M., González-Gamboa, I. & Zhang, Y.S. et al. (2019) The Tumor-on-Chip: Recent Advances in the Development of Microfluidic Systems to Recapitulate the Physiology of Solid Tumors. *Materials (Basel, Switzerland)*, 12(18). Available from: https://doi.org/10.3390/ma12182945.

Tu, J., Huo, Z., Gingold, J., Zhao, R., Shen, J. & Lee, D.-F. (2017) The Histogenesis of Ewing Sarcoma. *Cancer Reports and Reviews*, 1(2). Available from: https://doi.org/10.15761/CRR.1000111.

Tung, J.K., Berglund, K., Gutekunst, C.-A., Hochgeschwender, U. & Gross, R.E. (2016) Bioluminescence imaging in live cells and animals. *Neurophotonics*, 3(2), 25001. Available from: https://doi.org/10.1117/1.NPh.3.2.025001.

Turtle, C.J., Hanafi, L.-A., Berger, C., Gooley, T.A., Cherian, S. & Hudecek, M. et al. (2016) CD19 CAR-T cells of defined CD4+:CD8+ composition in adult B cell ALL patients. *The Journal of Clinical Investigation*, 126(6), 2123–2138. Available from: https://doi.org/10.1172/JCI85309.

Uhl, M., Aulwurm, S., Wischhusen, J., Weiler, M., Ma, J.Y. & Almirez, R. et al. (2004) SD-208, a novel transforming growth factor beta receptor I kinase inhibitor, inhibits growth and invasiveness and enhances immunogenicity of murine and human glioma cells in vitro and in vivo. *Cancer Research*, 64(21), 7954–7961. Available from: https://doi.org/10.1158/0008-5472.CAN-04-1013.

Vacanti, C. (2006) The history of tissue engineering. *Journal of Cellular and Molecular Medicine*, 1(3), 569–576. Available from: https://doi.org/10.2755/jcmm010.003.20.

Valkenburg, K.C., Groot, A.E. de & Pienta, K.J. (2018) Targeting the tumour stroma to improve cancer therapy. *Nature Reviews Clinical Oncology*, 15(6), 366–381. Available from: https://doi.org/10.1038/s41571-018-0007-1.

van Norman, G.A. (2019) Limitations of Animal Studies for Predicting Toxicity in Clinical Trials: Is it Time to Rethink Our Current Approach? *JACC: Basic to Translational Science*, 4(7), 845–854. Available from: https://doi.org/10.1016/j.jacbts.2019.10.008.

Vitale, I., Manic, G., Coussens, L.M., Kroemer, G. & Galluzzi, L. (2019) Macrophages and Metabolism in the Tumor Microenvironment. *Cell Metabolism*, 30(1), 36–50. Available from: https://doi.org/10.1016/j.cmet.2019.06.001.

Vuoriluoto, K., Haugen, H., Kiviluoto, S., Mpindi, J.-P., Nevo, J. & Gjerdrum, C. et al. (2011) Vimentin regulates EMT induction by Slug and oncogenic H-Ras and migration by governing Axl expression in breast cancer. *Oncogene*, 30(12), 1436–1448. Available from: https://doi.org/10.1038/onc.2010.509.

Wahba, H.A. & El-Hadaad, H.A. (2015) Current approaches in treatment of triple-negative breast cancer. *Cancer Biology & Medicine*, 12(2), 106–116. Available from: https://doi.org/10.7497/j.issn.2095-3941.2015.0030.

Waldman, A.D., Fritz, J.M. & Lenardo, M.J. (2020) A guide to cancer immunotherapy: from T cell basic science to clinical practice. *Nature Reviews Immunology*, 1–18. Available from: https://doi.org/10.1038/s41577-020-0306-5.

Wallstabe, L., Göttlich, C., Nelke, L.C., Kühnemundt, J., Schwarz, T. & Nerreter, T. et al. (2019) ROR1-CAR T cells are effective against lung and breast cancer in advanced microphysiologic 3D tumor models. *JCI Insight*, 4(18). Available from: https://doi.org/10.1172/jci.insight.126345.

Wallstabe, L., Mades, A., Frenz, S., Einsele, H., Rader, C. & Hudecek, M. (2018) CAR T cells targeting αvβ3 integrin are effective against advanced cancer in preclinical models. *Advances in Cell and Gene Therapy*, 1(2). Available from: https://doi.org/10.1002/acg2.11.

Wang, L., Cao, L., Wang, H., Liu, B., Zhang, Q. & Meng, Z. et al. (2017) Cancer-associated fibroblasts enhance metastatic potential of lung cancer cells through IL-6/STAT3 signaling pathway. *Oncotarget*, 8(44), 76116–76128. Available from: https://doi.org/10.18632/oncotarget.18814.

Wang, S., Zimmermann, S., Parikh, K., Mansfield, A.S. & Adjei, A.A. (2019) Current Diagnosis and Management of Small-Cell Lung Cancer. *Mayo Clinic Proceedings*, 94(8), 1599–1622. Available from: https://doi.org/10.1016/j.mayocp.2019.01.034.

Wang, X. & Rivière, I. (2016) Clinical manufacturing of CAR T cells: foundation of a promising therapy. *Molecular Therapy Oncolytics*, 3, 16015. Available from: https://doi.org/10.1038/mto.2016.15.

Warth, A., Cortis, J., Soltermann, A., Meister, M., Budczies, J. & Stenzinger, A. et al. (2014) Tumour cell proliferation (Ki-67) in non-small cell lung cancer: a critical reappraisal of its prognostic role. *British Journal of Cancer*, 111(6), 1222–1229. Available from: https://doi.org/10.1038/bjc.2014.402.

Wegner, A. (2017) Chimeric antigen receptor T cells for the treatment of cancer and the future of preclinical models for predicting their toxicities. *Immunotherapy*, 9(8), 669–680. Available from: https://doi.org/10.2217/imt-2017-0028.

Weinkove, R., George, P., Dasyam, N. & McLellan, A.D. (2019) Selecting costimulatory domains for chimeric antigen receptors: functional and clinical considerations. *Clinical & Translational Immunology*, 8(5), e1049. Available from: https://doi.org/10.1002/cti2.1049.

Wherry, E.J. & Kurachi, M. (2015) Molecular and cellular insights into T cell exhaustion. *Nature Reviews Immunology*, 15(8), 486–499. Available from: https://doi.org/10.1038/nri3862.

*WHO classification of tumours. Breast Tumours* (2019). International Agency for Research on Cancer: Lyon.

Wright, L.E., Ottewell, P.D., Rucci, N., Peyruchaud, O., Pagnotti, G.M. & Chiechi, A. et al. (2016) Murine models of breast cancer bone metastasis. *BoneKEy Reports*, 5, 804. Available from: https://doi.org/10.1038/bonekey.2016.31.

Wu, X., Tao, P., Zhou, Q., Li, J., Yu, Z. & Wang, X. et al. (2017) IL-6 secreted by cancer-associated fibroblasts promotes epithelial-mesenchymal transition and metastasis of gastric cancer via JAK2/STAT3 signaling pathway. *Oncotarget*, 8(13), 20741–20750. Available from: https://doi.org/10.18632/oncotarget.15119.

Xie, G., Dong, H., Liang, Y., Ham, J.D., Rizwan, R. & Chen, J. (2020) CAR-NK cells: A promising cellular immunotherapy for cancer. *EBioMedicine*, 59, 102975. Available from: https://doi.org/10.1016/j.ebiom.2020.102975.

Xu, S., Yang, Y., Sun, Y.-B., Wang, H.-Y., Sun, C.-B. & Zhang, X. (2014) Role of fibulin-3 in lung cancer: in vivo and in vitro analyses. *Oncology Reports*, 31(1), 79–86. Available from: https://doi.org/10.3892/or.2013.2799.

Yan, L., Zucker, S. & Toole, B.P. (2005) Roles of the multifunctional glycoprotein, emmprin (basigin; CD147), in tumour progression. *Thrombosis and Haemostasis*, 93(2), 199–204. Available from: https://doi.org/10.1160/TH04-08-0536.

Yang, J., Baskar, S., Kwong, K.Y., Kennedy, M.G., Wiestner, A. & Rader, C. (2011) Therapeutic potential and challenges of targeting receptor tyrosine kinase ROR1 with monoclonal antibodies in B-cell malignancies. *PLOS ONE*, 6(6), e21018. Available from: https://doi.org/10.1371/journal.pone.0021018.

Yang, J., Yan, J. & Liu, B. (2018) Targeting VEGF/VEGFR to Modulate Antitumor Immunity. *Frontiers in Immunology*, 9, 978. Available from: https://doi.org/10.3389/fimmu.2018.00978.

Yang, L., Pang, Y. & Moses, H.L. (2010) TGF-beta and immune cells: an important regulatory axis in the tumor microenvironment and progression. *Trends in Immunology*, 31(6), 220–227. Available from: https://doi.org/10.1016/j.it.2010.04.002.

Yeatts, A.B., Choquette, D.T. & Fisher, J.P. (2013) Bioreactors to influence stem cell fate: augmentation of mesenchymal stem cell signaling pathways via dynamic culture systems. *Biochimica Et Biophysica Acta*, 1830(2), 2470–2480. Available from: https://doi.org/10.1016/j.bbagen.2012.06.007.

Yee, K.O., Connolly, C.M., Duquette, M., Kazerounian, S., Washington, R. & Lawler, J. (2009) The effect of thrombospondin-1 on breast cancer metastasis. *Breast Cancer Research and Treatment*, 114(1), 85–96. Available from: https://doi.org/10.1007/s10549-008-9992-6.

Yıldırım, M., Atmaca, Z.E., Kayalar, O. & Oztay, F. (092017) Prevention the TGF-β induced epithelial-mesenchymal transition with atorvastatin in human A549 cell line. In: *Mechanisms of Lung Injury and Repair, ERS International Congress 2017 abstracts.* European Respiratory Society, PA1024.

Yoshida, G.J. (2020) Regulation of heterogeneous cancer-associated fibroblasts: the molecular pathology of activated signaling pathways. *Journal of Experimental & Clinical Cancer Research*, 39(1), 112. Available from: https://doi.org/10.1186/s13046-020-01611-0.

Yoshimura, T. (2018) The chemokine MCP-1 (CCL2) in the host interaction with cancer: a foe or ally? *Cellular & Molecular Immunology*, 15(4), 335–345. Available from: https://doi.org/10.1038/cmi.2017.135.

Yu, H., Ge, Y., Guo, L. & Huang, L. (2017) Potential approaches to the treatment of Ewing's sarcoma. *Oncotarget*, 8(3), 5523–5539. Available from: https://doi.org/10.18632/oncotarget.12566.

Završnik, J., Butinar, M., Prebanda, M.T., Krajnc, A., Vidmar, R. & Fonović, M. et al. (2017) Cystatin C deficiency suppresses tumor growth in a breast cancer model through decreased proliferation of tumor cells. *Oncotarget*, 8(43), 73793–73809. Available from: https://doi.org/10.18632/oncotarget.17379.

Zeltz, C., Primac, I., Erusappan, P., Alam, J., Noel, A. & Gullberg, D. (2020) Cancer-associated fibroblasts in desmoplastic tumors: emerging role of integrins. *Seminars in Cancer Biology*, 62, 166–181. Available from: https://doi.org/10.1016/j.semcancer.2019.08.004.

Zhang, R., Liu, Q., Li, T., Liao, Q. & Zhao, Y. (2019) Role of the complement system in the tumor microenvironment. *Cancer Cell International*, 19, 300. Available from: https://doi.org/10.1186/s12935-019-1027-3.

Zhang, W., Wang, H., Sun, M., Deng, X., Wu, X. & Ma, Y. et al. (2020) CXCL5/CXCR2 axis in tumor microenvironment as potential diagnostic biomarker and therapeutic target. *Cancer Communications*, 40(2-3), 69–80. Available from: https://doi.org/10.1002/cac2.12010.

Zhou, H.-M., Zhang, J.-G., Zhang, X. & Li, Q. (2021) Targeting cancer stem cells for reversing therapy resistance: mechanism, signaling, and prospective agents. *Signal Transduction and Targeted Therapy*, 6(1), 62. Available from: https://doi.org/10.1038/s41392-020-00430-1.

Zhou, J., Tang, Z., Gao, S., Li, C., Feng, Y. & Zhou, X. (2020) Tumor-Associated Macrophages: Recent Insights and Therapies. *Frontiers in Oncology*, 10, 188. Available from: https://doi.org/10.3389/fonc.2020.00188.

Ziani, L., Chouaib, S. & Thiery, J. (2018) Alteration of the Antitumor Immune Response by Cancer-Associated Fibroblasts. *Frontiers in Immunology*, 9, 414. Available from: https://doi.org/10.3389/fimmu.2018.00414.

# Supplementary Data

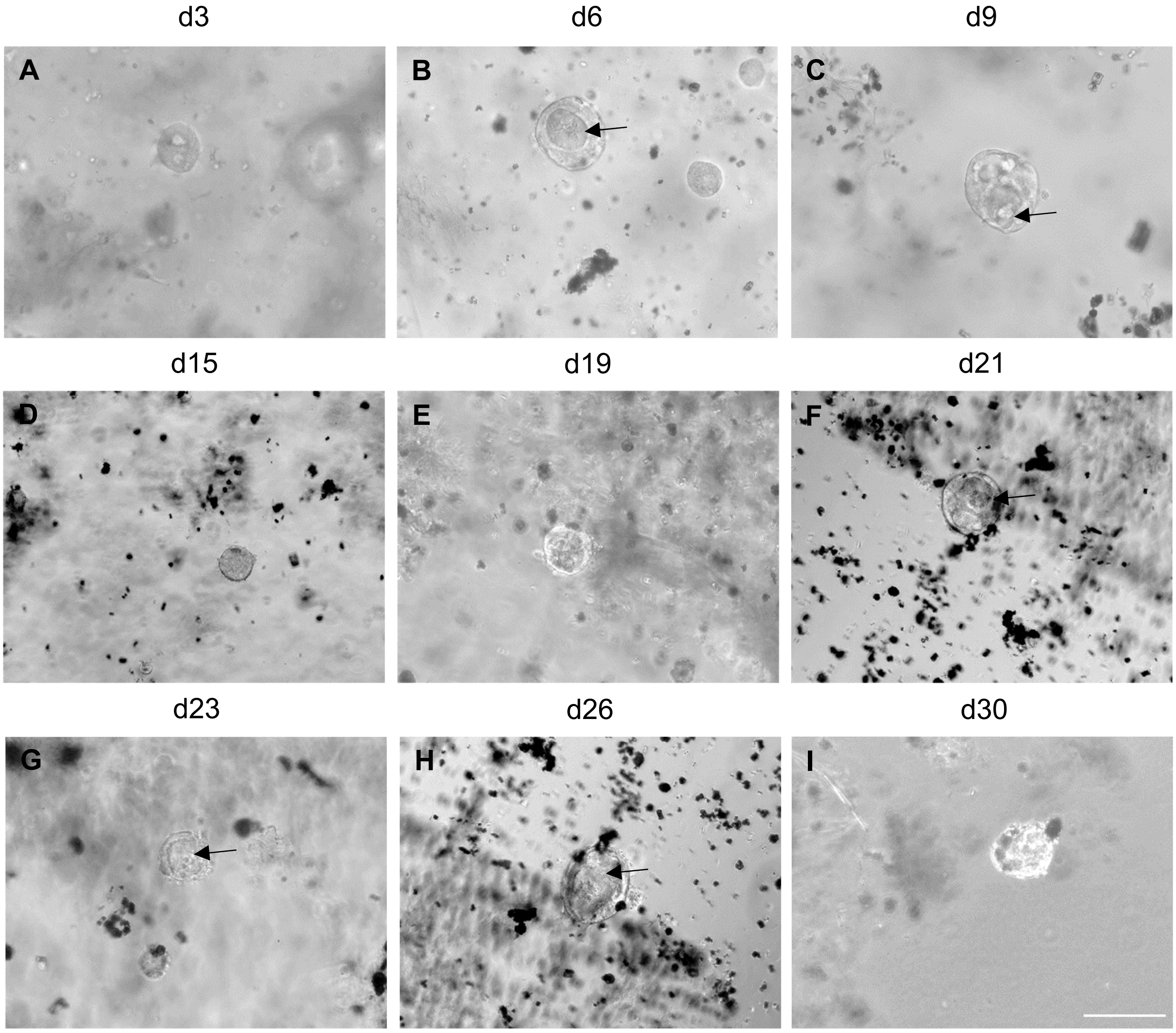

**Figure S1. Established organoids from healthy lung tissue in Matrigel® droplets.**

(A - I): Bright field images of organoids derived from healthy lung tissue that are cultured in Matrigel® for 30 days until growth stopped and the characteristic structure was lost. Until day 26 all organoids showed distinct core regions, which are indicated by black arrows. Scale bar indicates 100 µm. Representative images from one donor.

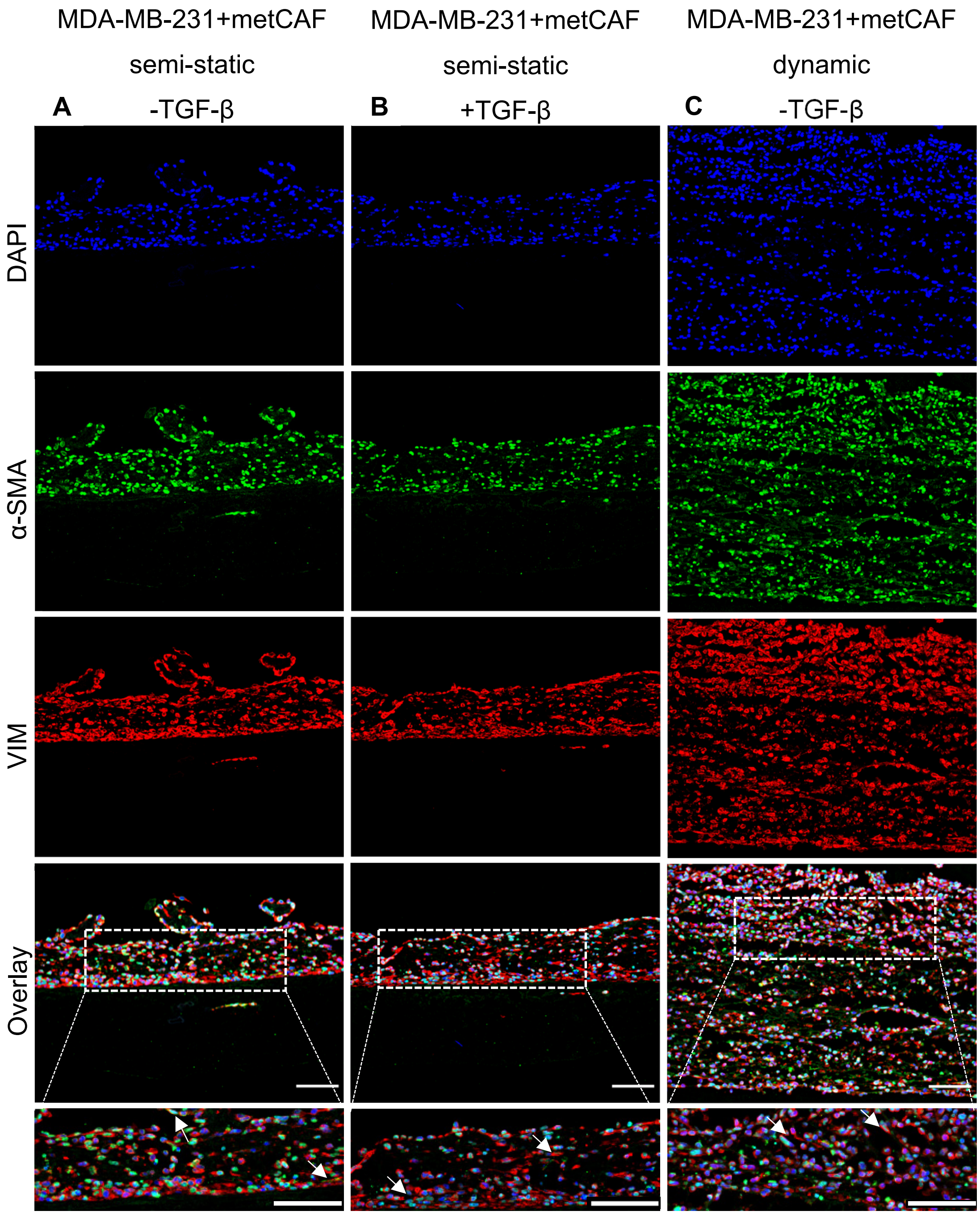

**Figure S2. Characterisation of stromal-enriched microphysiologic 3D breast tumour models with the CAF- marker alpha-SMA.**

(A - C): Immunofluorescence stainings of paraffin sections from semi-static or dynamic tumour models containing MDA-MB-231 cells and metCAFs. Medium was supplemented with 10 ng/ml TGF-β if indicated. Staining was directed against α-SMA (green), VIM (red). Nuclei are counterstained with DAPI (blue). Arrows in magnified images indicate stretched fibroblast cells, which were positively stained for α-SMA and VIM. Scale bars indicate 100 µm.

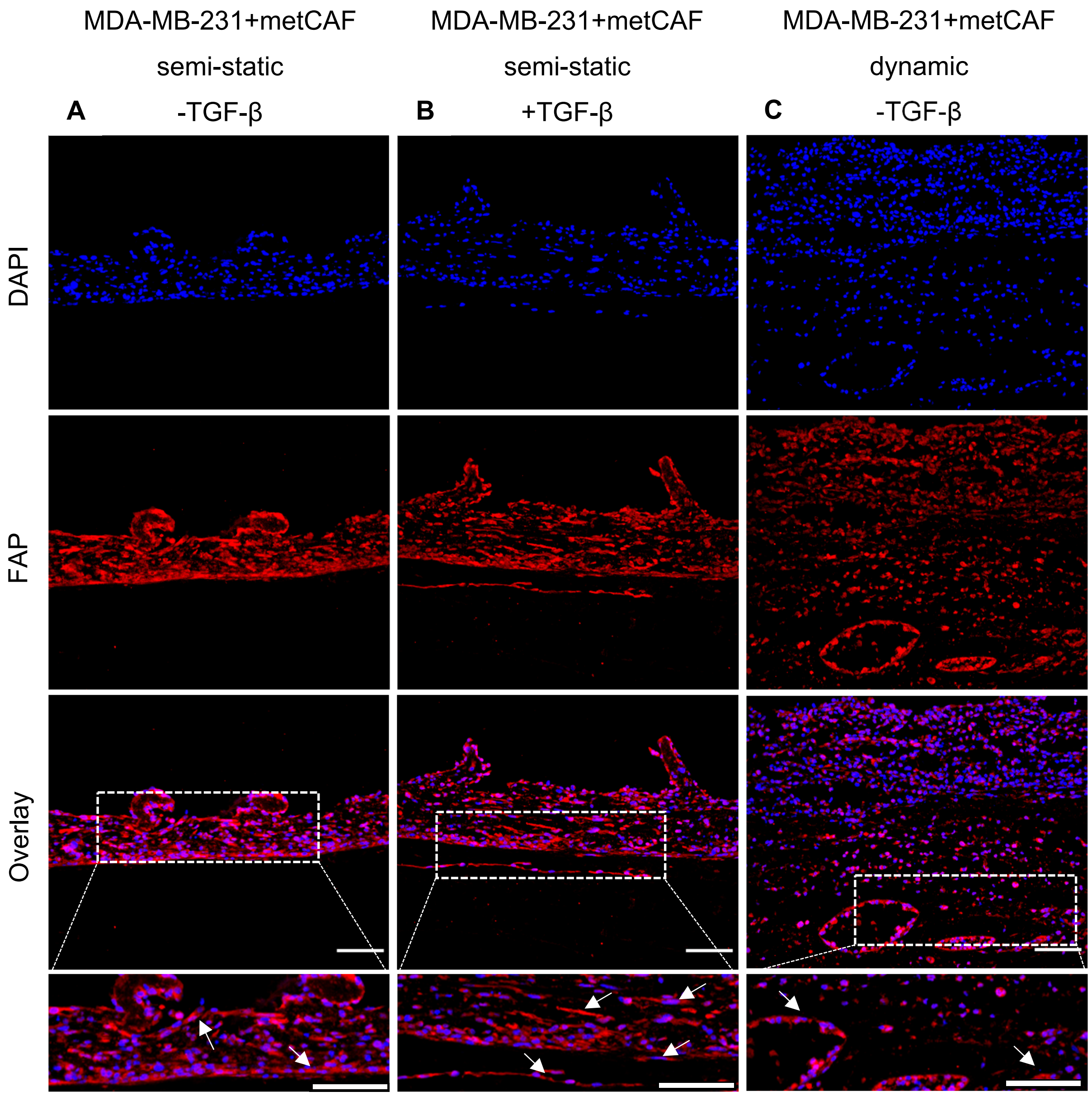

**Figure S3. Characterisation of stromal-enriched microphysiologic 3D breast tumour models for the CAF-specific marker FAP.**

(A - C): Immunofluorescence stainings of paraffin sections from semi-static or dynamic tumour models containing MDA-MB-231 cells and metCAFs. Culture was carried out in cell specific media that was supplemented with 10 ng/ml TGF-β if indicated. Staining was directed against FAP (red). Nuclei are counterstained with DAPI (blue). Arrows in magnified images indicated stretched fibroblast cells that are positively stained for FAP. Scale bars indicate 100 µm.

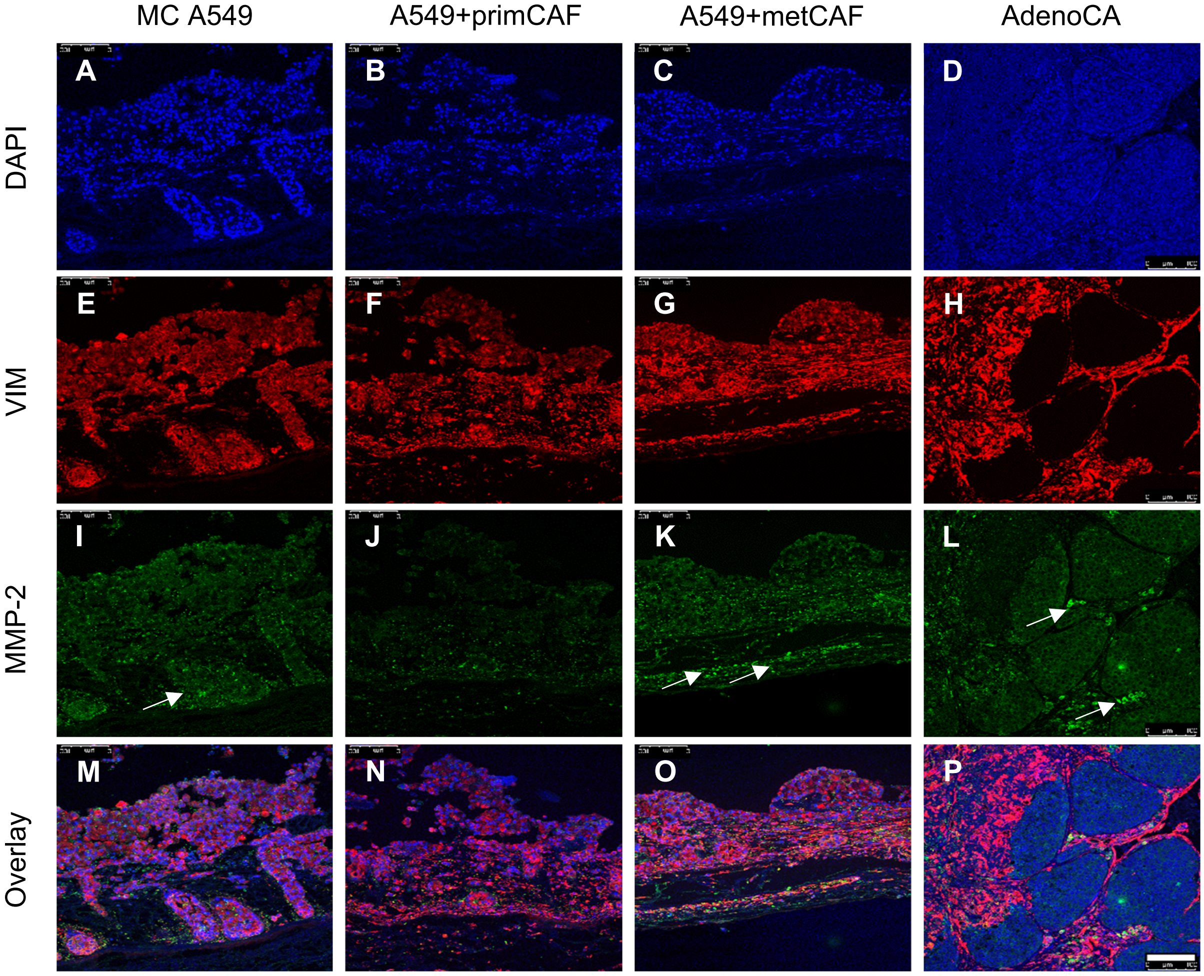

**Figure S4. Characterisation of implemented fibroblasts from lung tumour tissue with immunofluorescence staining of the CAF-associated marker Matrixmetalloproteasis 2 (MMP2).**

(A – P): Immunofluorescence staining of paraffin sections from dynamic tumour models containing A549 cells alone or in combination with either primCAFs or metCAFs. In addition, a biopsy of a lung adenocarcinoma was stained. Staining was directed against VIM (red) and MMP-2 (green). Monoculture of A549 cells and the co-culture containing metCAFs showed staining for MMP-2 located in areas of high cell density, indicated by white arrows. Nuclei are counterstained with DAPI (blue). Scale bar indicates 100 µm.

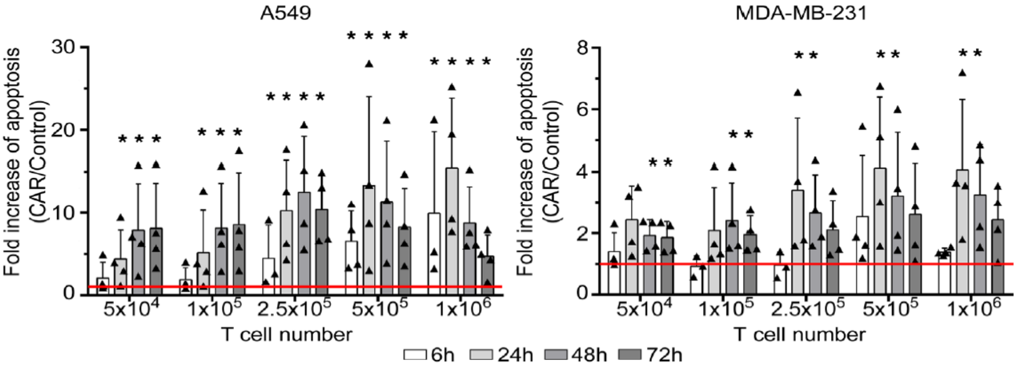

**Figure S5. Effect of ROR1 CAR T cell-treatment on static microphysiologic 3D lung and breast cancer models.**

Static tumour models containing either A549 or MDA-MB-231 cells were established for 11 days and treated with five different concentrations (5×$10^4$, 1x$10^5$, 2.5×$10^5$, 5x$10^5$, 1×$10^6$) of CDC$8^+$ ROR1 CAR T cells for 72 h. Non-transduced Control T cells (NT) served as control. Apoptosis was measured with M30 CytoDeath™ ELISA from supernatants that was sampled at the indicated time points and is presented as fold change compared to the same dose of control T cells (red line). The highest fold-increase of apoptosis was reached when 1x$10^6$ CAR T cells were administered with 4-fold (24h) for MDA-MB-231 cells and 15-fold (24h) for A549 cells. n = 4. Data are presented as arithmetic mean ± SD, Wilcoxon's rank-sum test: *$P < 0.05$. Image is adjusted from (Wallstabe, Göttlich, Nelke, Kühnemundt *et al.*, 2019)

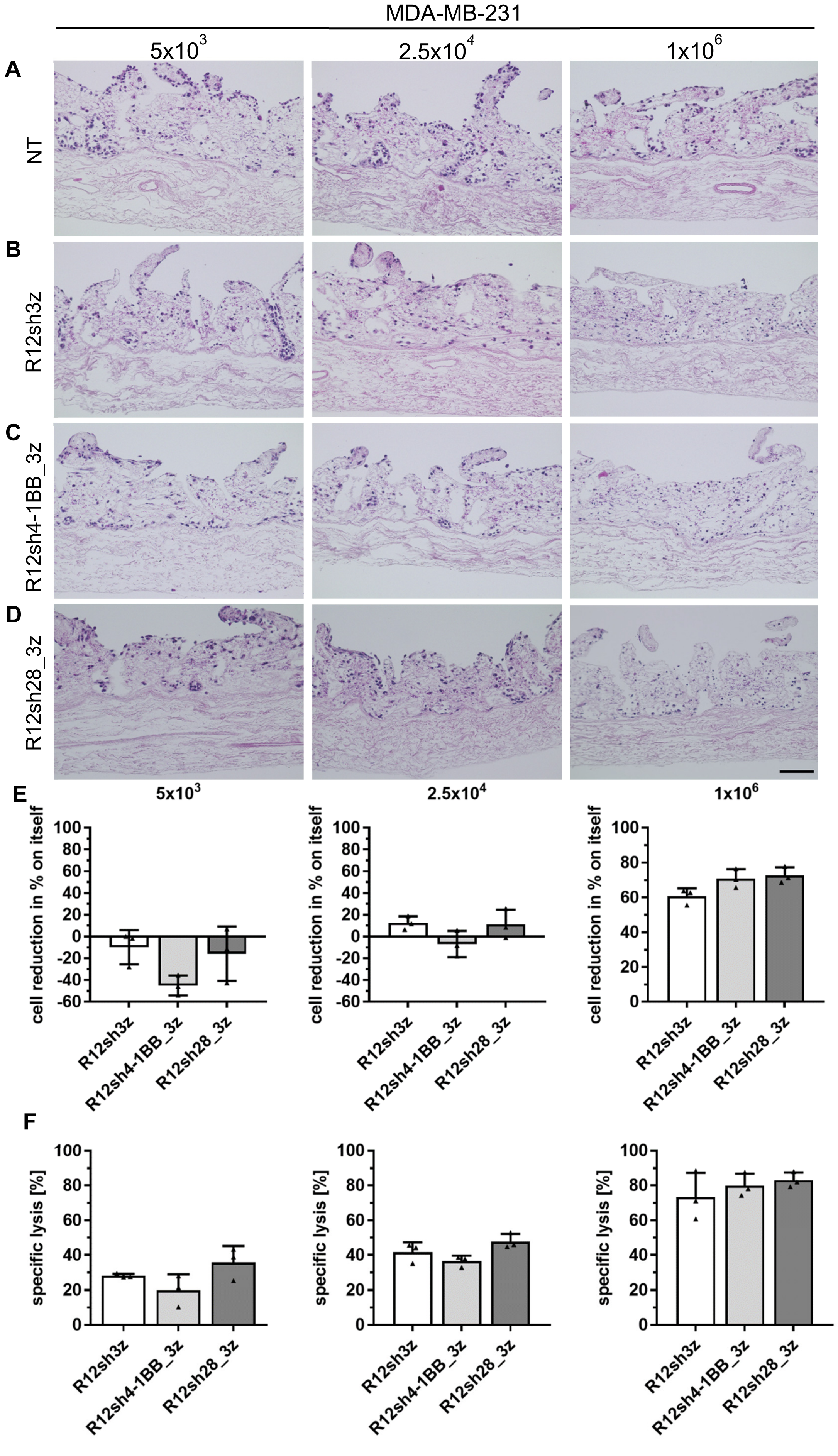
MDA-MB-231
5x10^3
2.5x10^4
1x10^6
A
NT
B
R12sh3z
C
R12sh4-1BB_3z
D
R12sh28_3z
E
5x10^3
2.5x10^4
1x10^6
cell reduction in % on itself
100
80
60
40
20
0
-20
-40
-60
R12sh3z
R12sh4-1BB_3z
R12sh28_3z
F
specific lysis [%]
100
80
60
40
20
0
R12sh3z
R12sh4-1BB_3z
R12sh28_3z

**Figure S6. ROR1 CAR T cells harbouring different costimulatory domains reduce tumour cells differently in static microphysiologic 3D breast tumour models.**

Static tumour models containing MDA-MB-231 cells were established and treated with three different concentrations ($5\times10^3$, $2.5\times10^4$, $1\times10^6$) of $CD8^+$ ROR1 CAR T cells for 3 days. ROR1 CAR T cells contained either no costimulatory domain (R12sh3z), a 4-1BB costimulatory domain (R12sh4-1BB_3z) or a CD28 costimulatory domain (R12sh28_3z). Models were either treated with ROR1 CAR T cells (CAR) or non-transduced control T cells (NT). (A – D): H&E staining of paraffin sections from tumour models containing MDA-MB-231 cells revealed a strong reduction of tumour cells when the highest concentration of CAR T cells was administered, while moderate effects occurred with $2.5\times10^4$ CAR T cells. Scale bar indicates 100 µm. (E & F): Quantification of specific lysis or cell reduction was performed via BLI-based measurements. Specific lysis and cell reduction revealed highest specific lysis for the ROR1 CAR T cells with CD28 costimulatory domain when $2.5\times10^4$ CAR T cells were administered, while the highest CAR T cell concentration induced comparable levels of lysis and cell reduction independent of implemented costimulatory domain. Data are presented as arithmetic mean of 3 cell crowns ± SD. n=1 experiment with 1 T cell donor.

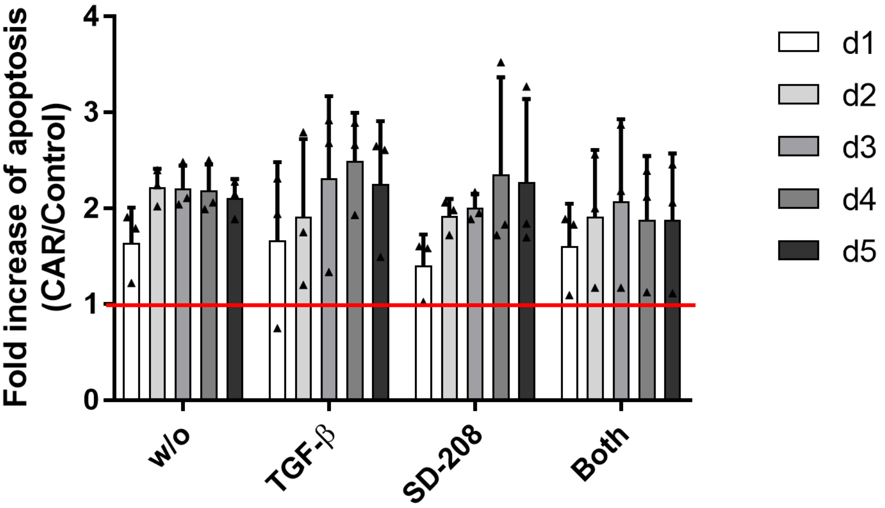

**Figure S7. Effects of ROR1 CAR T cells under the influence of TGF-β and the TGF-β receptor inhibitor SD-208 on the apoptosis of MDA-MB-231 cells, measured by M30 CytoDeath™ ELISA.**

Static models containing MDA-MB-231 tumour cells were treated over a 5 day period with a concentration of $5\times10^5$ $CD8^+$ control T cells or ROR1-CAR T cells. Models were cultured either in standard cell specific medium or under the presence of 10 ng/ml TGF-β and/or 1 µM SD-208**.** Supernatants were obtained every 24 h of the 5 day treatment period. Values were normalised to the respective control T cells (red line) and are indicated as fold-increase. Apoptosis was not significantly increased in one of the represented groups and never increased more than 2-fold. Values are presented as arithmetic mean ± SD from three independent experiments. 3 T cell donors.

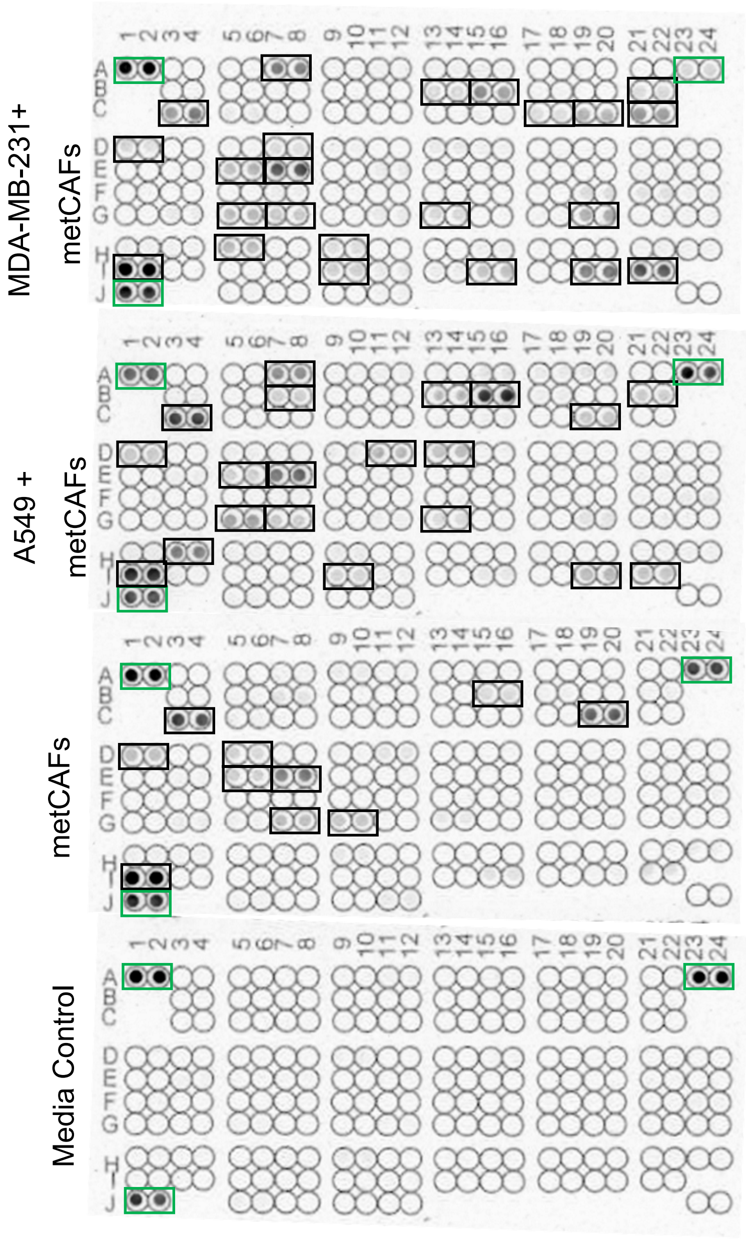

**Figure S8. Multiplex analysis using Proteome Profiler™ Array (Human XL Cytokine Array Kit) to analyse markers from the supernatant of semi-static microphysiologic 3D tumour models containing either metCAFs alone or in co-culture with either MDA-MB-231 or A549 tumour cells.**

Tumour models were cultured under semi-static conditions until homeostasis was reached at day 10 and supernatant was collected every 48 hours. Detailed information of array coordinates is provided in table S1. N=1.

*Table S1. Table Cytokines detected in stromal-enriched microphysiologic 3D tumour models and metCAFs monocultures by Proteome Profiler™ Array (Human XL Cytokine Array Kit).*

Colorcode: shared between all samples=green, shared between co-cultures=yellow; only detected in each sample itself=red

| Sample | Spot name | intensity | Coordinate |
|---|---|---|---|
| **Media Control** | Reference Spot | high | A 1-2 |
| | Reference Spot | high | A23-24 |
| | Reference Spot | high | J 1-2 |

| | | | |
|---|---|---|---|
| **Monoculture metCAF (MC metCAF)** | Reference Spot | high | A 1-2 |
| | Reference Spot | high | A23-24 |
| | Reference Spot | high | J 1-2 |
| | Dkk-1, Dickkopf-1 | low | B 15-16 |
| | ENA-78, CXCL5 | medium | C 3-4 |
| | GDF-15, MIC-1 | medium | C 19-20 |
| | GROα, CXCL1, MSGA-α | low | D 1-2 |
| | HGF, Scatter Factor, SF | low | D 5-6 |
| | IL-6 | low | E 5-6 |
| | IL-8, CXCL8 | medium | E 7-8 |
| | MCP-1, CCl2, MCAF | low | G 7-8 |
| | MCP-3, CCL7, MARC | low | G 9-10 |
| | Serpin E1, PAI-I, PAI-1, Nexin | high | I 1-2 |
| **Co-culture**<br>**A549 +metCAFs (CC A549)** | Reference Spot | medium | A 1-2 |
| | Reference Spot | high | A23-24 |
| | Reference Spot | high | J 1-2 |
| | Angiogenin | medium | A 7-8 |
| | Complement Factor D, Adipsin, CFD | low | B 7-8 |
| | Cystatin C, CST3, ARMD11 | low | B 13-14 |
| | Dkk-1, Dickkopf-1 | high | B 15-16 |
| | Emmprin, CD147, Basigin | low | B 21-22 |
| | ENA-78, CXCL5 | medium | C 3-4 |
| | GDF-15, MIC-1 | low | C 19-20 |
| | GROα, CXCL1, MSGA-α | low | D 1-2 |
| | IGFBP-2 | low | D 11-12 |
| | IGFBP-3 | low | D 13-14 |
| | IL-6 | low | E 5-6 |
| | IL-8, CXCL8 | medium | E 7-8 |
| | Lipocalin-2. NGAL, LCN2, Siderocalin | medium | G 5-6 |
| | MCP-1. CCL2, MCAF | low | G 7-8 |
| | MIF | low | G 13-14 |
| | Osteopontin, OPN | medium | H 3-4 |
| | Serpin E1, PAI-I, PAI-1, Nexin | strong | I 1-2 |
| | TFF3, ITF,TFI | low | I 9-10 |
| | uPAR, PLAUR | low | I 19-20 |
| | VEGF | low | I 21-22 |
| **Co-culture**<br>**MDA-MB-231 +metCAFs (CC MDA)** | Reference Spot | high | A 1-2 |
| | Reference Spot | low | A23-24 |
| | Reference Spot | high | J 1-2 |
| | Angiogenin | medium | A 7-8 |
| | Cystatin C, CST3, ARMD11 | low | B 13-14 |
| | Dkk-1, Dickkopf-1 | medium | B 15-16 |
| | Emmprin, CD147, Basigin | low | B 21-22 |
| | ENA-78, CXCL5 | medium | C 3-4 |
| | G-CSF, CSF3 | low | C 17-18 |
| | GDF-15, MIC-1 | medium | C 19-20 |
| | GM-CSF. CSF-2 | medium | C 21-22 |
| | GROα, CXCL1, MSGA-α | low | D 1-2 |
| | ICAM-1, CD54 | low | D 7-8 |
| | IL-6 | low | E 5-6 |
| | IL-8, CXCL8 | medium | E 7-8 |
| | Lipocalin-2. NGAL, LCN2, Siderocalin | low | G 5-6 |
| | MCP-1. CCl2, MCAF | low | G 7-8 |
| | MIF | low | G 13-14 |
| | MIP-3α | low | G 19-20 |
| | PDGF-AA | low | H 5-6 |
| | Pentraxin-3 | low | D 7-8 |
| | Serpin E1, PAI-I, PAI-1, Nexin | high | I 1-2 |
| | TFF3, ITF, TFI | low | I 9-10 |
| | Thrombospondin-1, THBS1, TSP-1 | low | I 15-16 |
| | uPAR, PLAUR | medium | I 19-20 |
| | VEGF | medium | I 21-22 |

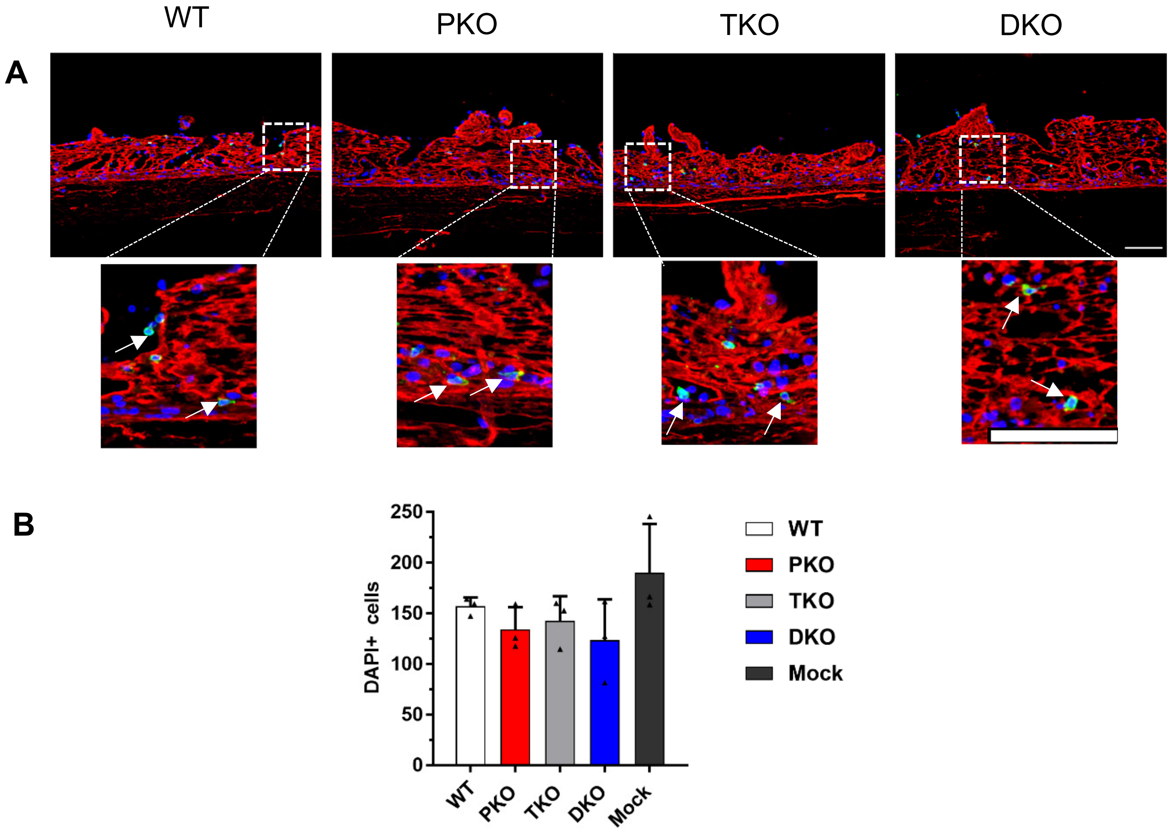

**Figure S9. Invasion of different gene-edited ROR1 CAR T cells into the stromal-enriched microphysiologic 3D breast tumour models.**

Tumour models contained MDA-MB-231 breast cancer cells together with primCAFs and were cultured under semi-static conditions. On day 10, 5x$10^4$ (equal amounts $CD4^+$ and $CD8^+$) different ROR1 CAR T cells were administered for 7 days. Models received either non-transduced control T cells (MOCK) or different gene-edited ROR1 CAR T cells (CAR) or models were left untreated (CTRL). Different gene-edited ROR1 CAR T cells are termed as follows: (WT) wild type=ROR1 CAR T cell without gene knock-out, (PKO) PD-1 KO, (TKO) TGF-β receptor KO, (DKO) KO of PD-1 KO and TGF-β receptor KO. Media was supplemented with 10 ng/ml TGF-β (A): Immunofluorescence staining of formalin fixed paraffin section against the leukocyte marker CD45 (green) and the matrix specific marker collagen IV (red) are shown. Nuclei are counterstained with DAPI (blue). Invading active $CD45^+$ CAR T cells were present in all groups, which are indicated by white arrows in magnified images. Representative images from 1 T cell donor are shown. (B): Quantification of $DAPI^+$ cells by cell counting (left). Only the control showed a slight increase of cells compared to CAR-treated models. Quantification of $CD45^+$ CAR T cells by manual counting (right). TKO and DKO showed higher numbers of active CAR T cells. Data shown are mean values ± SD from 1 cell crown (5 images per cell crown). N=4.

# Affidavit/Eidesstattliche Erklärung

## Affidavit

I hereby confirm that my thesis entitled

“***Defined microphysiologic 3D tumour models with aspects from the tumour microenvironment for the evaluation of cellular immunotherapies***”

is the result of my own work, I did not receive any help or support from commercial consultants. All sources and / or materials applied are listed and specified in the thesis.

Furthermore, I confirm that this thesis has not yet been submitted as part of another examination process neither in identical nor in similar form.

Place, Date

Signature

## Eidesstattliche Erklärung

Hiermit erkläre ich an Eides statt, die Dissertation

„***Definierte mikrophysiologische 3D-Tumormodelle mit Aspekten aus der Tumormikroumgebung zur Evaluierung von zellulären Immuntherapien***“

eigenständig, d.h. insbesondere selbstständig und ohne Hilfe eines kommerziellen Promotionsberaters angefertigt und keine anderen als die von mir angegebenen Quellen und Hilfsmittel verwendet zu haben.

Ich erkläre außerdem, dass die Dissertation weder in gleicher noch in ähnlicher Form bereits in einem anderen Prüfungsverfahren vorgelegen hat.

Ort, Datum

Unterschrift

# Statement of individual author contribution/Eigenanteilserklärung

Some figures include data that has been already published with respective co-authorships. Respective citations are included.

Fig. 10 Image A and D were modified from (Kühnemundt *et al.*, 2020)

Fig. 16 is modified from (Kailayangiri *et al.*, 2019)

Fig. 20, 22, S5 (modified) are from (Wallstabe, Göttlich, Nelke, Kühnemundt *et al.*, 2019)

Fig. 23 is from (Stüber *et al.*, 2020)

Parts of this work resulted from cooperation projects.

Dr Lars Wallstabe or Dr Razieh Monjezi provided ROR1 CAR T cells and performed cytokine ELISAs and flow cytometry analysis in most cases.

Dr Sareetha Kailayangiri provided $G_{D2}$ CAR T cells and performed flow cytometry analysis of the latter.

## Acknowledgement/Danksagung

While writing these lines I somewhat finished the majority of writing and it still does not feel like the finish line is even close. Even though, this work carries only one author name it would definitely not have been created without all the people from the following pages.

I want to thank my committee members, Prof. Heike Walles, who sparked my interest in tissue engineering in the first place several years ago. Thank you for all the inspiration, advice and help!
A huge thank you to Prof. Michael Hudecek - Thank you for introducing me into the fascinating world of CAR T cells, sparking my dedication, even though having, one of the fullest schedules, and for always giving me good advice when I needed it.

Thank you Dr Julia Schüler. Thank you for always being the help from the far distance of Freiburg and for giving me the opportunity to be an intern at Charles River/Oncotest. That time really inspired many good ideas for my project.

Next, I want to thank Dr Gudrun Dandekar, who has always been the rock in the river of a doctoral thesis. Thank you for the, sometimes heated and fruitful discussions, for believing and trusting in me and my gained knowledge.

After my committee, I want to thank all the members of the tumour group that stayed and left during my years in Würzburg. Dr Sarah Nietzer, thank you for all your input and ideas and your often-needed relaxed and calm attitude towards things, which already stressed me out. Matthias Peindl, thank you for being an excellent Master student and now PhD student-colleague and always bringing your humour and relaxed attitude to work. Thank you for the countless times of your help in the lab including tremendous mental support. I also want to thank Heide Häfner for the many answered questions und the help during the last years. For those who already left: Thank you Dr. Claudia Göttlich, Dr. Lena Nelke and Dr. Florentin Baur who taught me all the basic stuff and more in the beginning here in the lab, who mentored me, and cheered me up after first things failed. Thank you Florentin, for teaching me incredible stuff everyday from your endless knowledge. Thank you Claudia for your mentorship when I transitioned from being a master student to my PhD project.

Next, I want to thank the members of AG Hudecek, who provided their CAR T cells and knowledge and, therefore, made this whole work possible. Thank you Dr. Lars Wallstabe, for your support during the experiments, answering countless questions when I first started to work in this project (which, nevertheless, continued till the end). Thank you for the fun we had during experiments by confusing each other but still managing to finish the work. Thank you Dr. Miriam Alb, who jumped in for Lars. Thank you Dr. Razieh Monjezi for letting me use you sneakily designed CAR T cells and expanding this work even further. Thank you for all your help and I really hope your cells will one day cure many patients!

Additionally, I want to thank Dr. Sareetha Kailayangiri for the cooperation on the Ewing's sarcoma part, for providing the CAR T cells and making that part of the work interesting with great teamwork.

Thanks to Maxi Wussmann and Verena Schneider, who introduced me into working with skin models even though the results didn't make it into this work.

As being a scientist is a stressful task, I want to thank the whole TERM. The people who made the work fun and who make the TERM what it is: A sometimes chaotic but interdisciplinary and special place.

Additionally, after working with the SISmuc matrix I want to express my gratitude symbolically for the animals that had to give their lifes so that we can do our work. Thank you to all the nameless pigs. I hope that we will find a way to spare your future siblings by finding animal-free alternatives!

Next, I want to thank Kristina, who helped me a lot by correcting English mistakes and fought herself through the entire work. I will be forever grateful that you overtook this part ☺.

I want to give special thanks to my office-mates (for most times) and some of my best friends: Philipp Fey, Marius Gensler and Philipp's office wife Christina Fey ☺. Without you, I would surely not have finished. Thanks for all the fun, support inside the lab and out. For hilarious times, that hopefully continue. For being my lab family. As soon as Covid-19 allows there will be a lot of wine after finishing this, especially for you Muddi ☺.

I want to thank my friends and family and especially my grandparents. Thank your for always being so curious, supporting and just the best! Additionally, I want to thank the Sputh's-family, who always welcomed and supported me especially during the stressful final phase of submitting this work. Thank you all for everything!

Finally, I want to thank you Sebi, my love. Thank you for being my anchor, support, cheerleader in any way imaginable (but especially when technical issues or software problems shattered my last nerve…☺). Thank you for taking me as I am at any time. I will always try to do the same for you! There are no perfect words to put this but for a start: "*I love you x3000*"

# List of publications and conference contributions

## Articles

**Kühnemundt*, J.**, Leifeld*, H., Scherg*, F., Schmitt*, M., Nelke, L., Schmitt, T., Baur, F., Göttlich, C., Fuchs, M., Kunz, M., Peindl, M., Brähler, C., Kronenthaler, C., Wischhusen, J., Prelog, M., Walles, H., Dandekar, T., Dandekar, G., and Nietzer, S. L. 2020. Modular micro-physiological human tumor/tissue models based on decellularized tissue for improved preclinical testing. ALTEX.

Stüber*, T., Monjezi*, R., Wallstabe, L., **Kühnemundt, J.**, Nietzer, S. L., Dandekar, G., Wöckel, A., Einsele, H., Wischhusen, J., and Hudecek, M. 2020. Inhibition of TGF-β-receptor signaling augments the antitumor function of ROR1-specific CAR T-cells against triple-negative breast cancer. Journal for immunotherapy of cancer 8, 1.

Wallstabe*, L., Göttlich*, C., Nelke*, L. C., **Kühnemundt*, J.**, Schwarz, T., Nerreter, T., Einsele, H., Walles, H., Dandekar, G., Nietzer, S. L., and Hudecek, M. 2019. ROR1-CAR T cells are effective against lung and breast cancer in advanced microphysiologic 3D tumor models. JCI insight 4, 18.

Kailayangiri, S., Altvater, B., Lesch, S., Balbach, S., Göttlich, C., **Kühnemundt, J.**, Mikesch, J.-H., Schelhaas, S., Jamitzky, S., Meltzer, J., Farwick, N., Greune, L., Fluegge, M., Kerl, K., Lode, H. N., Siebert, N., Müller, I., Walles, H., Hartmann, W., and Rossig, C. 2019. EZH2 Inhibition in Ewing Sarcoma Upregulates GD2 Expression for Targeting with Gene-Modified T Cells. Molecular therapy: the journal of the American Society of Gene Therapy 27, 5, 933–946.

Lübtow, M. M., Nelke, L. C., Seifert, J., **Kühnemundt, J.**, Sahay, G., Dandekar, G., Nietzer, S. L., and Luxenhofer, R. 2019. Drug induced micellization into ultra-high capacity and stable curcumin nanoformulations: Physico-chemical characterization and evaluation in 2D and 3D in vitro models. Journal of controlled release: official journal of the Controlled Release Society 303, 162–180.

*equally contributing shared first co-authorship

## Oral Presentation

**Kühnemundt J.** *et al.,* “Novel 3D tumour models with stromal components to evaluate the efficacy of immunotherapy with gene-engineered ROR1-specific CAR T cells in solid tumours”, European Association for Cancer Research (EACR), Good Bye Flat Biology, 2018, Berlin. Germany

## Poster Presentations

**Kühnemundt J.** *et al.,* “Novel 3D models with tumour microenvironment to evaluate the efficacy of different immunotherapeutic approaches in solid tumours”, AEK Cancer Congress Heidelberg, 2019, Heidelberg, Germany

**Kühnemundt J.** *et al.,* “Novel 3D tumour models with stromal components to evaluate the efficacy of immunotherapy with gene-engineered ROR1-specific CAR T cells in solid tumours”, Deutsche Gesellschaft für Immunologie (DGfI) Autumn School, 2018, Merseburg, Germany

**Kühnemundt J.** *et al.,* “Novel 3D tumour models with stromal components to evaluate the efficacy of immunotherapy with gene-engineered ROR1-specific CAR T cells in solid tumours”, European Association for Cancer Research (EACR), Good Bye Flat Biology, 2018, Berlin. Germany

**Kühnemundt J.** *et al.*, “Novel 3D tumour models with stromal components to evaluate the efficacy of immunotherapy with gene-engineered ROR1-specific CAR T cells”, Gesellschaft für Chemische Technik und Biotechnologie e.V. (DECHEMA), 3D Cell Culture, 2018, Freiburg, Germany